

UNIVERSIDAD NACIONAL DEL LITORAL



Design, Simulation, Fabrication and Characterization of Mass Microsensors Embeddable to an Implantable Microvalve for Glaucoma Treatment

Martín Zalazar

FICH

FACULTAD DE INGENIERIA
Y CIENCIAS HIDRICAS

INTEC

INSTITUTO DE DESARROLLO TECNOLOGICO
PARA LA INDUSTRIA QUIMICA

Tesis de Doctorado **2013**



UNIVERSIDAD NACIONAL DEL LITORAL
Facultad de Ingeniería y Ciencias Hídricas
Instituto de Desarrollo Tecnológico para la Industria Química

**DESIGN, SIMULATION, FABRICATION AND
CHARACTERIZATION OF MASS MICROSENSORS
EMBEDDABLE TO AN IMPLANTABLE MICROVALVE
FOR GLAUCOMA TREATMENT**

Martín Zalazar

Tesis remitida al Comité Académico del Doctorado
como parte de los requisitos para la obtención
del grado de
DOCTOR EN INGENIERIA
Mención Mecánica Computacional
de la
UNIVERSIDAD NACIONAL DEL LITORAL

2013

Comisión de Posgrado, Facultad de Ingeniería y Ciencias Hídricas, Ciudad Universitaria, Paraje "El Pozo",
S3000, Santa Fe, Argentina

**DESIGN, SIMULATION, FABRICATION AND
CHARACTERIZATION OF MASS MICROSENSORS
EMBEDDABLE TO AN IMPLANTABLE MICROVALVE
FOR GLAUCOMA TREATMENT**

by

Martín Zalazar

Dissertation submitted to the Postgraduate Department of the

FACULTAD DE INGENIERÍA Y CIENCIAS HÍDRICAS

of the

UNIVERSIDAD NACIONAL DEL LITORAL

in partial fulfillment of the requirements for the degree of

Doctor en Ingeniería - Mención Mecánica Computacional

2013

Author Legal Declaration

This dissertation have been submitted to the Postgraduate Department of the Facultad de Ingeniería y Ciencias Hídricas in partial fulfillment of the requirements the degree of Doctor en Ingeniería - Mención Mecánica Computacional of the Universidad Nacional del Litoral. A copy of this document will be available at the University Library and it will be subjected to the Library's legal normative.

Some parts of the work presented in this thesis have been (or are going to be) published in the following journals: Applied Physics Letters, IEEE Transactions on Ultrasonics, Ferroelectrics and Frequency Control, and Mecánica Computacional.

Martín Zalazar

© Copyright by

Martín Zalazar

2013

In memory of my father

**DESIGN, SIMULATION, FABRICATION AND
CHARACTERIZATION OF MASS MICROSENSORS
EMBEDDABLE TO AN IMPLANTABLE MICROVALVE
FOR GLAUCOMA TREATMENT**

Thesis advisor:

Fabio A. Guarnieri INTEC (CONICET-UNL),
Facultad de Ingeniería y Ciencias Hídricas - UNL
Laboratorio de BioMEMS,
Facultad de Ingeniería, Bioingeniería - UNER

Evaluation committee members:

Dr. Oscar De Sanctis FCEIyA, IFIR - UNR
Dr. Alberto Cardona CIMEC - CONICET, UNL
Dr. Marcelo Otero FCEyN - UBA
Dr. Orlando Auciello University of Texas at Dallas

*FACULTAD DE INGENIERÍA Y CIENCIAS HÍDRICAS
UNIVERSIDAD NACIONAL DEL LITORAL*

Acknowledgements

This thesis has received financial support from Consejo Nacional de Investigaciones Científicas y Técnicas (CONICET), Universidad Nacional del Litoral (UNL), and Agencia Nacional de Promoción Científica y Tecnológica (ANPCyT). The research work was carried out at the Centro Internacional de Métodos Computacionales en Ingeniería (CIMEC) dependent of UNL-CONICET, and at the Facultad de Ingeniería, Bioingeniería, Universidad Nacional de Entre Ríos (UNER). Part of the R&D, specifically the work on synthesis and characterization of AIN and ultrananocrystalline diamond films and integration for piezoactuated UNCD-based MEMS drug delivery devices was done at Argonne National Laboratory, Argonne, IL, USA.

I would like to thank my advisor Fabio A. Guarnieri who gave me the opportunity to be part of this wonderful project. Furthermore I would like to thank Fernando Sasseti for his enthusiasm and support on the way. I also would like to thank the people at CIMEC for sharing with me their knowledge on computational mechanics.

I would like to take the opportunity to especially thank the person who have supported me throughout this process, both by keeping me harmonious and encouraging me: my wife Gisela. Finally, an honorable mention goes to my family for their understandings and supports on me in completing this thesis.

Contents

Author Legal Declaration.....	vii
Acknowledgements	xi
Contents	xiii
List of Abbreviations.....	xix
List of Symbols	xxiii
List of Figures	xxix
List of tables.....	xxxv
Introduction	xxxvii
Chapters description.....	xl
Bibliography.....	xlii
Objectives	xliv
General Objective.....	xliv
Specific Objectives.....	xliv
CHAPTER 1: Acoustic devices	1
1.1 Sensors	1
1.2 Crystallography	2
1.2.1 Crystal structures.....	2
1.2.2 Crystal systems.....	3
1.3 Linear Theory of Piezoelectricity.....	4
1.3.1 Origin of polarization	4
1.3.2 Crystallography Applied to Piezoelectric Crystals	6
1.3.3 Mathematical formulation of the piezoelectric effect	6
1.3.4 General constitutive equations	9
1.3.5 Boundary conditions	10
1.3.6 Alternate Forms of Constitutive Equations.....	11
1.4 Acoustic wave technology	11
1.4.1 Acoustic wave in solids.....	12
1.4.2 Electroacoustic resonator operation	12

1.5 Resonant piezoelectric sensors	15
1.5.1 Overview of piezoelectric resonators	15
1.5.2 Modes of actuation/sensing	15
1.5.3 Types of Resonant piezoelectric sensors	17
1.6 Piezoelectric coupling constant	20
1.7 Bibliography	23
CHAPTER 2: MEMS Technology	25
2.1 Photolithography	25
2.1.1 Masks ¹	27
2.1.2 Alignment	28
2.1.3 Photoresist deposition ¹	29
2.1.4 Soft baking ¹	30
2.1.5 Exposure ¹	31
2.1.5 Development ¹	31
2.1.6 Descumming ¹	32
2.1.7 Resists ¹	32
2.1.8 Resist stripping ¹	33
2.1.9 Soft Lithography	33
2.2 Pattern Transfer with Subtractive Techniques ²	34
2.2.1 Wet etching	34
2.2.2 Dry etching	35
2.3 Pattern Transfer with Additive Techniques ²	36
2.3.1 MEMS Thin Film Deposition Processes	36
2.3.2 Chemical Vapor Deposition	37
2.3.3 Electrodeposition	38
2.3.4 Molecular Beam Epitaxy (MBE)	38
2.3.5 Thermal oxidation	39
2.3.6 Physical Vapor Deposition	39
2.3.7 Casting	41
2.4 Bibliography	42
CHAPTER 3: Models for Piezoelectric Resonators	43
3.1 Analytical Model (Sauerbrey equation)	43

3.2 Lumped model (circuital).....	45
3.2.1 Equivalent Electrical Circuit	45
3.2.2 Effect of dissipation on the definition of frequencies near resonance and antiresonance	48
3.2.3 Surface loaded resonator	49
3.3 Mason model.....	49
3.3.1 One-dimensional equations for a nonpiezoelectric slab.....	50
3.3.2 One-dimensional equations for a piezoelectric slab.....	52
3.3.3 Closed form expression for the input impedance ⁹	54
3.4 FEM model.....	56
3.4.1 Discretization	57
3.4.2 Finite Element Equations	58
3.4.3 BoundaryConditions.....	59
3.4.4 Harmonic Analysis.....	60
3.4.5 Admittance	61
3.5 Implementation of FEM model.....	61
3.5.1 About the software	61
3.5.2 Piezoelectrical Constitutive Relations.....	62
3.5.3 Electrical Formulations	63
3.5.4 Piezoelectric Dissipation.....	63
3.6 Bibliography.....	65
CHAPTER 4: Devices simulations	67
4.1 Quartz Crystal Microbalance	67
4.1.1 Design	68
4.1.2 Circuital model.....	69
4.1.3 FEM model.....	72
4.1.4 Discussion and conclusions.....	78
4.2 PVDF mass microsensor	79
4.2.1 Design	80
4.2.2 Mason model.....	80
4.2.3 FEM model.....	82
4.2.4 Discussion and conclusions.....	87
4.3 AlN mass microsensor	88
4.3.1 Biosensor.....	89

4.3.2 Design.....	89
4.3.3 Mason model	90
4.3.4 FEM model.....	94
4.3.5 Discussion and conclusions	96
4.4 PVDF pressure microsensor	97
4.4.1 Design.....	97
4.4.2 FEM model.....	98
4.4.3 Discussion and conclusions	102
4.5 Bibliography	103
CHAPTER 5: Fabrication and Characterization.....	107
5.1 PVDF Resonator.....	107
5.1.1 Resonator fabrication.....	108
5.1.2 Characterization.....	109
5.1.3 Conclusions	112
5.2 FEM-Based Parameter Extraction of a PVDF Resonator.....	113
5.2.1 Materials and Methods	114
5.2.2 Results and Discussion	117
5.2.3 Conclusions	121
5.3 AlN Resonator	123
5.3.1 Deposition process.....	123
5.3.2 Characterization.....	124
5.3.3 Conclusions	128
5.4 Integration of AlN and UNCD Films	130
5.4.1 Experimental procedure for synthesis of thin Films and characterization.....	131
5.4.2 Influence of surface roughness on AlN synthesis and properties.....	134
5.4.3 Piezoelectric response of AlN films	136
5.4.4 Conclusions	138
5.5 AlN FBAR on UNCD	139
5.5.1 Geometry design.....	139
5.5.2 Mask design and fabrication.....	140
5.5.3 Membrane fabrication	142
5.5.4 Characterization.....	143
5.5.5 Conclusions	145

5.6 Bibliography.....	146
Conclusions and Future Works	149
Simulation	149
Fabrication.....	150
Future Works.....	151
Appendix A	153
CMOS Microtransponder for implantable microvalve	153
A.1 Introduction	153
A. 2 Circuit Block Diagram	154
A.3 Circuit Design	155
A.4 Simulations and Results	158
A.5 Conclusions	160
A.6 Bibliography.....	161
Appendix B	163
UNCD-based Drug Delivery Devices	163
B.1 Experimental.....	164
B.2 Conclusions	166
Appendix C	167
Resumen extendido	167
Introducción	171
Objetivos	174
Objetivo general	174
Objetivos particulares.....	174
C.1 Dispositivos acústicos	175
C.1.1 Piezoelectricidad.....	175
C.1.2 Tecnología electroacústica	177
C.1.3 Resonador electroacústico	177
C.2 Modelado.....	178
C.2.1 Modelo Analítico (Ecuación de Sauerbrey)	178
C.2.2 Modelo de Mason.....	178
C.2.3 Modelo Circuital.....	179

C.2.4 Modelo de Elementos Finitos	180
C.3 Simulación	182
C.3.1 Microbalanza de cristal de cuarzo (QCM).....	182
C.3.2 Microsensor de masa de PVDF.....	185
C.3.3 Microsensor gravimétrico de nitruro de aluminio (AlN)	187
C.3.4 Microsensor de presión de PVDF.....	188
C.3.5 Microtransponder CMOS para microválvula implantable	190
C.4 Fabricación y Caracterización	192
C.4.1 Resonador de PVDF	192
C.4.2 Resonador piezoeléctrico de AlN	194
C.4.3 Integración de AlN sobre películas de UNCD.....	195
C.4.4 FBAR de AlN sobre UNCD	197
C.4.5 Membrana de UNCD para delivery de drogas.....	200
C.5 Conclusiones.....	201

List of Abbreviations

AE	Auxiliary electrode
AlN	Aluminium Nitride
ASK	Amplitude Shift Keying
BAW	Bulk acoustic wave
BC	Boundary condition
BioMEMS	MEMS applied to the medical and biotechnology field
B-UNCD	Boron doped UNCD
BVD	Butterworth-Van Dike equivalent circuit
CAD	Computer aided design
CAD	Computer-aided design
CMOS	Complementary metal-oxide-semiconductor
CMP	Chemical mechanical polishing
CP	Conjugated polymer
CVD	Chemical Vapor Deposition
DDS	Drug delivery system
DDS	Drug Delivery Devices
DOF	Degrees of freedom
DRIE	Deep reactive ion etching
FBAR	Thin film bulk acoustic wave resonator
FD	Fully differential potentiostat architecture

FEM	Finite Element Method
FIB	Focused ion beam
IC	Integrated Circuit
IDT	Interdigitated transducer
IOP	Intraocular pressure
KOH	Potassium hydroxide
LPCVD	Low Pressure Chemical Vapor Deposition
LSLPCVD	Low stress, low pressure chemical vapor deposition
MBVD	Modified Butterworth-Van Dike equivalent circuit
MCD	Microcrystalline diamond
MEMS	MicroElectroMechanical Systems
NEMS	NanoElectroMechanical Systems
MPCVD	Microwave plasma enhanced chemical vapor deposition
NCD	Nanocrystalline diamond
N-UNCD	Nitrogen-incorporated UNCD
PCB	Printed Circuit Board
PDEs	Partial differential equations
PDMS	Poly(dimethylsiloxane)
PECVD	Plasma Enhanced Chemical Vapor Deposition
PFM	Piezoresponse Force Microscopy
PR	Photoresist
PVD	Physical Vapor Deposition
PVDF	Polyvinylidene fluoride
PZT	Lead zirconium titanate
QCM	Quartz crystal microbalance
RFID	Radio frequency identification
RIE	Reactive ion etching
RTDs	Resistance temperature detectors
SAW	Surface acoustic wave

SE	Single-ended potentiostat architecture
SEM	Scanning electron microscopy
SMR	Solidly-mounted resonator
TSM	Thickness-Shear-Mode resonators
ULSI	Ultra Large Scale Integration
UNCD	Ultrananocrystalline diamond
VLSI	Very Large Scale Integration
WE	Working electrode
XRD	X-ray diffraction

List of Symbols

β	Complex wave propagation constant
Δf_a	Analytical frequency shift
Δf_c	Frequency shift of the circuital model
Δ_{ffem}	Frequency shift of the FEM model
Δ_{fM}	Frequency shift of the Mason model
Δf_r	Frequency shift
δ	Dirac delta function
δ_{ij}	Kronecker delta
δW	Variational electrical energy
$\tilde{\boldsymbol{\epsilon}}$	Complex permittivity matrix
ϵ_0	Permittivity in free space
$\boldsymbol{\epsilon}$	Permittivity matrix
ϵ_p	Permittivity of the piezoelectric material
ϵ_r	Relative permittivity
η_a	Viscosity of the liquid
η_p	Piezoelectric viscosity
η_x	Loss factor
θ	Absolute temperature of a material
$\boldsymbol{\kappa}$	Electric susceptibility
λ	Wavelength

ρ	Density of a material
ρ_a	Density of the liquid
ρ_f	Density of the deposited film
ρ_p	Density of the piezoelectric material
ρ_s	Mass per area of the deposited layer
σ	Entropy
σ_n	Normal stress
ϕ	Electric potential
ω	Angular frequency
ω_0	Fundamental angular frequency
Ω	Volume of the piezoelectric medium
A_e	Electrode area
$\mathbf{A}_{e=1}^{n_e}$	Assembly operator
\mathbf{c}, c_{33}	Linear elastic matrix or stiffness matrix
$\tilde{\mathbf{c}}$	Complex linear elastic matrix
\bar{c}	Piezoelectrically stiffened constant
C_0	Static or clamped capacitance
C_1	Electric capacitance
c_p	Elastic constant or stiffness coefficient of the piezoelectric material
\mathbf{C}_{uu}	Damping matrix
$\tilde{\mathbf{d}}$	Complex piezoelectric coupling matrix
\mathbf{d}	Piezoelectric coupling matrix
\mathbf{D}	Electrical displacement vector
d_q	Distance of separation between p and q
\mathbf{e}	Piezoelectric coupling matrix
$\tilde{\mathbf{e}}$	Complex piezoelectric coupling matrix
\mathbf{E}	Electric field vector
$\hat{\mathbf{E}}$	Test function for the electric field
F	Applied force
\mathbf{F}	Nodal mechanical force vector

\mathbf{f}_{pk}	Mechanical point force
f_0	Natural vibration fundamental frequency or resonant frequency
f_1	Admittance maxima for a lossless resonator
f_2	Impedance maxima for a lossless resonator
f_a	Antiresonance frequency for a lossy resonator
f_n	Frequency of minimum admittance for a lossy resonator
f_m	Frequency of maximum admittance for a lossy resonator
f_p	Parallel resonance frequency for a lossy resonator
f_s	Series resonance frequency for a lossy resonator
f_r	Resonance frequency for a lossy resonator
G	Complex dynamic modulus
G	Gibbs thermoelectric state function
G'	Storage moduli
G''	Loss moduli
hC_0	Turns ratio of the transformer
h_f	Thickness of the deposited film
h_p	Piezoelectric thickness
J	Displacement current density
k	Wave number
k_{eff}^2	Effective coupling factor
K^2	Piezoelectric coupling constant
k_t^2, k_{33}^t	Electromechanical coupling constant
\mathbf{K}_{uu}	Mechanical stiffness matrix
$\mathbf{K}_{u\phi}$	Piezoelectric coupling matrix
$\mathbf{K}_{\phi\phi}$	Dielectric stiffness matrix
L_1	Electric inductance
p	Electric dipole moment
\mathbf{P}	Piezoelectric polarization vector
\mathbf{p}	Dipole moment

Q	Quality factor
\mathbf{Q}	Vector of nodal electrical charge
$N_j(\mathbf{x})$	Shape functions
M	Figure of merit
\mathbf{M}_{uu}	Mechanical mass matrix
q	Dipole charge
\mathbf{Q}_Q	Nodal charge at nodes with fixed potential
r	Capacitance ratio
R_1	Electric resistance
R_e	Resistive component of the equivalent electric network
$\tilde{\mathbf{s}}$	Complex compliance matrix
\mathbf{s}	Compliance matrix
\mathbf{S}	Mechanical strain vector
\mathbf{t}_n	Mechanical surface force (traction)
\mathbf{T}	Mechanical stress vector
\mathbf{T}_C	Complete stress tensor
\mathbf{T}_0	Pre-stress tensor
u	Particle displacement
\dot{u}	Particle velocity
$\ddot{\mathbf{u}}$	Acceleration
V	Voltage
v_0	Phase velocity of an acoustic wave in a material
v	Particle velocity
\mathbf{x}	Position vector
X_1	Reactance of the C_1, L_1, R_1 branch
X_e	Reactive component of the equivalent electric network
Y	Admittance
$ Z $	Magnitude of the impedance of the equivalent electric network
Z_0	Viscoelastic film characteristic impedance
Z_1	Surface mechanical impedance for a Newtonian fluid

Z_{in}	Input impedance
Z_n	Maximum impedance of the equivalent electric network
Z_m	Minimum impedance of the equivalent electric network
Z_L	Acoustic load impedance
Z_p	Characteristic acoustic impedance
Z_S	Impedance of the substrate
Z_T	Resonator impedance

List of Figures

Figure 1.1: Schematic diagram of a sensor producing an electrical output in response to an input quantity (top). Biosensor comprising the generic device shown at top with a molecular recognition layer that has a highly selective response (bottom).....	1
Figure 1.2: Simple molecular model explaining the piezoelectric effect. a) Unperturbed molecule, b) molecule subjected to an external force and c) polarizing effect on the material surfaces.	5
Figure 1.3: Symmetries in the piezoelectric coupling matrix for the hexagonal crystal class	9
Figure 1.4: Figures explaining the natural vibration of a piezoelectric resonator: The upper part shows the resonator bar subjected to an external stress, the central part shows the forces that an internal thin slice of a strained piezoelectric material experience, and the lower part shows the displacement profile of a piezoelectric material subjected to a sinusoidal electric field. ³	13
Figure 1.5: Common piezoelectric actuator designs. a) stacked design and b) laminar design. ⁶	17
Figure 1.6: Diagram of a quartz crystal microbalance.....	18
Figure 1.7: AT-cut angle.	18
Figure 1.8: Film bulk acoustic resonator (FBAR) sensors. a) free-standing structure and b) solidly-mounted resonator (SMR) structure.....	19
Figure 1.9: General structure of a surface acoustic wave sensor with connections to an AC voltage source and a signal processing unit. In some sensors, the acoustic absorbers are replaced with reflectors to decrease insertion loss.....	20
Figure 2.1: Basic photolithography and pattern transfer. Example used an oxidized silicon wafer and negative photoresist system. Process steps include exposure, development, oxide etching and resist stripping.....	26
Figure 2.2: Pattern drawn on a computer-aided design (CAD) system to generate a mask by the e-beam lithography technique.....	27
Figure 2.3: Use of alignment marks to register subsequent layers. ²	28

Figure 2.4: Mask alignment to the wafer flat. ²	29
Figure 2.5: Difference between anisotropic and isotropic wet etching.....	35
Figure 2.6: Typical parallel-plate reactive ion etching system.....	36
Figure 2.7: Typical hot-wall LPCVD reactor.....	38
Figure 2.8: Typical setup for electrodeposition.....	38
Figure 2.9: Typical wafer oxidation furnace.	39
Figure 2.10: Typical system for e-beam evaporation of materials.....	40
Figure 2.11: Typical RF sputtering system.....	41
Figure 2.12: The spin casting process as used for photoresist in photolithography.....	41
Figure 3.1: Distribution of the displacement amplitude of a QCM. The quartz and the electrodes are represented the rectangle and the dark lines respectively.....	44
Figure 3.2: Mass sensitivity related D_f and vibration amplitude related U distribution along one of the quartz resonator diameters. ³	45
Figure 3.3: Equivalent electrical circuit of a piezoelectric vibrator.....	45
Figure 3.4: Mechanical and electrical representations of a piezoelectric resonator.....	46
Figure 3.6: Modified Butterworth-Van Dyke equivalent circuit for a surface-loaded piezoelectric resonator.....	49
Figure 3.7: Finite thickness acoustic medium: at all points in the medium, there are right and left propagating plane waves.....	51
Figure 3.8: Equivalent circuit of a finite thickness acoustic delay line.....	52
Figure 3.9: Three-port Mason model equivalent circuit for a one-dimensional piezoelectric slab.....	54
Figure 3.10: Equivalent circuit diagram of a multilayer acoustic resonator.....	56
Figure 3.11: Simple piezoelectric resonator defining the problem domain Ω . For clarity, only the part of the volume-element mesh located on the boundary S of volume Ω is shown. The boundary S with unit outward normal ni is divided into two parts: the part covered with electrodes Se and the remaining non-metalized part Su . The piezoelectric material (white) is between two electrodes (gray).....	57
Figure 4.1: Typical quartz disk showing the QCM aspect (left) and the shear displacement of the generated vibrations (right).....	68
Figure 4.2: Butterworth-Van Dike equivalent circuit for a QCM.....	70
Figure 4.3: Equivalent impedance and phase spectra for a QCM using the Butterworth-Van Dike equivalent circuit.....	70
Figure 4.4: Frequency shifts obtained by applying the Modified Butterworth-Van Dike equivalent circuit for the QCM.....	72

Figure 4.5: Orientation of 3D material xyz relative to the 2D analysis coordinate system XYZ	73
Figure 4.6: Resonance frequency for the QCM with no deposition (air-loaded).....	75
Figure 4.7: Shear vibrations of the QCM at resonance.....	75
Figure 4.8: Distribution of the displacement in the bulk of the resonator QCM.....	76
Figure 4.9: Cross-section of the quartz resonator showing the displacement amplitude.....	76
Figure 4.10: Physical aspect of the quartz disk for a 20 μm Parylene [®] deposition (red) (left), meshing (center) and vibrational response (right).	77
Figure 4.11: Input admittance for a 1 μm -Parylene [®] loaded QCM.....	77
Figure 4.12: Frequency shifts (analytical and FEM) for different Parylene [®] deposition films.....	78
Figure 4.13: Imaginary part of the acoustic contribution to the input impedance for the unloaded PVDF resonator with a thickness of 10 μm	82
Figure 4.14: Meshing aspect of the unloaded PVDF resonator using an structured mesh of 8720 prism elements.	84
Figure 4.15: Imaginary part of the acoustic contribution to the input impedance for the unloaded PVDF resonator extracted from the FEM model for a thickness of 10 μm	85
Figure 4.16: Meshing aspect of the 10 μm thickness PVDF (left) and it vibrational response (right).....	86
Figure 4.17: Shift frequency (Mason and FEM) for Parylene [®] deposition.	87
Figure 4.18: Schematic definition of a general biosensor. ²⁰	89
Figure 4.19: Imaginary part of the acoustic contribution to the input impedance for the unloaded PVDF resonator with a thickness of 10 μm	91
Figure 4.20: The transmission line representation of a nonpiezoelectric sensing film on a piezoelectric resonator surface. The additional mechanical load ZI can be produced by any of several materials at the film surface.....	91
Figure 4.21: Frequency response of the AlN mass microsensors for streptavidin film depositions of 50nm, 100nm and 150nm.	92
Figure 4.22: AlN mass microsensors water loaded and unloaded.	93
Figure 4.23: Vibrational response of the 2 μm -thickness AlN (left) and it meshing aspect (right).	96
Figure 4.24: Vibrational response of the 10 μm -thickness PVDF pressure microsensors (left) and it meshing aspect (right).	101
Figure 4.25: Resonance frequency of the PVDF disk for a pressure of 0.65MPa.....	101
Figure 5.1: Unidirectional and bidirectional PVDF.	108
Figure 5.2: Disk-shaped piezoelectric PVDF with silver ink electrodes.	108

Figure 5.3: Custom polyamide setup (left) and system connection (right).	110
Figure 5.4: Cu-electrode PVDF vs. Ag-electrode PVDF.....	110
Figure 5.5: Comparison between unloaded copper-electrode disk and with photoresist thin film deposition.	111
Figure 5.6: Effect caused by the use of two different disk diameters (20 mm and 25 mm).....	111
Figure 5.7: PVDF resonator experiment setup.	114
Figure 5.8: Frequency response of the PVDF resonator using the initial set of parameters.....	118
Figure 5.9: Experimental and simulated frequency response of the PVDF resonator with silver ink printed electrodes.	119
Figure 5.10: Vvibrational response of the 110 μm thickness PVDF.	119
Figure 5.11: Experimental and simulated frequency response of the PVDF resonator for Cu and silver ink electrodes in addition to the electrodeless case.	120
Figure 5.12: Scheme of the heterostructure of AlN/Pt/Ti/SiO ₂ /Si.....	124
Figure 5.13: AJA ATC Orion thin film deposition system.	124
Figure 5.14: XRD spectrum of an AlN/Pt/Ti/SiO ₂ /Si heterostructure showing he characteristic peaks of the Pt and Ti layers and the Si substrate, in addition to the critical AlN (002) peak that reveals the high orientation of AlN necessary to yield the high piezoelectric coefficient measured for these films.	125
Figure 5.15: XRD spectrum of an AlN/Pt/Ti/Si ₃ N ₄ /Si heterostructure showing he characteristic peaks of the Pt and Ti layers and the Si substrate, in addition to the critical AlN (002) peak that reveals the high orientation of AlN necessary to yield the high piezoelectric coefficient measured for these films.	128
Figure 5.16: Typical Raman spectrum from the Raman analysis of a typical UNCD film showing the 1332 cm ⁻¹ peak characteristic of diamond sp ³ c-atoms bonding and the 1532 cm ⁻¹ revealing the presence of sp ² -bonded carbon at the grain boundaries of the film.....	133
Figure 5.17: SEM micrograph of the surface morphology of the AlN layer and cross-section of the AlN/Pt/Ti/UNCD/SiO ₂ /Si heterostructure.	134
Figure 5.18: Cross-section SEM analysis of AlN growth on different substrates and the corresponding XRD spectra for each substrate.	135
Figure 5.19: XRD scan of a Si wafer showing the peak coming from the silicon wafer.....	136
Figure 5.20: PFM imaging of piezoelectric activity in (002) oriented AlN film (~200 nm thick) grown on CMP BUNCD with rms surface roughness of about 0.2 nm. The PFM measurement was used to determine the piezoelectric coefficient of the AlN film, which was 5.3 pm/V, one of the highest demonstrated today for AlN.....	137

Figure 5.21: AlN FBAR on UNCD. a) 3D longitudinal cut image of the freestanding FBAR heterostructure and b) lateral view scheme of the device describing the deposited layers.....	140
Figure 5.22: Mask layout for the Si cavity. It can be observed the four different sizes used in this experimental step, where the value in microns is the calculated length of the square and in brackets is the real length due to undercuts.	141
Figure 5.23: Si (100) showing characteristic V anisotropic etch of the walls forming an angle of 54.7° with respect to the main surface.	141
Figure 5.24: Generated chrome pattern on glass substrate.	142
Figure 5.25: First cavity prototype. a) Frontside of the UNCD film and b) backside showing the different sizes of the cavities within dices.	143
Figure 5.26: Square UNCD membranes. a) Membrane (mask 300 μm) seen from the frontside, and b) membrane (mask 150 μm) seen from the backside (cavity).	144
Figure 5.27: SEM cross section of the film for the AlN/Pt/Ti/UNCD membrane. a) Cantilevered membrane and b) measurements on the SEM image.	145
Figure 5.28: SEM image of the freestanding AlN/Pt/Ti/UNCD membrane on the Si substrate.	145
Figure A.1: Conceptual schematic of active valve for treatment of glaucoma.....	154
Figure A2: Circuit block diagram of active valve for treatment of glaucoma.....	155
Figure A.3: RF resonant and clamp circuit.	156
Figure A.4: Voltage rectifier circuit.	156
Figure A.5: Voltage regulator circuit.	156
Figure A.6: Bias Circuit.	157
Figure A.7: Data detection circuit.	157
Figure A.8: Fully differential potentiostat architecture.	158
Figure A.9: Simulation plots of inductive coupling with 50% modulation index. (a) Voltage on the reader antenna. (b) Induced voltage in implantable antenna.....	158
Figure A.10: Simulation plots of Clamp, Rectifier and Regulator Circuits with 50% modulation index. (a) Voltage RF Clamp. (b) Voltage RF Rectifier, (c) Voltage Regulator.....	159
Figure A.11: Data modulation simulations with 50% modulation index. (a) Input modulated ASK signal. (b) Demodulated signal. (c) Voltage Comparator (d) Low pass Voltage. (e) Actuator Voltage.	159
Figure A.12: Complete Circuit Layout.....	160
Figure B.1: SEM micrograph of the passive UNCD drug delivery device.	164

Figure B.2: Drug delivery device with selective UNCD membrane and polymer reservoirs. a) Complete system and b) holey membrane attached to polymer reservoirs.165

Figure B.3: Cantilever as part of the active system.....165

Figure B.4: Morphology and operation of the cantilever actuator.....166

List of tables

Table 1.1: Lattice parameter relationships and figures showing unit cell geometries for the seven crystal systems.	4
Table 4.1: Dimensions for the proposed QCM.	69
Table 4.2: Parameters used for the QCM with Parylene [®] deposition.	69
Table 4.3: Comparison of analytical and circuital values for Parylene [®] deposition , where hf is the film thickness, Δfa the analytical frequency shift, Δfc the frequency shift of the circuital model and E the error of Δfc with respect to Δfa	71
Table 4.4: QCM Matrix constants.	73
Table 4.5: Parameter values for Parylene [®]	73
Table 4.6: Comparison of analytical and FEM values for Parylene [®] deposition, where hf is the film thickness, Δfa the analytical frequency shift, $\Delta ffem$ the frequency shift of the FEM model and E the $\Delta ffem$ error with respect to Δfa	77
Table 4.7: Dimensions for the proposed PVDF resonator.	81
Table 4.9: PVDF Matrix constants.	83
Table 4.10: Parameter values used for Parylene [®]	85
Table 4.11: Mesh convergence study for the unloaded PVDF microbalance.	86
Table 4.12: Comparison between Mason model and FEM model results for Parylene [®] deposition, where hf is the film thickness, ΔfM the Mason frequency shift, $\Delta ffem$ the frequency shift of the FEM model and E the $\Delta ffem$ error with respect to Δfa	86
Table 4.13: Dimensions for the proposed AlN resonator.	89
Table 4.14: Parameters used for the piezoelectric AlN, streptavidin and water.....	90
Table 4.15: Frequency shifts for the Mason model using streptavidin depositions, where $hvisco$ is the viscoelastic streptavidin film thickness and ΔfM the Mason shift frequency.....	92
Table 4.16: AlN Matrix constants.	95
Table 4.17: Dimensions for the proposed PVDF pressure sensor.	97

Table 4.18: PVDF Matrix constants.....	100
Table 4.19: Frequency shifts for numerical model and experimental results.	101
Table 4.20: Results after the comparison between the two analyses: static+harmonic and harmonic.....	102
Table 5.1: Dimensions for the PVDF disk-shaped resonator with silver ink electrodes.....	109
Table 5.2: PVDF matrix constants.	117
Table 5.4: Material constants extracted from curve fitting.	118
Table 5.5: Deposition parameters for the AlN/Pt/Ti/SiO ₂ /Si heterostructure.	125
Table 5.6: Performed experiments.....	127
Table 5.7: Deposition parameters for the AlN/Pt/Ti/ Si ₃ N ₄ /Si heterostructure.	128
Table 5.8: Sputtering parameters for AlN, Pt and Ti depositions.	133
Table A.1: Actuator Voltage vs Modulation Index.	160

Introduction

Glaucoma is a disease that affects tens of millions of people around the world and represents a common cause of blindness. Patients with glaucoma present high intraocular pressure values that evolve in a progressive damage to the optic nerve and the retina. The intraocular pressure (IOP) in the general population is in the range 15.5 ± 2.6 mmHg.¹

The IOP is determined by the production, circulation and drainage of ocular aqueous humor. Ciliar body produce aqueous humor with an average rate of $2.4 \pm 0.6 \mu\text{l}/\text{min}$ with a turnover rate of 1% of the anterior chamber volume per minute. The hydraulic resistance of the flow network for the aqueous humor is in the range of 2.5 to 10 mmHg/ $\mu\text{l}/\text{min}$. The drain is achieved on the episcleral vein at a pressure in the range of 8-10 mmHg.²

Patients with glaucoma are treated with drugs to decrease IOP. When these treatments are not effective, surgery is required, and more complex cases require an implant of an aqueous shunt. The Molteno's device (1969) and similar for aqueous humor drainage do not offer enough hydraulic resistance, they increase complications related with the hypotony in the postoperative period.

This problem was solved by adding hydraulic resistance in the shunt (e.g. Ahmed Glaucoma ValveTM). Another cause of failure of implants is associated with increased intraocular pressure caused by the tissue-implant reaction.³ With the aim of decreasing problems associated with high IOP in long term, the devices were modified by increasing plate area, substituting structural materials,⁴ or inserting bypass resistances, with microtubes.⁵

Considering an ideal valve, the hydraulic resistance must change to maintain the IOP in the physiological range. The design of the device has to consider the variability in flow and pressure parameters, related to age, sex, and ethnicity.

The most important antecedent in this topic was the proposal and design of a MEMS-based active microvalve by Guarnieri, 2007.^{6,7,8} Guarnieri is the Director of the research group of

BioMEMS at the FI-UNER and CIMEC-UNL/CONICET (Argentina) of which the author of this thesis is member.

The active microvalve is based on the use of conjugates polymers as the actuation mechanism of a diaphragm; it is supply by an electric voltage between 1-2 volts thus reducing the size of the auxiliary circuits improving its biocompatibility. In order to perform a close-loop control, the active microvalve also has to possess a pressure sensor thus being capable of handle the hydraulic circuit of the implant as described in the FigureI.

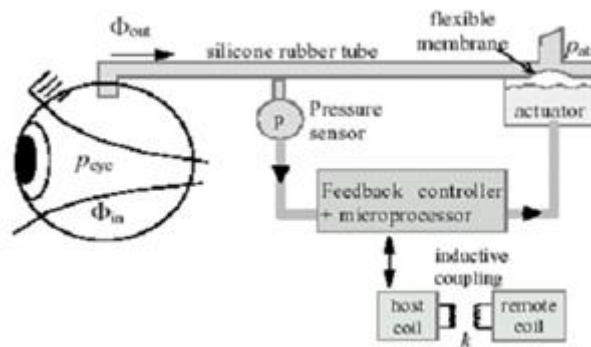


Figure I: Conceptual schematic of an active valve for the treatment of glaucoma.

MEMS (MicroElectroMechanical Systems) technology is based in a number of tools and methodologies, which are used to fabricate small structures with dimensions in the micrometer scale. This technology is inherited from the Integrated Circuit (IC) industry and results from the integration of structural and functional microparts such as micro channels, microreservoirs, microsensors and microactuators and have recently been developed to overcome several limitations imposed by the current state of the art in biomedical technology (BioMEMS).

The development of MEMS and the generation of new materials allow an approach to the development of implantable micro-devices with improved biocompatibility due to the reduction in the devices size as the damage in the surgical implant. Novel devices employ different ways to control IOP, i.e. passively^{9,10} or actively, based on electrochemical and magnetic actuation.^{11,12}

High intraocular pressure has long been considered the most important risk factor for the onset and progression of glaucoma. Ever since, it was defined as a clinical condition and until a decade ago, treatment for glaucoma has focused on lowering intraocular pressure to stop progression. Yet, glaucomatous optic nerve damage progresses even when intraocular pressure is under control and, in normal tension glaucoma, optic disc changes and visual field defects appear while intraocular pressure is considered normal.¹⁴

Current research is focused on elucidating the mechanisms involved in the survival, adaptation and death of retinal ganglion cells in hopes of uncovering factors which cause damage to and factors which protect these cells. New discoveries might contribute to the development of effective therapeutic means for protecting retinal nerve cells and

counteracting the physiopathologic processes involved in glaucoma. In this sense, Alexandrescu et al. 2010¹³ has found the influence of glycoprotein (CD44) and some molecules (TGF-beta2, TNF alfa) related with glaucoma pathology. Grus et al. 2008¹⁴ states that Transthyretin might play a role in the onset of glaucoma since it has been shown to form amyloid deposits which cause outflow obstructions thereby increasing IOP. Also, Rao et al. 2008¹⁵ demonstrates that inhibition of geranylgeranyl isoprenylation of CaaX proteins in the aqueous outflow pathway, increases aqueous humor outflow.

The ideal active microvalve has to be capable of sensing the IOP and actuate the active diaphragm regarding these sensed values. Moreover, the knowledge of some kind of molecule associated with the processes involved in the glaucoma pathology will increase the effectiveness of the implant. In this sense, a mass microsensors (gravimetric sensor) capable of sensing mass deposition (e.g. proteins) is desirable; also the microsensors has to possess the capacity to be implanted and integrated with the active microvalve. Additionally to these aspects, the ideal active microvalve must comply with the requirements of an active implant: wireless communication, thus allowing telemetric monitoring and remote energy supply.

This thesis is focused on the design, simulation, fabrication and characterization of MEMS-based mass microsensors with protein sensing as the final goal. The thesis starts with a modeling&simulation chapter where it is developed different types of MEMS-based mass microsensors using piezoelectric resonators in addition to a microtransponder chip circuit for the energization of the microvalve. It follows a fabrication chapter where a description is presented for the synthesis and characterization of the materials used for the device, and for the design and simulation of the microsensors based on sensing mass changes. Figure II describes the focus of this thesis, showing the integration of the piezoelectric sensors and the microtransponder chip circuit in the active microvalve:

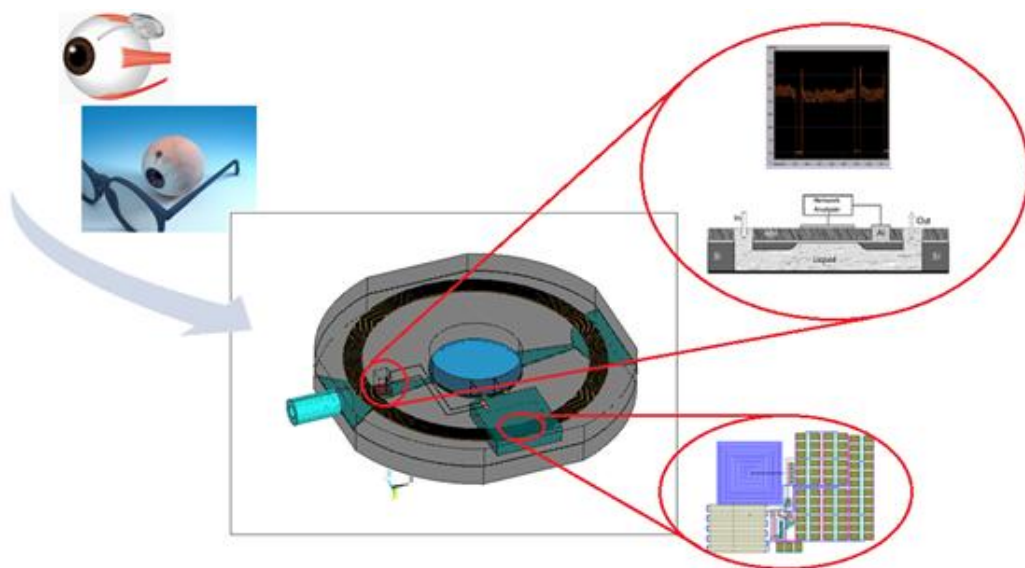


Figure II: Microvalve design showing the integration of the system with the piezoelectric microsensors and the RF microtransponder.

Chapters description

The design and development of a device performing innovative characteristics, is time consuming and requires important resources to be implemented. In this case of innovative technologies, the maturation of new concepts and the application of knowledge are necessary. There exist tools that facilitate somehow these tasks, thus saving time and costs. Numerical simulation is of vital importance in a system design step since it allows checking assumptions and a deep understanding of the represented phenomena, so CHAPTER 4 deals with the implementation of different numerical models for the analysis of the piezoelectric sensors performances; in addition, CHAPTER 5 describes the fabrication and characterization of the used materials, and the mass microsensors.

A piezoelectric resonator is a sensor that responds to mechanical excitation produced by the environment around it, inducing changes in the resonance frequency. Quartz is the most frequently used piezoelectric matrix for this kind of resonators because of its stability with respect to temperature. Thus, a quartz crystal microbalance (QCM) has been modeled and simulated (*Section 4.1*) for different amounts of deposited material on its surface.

Piezoelectric polymers are a good option to develop piezoelectric devices as sensors as well as actuators. The polyvinylidene fluoride (PVDF) and its copolymers are the polymers with the highest piezoelectric effect. One of the mayor advantages of these piezoelectric films is the low acoustic impedance close to the water, human tissue and other organic materials, allowing a more efficient transduction of acoustic signals due to close impedance match thus been suitable for BioMEMS applications. Therefore, the analysis of the behaviour of a PVDF piezoelectric mass sensor was carried out using FEM (Finite Element Method) models (*Section 4.2*) and also a prototype of the system was fabricated and characterized (*Section 5.1*), and results from simulations were matched with the experimental results (*Section 5.2*).

Section 4.4 describes the advantage of using piezoelectric PVDF for pressure sensors. These sensors generate electrical signals in response to the applied force, then working as dynamic force sensors. The work presented in this section relates to the simulation of the behaviour of a PVDF piezoelectric sensor subjected to different amounts of pressure on its surface.

Aluminium Nitride (AlN) is a piezoelectric material, primarily used before in the electronics industry as circuit substrates. It is a very attractive piezoelectric material for use in BioMEMS because it is biocompatible, exhibits high resistivity, high breakdown voltage, high acoustic velocity and it can be grown by reactive sputtering technique at relatively low temperature thus being compatible with CMOS technology.^{16,17} Material compatibility with IC fabrication opens the way for monolithic integration of the traditionally incompatible IC and electro-acoustic technologies. Motivated by these advantages and potential applications, the analysis of the behaviour of an AlN piezoelectric biosensor using different models was achieved for protein deposition in an aqueous media

(*Section 4.3*). Moreover, the deposition of AlN on silicon substrate and its characterization was carried out (*Section 5.3*).

It is also becoming important to be able to integrate piezoelectric films with materials used in medical devices. Ultrananocrystalline diamond (UNCD), in thin film form, is a multifunctional material, which is extremely bioinert and biocompatible.^{18,19,20,21} Since both UNCD and AlN films can be processed via photolithography and reactive ion etching (RIE) processes used in fabrication of MEMS/NEMS, it is expected that the integration of UNCD and AlN films will provide the bases for developing a new generation of biocompatible Bio-MEMS/NEMS. Thus, the integration of piezoelectric AlN and UNCD films for biomedical MEMS devices was achieved (*Section 5.4*). The study was focused on determining the best AlN film with the highest piezoelectric coefficient integrated on UNCD layers.

Because of diamond based substrates have the highest sound velocity among all materials²² and AlN has the highest phase velocity among all piezoelectric materials,²³ AlN/diamond structure is a very promising device for thin film bulk acoustic wave resonator (FBAR) applications. In this sense, AlN-UNCD integration becomes an important option for implantable resonators sensors as well as actuators. *Section 5.5* is focused on the fabrication of the previously modeled and simulated AlN/UNCD-based FBAR for biosensor applications.

These devices will have a profound impact in drug delivery inside the human body for treatment of different pathological conditions, since the drug delivery can be actively controlled to tune the pharmacokinetics of the delivered drug. In addition, the implanted MEMS/NEMS devices will enable local drug delivery inhibiting toxic side effects. The use of piezoelectric materials as the active part of drug delivery system (DDS) is appealing. Piezoelectric actuation could be used to break a membrane covering drug reservoirs, as a switch valve for opening the reservoirs, or by pushing the liquid outside of the reservoir. Therefore the design, fabrication and characterization of two different kinds of UNCD-based membranes for drug delivery devices were carried out (*Appendix B*).

As stated previously, energizing the microvalve actuator has to be performed remotely based on the principles of radio frequency identification (RFID). In recent years, RFID technology has seen rapid growth in areas of supply chain management, access control, public transportation, airline baggage tracking and biomedical applications such as implantable sensors and actuators. For that reason, finally *Appendix A* presents a microtransponder chip circuit design and simulation for the energization of an active microvalve for the treatment of glaucoma.

Bibliography

-
- ¹ C. R. Ethier, M. Johnson and J. Ruberti "Ocular biomechanics and biotransport", *Annu. Rev. Biomed. Eng.*, vol. 6, pp. 249-73, 2004.
 - ² R. N. Weinreb, *Intraocular Pressure*. Amsterdam, The Netherlands, Kugler, pp. 1–16, 2007.
 - ³ C. H. Hong, A. Arosemena, D. Zurakowski, and R. S. Ayyala, "Glaucoma drainage devices: a systematic literature review and current controversies", *Surv Ophthalmol*, vol.50, pp. 48-60, 2005.
 - ⁴ K. Ishida, P. A. Netland, V. P. Costa, L. Shiroma, B. Khan, I. Ike, K. Ahmed, "Comparison of Polypropylene and Silicone Ahmed Glaucoma Valves", *Ophthalmology*;113:1320–1326, 2006.
 - ⁵ T. Pan, M. S. Stay, V. H. Barocas, J. D. Brown, and B. Ziaie, "Modeling and Characterization of a Valved Glaucoma Drainage Device With Implications for Enhanced Therapeutic Efficacy", *IEEE Transactions on Biomedical Engineering*, vol. 52, 2005.
 - ⁶ F. A. Guarnieri, PICT 2004. Número 25791 Proyecto Diseño, Simulación y fabricación de BioMEMS, 2004.
 - ⁷ F. A. Guarnieri, Concurso Nacional de Innovaciones - Innovar 2007 www.innovar.gov.ar/galeria/ver-proyecto?proyecto=1879, 2007.
 - ⁸ F. A. Guarnieri, Patente de Invención AR058947 (A1) "Microaparato implantable en el ojo para aliviar glaucoma o enfermedad causante de sobrepresión ocular"; WO2008084350 (A2) "Implantable ocular microapparatus to ameliorate glaucoma or ocular overpressure causing disease".
 - ⁹ E. Meng, P.-J. Chen, D. Rodger, Y.-C. Tai and M. Humayun, "Implantable parylene MEMS for glaucoma therapy", technical digest, The 3rd International IEEE EMBS Special Topic conference on Microtechnologies in Medicine and Biology 12–15 May Oahu, HI, USA, pp. 116–119, 2005.
 - ¹⁰ P. J. Chen, D. C. Rodger, M. S. Humayun, Y. C. Tai, "Floating-Disk Parylene Microvalve for Self-Regulating Biomedical Flow Controls," *Proc. MEMS 2008 Conference*, Tucson, Ariz., USA, Jan. 13-17, pp. 575-578, 2008.
 - ¹¹ B. Bae, N. Kim, H. Kee, S. Kim, Y. Lee, S. Lee, and K. Park, "Feasibility test of an Electromagnetically driven valve actuator for glaucoma treatment", *Journal of Microelectromechanical Systems* Vol 11, No. 4, August 2002.
 - ¹² T. Pan, A. Baldi, B. Ziaie "Remotely adjustable check-valves with an electrochemical release mechanism for implantable biomedical Microsystems" Birck Nanotechnology Center. Other Nanotechnology Publications Purdue Libraries 2007.
 - ¹³ C. Alexandrescu, A. Dascalu, C. Mitulescu, A. Panca, R. Pascu, R. Ciuluvica, V. Potop, and L. Voinea, "Evidence-based pathophysiology of glaucoma", *Maedica A Journal of Clinical Medicine*, Volume 5 No.3 2010
 - ¹⁴ F. Grus, S. Joachim, S. Sandmann, U. Thiel, K. Bruns, K. Lackner, and N. Pfeiffer, "Transthyretin and complex protein pattern in aqueous humor of patients with primary open-angle glaucoma", *Molecular Vision* 2008; 14:1437-1445.
 - ¹⁵ P. Vasantha Rao, Y. Peterson, T. Inoue and P. Casey "Pharmacological Inhibition of Protein Geranylgeranyltransferase Type I Increases Aqueous Humor Outflow through the Trabecular Meshwork", *IOVS Papers in Press*. Published on MIOaVrSch 3, 2008 as Manuscript iovs.07-1639
 - ¹⁶ C. H. Chou, Y. C. Lin, J. H. Huang, N. H. Tai, and I. Lin, *Diamond Relat. Mater.* 15, 404 (2006).
 - ¹⁷ M. Dubois and P. Muralt, *Appl. Phys. Lett.* 74, 3032 (1999).
 - ¹⁸ O. Auciello and A. V. Sumant, *Diamond Relat. Mater.* 19, 699 (2010).
 - ¹⁹ O. Auciello and B. Shi, *Biological and Medical Physics, Biomedical Engineering*, 63 (2010).

-
- ²⁰ P. Bajaj, D. Akin, A. Gupta, D. Sherman, B. Shi, O. Auciello, and R. Bashir, *Biomed. Microdevices* 9, 787 (2007).
- ²¹ O. Auciello, J. Birrell, J. A. Carlisle, J. E. Gerbi, X. Xiao, B. Peng, and H. D. Espinosa, *J. Phys.: Condens. Matter* 16, 539 (2004).
- ²² M. B. Assouar, O. Elmazria, P. Kirsch, and P. Alnot, *J. Appl. Phys.* 101, 114507 (2007).
- ²³ M. Ishihara, T. Nakamura, F. Kokai, and Y. Koga, *Diamond Relat. Mater.* 11, 408 (2002).

Objectives

General Objective

To design, simulate, fabricate and characterize MEMS-based microsensors detecting mass changes on the active component. The microsensor is to be integrated in an implantable active microvalve for glaucoma treatment.

Specific Objectives

- To model and simulate mass detection microsensors using Finite Element Method.
- To fabricate mass detection microsensors using MEMS technology and characterize them.
- To optimize the mass detection microsensors designs by comparing simulation results and experimental results.
- To evaluate functionality and applicability of the mass detection microsensors by using different materials potentially suitable for implantable devices.
- To determine the best AlN film with the highest piezoelectric coefficient integrated on UNCD layers.
- To design, fabricate and characterize two different kinds of UNCD-based membranes for drug delivery devices.
- To model and simulate a microtransponder chip circuit for the wireless connection to the implantable active microvalve.
- To analyze the feasibility in the development of pressure microsensors.

CHAPTER 1: Acoustic devices

Precise measurement tools are necessary parts of most successful scientific and engineering enterprises. The sensing devices considered in this chapter are such tools, capable of measuring physical, chemical, and biological quantities. What they have in common is that they all employ acoustic waves in their operation.

This chapter gives the background of sensor devices with emphasis in piezoelectric devices.

1.1 Sensors

Sensors produce an output signal in response to some input quantity (Figure 1.1). The output signal is usually electrical such as an analog voltage or current, a stream of digital voltage pulses or an oscillatory voltage whose frequency represents the value of the input quantity. The range of input quantities includes physical quantities such as the mechanical properties of thin films and chemical and biological quantities such as the concentrations and identities of unknown species in air or liquid media.

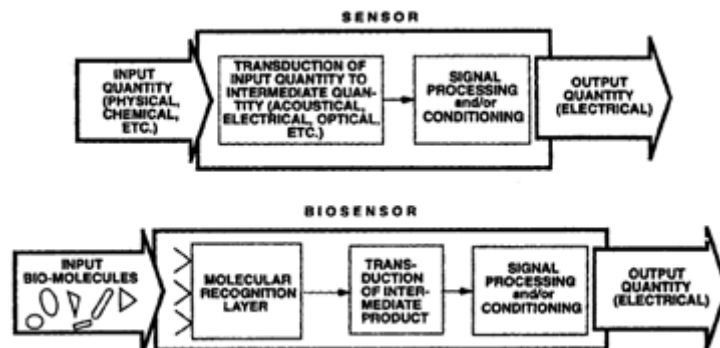


Figure 1.1: Schematic diagram of a sensor producing an electrical output in response to an input quantity (top). Biosensor comprising the generic device shown at top with a molecular recognition layer that has a highly selective response (bottom).¹

Inside the sensor shown in Figure 1.1 the transduction process is carried out, converting an input event in an electric signal. Also, the sensor could contain the needed circuitry for conditioning the transduction process signal into a more robust and suitable for use outside the sensor itself.

It is known that the dominant physical quantities may change as a function of length scale. In this context, devices at the microscale show that inertial forces become less affective whereas Van Der Waals forces, electrostatic forces and surface tension forces become dominant. In this sense, it is important to have a proof knowledge about the scaling behavior and other properties of the sensors in order to take a decision on what sensor to use.

Sensors are characterized in many different ways: Their sensitivity is a measure of the magnitude of the output signal produced in response to an input quantity of a given magnitude; their *resolution* is a measure of the minimum change of input quantity to which they can respond; their *selectivity* characterizes the degree to which they can distinguish one input quantity from another; their *bandwidth* is the range of input signals that may be converted to output signals and the *accuracy* is defined as largest error between actual and ideal output signals, to name a few.

A sensor based on a self-generating principle does not require an auxiliary energy source and they are call passive sensors. Examples of passive transducers are strain gauges, resistance temperature detectors (RTDs) and thermistors. On the other hand, sensors which require an auxiliary energy source are referred as active sensors. Examples of active sensors are thermocouples in which a change in temperature directly results in an electrical signal and piezoelectric accelerometers where the displacement of an accelerated mass is measured by converting the mechanical motion into an electrical signal.

1.2 Crystallography²

1.2.1 Crystal structures

Solid materials may be classified according to the regularity with which atoms or ions are arranged with respect to one another. A crystalline material is one in which the atoms are situated in a repeating or periodic array over large atomic distances.

Some of the properties of crystalline solids depend on the crystal structure of the material, the manner in which atoms, ions, or molecules are spatially arranged. There is an extremely large number of different crystal structures all having long-range atomic order;

these vary from relatively simple structures for metals, to exceedingly complex ones, as displayed by some of the ceramic and polymeric materials.

The atomic order in crystalline solids indicates that small groups of atoms form a repetitive pattern. Thus, in describing crystal structures, it is often convenient to subdivide the structure into small repeat entities called unit cells. Unit cells for most crystal structures are parallelepipeds or prisms having three sets of parallel faces. The unit cell is the basic structural unit or building block of the crystal structure and defines the crystal structure by virtue of its geometry and the atom positions within.

1.2.2 Crystal systems

Since there are many different possible crystal structures, it is sometimes convenient to divide them into groups according to unit cell configurations and/or atomic arrangements. One such scheme is based on the unit cell geometry, that is, the shape of the appropriate unit cell parallelepiped without regard to the atomic positions in the cell. Within this framework, an x, y, z coordinate system is established with its origin at one of the unit cell corners; each of the $x, y,$ and z axes coincides with one of the three parallelepiped edges that extend from this corner. The unit cell geometry is completely defined in terms of six parameters: the three edge lengths $a, b,$ and $c,$ and the three interaxial angles α, β and $\gamma.$ These are sometimes termed the lattice parameters of a crystal structure.

On this basis there are found crystals having seven different possible combinations of $a, b,$ and $c,$ and α, β and γ each of which represents a distinct crystal system. These seven crystal systems are cubic, tetragonal, hexagonal, orthorhombic, rhombohedral, monoclinic, and triclinic. The lattice parameter relationships and unit cell sketches for each are represented in Table 1.1. The cubic system, for which $a = b = c$ and $\alpha = \beta = \gamma = 90^\circ$ has the greatest degree of symmetry. Least symmetry is displayed by the triclinic system, since $a \neq b \neq c$ and $\alpha \neq \beta \neq \gamma.$

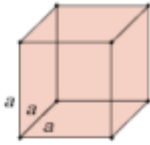
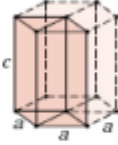


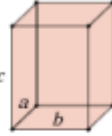
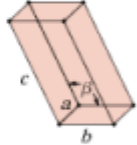
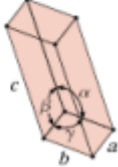
Crystal System	Axial Relationships	Interaxial Angles	Unit Cell Geometry
Cubic	$a = b = c$	$\alpha = \beta = \gamma = 90^\circ$	
Hexagonal	$a = b \neq c$	$\alpha = \beta = 90^\circ, \gamma = 120^\circ$	
Tetragonal	$a = b \neq c$	$\alpha = \beta = \gamma = 90^\circ$	
Rhombohedral	$a = b = c$	$\alpha = \beta = \gamma \neq 90^\circ$	
Orthorhombic	$a \neq b \neq c$	$\alpha = \beta = \gamma = 90^\circ$	
Monoclinic	$a \neq b \neq c$	$\alpha = \gamma = 90^\circ \neq \beta$	
Triclinic	$a \neq b \neq c$	$\alpha \neq \beta \neq \gamma \neq 90^\circ$	

Table 1.1: Lattice parameter relationships and figures showing unit cell geometries for the seven crystal systems.

1.3 Linear Theory of Piezoelectricity

1.3.1 Origin of polarization

Piezoelectricity is the phenomena whereby ions in the lattice of piezoelectric materials are displaced upon application of mechanical stress on the material; this is called direct piezoelectric effect. Pierre and Paul-Jacques Curie, in 1880, discovered that external forces applied to single crystals of quartz and some other minerals generate a charge on the surface of these crystals. The word Piezoelectricity comes from Greek and means “electricity by pressure”. This name was proposed by Hankel in 1881 to name the phenomenon discovered a year before by the Curie brothers.

The piezoelectricity effect can be observed from a simple molecular model (Figure 1.2). When the piezoelectric material is not subject to external mechanical stress, the centers of symmetry of the positive and negative charges of each molecule coincide. Therefore, the external effects of the negative and positive charges are reciprocally cancelled. As a result, an electrically neutral molecule appears. When exerting some pressure on the material, its internal reticular structure can be deformed, causing the separation of the positive and negative gravity centers of the molecules and generating little dipoles. The facing poles inside the material are mutually cancelled and a distribution of a linked charge appears in the material’s surfaces. This polarization generates an electric field and can be used to transform the mechanical energy used in the material’s deformation into electrical energy.

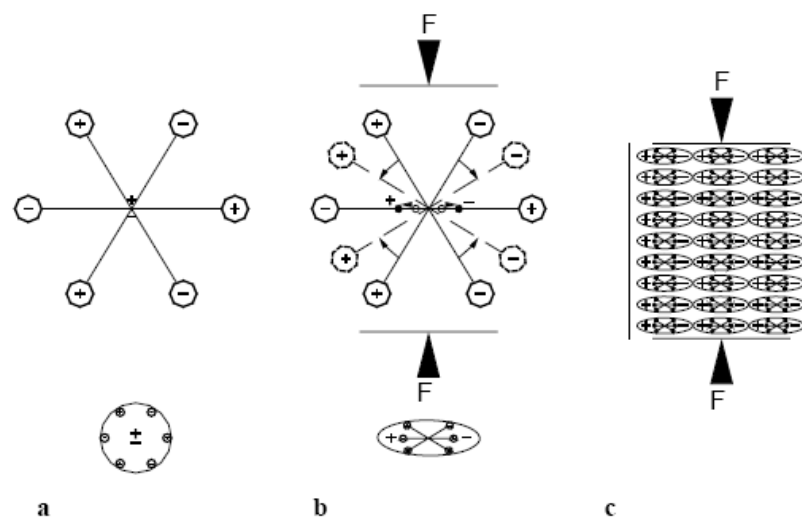


Figure 1.2: Simple molecular model explaining the piezoelectric effect. a) Unperturbed molecule, b) molecule subjected to an external force and c) polarizing effect on the material surfaces.³

If arbitrarily it names direct piezoelectric effect to the generation of an electric charge and hence of an electric field, in certain materials and under certain laws due to a mechanical stress, there would also exists a reverse or converse piezoelectric effect by which the application of an electric field, under similar circumstances, would cause deformation in those materials.

Piezoelectric materials include titanates of barium and lead, lead zirconate (PbZrO_3), ammonium dihydrogen phosphate ($\text{NH}_4\text{H}_2\text{PO}_4$), and quartz. This property is characteristic of materials having complicated crystal structures with a low degree of symmetry.

1.3.2 Crystallography Applied to Piezoelectric Crystals

Depending on their degrees of symmetry, crystals are commonly classified into seven systems: triclinic (the least symmetrical), monoclinic, orthorhombic, tetragonal, trigonal, hexagonal, and cubic. The seven systems, in turn, are divided into point groups (classes) according to their symmetry with respect to a point. There are 32 such classes, eleven of which contain enantiomorphous forms (see *Section 1.2.2*). Twelve classes have a high degree of symmetry to show piezoelectric properties. Thus twenty classes can be piezoelectric. Every system contains at least one piezoelectric class.⁴

In the international crystallographic system, an axis of rotation is indicated by one of the numbers 1, 2, 3, 4, 6. The number indicates through its reciprocal, the part of a full rotation about the axis which is required to bring the crystal into an equivalent position in regard to its internal structural properties. m symbol is equivalent to a reflection plane. If an axis has a reflection plane perpendicular to it, this fact is written as part of the symbol for that axis by following the number which describes the symmetry of the axis with the notation $/m$.

The designation for any class of symmetry is made up in the international system of one, two, or three symbols, each indicating the symmetry with respect to one type of direction in the crystal. Crystallographically identical directions are grouped together under one symbol. Only where the crystallographic directions are not identical are different symbols used

In the eleven crystal classes (point groups) having no center of inversion or plane of symmetry, two different types of the same species may exist. Each type is the mirror image of the other, neither type can be made to look exactly like the other by a simple rotation. If the right crystal has right-handed rectangular axes, the axes of the left crystal will then appear left-handed.

The eleven classes (point groups) that permit either right- or left-handed forms are triclinic 1, monoclinic 2, orthorhombic 222, tetragonal 4 and 422, trigonal 3 and 32, hexagonal 6 and 622, and cubic 23 and 432. All but 432 are piezoelectric. All eleven are included among the fifteen optically active classes. The signs of all elastic constants are the same for left- and right-handed crystals. All piezoelectric constants, however, have opposite signs for left- and right-handed crystals.

1.3.3 Mathematical formulation of the piezoelectric effect

For every electric dipole, there is a separation between a positive and a negative electric charge as demonstrated in Figure 1.2a. An electric dipole moment p is associated with each dipole as follows:

$$p = qd_q \quad (1.1)$$

where q is the magnitude of each dipole charge and d_q is the distance of separation between them. In reality, a dipole moment is a vector that is directed from the negative to the positive charge. In the presence of an electric field \mathbf{E} , which is also a vector quantity, a force will come to bear on an electric dipole to orient it with the applied field. The process of dipole alignment is termed polarization.

Piezoelectricity involves the coupling between mechanical and electrical properties of a material. In a three-dimensional system, the relationship between these two properties is given by the piezoelectric polarization vector \mathbf{P} (1x3).

An electric field causes a physical separation of positive and negative charges establishing a dipole moment \mathbf{p} (1x3) expressed in Cm . Polarization \mathbf{P} expressed in C/m^2 is defined as:

$$\mathbf{P} = N\mathbf{p} \quad (1.2)$$

where N is the number of dipoles per unit volume. The polarization \mathbf{P} is a vector and, generally, is proportional to the electric field:

$$\mathbf{P} = \varepsilon_0 \boldsymbol{\kappa} \mathbf{E} \quad (1.3)$$

where \mathbf{E} (3x1) is the external electric field, $\varepsilon_0 = 8.85 \times 10^{-12}$ F/m is the permittivity in free space and the electric susceptibility $\boldsymbol{\kappa}$ provides the connection between \mathbf{E} and \mathbf{P} . The susceptibility is a property exclusive of the material that states how easy the material is polarized while subjected to an electric field. Since \mathbf{E} and \mathbf{P} are vectors, $\boldsymbol{\kappa}$ must be a matrix of 3x3.

The displacement vector is defined as:

$$\mathbf{D} = \varepsilon_0 \mathbf{E} + \mathbf{P} = \varepsilon_0 \mathbf{E} + \varepsilon_0 \boldsymbol{\kappa} \mathbf{E} = \varepsilon_0 (1 + \boldsymbol{\kappa}) \mathbf{E} = \boldsymbol{\varepsilon} \mathbf{E} \quad (1.4)$$

For an isotropic media the matrix $\boldsymbol{\varepsilon}$ reduces to a scalar, thus:

$$\boldsymbol{\varepsilon} = \varepsilon_r \varepsilon_0 \quad (1.5)$$

where ε_r is the relative permittivity being a real positive number bigger than the unit.

In a piezoelectric media, a polarization vector is created not only by an external electric field but for the applied mechanical stress deforming the crystalline structure thus causing the charge separation; the resultant polarization is added to the one generated by the external electric field. It can be written:

$$\mathbf{P} = \mathbf{d} : \mathbf{T} \quad (1.6)$$

where \mathbf{d} is the piezoelectric coupling matrix expressed in C/N and \mathbf{T} is the mechanical stress vector expressed in N/m^2 . Now \mathbf{D} possesses two components, one proportional to \mathbf{E} and the other one to \mathbf{T} . However the coupling between polarization and stress depends of the symmetry of the material. Considering the symmetry of $\mathbf{T} \rightarrow (T_{ij} = T_{ji})$, matrix \mathbf{d} has 18 independent components. In indicial notation it can be written:

$$P_i = d_{ij} T_j \quad (1.7)$$

where the index i takes values starting from 1 to 3 and the index j takes values from 1 to 6. The converse piezoelectric effect is defined by the following relation:

$$S_j = d_{ji} E_i \quad (1.8)$$

where d_{ji} is the transposed matrix of d_{ij} , having the same units and S_j is the mechanical strain vector. This relation was obtained using thermodynamics arguments.⁵

In summary, it can be written:

$$P_i = \kappa_{ij} \varepsilon_0 E_j + d_{ij} T_j \quad (1.9)$$

$$S_j = d_{jk} E_k + s_{jk} T_k \quad (1.10)$$

where s_{jk} is the elastic compliance matrix of the material (from the Hooke's law) expressed in m^2/N . Moving the electrical variables to E and D :

$$D_i = \varepsilon_{ij}^T E_j + d_{ij} T_j \quad (1.11)$$

$$S_j = d_{jk} E_k + s_{jk}^E T_k \quad (1.12)$$

where superscripts T and E denotes that permittivity and compliance must be measured under constant stress and electric field. Modifying the previous equations in order to have the strain as independent variable, the following equations are obtained:

$$D_i = \varepsilon_{ik}^S E_k + e_{ij} S_j \quad (1.13)$$

$$T_i = -e_{ik} E_k + c_{ij}^E S_j \quad (1.14)$$

where $e_{ik} = c_{kj}^E d_{jk}$ is the piezoelectric coupling matrix expressed in C/m^2 with c_{kj}^E the elastic matrix at constant electric field. These are the constitutive relations for the linear piezoelectricity. In matrix notation, it may be written as:

$$\mathbf{D} = \boldsymbol{\varepsilon}^S \mathbf{E} + \mathbf{e}^T \mathbf{S} \quad (1.15)$$

$$\mathbf{T} = -\mathbf{e} \mathbf{E} + \mathbf{c}^E \mathbf{S} \quad (1.16)$$

with \mathbf{T} (6x1) the mechanical stress vector, \mathbf{S} (6x1) the mechanical strain vector, \mathbf{E} (3x1) the electrical field vector, \mathbf{D} (3x1) the electrical displacement vector, \mathbf{c} (6x6) the linear elastic matrix or stiffness matrix at constant electric field, $\boldsymbol{\varepsilon}$ (3x3) the dielectric coefficients matrix at constant strain and \mathbf{e} (6x3) the piezoelectric coupling matrix.

It is possible to express the relation between the stress, strain, electric field, and electric displacement field not only in stress-charge but also in strain-charge form:

$$\mathbf{D} = \boldsymbol{\varepsilon}^T \mathbf{E} + \mathbf{d} \mathbf{T} \quad (1.17)$$

$$\mathbf{S} = \mathbf{d}^T \mathbf{E} + \mathbf{s}^E \mathbf{T} \quad (1.18)$$

where \mathbf{d} (3x6) is the piezoelectric coupling matrix and \mathbf{s} (6x6) is the compliance matrix at constant electric field.

Because of crystal symmetries, piezoelectric coupling matrices \mathbf{e} and \mathbf{d} possess some nonzero elements. Symmetries in the piezoelectric coupling matrices for the hexagonal crystal class are depicted in the following picture:

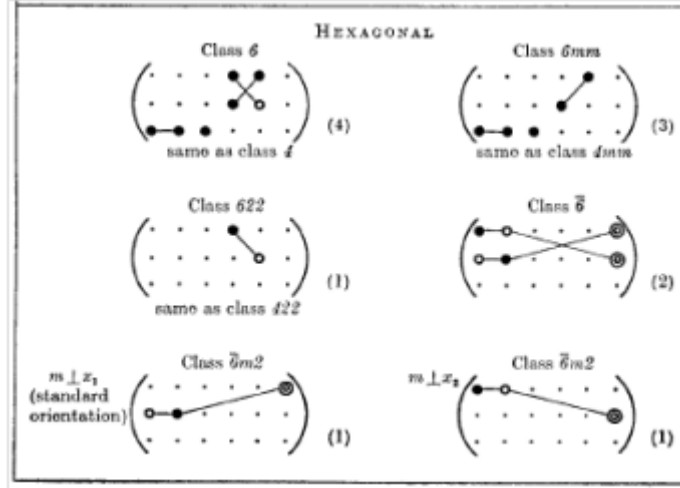


Figure 1.3: Symmetries in the piezoelectric coupling matrix for the hexagonal crystal class ⁶

1.3.4 General constitutive equations

Thermodynamic relations^{7,8}

The coupling between the thermal, elastic and electrical parameters of a material can be introduced formally using the thermodynamic approach. The results are equations of state which give relations between material parameters measured under different experimental conditions.

The conservation of energy for a piezoelectric linear solid result in the first thermodynamic law considering the three contributions of the variation in the stored internal energy: the work done by external forces, the work done by the applied electric fields and the thermal energy carried to the system. Thus, the reversible change dU in the internal energy U of an elastic dielectric subjected to a small change in the strain dS , electric displacement dD , and entropy $d\sigma$ is given by:

$$dU = \theta d\sigma + T_i dS_i + E_j dD_j \quad (1.19)$$

where θ is the absolute temperature of the material and $d\sigma$ the infinitesimal change of the entropy. Since in most experimental situations they work under isothermal conditions,

it is common to use the electric field and the stress as independent variables. Hence, it is useful to change the set of independent variables from $(\sigma, \mathbf{S}, \mathbf{D})$ to $(\theta, \mathbf{T}, \mathbf{E})$ performing the Legendre transformation of U . Thus, the resulting free energy function is given by:

$$G = U - \theta\sigma - T_i S_i - E_j D_j \quad (1.20)$$

that is the Gibbs thermoelectric state function, used to describe the behavior of a thermopiezoelectric solid as a thermodynamic system. The differential of G gives together with Eq. (1.20):

$$dG = -\sigma d\theta - S_i dT_i - D_j dE_j \quad (1.21)$$

From Eq. (1.21) it can be obtained:

$$\sigma = -\left(\frac{\partial G}{\partial \theta}\right)_{T,E} \quad S_i = -\left(\frac{\partial G}{\partial T_i}\right)_{\theta,E} \quad D_j = -\left(\frac{\partial G}{\partial E_j}\right)_{\theta,T} \quad (1.22)$$

where subscripts indicate variables kept constant. Small changes in the temperature, strain and electrical displacement may be written as total derivatives:

$$d\sigma = -\left(\frac{\partial \sigma}{\partial \theta}\right)_{T,E} d\theta + \left(\frac{\partial \sigma}{\partial T_i}\right)_{\theta,E} dT_i + \left(\frac{\partial \sigma}{\partial E_j}\right)_{\theta,T} dE_j \quad (1.23)$$

heat capacity piezocaloric effect electrocaloric effect

$$dS_i = -\left(\frac{\partial S_i}{\partial \theta}\right)_{T,E} d\theta + \left(\frac{\partial S_i}{\partial T_i}\right)_{\theta,E} dT_i + \left(\frac{\partial S_i}{\partial E_j}\right)_{\theta,T} dE_j \quad (1.24)$$

thermal expansion elastic compliance converse piezoelectricity

$$dD_j = -\left(\frac{\partial D_j}{\partial \theta}\right)_{T,E} d\theta + \left(\frac{\partial D_j}{\partial T_i}\right)_{\theta,E} dT_i + \left(\frac{\partial D_j}{\partial E_j}\right)_{\theta,T} dE_j \quad (1.25)$$

pyroelectric effect direct piezoelectricity dielectric permittivity:

Each of the partial derivatives in equations (1.23)-(1.25) identifies a physical effect as indicated in the equations. Evaluating these equations in the values of the thermodynamic state variables, they are obtained the linear state equations for the material.

1.3.5 Boundary conditions

If there is a material surface of discontinuity, then across the surface there are continuity conditions:

$$n_i T_{ij}^I = n_i T_{ij}^{II} \quad (1.26)$$

$$u_j^I = u_j^{II} \quad (1.27)$$

$$n_i D_i^{\mathbf{I}} = n_i D_i^{\mathbf{II}} \quad (1.28)$$

$$E_i^{\mathbf{I}} = E_i^{\mathbf{II}} \quad (1.29)$$

where \mathbf{I} indicates the values of the variables on one side and \mathbf{II} the values of the variables on the other side of the surface of discontinuity and n_i denotes the components of the unit normal to the surface. At traction-free surface, the boundary conditions, Eq. (1.26), become

$$n_i T_{ij} = 0 \quad (1.30)$$

At a displacement-free surface, the boundary conditions, Eq. (1.27), become

$$u_j = 0 \quad (1.31)$$

1.3.6 Alternate Forms of Constitutive Equations

For the unbounded piezoelectric medium, the only form of the constitutive equations which is of any value is given in Eqs. (1.15), (1.16), (1.17) and (1.18). Some other forms of the constitutive equations are:

$$\mathbf{S} = \mathbf{s}^{\mathbf{D}} \mathbf{T} + \mathbf{g} \mathbf{D} \quad (1.32)$$

$$\mathbf{E} = -\mathbf{g} \mathbf{T} + \boldsymbol{\beta}^{\mathbf{T}} \mathbf{D} \quad (1.33)$$

and

$$\mathbf{T} = \mathbf{c}^{\mathbf{D}} \mathbf{S} - \mathbf{h} \mathbf{D} \quad (1.34)$$

$$\mathbf{E} = -\mathbf{h} \mathbf{S} + \boldsymbol{\beta}^{\mathbf{S}} \mathbf{D} \quad (1.35)$$

These latter forms of the constitutive equations, although exact, are employed in approximations which are valid under certain limiting circumstances. The set to use in a given instance depends crucially on the specific geometrical, mechanical, and electrical circumstances.

1.4 Acoustic wave technology

The operation of acoustic wave devices is based on the propagation of bulk or surface launched acoustic waves through piezoelectric and other materials. Electroacoustics deals with the transformation of acoustic energy into electric energy or vice versa. Most often this transformation is conducted within a piezoelectric material. The applications for the

electroacoustic technology range from frequency control, sonar and ultra sound investigations, filter applications, sensors, etc.

1.4.1 Acoustic wave in solids

The application of a periodic perturbation (stress) to a solid, results in elastic deformations (strain), which travel as waves through the solid. The type of wave (transversal or longitudinal) and the phase velocity both depend on crystal structure. In order to obtain the wave equation that describes the acoustic wave in a solid, it is required a set of equations relating the mechanical variables. In three-dimensional system these four relations are:⁹

Newton's Law

$$\nabla \cdot \mathbf{T} = \rho \frac{\partial^2 \mathbf{u}}{\partial t^2} \quad (1.36)$$

Particle velocity

$$\mathbf{v} = \frac{\partial \mathbf{u}}{\partial t} \quad (1.37)$$

is the time derivative of particle displacement.

Strain definition

$$\mathbf{S} = \nabla^s \mathbf{u} \quad (1.38)$$

Hooke's Law

$$\mathbf{T} = \mathbf{cS} \quad (1.39)$$

where \mathbf{T} is the mechanical stress tensor, \mathbf{S} is the mechanical strain tensor, \mathbf{u} is the displacement vector of the particle, \mathbf{c} the tensor of elasticity, t denotes time and ρ the density of the material. The two first equations are the fundamental physical laws and the other two the constitutive equations. Therefore, the wave equation in three dimensions is described by the Christoffel equation as follows:

$$\mathbf{c}\nabla^2 \mathbf{u} = \rho \frac{\partial^2 \mathbf{u}}{\partial t^2} \quad (1.40)$$

1.4.2 Electroacoustic resonator operation

*Natural Vibrating Frequencies*³

In order to study the concept of natural vibrating frequencies, it is convenient to start with a piezoelectric material subjected to a strain as the one illustrated in Figure 1.4 (top). The stress that the particles present under these conditions is given by the Hooke's Law (Eq. (1.39)). At a certain instant, the external force which maintains the strain is removed and the material starts to vibrate freely. Now a slice of material with thickness dy is located at the coordinate y . This slice is subjected to forces at both ends, as shown in Figure 1.4 (central part). The resultant of the forces will be equal to the product of the slice's mass by the acceleration to which the slice is subjected as shown by the Newton's Law (Eq. (1.36)) which together with Eq. (1.39) results into Eq. (1.40).

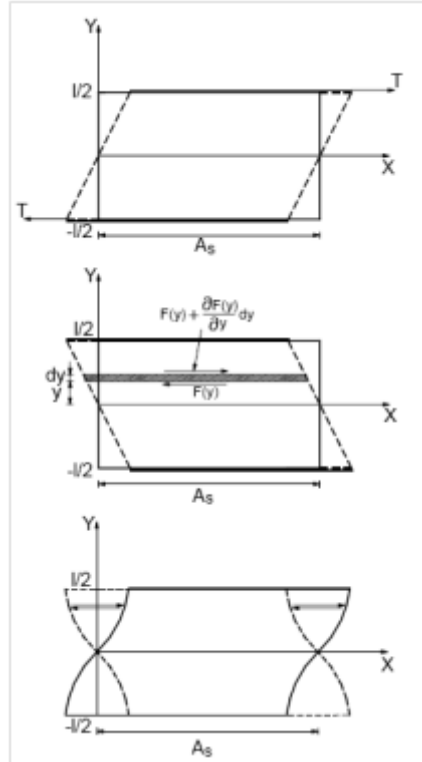


Figure 1.4: Figures explaining the natural vibration of a piezoelectric resonator: The upper part shows the resonator bar subjected to an external stress, the central part shows the forces that an internal thin slice of a strained piezoelectric material experience, and the lower part shows the displacement profile of a piezoelectric material subjected to a sinusoidal electric field.³

Now it is assumed that the particle displacement near equilibrium has a sinusoidal dependence with time. Thus, the time derivative of particle displacement can be replaced by the product $j\omega$ where j is the complex base -1 and $\omega = 2\pi f$ is the oscillating angular frequency of the particles, where f is the frequency. Therefore Eq (1.40) becomes:

$$v_0 \frac{\partial^2 \mathbf{u}}{\partial y^2} + \omega^2 \mathbf{u} = 0 \quad (1.41)$$

where $v_0 = \sqrt{\bar{c}/\rho}$ is the phase velocity of the acoustic wave in the material as the result of solving the Christoffel equation. \bar{c} is the piezoelectrically stiffened constant, which

includes the increase in the value of the elastic constant due to the piezoelectric effect (showed in section 1.6).

In Figure 1.4 (bottom) it can be seen the instantaneous profiles of the particle displacement with regard to the coordinate y , once resolved Eq. (1.41). The displacement function fulfilling this equation is:

$$u = u_0 \sin (2\pi k y + \sigma) = u_0 \sin \left(\frac{2\pi}{\lambda} y + \psi \right) \quad (1.42)$$

where $\lambda = v_0/f$ is the wavelength, $k = 1/\lambda = f/v_0 = \omega/2\pi v_0$ is called the wave number since it corresponds to the number of complete wave lengths in the distance unit; u_0 is the maximum amplitude of oscillation and ψ is a constant to determine consistently with the boundary conditions.

In this case, the particles displacement is null at the coordinate $y = 0$. This condition implies $\psi = 0$. Also, the amplitude of oscillation must be a maximum at the ends where $y = \pm l/2$. Therefore, it is necessary that the following condition be fulfilled:

$$2\pi k \frac{l}{2} = n \frac{\pi}{2} \Rightarrow n = 1, 2, 3 \dots \quad (1.43)$$

This condition forces the oscillation at frequencies f_{n0} which have to be odd multiples of a frequency f_0 according to the following expression:

$$f_{n0} = n f_0 = n \frac{v_0}{2l} \Rightarrow n = 1, 2, 3 \dots \quad (1.44)$$

Frequency f_0 is called natural vibration fundamental frequency or resonant frequency and its multiples are called harmonics of the fundamental frequency. Notice that v_0 is the phase velocity of the acoustic wave in the material without losses. Indeed, the velocity is the ratio between the distance covered by the perturbation and the time it takes to go through that distance. From the definition of v_0 as a function of the wave length and the oscillation frequency we get $v_0 = \lambda f$. This equation indicates that the perturbation covers a space corresponding to a wave length in the time corresponding to a period of the oscillation. This is precisely the definition of the propagation velocity. Eq. (1.44) also indicates that the frequencies of natural vibration depend solely on the material's physical properties and on its thickness. It also seems to indicate that the only possible vibrating frequencies are the ones that fulfill that condition. In fact, Eq. (1.44) is the result of simplifying the problem to only one dimension. When the lateral dimensions are infinite in comparison with thickness, the vibrating frequencies relative to those directions are null. However, in practice, the portions of material are three-dimensional with finite dimensions. In these cases, additional possible vibrating modes take place.

1.5 Resonant piezoelectric sensors

A piezoelectric sensor is a device that responds to changes occurring in its environment with changes of the resonant (fundamental or harmonic) frequency, or wave (phase) speed. Bulk and surface acoustic wave piezoelectric sensors are distinguished depending on the way of the wave propagation. The resonant frequency primarily depends on thickness of the piezoelectric crystal and the attached layer, on the viscoelastic properties of the crystal and that of the adjacent phase, as determined by the coupling boundary conditions. Mass loading, ambient viscosity, and electric permittivity, compression or extension stresses, local electric fields, charge, film conductivity, and surface tension affect the coupling conditions.

1.5.1 Overview of piezoelectric resonators

The basic principle of operation for a generic acoustic-wave sensor is a traveling wave combined with a confinement structure to produce a standing wave whose frequency is determined jointly by the velocity of the traveling wave and the dimensions of the confinement structure. Therefore, there are two main effects that a measurement can have on an acoustic-wave microsensors: the wave velocity can be perturbed or the confinement dimensions can be changed.

In the case of a piezoelectric resonator, the traveling wave is either a bulk acoustic wave (BAW) propagating through the interior of the substrate or a surface acoustic wave (SAW) propagating on the surface of the substrate

In the bulk of a solid, two types of bulk acoustic waves can propagate: longitudinal waves, also called compressional/extensional waves and the transverse waves, also called shear waves.

When a single plane boundary interface is present forming a semi-infinite solid, surface acoustic waves can propagate along the boundary. Probably the most common type of SAWs are the Rayleigh waves, which are actually two-dimensional waves given by the combination of longitudinal and transverse waves and are confined at the surface down to a penetration depth of the order of the wavelength.

1.5.2 Modes of actuation/sensing

Because of crystal symmetries, piezoelectric coupling matrices have few non-zero elements (see Figure 1.3). The design of actuation and sensing devices is dictated by the available coupling modes as shown in the following matrices:

$$\begin{Bmatrix} S_{11} \\ S_{22} \\ S_{33} \\ 2S_{23} \\ 2S_{13} \\ 2S_{12} \end{Bmatrix} = \underbrace{\begin{bmatrix} s_{11} & s_{12} & s_{13} & 0 & 0 & 0 \\ s_{12} & s_{22} & s_{23} & 0 & 0 & 0 \\ s_{13} & s_{23} & s_{33} & 0 & 0 & 0 \\ 0 & 0 & 0 & s_{44} & 0 & 0 \\ 0 & 0 & 0 & 0 & s_{55} & 0 \\ 0 & 0 & 0 & 0 & 0 & s_{66} \end{bmatrix}}_{\text{compliance}} \begin{Bmatrix} T_{11} \\ T_{22} \\ T_{33} \\ T_{23} \\ T_{13} \\ T_{12} \end{Bmatrix} + \underbrace{\begin{bmatrix} 0 & 0 & d_{31} \\ 0 & 0 & d_{32} \\ 0 & 0 & d_{33} \\ 0 & d_{24} & 0 \\ d_{15} & 0 & 0 \\ 0 & 0 & 0 \end{bmatrix}}_{\text{coupling}} \begin{Bmatrix} E_1 \\ E_2 \\ E_3 \end{Bmatrix}$$

$$\begin{Bmatrix} D_1 \\ D_2 \\ D_3 \end{Bmatrix} = \underbrace{\begin{bmatrix} 0 & 0 & 0 & 0 & d_{15} & 0 \\ 0 & 0 & 0 & d_{24} & 0 & 0 \\ d_{31} & d_{32} & d_{33} & 0 & 0 & 0 \end{bmatrix}}_{\text{coupling}} \begin{Bmatrix} T_{11} \\ T_{22} \\ T_{33} \\ T_{23} \\ T_{13} \\ T_{12} \end{Bmatrix} + \underbrace{\begin{bmatrix} \varepsilon_{11} & 0 & 0 \\ 0 & \varepsilon_{22} & 0 \\ 0 & 0 & \varepsilon_{33} \end{bmatrix}}_{\text{permittivity}} \begin{Bmatrix} E_1 \\ E_2 \\ E_3 \end{Bmatrix}$$

The most commonly used piezo materials for actuation and sensing are the piezoceramics (e.g. PZT) and the piezopolymers (e.g. PVDF). The available modes of actuation for a piezoelectric material are determined by its coupling matrix. Therefore it can be anticipated that three main modes of actuation/sensing are available: inplane mode (d_{31} , d_{32}), the thickness mode (d_{33}) and shear mode (d_{15} , d_{24}).

The first two configurations mentioned above are the most commonly used (Figure 1.5). A linear actuator consists of a stack of thin ceramic disks separated by electrodes (Figure 1.5a). The material is such that the coefficient d_{33} dominates the other piezoelectric constants in the constitutive equations. As a result, the direction of expansion coincides with that of the electric field. The stacked design is often referred to as d_{33} design. This design is mainly used for precision position control.

In the laminar design (Figure 1.5b), thin piezoelectric films are generally grown on the structure to obtain a bending action. The geometrical arrangement is such that d_{31} (d_{32}) dominates the design and the useful direction of expansion is normal to that of the electric field. It is the shape of the electrodes which determines the effective part of the material. This property is widely used for distributed actuation and sensing.

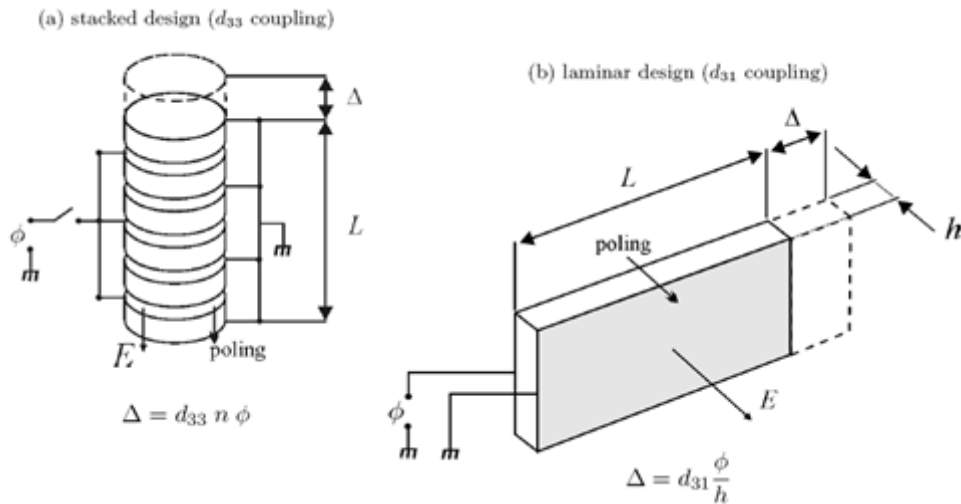


Figure 1.5: Common piezoelectric actuator designs. a) stacked design and b) laminar design.⁶

1.5.3 Types of Resonant piezoelectric sensors

An important aspect of piezoelectric resonators devices is that they often operate with the so-called *high-frequency modes*. For instance, in a resonator plate the high frequency modes, e.g., thickness-shear and thickness-stretch, are modes whose frequencies are determined by the plate thickness, the smallest dimension. This is in contrast to the low frequency modes of extension and flexure in traditional structural engineering, whose frequencies depend strongly on the length and/or width of the plate. Another characteristic of the high frequency modes is that for long waves their frequencies do not go to zero but have finite cutoff frequencies. This has implications in certain unique behaviors of the high frequency modes such as the useful energy trapping phenomenon.

1.5.3.1 Thickness-Shear-Mode (TSM) resonators

Quartz is the most frequently used piezoelectric matrix for this kind of resonators because of its stability with respect to temperature. Thus, quartz crystal microbalance (QCM) has become in the most important device as a mass sensor.

Quartz crystal microbalance devices are highly sensible to small mass variations due to changes in quartz crystal resonance frequency. Some microbalances reach a resolution up to 0,05ng. QCMs have mayor sensibility than conventional analytical microbalances actually used in laboratories. This high mass sensibility could be explained by the huge acceleration acting on the deposited film.

The crystal frequency response depends on it physical properties and the properties of the adjacent media. The microbalance presents a decrease in it resonant frequency caused by

the added surface mass in the form of film. Sauerbrey equation (see Eq.(1.45)) relates these changes occurring in the f_0 with the accumulated mass on the crystal:

$$\Delta f = k_s \Delta m \quad (1.45)$$

where Δf is the change in resonance frequency, Δm is the deposited mass and k_s is a constant considering quartz parameters like the resonance frequency, thickness, density and shear modulus. Within a certain range, the frequency shift Δf is sufficiently linear with the added loading mass Δm regardless of the film material properties.

QCMs are fabricated using a thin quartz crystal disc with electrodes fabricated by growing gold or platinum films on the surface of the crystal (Figure 1.6). The application of an external electric potential to the piezoelectric material generates internal mechanical stress. An alternating electrical field applied on the faces of the device induces an acoustic wave that propagates through the crystal.

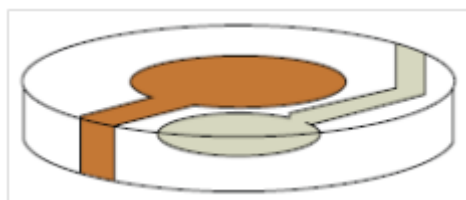


Figure 1.6: Diagram of a quartz crystal microbalance.

The oscillation modes of the crystals correspond to its deformation, which is dependent on the glass cut. In the shear vibrational mode, the crystal has an AT-cut which has a specific orientation of $35^{\circ}15'$ with respect to the optical axis (Figure 1.7). This mode is used for the manufacture of microbalances due to its low temperature coefficient, with minimal changes in frequency as a function of temperature variations. They operate at a relatively low frequency of between 3 MHz and 15 MHz. Usual applications of these devices are found in depositional systems, gas phase detection (humidity, etc.), immunosensors by a layer of antibodies, DNA biosensors (tying the single-stranded DNA and detecting the hybridization) and drug analysis through a specific adsorbents layer.

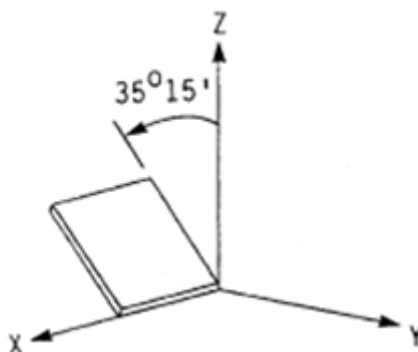


Figure 1.7: AT-cut angle.

1.5.3.2 Thin film bulk acoustic wave resonator

Currently, there efforts are focused on the development of thin film-based acoustic resonators. This technology was born as a direct extension of the quartz crystal resonators. These are BAW-based thickness mode wave resonators, permitting a reduction in the piezoelectric thickness of the resonator thus conducting to an increased resonance frequency (>1GHz). Thin film-based resonators provide much higher sensitivity and resolution in mass detection, and in addition they are much easily integrated with microelectronic drivers.

FBAR resonators could be suspended on a substrate, usually silicon, in order to facilitate it resonance thus avoiding vibrations damping (system loses). As opposed to free-standing or suspended resonators, composite resonators can also be used where the piezoelectric film is deposited on a nonpiezoelectric substrate, such as silicon, with intermediate layers with different acoustic impedances. Composite film resonators can display improved thermal stability due to the property matching that can be obtained among different layers. A significant case is when the layers have alternate high and low acoustic impedances, thereby forming a Bragg reflector which acts as an acoustic mirror that isolates the film from the substrate, often termed solidly-mounted resonator (SMR). The structures of suspended and SMR FBARs are shown in Figure 1.8.

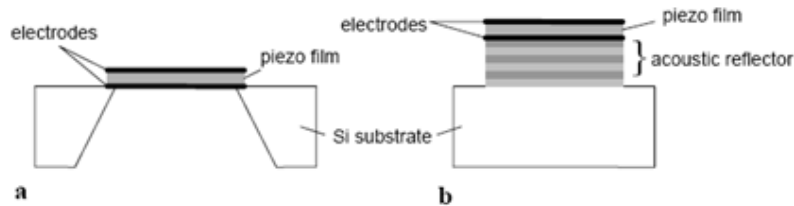


Figure 1.8: Film bulk acoustic resonator (FBAR) sensors. a) free-standing structure and b) solidly-mounted resonator (SMR) structure

1.5.3.3 Surface Acoustic Wave Sensors

Surface acoustic wave sensors are made by a thick plate of piezoelectric material, typically ST-cut quartz, lithium niobate or lithium tantalate, where predominantly Rayleigh waves propagate along the upper surface.

SAW technology utilizes an interdigitated transducer (IDT) to convert electrical energy into an acoustic wave. The acoustic wave then travels across the surface of the device substrate to another interdigitated transducer, converting the wave back into an electrical signal. As the characteristics of the surface acoustic wave can be modified by changes in the surface properties as a result of various physical phenomena, sensors can be designed to quantify many different phenomena.

An IDT, in its simple version, is formed by two identical comb-like structures whose respective fingers are arranged on the surface in an interleaved alternating pattern (see

Figure 1.9). The IDT period length d , or pitch, is the spacing between the center of two consecutive fingers of the same comb. When an AC voltage is applied to the IDT, acoustic waves are generated which propagate along the axis perpendicular to the fingers in both directions. The maximum wave amplitude is obtained when constructive interference among the fingers occurs. This happens at the characteristic or synchronous frequency $f_0 = v/d$, where v is the SAW velocity in the material. Typical SAW characteristic frequencies are 30-500 MHz.³

The surface particles move elliptically, resulting in a wave consisting of both shear and compressional components. The latter provokes an important attenuation effect in liquids which prevents the application of SAW devices in such media. The particle displacements of the shear wave are transverse relative to the propagation direction and normal to the plane of the surface, so that the generated wave is categorized as shear vertical.

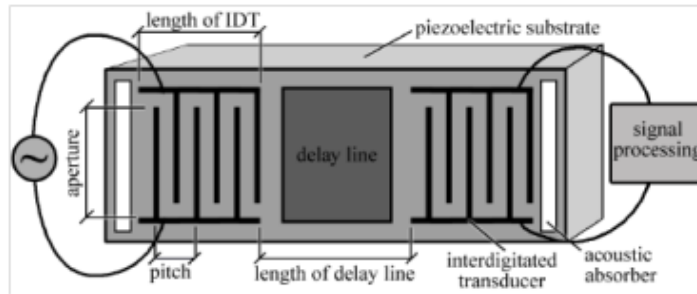


Figure 1.9: General structure of a surface acoustic wave sensor with connections to an AC voltage source and a signal processing unit. In some sensors, the acoustic absorbers are replaced with reflectors to decrease insertion loss.¹⁰

1.6 Piezoelectric coupling constant

Equations (1.15) to (1.18) show the constitutive relations for the linear piezoelectricity expressing the relation between the stress, strain, electric field, and electric displacement field in either a stress-charge and strain-charge form. In the case of stress-charge form and in the absence of piezoelectricity ($\mathbf{e} \rightarrow 0$), they reduce to the “regular” uncoupled wave equations for the acoustic and electric fields.

If it is assumed that the presence of the acoustic wave does not cause electromagnetic radiation in the crystal, that is, there is no coupling between \mathbf{E} (created by the acoustic wave) and \mathbf{H} , there will be no electromagnetic energy carried due to the acoustic wave. This assumption is called the *quasistatic approximation*.

The assumption that there is no coupling between the electromagnetic and acoustic wave, and thus no acoustically generated magnetic field, implies that:

$$\nabla \times \mathbf{E} = 0 \quad (1.46)$$

From (1.46) it can be written the electric field as the gradient of a scalar potential:

$$\mathbf{E} = -\nabla \phi \quad (1.47)$$

The implication of (1.46) is that the electric field continuously being generated by the strain wave propagates at the acoustic velocity.

Now, considering the Christoffel equation (Eq. (1.40)) with an electrical perturbation term, a new equation of identical form can be derived, but with extra terms.¹¹ These terms, dependent on the piezoelectric and permittivity matrices, have been added to the stiffness matrix. It can be said that the components of the stiffness matrix have been piezoelectrically *stiffened*. For a given propagation direction, the form of the stiffness components is:

$$\bar{c} = c^E + \frac{e^2}{\epsilon^S} \quad (1.48)$$

Therefore, the *stiffened* phase velocity obtained solving the Christoffel equation is determined by \bar{c} rather than by c :

$$\bar{v}_0 = \sqrt{\frac{\bar{c}}{\rho}} = \sqrt{\frac{c^E + e^2/\epsilon^S}{\rho}} \quad (1.49)$$

To determine the piezoelectric correction quantitatively, the unstiffened phase velocity is used:

$$v_0 = \sqrt{\frac{c^E}{\rho}} \quad (1.50)$$

Note that this velocity is fictitious. The true velocity involves the stiffened constant \bar{c} . It'll be used c simply as a mathematical convenience to calculate the effects of piezoelectricity on acoustic wave propagation. Rewriting (1.49), it can be obtained:

$$\bar{v}_0 = v_0 \left(1 + K^2\right)^{1/2} \quad (1.51)$$

where

$$K^2 = \frac{e^2}{c^E \epsilon^S} \quad (1.52)$$

is called the piezoelectric coupling constant. It can be also defined the electromechanical coupling constant:

$$k_t^2 = \frac{K^2}{1 + K^2} \quad (1.53)$$

where the subscript t refers to the requirement that the electric field is applied across the thickness of the crystal. The electromechanical coupling constant is important when the piezoelectric crystal is used to convert electrical energy to mechanical energy (or vice

versa). For most piezoelectric materials, $K^2 < 0.3$, so the difference between the two coupling constants is very small. Also, the electromechanical coupling constant can be determined from the series resonance frequency f_s and the parallel resonance frequency⁴ f_p (see *Section 3.2.2* for more details):

$$k_t^2 = \frac{\pi}{2} \frac{f_s}{f_p} \tan \left\{ \frac{\pi}{2} \frac{(f_p - f_s)}{f_p} \right\} \quad (1.54)$$

1.7 Bibliography

-
- ¹ D. S. Ballantine Jr., R. M. White, S. J. Martin, A. J. Ricco, E. T. Zellers, G. C. Frye, H. Wohltjen, *Acoustic Wave Sensors: Theory, Design, & Physico-Chemical Applications*, Academic Press Inc., 1997.
 - ² W. Callister, *Fundamentals of Materials Science and Engineering*, John Wiley & Sons, Inc., 2001.
 - ³ A. Arnau, *Piezoelectric transducers and applications*. Springer Verlag, 2008.
 - ⁴ IEEE Standard on Piezoelectricity, ANSI/IEEE Std 176-1987.
 - ⁵ J. Nye, *Physical Properties of Crystals*, Oxford University Press, London, 1957, Chapter 7
 - ⁶ V. Piefort, “Finite element modelling of piezoelectric active structures”, Ph.D. dissertation, Universite Libre de Bruxelles, 2001.
 - ⁷ D. Damjanovic, “Ferroelectric, dielectric and piezoelectric properties of ferroelectric thin films and ceramics”, *Rep. Prog. Phys.* 61, 1267–132, 1998.
 - ⁸ D. J. Leo, *Engineering analysis of smart material systems*, 2007.
 - ⁹ J. Rosenbaum, *Bulk Acoustic Wave Theory and Devices*, Artech House, Inc., 2000.
 - ¹⁰ J. Kirschner, “Surface Acoustic Wave Sensors (SAWS):Design for Application”, *Surface Acoustic Wave Sensors (SAWs): Design for Fabrication*. Microelectromechanical Systems, december, 2010.
 - ¹¹ J. Rosenbaum, *Bulk Acoustic Wave Theory and Devices*, Artech House, Inc., 2000.

CHAPTER 2: MEMS Technology

MEMS technology is based on a number of tools and methodologies, which are used to form small structures with dimensions in the micrometer scale (one millionth of a meter). Significant parts of the technology have been adopted from integrated circuit technology. For instance, almost all devices are built on wafers of silicon, like ICs. The structures are realized in thin films of materials, like ICs. They are patterned using photolithographic methods, like ICs. There are however several processes that are not derived from IC technology, and as the technology continues to grow, the gap with IC technology also grows.

Most MEMS devices and systems involve some form of lithography-based microfabrication, borrowed from the microelectronics industry and enhanced with specialized techniques generally called “micromachining.” The batch fabrication that is characteristic of the microelectronics industry offers the potential for great cost reduction when manufacturing in high volume.

In this chapter it is described the manufacturing techniques for microfabrication: The first part is an overview of the photolithography process and covers the different steps involved; the following part deals with material removal processes and finally additive processes, where materials are added, are covered.

2.1 Photolithography

The word *lithography* refers to the process invented in 1796 by Aloys Senefelder, who found that stone, when properly inked and treated with chemicals, could transfer a carved image onto paper. As a result of the chemical treatment of the stone, image and nonimage areas became oil receptive (water repellent) and oil repellent (water receptive), respectively, attracting ink onto the image and attracting water on nonimage areas.

Lithography in the MEMS context is typically the transfer of a pattern to a photosensitive material by selective exposure to a radiation source such as light. A photosensitive material is a material that experiences a change in its physical properties when exposed to a radiation source. If it is selectively exposed a photosensitive material to radiation (e.g. by masking some of the radiation) the pattern of the radiation on the material is transferred to the material exposed, as the properties of the exposed and unexposed regions differs.

The most widely used form of lithography is photolithography. In the IC industry, pattern transfer from mask onto thin films is accomplished almost exclusively via photolithography. Photolithography and pattern transfer involve a set of process steps summarized in Figure 2.1.

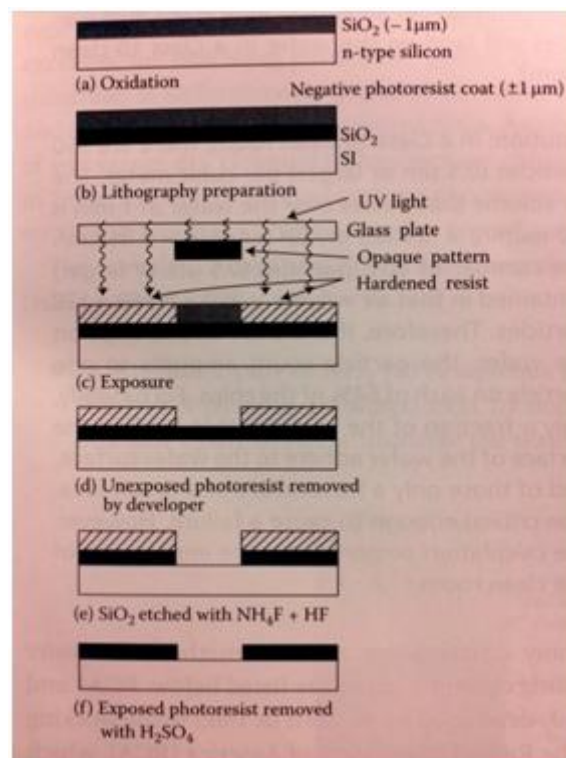


Figure 2.1: Basic photolithography and pattern transfer. Example used an oxidized silicon wafer and negative photoresist system. Process steps include exposure, development, oxide etching and resist stripping.¹

In the figure showed above, an oxidized wafer (Figure 2.1a) is coated with a 1 μm -thick negative photoresist layer (Figure 2.1b). After exposure (Figure 2.1c), the wafer is rinsed in a developing solution or sprayed with spray developer, which removes the unexposed areas of photoresist and leaves a pattern of bare and photoresist-coated oxide on the wafer surface (Figure 2.1d). The photoresist pattern is the negative image of the pattern on the photomask. In a typical ext step after development, the wafer is placed in a solution of HF or HF+ NH_4F , meant to attack the oxide but not the photoresist or the underlying silicon (Figure 2.1e). The photoresist protect the oxide areas it covers. Once the exposed oxide have been etched away, the remaining photoresist can be stripped off with an strong acid such as H_2SO_4 or an acid-oxidant combination such as $\text{H}_2\text{SO}_4\text{-Cr}_2\text{O}_3$ attacking the photoresist but not the oxide or the silicon (Figure 2.1f). Other liquid strippers include

organic solvent strippers and alkaline strippers. The oxidized Si wafer with the etched window in the oxide (Figure 2.1f) now is ready for further processing, which might entail a wet anisotropic etch of the silicon in the etched windows with SiO_2 as the etch mask.

2.1.1 Masks¹

The stencil used to repeatedly generate a desired pattern on resist-coated wafers is called *mask*. In typical use, a photomask (a nearly optically flat glass or quartz plate with an absorber pattern metal) is placed above the photoresist-coated surface and the mask/wafer system is exposed to UV radiation. The absorber pattern on the photomask is opaque to UV light, whereas the glass or quartz is transparent. The absorber pattern on the mask is generated by e-beam lithography, a technique that yields higher resolution than photolithography. In e-beam lithography, a pattern drawn on a computer-aided design (CAD) system is exposed onto the mask (see Figure 2.2). Like resist, masks can be positive or negative. A *positive* or *dark field* mask is a mask on which the pattern is clear with the background dark. A *negative* or *clear field* mask is a mask on which the pattern is dark with the background clear. The procedure results in a 1:1 image of the entire mask onto the silicon wafer.

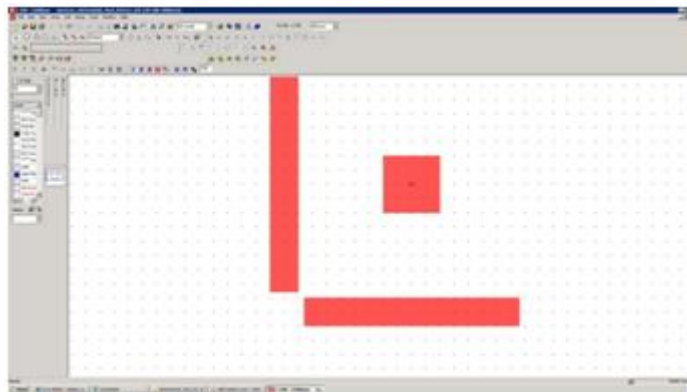


Figure 2.2: Pattern drawn on a computer-aided design (CAD) system to generate a mask by the e-beam lithography technique.

Mask making direct physical contact (*hard contact*) with the substrate is called *contact masks*. Unfortunately, these masks degrade faster because of wear than noncontact, proximity masks (*soft contact*), which are slightly raised, e.g. 10-20 μm , above the wafer. The defect resulting from hard contact masks on both the wafer and the mask, make this method of optical pattern transfer unsuitable for Very Large Scale Integration (VLSI) manufacturing. In VLSI, ICs have between 100000 and 1 million components and in Ultra Large Scale Integration (ULSI), there are more than 1 million circuit elements on a single chip.

If the feature sizes of interest are relatively large, greater than about 50 μm , an alternate low-cost mask-making method can be used. The artwork is drawn using any standard

personal-computer software, and then printed onto transparencies using a high-resolution laser printer. Depending on the wafer size, one can fit several mask layers onto a single transparency. Since commercial quartz masks can cost U\$S1000 per layer and may require several weeks to obtain from a vendor, the single-transparency approach has obvious appeal when it can be used.

2.1.2 Alignment²

In order to make useful devices the patterns for different lithography steps that belong to a single structure must be aligned to one another. The first pattern transferred to a wafer usually includes a set of alignment marks, which are high precision features that are used as the reference when positioning subsequent patterns to the first pattern (Figure 2.3). Often alignment marks are included in other patterns, as the original alignment marks may be obliterated as processing progresses. It is important for each alignment mark on the wafer to be labeled so it may be identified and for each pattern to specify the alignment mark (and the location thereof) to which it should be aligned. By providing the location of the alignment mark it is easy for the operator to locate the correct feature in a short time. Each pattern layer should have an alignment feature so that it may be registered to the rest of the layers.

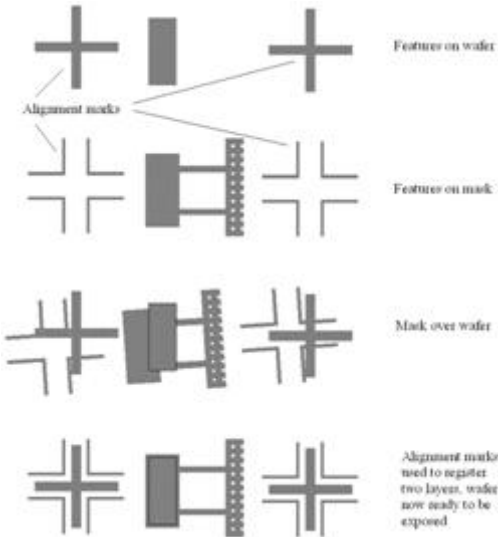


Figure 2.3: Use of alignment marks to register subsequent layers.²

As there is no pattern on the wafer for the first pattern to align to, the first pattern is typically aligned to the primary wafer flat (Figure 2.4). Depending on the lithography equipment used, this may be done automatically, or by manual alignment to an explicit wafer registration feature on the mask.

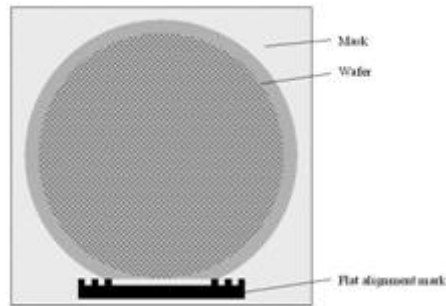


Figure 2.4: Mask alignment to the wafer flat.²

2.1.3 Photoresist deposition¹

Lithography is the most expensive step in microelectronics technology, representing up to 35% of the wafer manufacturing cost. Within lithography, photoresist coating is one of the more expensive steps. Photoresists make cost U\$\$100/L, and several of the resist deposition processes used waste significant amounts of material. For silicon ICs, the resist thickness after a prebake typically ranges between 0.5 and 2 μm . For miniaturized 3D structures, much greater resist thicknesses are often required and complex topography may also call for a conformal resist coat over very high-aspect-ratio features. For thick resist coats, techniques such as casting and the use of thick sheets of dry photoresists replace the ineffective resist spinners. For conformal coating, resist spraying or, better yet, electrodeposition of photoresist may be preferable.

2.1.3.1 Spin coating

As the first step in the lithography process itself, a thin layer of inorganic polymer, a photoresist sensitive to UV radiation, is deposited on the oxide surface. The photoresist is dispensed onto the wafer lying on a wafer platen in a resist spinner. A vacuum chuck holds the wafer in place. Speed of about 500 rpm is commonly used during the dispensing step enabling the spread of the fluid over the substrate. After the dispense step it is common to accelerate to a relatively high speed to thin the fluid to near its final desired thickness. Typical spin speeds for this step range from 1500-6000 rpm depending of the properties of the fluid as well as the substrate.

This step can take from 10 seconds to several minutes. The combination of spin speed and time selected for this step will generally define the final film thickness. At these speeds, centrifugal force causes the solution to flow to the edges, where it builds up until expelled when surface tension is exceeded. The resulting polymer thickness is a function of spin speed, solution concentration and molecular weight.

The resist spinning process is of primary importance to the effectiveness of pattern transfer. The quality of the resist coating determines the density of defects transferred to the device under construction.

The photoresist film, after application to the substrate, must have a uniform thickness and must be chemically isotropic so that its response to exposure and development is uniform. The coating thickness of the thin, glassy resist film depends on the chemical resistance required for image transfer and the fineness of the lines and spaces to be resolved. The coating process should take place in Class 100 laminar flow air conditions and a minimum spin time of 30 seconds is necessary for coating uniformity. The photoresist should also be filtered just before application. The application of too much resist results in edge covering or run-out, hillocks and ridges, reducing manufacturing yield. Application of too little resist may leave uncovered areas. Optimization of the “regular” photoresist coating process in terms of resist dispense rates, dispense volume, spin speed, ambient temperature, venting of the resist spin station and humidity presents a growing challenge.

The need for an alternative photoresist deposition technique may arise as the amount of waste material generated by spin coating is high, with most of the resist solutions (>95%) thrown off the substrate during the spin casting process. Also inherent to this process is the formation of edge beads, which require an additional removal process before subsequent process steps. The edge of a wafer might exhibit resist ridges that are about 10 times the mean thickness on the rest of the substrate.

2.1.3.2 Spray coating

In spray coating, the substrates to be coated pass under a spray of photoresist solution. The spray system includes an ultrasonic spray nozzle that generates a distribution of droplets in the micrometer range.

2.1.3.3 Dip coating

In dip coating, one dips the substrate into a solution of liquid resist to apply a coating. The method is simple in that the substrate after cleaning and drying is dipped into a tank containing the photoresist and withdrawn slowly.

2.1.4 Soft baking¹

After resist coating, the resist still contains up to 15% solvent and may contain built-in stresses. Therefore, the wafers are soft baked (also pre-exposure baked or prebaked) at 90-100°C for about 20 minutes in a convection oven or at 75-85°C for 1-3 min. with a vacuum hot plate to remove solvents and stress, and to promote adhesion of the resist layer to the

substrate. This is a critical step in that failure to sufficiently remove the solvent will affect the resist profile. Excessive baking destroys the photoactive compound and reduces sensitivity.

Hot plating the resist is faster, more controllable, and thus not traps solvent like convection oven baking. In convection ovens, the solvent at the surface of the resist is evaporated first, and this can cost an impermeable resist skin, trapping the remaining solvent inside.

2.1.5 Exposure¹

After soft baking, the resist-coated wafers are transferred to an illumination or exposure system where they are aligned with the features on the mask. For any lithographic technique to be of value, it must provide an alignment technique capable of a superposition precision of mask and wafer that is a small fraction of the minimum feature size of the devices under construction. In the simplest case, an exposure system consists of a UV lamp illuminating the resist-coating wafer through a mask without any lenses between the two. The purpose of illumination is to deliver light with the proper intensity, directionality, spectral characteristics and uniformity across the wafer, allowing a nearly perfect transfer or printing of the mask image onto the resist in the form of a latent image.-

In photolithography, wavelengths of the light source used for exposure of the resist-coated wafer range from the very short wavelengths of extreme UV (10-14 nm), to deep UV (150-300 nm) to near UV (350-500 nm). In near UV, one typically uses the g-line (435 nm) or i-line (365 nm) of a mercury lamp.

2.1.5 Development¹

Development is the dissolution of unpolymerized resist that transform the latent resist image, formed during exposure, into a relief image that will serve as a mask for further subtractive and additive steps. During the development of an exposed resist, selecting dissolving takes place. Two main technologies are available for development: wet development is widely used in circuits and miniaturization manufacture in general and dry development which is starting to replace wet development for some of the ultimate line-width resolution applications.

Wet development by solvents can be based on at least three different types of exposure-induced changes: variation in molecular weight of the polymers (by cross-linking or by chain scission), reactivity change and polarity change. Two main types of wet development setups are used: immersion and spray developers. During batch immersion developing, cassette-loaded wafer are batch-immersed for a timed period in a developer bath and agitated at a specific temperature.

During batch spray development, fan-type sprayers direct fresh developing solution across wafer surfaces. Positive resists are typically developed in aqueous alkaline solutions, and negative resists are developed in organic ones.

Aqueous development is highly favored for health reasons. The aqueous development rate depends on the pH of the developer and the temperature.

The use of organic solvent leads to some swelling of the resist (especially for negative resists) and loss of adhesion of the resist to the substrate. Dry development overcomes these problems, as it is based either on a vapor phase process or a plasma. In the latter, oxygen-reactive-etching is used to develop the latent image. The image formed during exposure exhibits a differential etch rate to oxygen-reactive-etching rather than differential solubility to a solvent.

2.1.6 Descumming¹

A mild oxygen plasma treatment, so called descumming, removes unwanted resist left behind after development. Negative and, to a lesser degree, positive resists, leave a thin polymer film at the resist/substrate interface. The problem is more severe in small (<1 μm) high-aspect-ratio structures where the mass transfer of a wet development is poor. Patterned resist areas are also thinned in the descumming process, but it is usually of little consequence. Before etching the substrate or adding a material, the wafer must be post baked. Post baking or hard baking removes residual coating solvent and developer and anneals the film to promote interfacial adhesion of the resist that has been weakened either by the developer penetration along the resist/substrate interface or by swelling of the resist (mainly for negative resists).

2.1.7 Resists¹

The principal components of photoresists are a polymer (based resin), a sensitizer, and a casting solvent. The polymer changes structure when exposed to radiation; the solvent allows spin application and formation of thin layers on the wafer surface; sensitizers control the chemical reaction in the polymeric phase. Resists without sensitizers are single-component or one-component systems, whereas sensitizer-based resists are two-component systems. Solvent and other potential additives do not directly relate to the photoactivity of the resist.

Resist tone

If the photoresist is of the type called positive (also positive tone), the photochemical reaction during exposure of a resist weakens the polymer by rupture or scission of the main and side polymer chains, and the exposed resist becomes more soluble in the developing solutions. In other words the development rate for the exposed resist is about 10 times faster than the development rate for the unexposed resist. If the photoresist is of the type called negative (also negative tone), the reaction strengthens the polymer by random cross-linkage of main chains or pendant side chains, becoming less soluble.

2.1.8 Resist stripping¹

2.1.8.1 Wet stripping

Photoresist stripping in slightly oversimplified terms, is organic polymer etching. The primary consideration is complete removal of the photoresist without damaging the device under construction. The remaining photoresist can be stripped off with a strong acid as H_2SO_4 or an acid-oxidant combination. Other liquid strippers include organic solvent stripper and alkaline strippers (with or without oxidants). Acetone can be used if the post bake is not too long or occurs at a low enough temperature. Other popular commercial strippers are piranha and RCA clean.

2.1.8.2 Dry stripping

Dry stripping or oxygen plasma stripping, also known as ashing has become more popular as it poses fewer disposal problems with toxic, flammable, and dangerous chemicals. Wet stripping solutions lose potency in use causing stripping rates to change with time. Accumulated contamination in solutions can be a source of particles and liquid surface tension and must transport tend to make photoresist removal difficult and uneven. Dry stripping is more controllable than liquid stripping, less corrosive with respect to metal features on the wafer, and more importantly, it leaves a cleaner surface under the right conditions. Finally, it does not cause undercutting and broadening photoresist features that can be caused by wet strippers.

Plasma stripping uses a low-pressure electrical discharge to split molecular oxygen (O_2) into its more reactive atomic form (O). This atomic oxygen converts an organic photoresist into gaseous products that may be pumped away. This type of plasma stripping belongs in the category of chemical dry stripping and is isotropic in nature.

2.1.9 Soft Lithography³

The so-called *soft lithography* is a relatively recent development for transferring patterns. Unlike conventional optical lithography, it uses a molded polymeric body to accomplish physical pattern transfer, just like a rubber stamp used to press onto an ink pad then onto paper. The mold is formed by casting a silicone rubber, poly(dimethylsiloxane) (PDMS), onto a master that contains the desired relief pattern. The master can be formed by conventional lithography and etching. The molded parts are stripped from the master, and are then used as flexible printing devices, especially for non-planar substrates. When coated with the material to be transferred and then pressed onto the desired surface, patterned material transfer can be achieved. The production of the patterns and molds can be done in a few steps, permitting rapid prototyping to explore new ideas. While this new approach is not yet a standard manufacturing method, it appears to hold significant promise for the future of MEMS.

2.2 Pattern Transfer with Subtractive Techniques²

In order to form a functional MEMS structure on a substrate, it is necessary to etch the thin films previously deposited and/or the substrate itself. In general, there are two classes of etching processes:

- Wet etching where the material is dissolved when immersed in a chemical solution
- Dry etching where the material is sputtered or dissolved using reactive ions or a vapor phase etchant

In the following, we will briefly discuss the most popular technologies for wet and dry etching.

2.2.1 Wet etching

This is the simplest etching technology. All it requires is a container with a liquid solution that will dissolve the material in question. Unfortunately, there are complications since usually a mask is desired to selectively etch the material. One must find a mask that will not dissolve or at least etches much slower than the material to be patterned. Secondly, some single crystal materials, such as silicon, exhibit anisotropic etching in certain chemicals. Anisotropic etching in contrast to isotropic etching, means different etch rates in different directions in the material. The classic example of this is the $\langle 111 \rangle$ crystal plane sidewalls that appear when etching a hole in a $\langle 100 \rangle$ silicon wafer in a chemical such as potassium hydroxide (KOH). The result is a pyramid shaped hole instead of a hole

with rounded sidewalls with a isotropic etchant. The principle of anisotropic and isotropic wet etching is illustrated in the figure below.

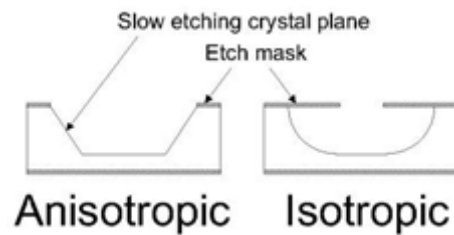


Figure 2.5: Difference between anisotropic and isotropic wet etching.²

2.2.2 Dry etching

The dry etching technology can split in three separate classes called reactive ion etching (RIE), sputter etching, and vapor phase etching.

In RIE, the substrate is placed inside a reactor in which several gases are introduced (Figure 2.6). A plasma is struck in the gas mixture using an RF power source, breaking the gas molecules into ions. The ions are accelerated towards and react at the surface of the material being etched, forming another gaseous material. This is known as the chemical part of reactive ion etching. There is also a physical part which is similar in nature to the sputtering deposition process. If the ions have high enough energy, they can knock atoms out of the material to be etched without a chemical reaction. It is a very complex task to develop dry etching processes that balance chemical and physical etching, since there are many parameters to adjust. By changing the balance it is possible to influence the anisotropy of the etching, since the chemical part is isotropic and the physical part highly anisotropic the combination can form sidewalls that have shapes from rounded to vertical. A schematic of a typical reactive ion etching system is shown in the figure below.

A special subclass of RIE which continues to grow rapidly in popularity is deep RIE (DRIE). In this process, etch depths of hundreds of microns can be achieved with almost vertical sidewalls. The primary technology is based on the so-called "Bosch process", named after the German company Robert Bosch which filed the original patent, where two different gas compositions are alternated in the reactor. The first gas composition creates a polymer on the surface of the substrate, and the second gas composition etches the substrate. The polymer is immediately sputtered away by the physical part of the etching, but only on the horizontal surfaces and not the sidewalls. Since the polymer only dissolves very slowly in the chemical part of the etching, it builds up on the sidewalls and protects them from etching. As a result, etching aspect ratios of 50 to 1 can be achieved. The process can easily be used to etch completely through a silicon substrate, and etch rates are 3-4 times higher than wet etching.

Sputter etching is essentially RIE without reactive ions. The systems used are very similar in principle to sputtering deposition systems. The big difference is that substrate is now subjected to the ion bombardment instead of the material target used in sputter deposition.

Vapor phase etching is another dry etching method, which can be done with simpler equipment than what RIE requires. In this process the wafer to be etched is placed inside a chamber, in which one or more gases are introduced. The material to be etched is dissolved at the surface in a chemical reaction with the gas molecules. The two most common vapor phase etching technologies are silicon dioxide etching using hydrogen fluoride (HF) and silicon etching using xenon difluoride (XeF_2), both of which are isotropic in nature. Usually, care must be taken in the design of a vapor phase process to not have bi-products form in the chemical reaction that condense on the surface and interfere with the etching process.

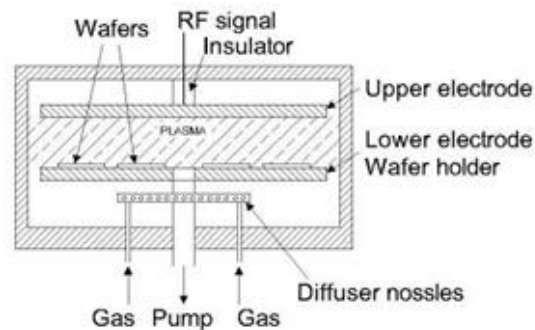


Figure 2.6: Typical parallel-plate reactive ion etching system.²

2.3 Pattern Transfer with Additive Techniques²

2.3.1 MEMS Thin Film Deposition Processes

One of the basic building blocks in MEMS processing is the ability to deposit thin films of material. MEMS deposition technology can be classified in two groups:

Depositions that happen because of a chemical reaction:

- Chemical Vapor Deposition (CVD)
- Electrodeposition
- Molecular Beam Epitaxy (MBE)
- Thermal oxidation

These processes exploit the creation of solid materials directly from chemical reactions in gas and/or liquid compositions or with the substrate material. The solid material is usually not the only product formed by the reaction. Byproducts can include gases, liquids and even other solids.

Depositions that happen because of a physical reaction:

- Physical Vapor Deposition (PVD)
- Casting

Common for all these processes are that the material deposited is physically moved on to the substrate. In other words, there is no chemical reaction which forms the material on the substrate. This is not completely correct for casting processes, though it is more convenient to think of them that way.

This is by no means an exhaustive list since technologies evolve continuously.

2.3.2 Chemical Vapor Deposition

In this process, the substrate is placed inside a reactor to which a number of gases are supplied. The fundamental principle of the process is that a chemical reaction takes place between the source gases. The product of that reaction is a solid material with condenses on all surfaces inside the reactor.

The two most important CVD technologies in MEMS are the Low Pressure CVD (LPCVD) and Microwave Plasma Enhanced CVD (MPCVD). The LPCVD process produces layers with excellent uniformity of thickness and material characteristics. The main problems with the process are the high deposition temperature (higher than 600°C) and the relatively slow deposition rate.

The MPCVD process can operate at lower temperatures (down to 300° C) thanks to the extra energy supplied to the gas molecules by the plasma in the reactor. However, the quality of the films tends to be inferior to processes running at higher temperatures. Secondly, most MPCVD deposition systems can only deposit the material on one side of the wafers on 1 to 4 wafers at a time. Also, MPCVD is the technique used for growing UNCD and many other diamond films for MEMS and NEMS devices. LPCVD systems deposit films on both sides of at least 25 wafers at a time. A schematic diagram of a typical LPCVD reactor is shown in the figure below.

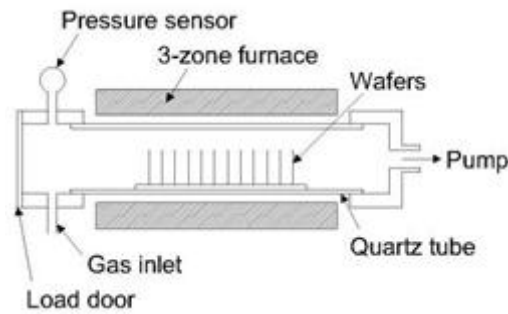


Figure 2.7: Typical hot-wall LPCVD reactor.²

2.3.3 Electrodeposition

This process is also known as "electroplating" and is typically restricted to electrically conductive materials. There are basically two technologies for plating: Electroplating and Electroless plating. In the electroplating process the substrate is placed in a liquid solution (electrolyte). When an electrical potential is applied between a conducting area on the substrate and a counter electrode (usually platinum) in the liquid, a chemical redox process takes place resulting in the formation of a layer of material on the substrate and usually some gas generation at the counter electrode (Figure 2.8).

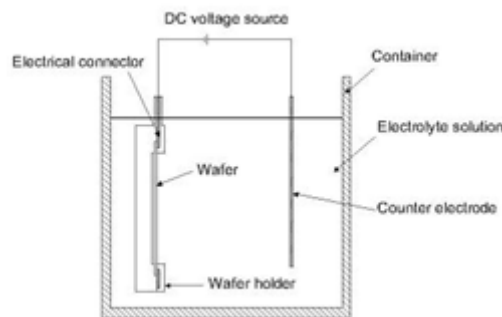


Figure 2.8: Typical setup for electrodeposition.²

In the electroless plating process a more complex chemical solution is used, in which deposition happens spontaneously on any surface which forms a sufficiently high electrochemical potential with the solution. This process is desirable since it does not require any external electrical potential and contact to the substrate during processing. Unfortunately, it is also more difficult to control with regards to film thickness and uniformity. A schematic diagram of a typical setup for electroplating is shown in the figure below.

2.3.4 Molecular Beam Epitaxy (MBE)

This technology is quite similar to what happens in CVD processes, however, if the substrate is an ordered semiconductor crystal (i.e. silicon, gallium arsenide), it is possible with this process to continue building on the substrate with the same crystallographic orientation with the substrate acting as a seed for the deposition. If an amorphous/polycrystalline substrate surface is used, the film will also be amorphous or polycrystalline.

There are several technologies for creating the conditions inside a reactor needed to support epitaxial growth, of which the most important is Vapor Phase Epitaxy. In this process, a number of gases are introduced in an induction heated reactor where only the substrate is heated. The temperature of the substrate typically must be at least 50% of the melting point of the material to be deposited.

An advantage of epitaxy is the high growth rate of material, which allows the formation of films with considerable thickness ($>100\ \mu\text{m}$). Epitaxy is a widely used technology for producing silicon on insulator substrates. The technology is primarily used for deposition of silicon. Actually MBE is used to grow also many oxides not only Si based films.

2.3.5 Thermal oxidation

This is one of the most basic deposition technologies. It is simply oxidation of the substrate surface in an oxygen rich atmosphere (Figure 2.9). The temperature is raised to 800°C - 1100°C to speed up the process. This is also the only deposition technology which actually consumes some of the substrate as it proceeds. The growth of the film is spurred by diffusion of oxygen into the substrate, which means the film growth is actually downwards into the substrate. As the thickness of the oxidized layer increases, the diffusion of oxygen to the substrate becomes more difficult leading to a parabolic relationship between film thickness and oxidation time for films thicker than $\sim 100\ \text{nm}$. This process is naturally limited to materials that can be oxidized, and it can only form films that are oxides of that material. This is the classical process used to form silicon dioxide on a silicon substrate.

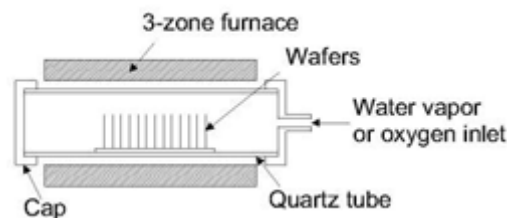


Figure 2.9: Typical wafer oxidation furnace.²

2.3.6 Physical Vapor Deposition

PVD covers a number of deposition technologies in which material is released from a source and transferred to the substrate. The two most important technologies are evaporation and sputtering.

2.1.6.1 Evaporation

In evaporation the substrate is placed inside a vacuum chamber, in which a block (source) of the material to be deposited is also located as shown in Figure 2.10. The source material is then heated to the point where it starts to boil and evaporate. The vacuum is required to allow the molecules to evaporate freely in the chamber, and they subsequently condense on all surfaces. This principle is the same for all evaporation technologies, only the method used to heat the source material differs. There are two popular evaporation technologies, which are e-beam evaporation and resistive evaporation each referring to the heating method. In e-beam evaporation, an electron beam is aimed at the source material causing local heating and evaporation. In resistive evaporation, a tungsten boat, containing the source material, is heated electrically with a high current to make the material evaporate. Many materials are restrictive in terms of what evaporation method can be used (i.e. aluminum is quite difficult to evaporate using resistive heating), which typically relates to the phase transition properties of that material.

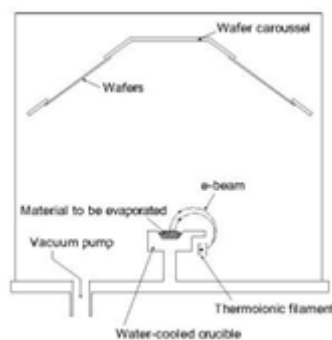


Figure 2.10: Typical system for e-beam evaporation of materials.²

2.1.6.2 Sputtering

Sputtering is a technology in which the material is released from the source at much lower temperature than evaporation. The substrate is placed in a vacuum chamber with the source material, named a target, and an inert gas (such as argon) is introduced at low pressure. A gas plasma is struck using an RF power source, causing the gas to become ionized. The ions are accelerated towards the surface of the target, causing atoms of the source material to break off from the target in vapor form and condense on all surfaces including the substrate. As for evaporation, the basic principle of sputtering is the same for all sputtering technologies. A schematic diagram of a typical RF sputtering system is shown in the Figure 2.11.

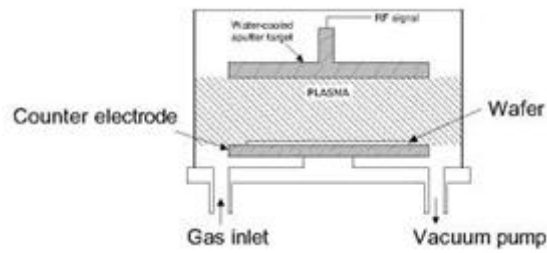


Figure 2.11: Typical RF sputtering system.²

2.3.7 Casting

In this process the material to be deposited is dissolved in liquid form in a solvent. The material can be applied to the substrate by spraying or spinning. Once the solvent is evaporated, a thin film of the material remains on the substrate. This is particularly useful for polymer materials, which may be easily dissolved in organic solvents, and it is the common method used to apply photoresist to substrates (in photolithography). The thicknesses that can be cast on a substrate range all the way from a single monolayer of molecules (adhesion promotion) to tens of micrometers. In recent years, the casting technology has also been applied to form films of glass materials on substrates. The spin casting process is illustrated in the figure below.

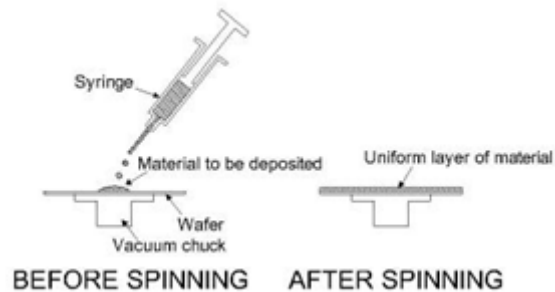


Figure 2.12: The spin casting process as used for photoresist in photolithography.²

2.4 Bibliography

¹ M. Madou, *Fundamentals of Microfabrication and Nanotechnology*, CRC Press, Taylor & Francis Group, 2012.

² www.memsnet.org

³ S. Senturia, *Microsystem Design*, Kluwer Academic Publishers, 2002.

CHAPTER 3: Models for Piezoelectric Resonators

The design and development of a device performing innovative characteristics, is time consuming and requires important resources to be implemented. In this case of innovative technologies, the maturation of new concepts and the application of knowledge are necessary.

There exist tools that facilitate somehow these tasks, thus saving time and costs. Numerical simulation is of vital importance in a system design step since it allows checking assumptions and a deep understanding of the represented phenomena. Furthermore, the design insights provided by these models are invaluable, especially the insights into the effects of varying either device dimensions or material properties.

Models can be developed in analytical form or they can take the form of numerical simulations carried out on high-speed workstations. Experience suggests that there is a natural progression from approximate analytical models early in the design cycle to more detailed and comprehensive numerical simulations later in the design cycle, continuing into device development and manufacture.

In this chapter it is described the different models implemented for the analysis of the piezoelectric sensors performances. These models are the Sauerbrey equation (analytical model) (*Section 3.1*), the Lumped model (circuital) (*Section 3.2*), the Mason model (*Section 3.3*) and the Finite Element Method model (*Section 3.4*).

3.1 Analytical Model (Sauerbrey equation)

Ever since the use of piezoelectric quartz crystal resonators for frequency control applications in radio-communication equipment began, the effect of a foreign material deposited on their surfaces on their resonant frequency has been known. The quartz crystal

microbalance is a thickness-shear-mode acoustic wave mass-sensitive detector based on the effect of an attached foreign mass on the resonant frequency of an oscillating quartz crystal. The QCM responds to any interfacial mass change.

In order to relate the changes in the behavior of the resonance to the properties of the load, it is necessary to employ a quantitative model. A number of these exist, and most of them are based on a one-dimensional analysis of the resonator and load. The model assumes a disc of infinite lateral extent, with the only dimensional variable being along the direction perpendicular to the disc. The actual behavior of the resonator is not one-dimensional however, but methods have been used to minimize this effect.

The possibility of using quartz crystal resonators as quantitative mass measuring devices was first explored by Sauerbrey in 1959. The decrease of the resonant frequency of a thickness shear vibrating quartz crystal resonator, having AT or BT cut, was found to be proportional to the added mass of the deposited film as shown by the Sauerbrey equation:¹

$$\Delta f_r = -\frac{2f_r^2 \rho_s}{\sqrt{\rho_p c_p}} \quad (3.1)$$

where Δf_r is the frequency shift, ρ_s is the mass per area of the deposited layer, ρ_p is the density of the piezoelectric material and c_p the elastic constant. In this thesis this analytical model was used to validate, in some cases, the rest of the models.

Early studies treated the quartz and film as lossless. A steady-state sinusoidal acoustic shear vibration at a frequency f_0 was assumed. The frequency f_0 is a real quantity. Sauerbrey had in mind such a model when for thin elastic films he understood that the film mass could then be approximated as an additional quartz mass. This resulted in a linear relation between the decrease in resonant frequency and the mass loading of the film with a proportionality constant dependent only on the quartz parameters. The linear behavior was valid for approximately 2% or less change in frequency.² When the deposited film covers the whole sensitive area of the quartz resonator it is easy to use the density to further calculate the film thickness.

The displacement of the device is not uniform over the surface and has a maximum at the center and decreases towards the electrode edges (see Figure 3.1). In fact, this effect can be used for specific purposes such as rupture event scanning or for binding perturbations studies.² For general cases, the one-dimensional models have been found to be quite adequate for the determination of load properties.

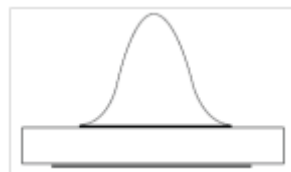


Figure 3.1: Distribution of the displacement amplitude of a QCM. The quartz and the electrodes are represented the rectangle and the dark lines respectively.

There are also experimental data showing that on the surface of a quartz crystal resonator there is a mass sensitivity distribution that closely follows the vibration amplitude distribution as shown in Figure 3.2.³ Both the mass sensitivity and amplitude distribution curves follow a Gaussian function.

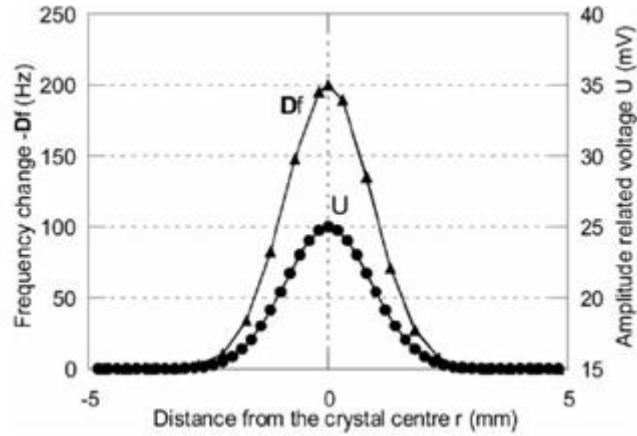


Figure 3.2: Mass sensitivity related Df and vibration amplitude related U distribution along one of the quartz resonator diameters.³

3.2 Lumped model (circuital)

3.2.1 Equivalent Electrical Circuit

The electrical behavior of a lightly damped mechanical vibrating system which is excited piezoelectrically through electrodes forming a two-terminal network, can be represented in the vicinity of any mechanical resonance by an equivalent electric circuit which consists of a capacitance C_1 , inductance L_1 and resistance R_1 in series, shunted by the parallel capacitance C_0 (see Figure 3.3). The parameters are independent of frequency for isolated modes of motion. Generally, the mode in question is sufficiently isolated from other modes to permit this assumption.

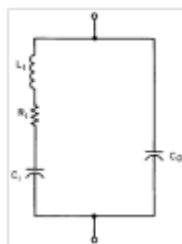


Figure 3.3: Equivalent electrical circuit of a piezoelectric vibrator.

The circuit shown above is called the Butterworth-Van Dike (BVD) equivalent circuit. The BVD equivalent circuit is the result of replacing a mass-spring-damper system that simplifies the mechanical structure of the piezoelectric resonator as is depicted in the following picture:

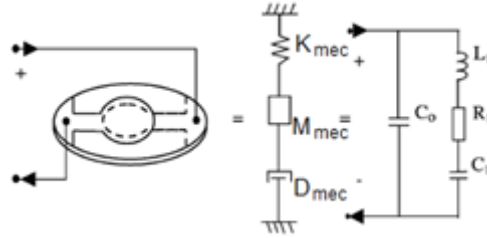


Figure 3.4: Mechanical and electrical representations of a piezoelectric resonator.⁴

As shown in Figure 3.4, the mass M_{mec} , the spring constant K_{mec} , the damping coefficient D_{mec} and the resonator electrodes are replaced respectively by the inductance L_1 (representing vibrations moving charges in space), the dynamic capacitance C_1 (representing the separation of charges in symmetrical vibration), the resistance R_1 (representing the energy loss) and the static capacitance C_0 (representing the separation of charges at the electrodes). These components can be calculated based on material and geometric parameters:⁵

$$L_1 = \frac{1}{\omega_0^2 C_1} \quad (3.2)$$

$$C_1 = \frac{8C_0 k_t^2}{\pi^2} \quad (3.3)$$

$$R_1 = \frac{\eta_p}{c_p C_1} \quad (3.4)$$

$$C_0 = \frac{\varepsilon_p A_e}{h_p} \quad (3.5)$$

with ω_0 the fundamental angular frequency, c_p the stiffness coefficient of the piezoelectric material, k_t^2 the electromechanical coupling constant, η_p the piezoelectric viscosity, ε_p the permittivity of the piezoelectric material, A_e the electrode area and h_p the piezoelectric thickness.

The resonance frequency for this circuit is given by the following equation (Cernosek et al. 1998⁵ equation (14), considering $\omega_0 = 2\pi f$ and the first harmonic):

$$f_0 = \frac{1}{2h_p} \sqrt{\frac{c_p}{\rho_p}} \sqrt{1 - \frac{8k_t^2}{\pi^2}} \quad (3.6)$$

where ρ_p is the density of the piezoelectric material.

The fundamental parameters C_1 , L_1 , R_1 and C_0 , define the BVD equivalent circuit shown above and all other parameters may be derived from them. A dimensionless measure of the dissipation is the quality factor Q :

$$Q = \frac{(L_1/C_1)^{1/2}}{R_1} \quad (3.7)$$

Another important definitions that came off from the circuit are the capacitance ratio r and the figure of merit M :

$$r = \frac{C_0}{C_1} \quad (3.8)$$

$$M = \frac{Q}{r} \quad (3.9)$$

The magnitude of the impedance of the equivalent electric network ($|Z|$), its resistive component (R_e), its reactive component (X_e) and the reactance X_1 , of the C_1 , L_1 and R_1 branch are plotted as functions of frequency in Figure 3.5, for the purpose of defining the different characteristic frequencies. Z_m and Z_n denote minimum and maximum impedance respectively, and R_r and R_s , the impedances at zero phase angle. These curves, however, have only qualitative character and do not represent a particular piezoelectric vibrator.

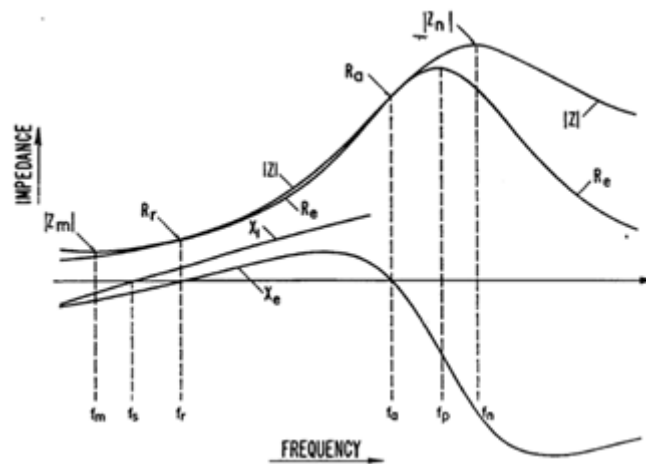


Figure 3.5: Impedance $|Z|$, resistance R_e , reactance X_e , and series arm reactance X_1 of a piezoelectric vibrator as a function of frequency. Z_m and Z_n denote minimum and maximum impedance respectively, R_r and R_s , the impedances at zero phase angle. f_r is defined as the resonance frequency, f_a the antiresonance frequency, f_s the series resonance frequency, f_p the parallel resonance frequency, f_m the frequency of maximum admittance (minimum impedance) and f_n is the frequency of minimum admittance (maximum impedance).⁶

3.2.2 Effect of dissipation on the definition of frequencies near resonance and antiresonance

Whereas in a lossless resonator there are single frequencies (f_1 and f_2) which coincide with the admittance and impedance maxima, respectively, there are, in a lossy resonator, three frequencies of interest near the admittance maximum and, similarly, three frequencies near the impedance maximum. Accordingly, the critical frequencies f_1 and f_2 each have three associated frequencies, $f_1 \rightarrow (f_m, f_s, f_r)$ and $f_2 \rightarrow (f_n, f_p, f_a)$. These frequencies are showed in Figure 3.5 and are very important in order to characterize the piezoelectric resonator. In this standard f_r is defined as the resonance frequency, f_a the antiresonance frequency, f_s the series resonance frequency, f_p the parallel resonance frequency, f_m the frequency of maximum admittance (minimum impedance) and f_n is the frequency of minimum admittance (maximum impedance).⁶ These definitions are independent of the lumped-parameter equivalent circuit. As a first approximation sufficient for many practical purposes, the following assumptions can be made: $f_m = f_s = f_r$ and $f_n = f_p = f_a$.

Different is the case for a very lossy resonator where these assumptions are not applicable. In this sense, the application of the IEEE Standards⁶ approximation for k_t^2 from the resonant and antiresonance frequencies (Eq. (1.54)) will be no longer valid and will yield an error in the estimate of the electromechanical coupling constant (as shown by Brown, 2000⁷).

The relative difference in the frequencies f_s and f_p depends on both the material coupling constant and the resonator geometry. For this reason a quantity called the *effective coupling factor* has been used, particularly in filter design literature, as a convenient measure of this difference:

$$k_{eff}^2 = (f_p^2 - f_s^2) / f_p^2 \quad (3.10)$$

The critical frequencies of the lossy resonator must correspond to the critical frequencies of an ideal resonator made from a lossless material having the same electroelastic constants as the actual resonator material.

For resonators with $M > 5$, an experimental value of f_p is equal to f_2 within the experimental error in determining the resistance maximum. In general, f_p differs from f_2 by about $1/Q^2$. For resonators having $M > 50$ it is sufficient to use a measured value of f_m or f_r directly for f_1 , and a measured value of f_n or f_a directly for f_2 . When $M < 5$ the frequency f_p cannot be measured accurately, although f_s can still be measured with reasonable accuracy as long as $Q > 5$.

3.2.3 Surface loaded resonator

It was shown that the unperturbed resonator can be represented by the simple BVD equivalent circuit with a high degree of computational precision; this situation corresponds to the case in which the piezoelectric resonator is undisturbed, i.e., with no mass change due to the deposition of material. The loaded resonator then can be modeled by using the Modified Butterworth-Van Dike (MBVD) equivalent circuit as depicted in Figure 3.6.



Figure 3.6: Modified Butterworth-Van Dyke equivalent circuit for a surface-loaded piezoelectric resonator.

This new configuration adds a series impedance, the movement impedance, created by the charge on the surface (see Eq. (3.11)). But these changes in the mass does not appear directly as linear changes in the electrical parameters, but from changes in the acoustic properties at the interface between the piezoelectric resonator and the deposited material. For the case of small and rigid material deposition thicknesses (stiffness coefficient $G > 1\text{MPa}$)⁸, the equation for this new impedance is (Cernosek et al. 1998⁵, equation (17) and (20) considering $\rho_s = h_f \rho_f$):

$$Z_m^L = \left(\frac{\pi}{4k_t^2 \omega_0 C_0} \right) \left(\frac{Z_L}{Z_q} \right) \quad (3.11)$$

with

$$Z_L = \omega_0 h_f \rho_f \quad (3.12)$$

$$Z_p = \sqrt{\rho_p c_p} \quad (3.13)$$

where Z_L is the acoustic load impedance and Z_p characteristic acoustic impedance, with h_f and ρ_f the thickness and density of the deposited film respectively. The layer must be sufficiently thin and rigid so that an acoustic wave traversing the layer has a negligible phase shift; it moves synchronously with the resonator surface. This new impedance Z_m^L is implemented as an inductance L_2 (see Figure 3.6) in series with C_1 , L_1 and R_1 , whose value is given by Z_m^L / ω_0 .

3.3 Mason model

In a piezoelectric resonator, the propagation analysis of the acoustic wave in one dimension leads to the obtaining of an equivalent electric model. The Mason model describes the ideal one-dimensional behavior of the resonator, using electro-acoustic coupling equations and modeling each resonator layer by lumped elements or transmission lines, imposing boundary conditions at the ends.

For a fully resonator modeling considering both the layers of a piezoelectric material as well as the non piezoelectric ones, it can be carried out the Mason model by concatenating the equivalent circuit cells for each layer.

3.3.1 One-dimensional equations for a nonpiezoelectric slab

Here it will be developed a one-dimensional model describing the electrical characteristics of an acoustic structure. Using the following analogies:

force \rightarrow voltage

particle velocity \rightarrow current

The acoustic impedance is a property of the medium and is given by:

$$Z = \frac{-T}{v} = \sqrt{\rho c} = \rho v_0 = \frac{ck}{\omega} \quad (3.14)$$

where v is the particle velocity and k is the phase constant defined as:

$$k = \sqrt{\omega^2 \frac{\rho}{c}} = \frac{\omega}{v_0} \quad (3.15)$$

being v_0 the phase velocity of the acoustic wave as showed in *Section 1.4.2*.

The use of force instead of tension is permissible here because of the one-dimensional geometry and therefore shear and longitudinal waves are treated identically. It can be defined the mechanical stress as the quotient between the force and the area of the body surface (A) thus the applied force is $F = AT$. From equations (1.38) and (3.14):

$$F = AZv = \frac{Ackv}{\omega} \quad (3.16)$$

and

$$F = AcS = Ac \frac{\partial u}{\partial z} \quad (3.17)$$

Do not confuse the particle velocity v (1.37) with v_0 (the phase velocity of the acoustic wave). Now, if it is consider a finite slab bounded by the planes $z = z_1$ and $z = z_2$, as

shown in Figure 3.7, because there is an acoustic reflection from each boundary, there must be two waves in the slab (one traveling to the left and the other to the right).



Figure 3.7: Finite thickness acoustic medium: at all points in the medium, there are right and left propagating plane waves.⁹

Regarding equations (1.41) and (1.42), the particle displacement is then (suppressing time variation):

$$u = \underbrace{a e^{-jkz}}_{\substack{\text{traveling} \\ \text{to right}}} + \underbrace{b e^{jkz}}_{\substack{\text{traveling} \\ \text{to left}}} \quad (3.18)$$

The interaction of these waves causes the resonance conditions that dramatically alter the electrical characteristics of acoustic devices. The coefficients a and b depend on the acoustic impedance mismatch at the boundaries. At the left boundary ($z = z_1$), the particle velocity is:

$$\dot{u}_1 = v_1 = j\omega \left(a e^{-jkz_1} + b e^{jkz_1} \right) \quad (3.19)$$

At the right boundary ($z = z_2$), the particle velocity is:

$$\dot{u}_2 = v_2 = j\omega \left(a e^{-jkz_2} + b e^{jkz_2} \right) \quad (3.20)$$

Solving for the coefficients a and b in terms of v_1 and v_2 it finally gives:

$$F_1 = \frac{Z}{j \sin(kd)} (v_1 - v_2) + jZ \tan\left(\frac{kd}{2}\right) v_1 \quad (3.21)$$

$$F_2 = \frac{Z}{j \sin(kd)} (v_1 - v_2) - jZ \tan\left(\frac{kd}{2}\right) v_2 \quad (3.22)$$

where F_1 and F_2 are the forces on the slab at the left and right boundaries respectively. With the solutions of this equations system, the equivalent circuit of Figure 3.8 is obtained:

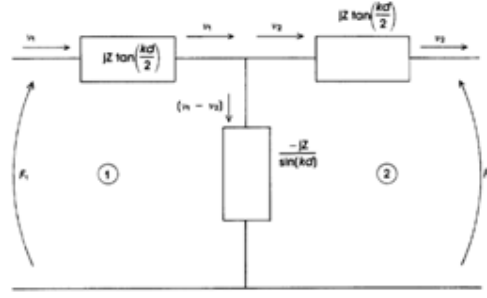


Figure 3.8: Equivalent circuit of a finite thickness acoustic delay line.

The current is represented by the particle velocity v and the voltage by the force F as shown previously. Applying Kirchhoff's voltage law to loop 1, it has:

$$F_1 = \underbrace{jZ \tan\left(\frac{kd}{2}\right)}_{\substack{\text{"voltage" drop} \\ \text{across } jZ \tan\left(\frac{kd}{2}\right)}} v_1 - \underbrace{\frac{jZ}{\sin(kd)}}_{\substack{\text{"voltage" drop} \\ \text{across } \frac{-jZ}{\sin(kd)}}} (v_1 - v_2) \quad (3.23)$$

In this equation, v_1 is the “acoustic” current and Z is the acoustic impedance. Writing Kirchhoff's voltage equation for loop 2 reproduces Eq. (3.22), and thus the circuit of Figure 3.8 is a valid representation for the acoustic equations in a nonpiezoelectric medium. It is a lumped element representation of an acoustic transmission or delay line of “acoustic” length kd .

3.3.2 One-dimensional equations for a piezoelectric slab

For a piezoelectric slab of thickness d , there is an extra term relating the coupling between the electrical and acoustic fields. As shown in Eq. (1.16), in place of Eq. (1.39), it is written:

$$\mathbf{T} = -\mathbf{e}\mathbf{E} + \mathbf{c}^E\mathbf{S}$$

As have been shown, piezoelectric materials present a dipolar moment in the presence of an electric field. These materials will present a non-zero dipolar moment in the presence of mechanical phenomena thus increasing the flux of electric field through the material.

Taking into account this premise it can be said that the electrical displacement vector for a piezoelectric material has two components, one due to the electric field and the other due to the strain as shown by Eq. (1.15):

$$\mathbf{D} = \boldsymbol{\epsilon}^S\mathbf{E} + \mathbf{e}^T\mathbf{S}$$

The aim is to solve for the input impedance Z_{in} as a function of frequency for a piezoelectric resonator so it become important the “current-voltage” ($I-V$) characteristics.

Following the same methodology carried out for the solution in the problem of one-dimensional nonpiezoelectric slab and adding these new expressions, it can be obtained a new set of equations.

The current is purely a displacement current if the piezolayer is dielectric, so:

$$J = \frac{\partial \mathbf{D}}{\partial t} = j\omega D \quad (3.24)$$

and

$$I = j\omega DA \quad (3.25)$$

where J is the displacement current density with units of $[J] = A/m^2$. In order to find the voltage, the electric field has to be integrated. Using Eq. (1.13), with $\dot{u} = v = j\omega u$ and solving for I :

$$I = j\omega C_0 V + hC_0 (v_1 - v_2) \quad (3.26)$$

where

$$h = \frac{e}{\varepsilon^S} \quad (3.27)$$

$$C_0 = \frac{\varepsilon^S A}{d} \quad (3.28)$$

is the static or “clamped” capacitance, because it includes the permittivity at zero strain. The current in the piezoelectric is composed of two terms:

- The displacement current through a capacitance $j\omega C_0 V$.
- The current due to the conversion of mechanical energy (the piezoelectric effect) $hC_0 (v_1 - v_2)$.

The assumption is that there is an incident wave and a reflected wave at each boundary and the operation leads to an expression similar to equations (3.21) and (3.22) with an additional term representing the electrical component. Therefore, the piezoelectric equations for the resonator are:⁹

$$F_1 = \frac{Z_T}{j \sin(kd)} (v_1 - v_2) + jZ_T \tan\left(\frac{kd}{2}\right) v_1 + \frac{h}{j\omega} I \quad (3.29)$$

$$F_2 = \frac{Z_T}{j \sin(kd)} (v_1 - v_2) - jZ_T \tan\left(\frac{kd}{2}\right) v_2 + \frac{h}{j\omega} I \quad (3.30)$$

where Z_T is the resonator impedance. The equivalent circuit of a piezoelectric slab is shown in Figure 3.9. The transformer represents the conversion of electrical energy to

acoustic energy (or vice versa). An acoustic current ($v_1 - v_2$) is present on the right side (terminals c-d) while an electrical current is present on the left side (terminals a-b).

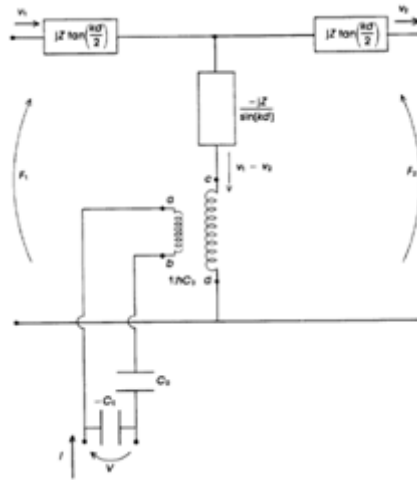


Figure 3.9: Three-port Mason model equivalent circuit for a one-dimensional piezoelectric slab.

From Eq. (3.26), which relates the electrical current to the acoustic current, the turns ratio of the transformer is just hC_0 .

This circuit is often referred to as the Mason model, after Warren Mason, who performed much of the pioneering work in crystal acoustics. The complete circuit has three ports and, in general, it is rather cumbersome to work with.

3.3.3 Closed form expression for the input impedance⁹

In general, it is not possible to obtain a closed-form solution for the electrical impedance, due to the complexity of the various layers in the Mason model. However, it is possible to obtain closed form solutions. One case is a piezoelectric resonator that is stress free on either side (no metallic or substrate layers). In this case, the metallic layers are assumed to be acoustically thin enough to neglect, and the substrate is infinitely long. The latter assumption implies that there is no reflected wave and thus no possibility of acoustic standing waves in the substrate (thus, only the transducer supports standing waves).

Equations (3.29) and (3.30) are valid for a piezoelectric slab of arbitrary length. Now it is assumed that the substrate is infinitely long and thus supports only one wave traveling to the right (assuming that F_1 is the force on the left face and F_2 is the force on the right side of the piezoelectric slab of length d). The air interface on the left side of the piezolayer cannot exert a force, and thus $F_1 = 0$. The right side of the piezolayer pushes against the substrate, which pushes back with force:

$$F_2 = -Z_S v_2 \quad (3.31)$$

Where Z_s is the impedance of the substrate ($T/v=Z$). Equation (3.31) is valid only if the substrate is either infinitely long or of finite length but very lossy (so that it possesses only a forward propagating wave). A wave that impinges on the piezolayer from its right (a left traveling wave) will interfere (either constructively or destructively) and change the force relationship. With these substitutions, equations (3.26), (3.29) and (3.30) become:

$$0 = Z_T \left(\frac{v_1}{j \tan(kd)} - \frac{v_2}{j \sin(kd)} \right) + \frac{h}{j\omega} I \quad (3.32)$$

$$-Z_s v_2 = Z_T \left(\frac{v_1}{j \sin(kd)} - \frac{v_2}{j \tan(kd)} \right) + \frac{h}{j\omega} I \quad (3.33)$$

$$V = \frac{h}{j\omega} (v_1 - v_2) + \frac{I}{j\omega C_0} \quad (3.34)$$

where Z_T is the resonator impedance. These three equations contain the four unknowns v_1 , v_2 , V and I .

Now, considering the assumptions shown above, the input impedance as a function of frequency for a piezoelectric resonator is given by the following equations:

$$Z_{in} = \frac{1}{j\omega C_0} + P(\omega) \frac{R_0}{\omega_2 C_0^2} \quad (3.35)$$

where

$$R_0 = \frac{k_t^2 v_0 C_0}{d} \quad (3.36)$$

and

$$P(\omega) = \frac{(Z_s/Z_T) \sin(kd) + 2j(1 - \cos(kd))}{\sin(kd) - j(Z_s/Z_T) \cos(kd)} \quad (3.37)$$

3.3.3.1 Generalization of the Mason model to a multilayer system

After the obtention of the equivalent circuit model for the propagation of the acoustic wave in a piezoelectric material, it can be extended the Mason model to a more complex multilayer structure considering all the layers in a resonator. Taking into account the model depicted in Figure 3.9 using air reflection, it can be seen the new equivalent circuit diagram of a multilayer acoustic device composed by a piezoelectric resonator with both top and bottom electrodes:

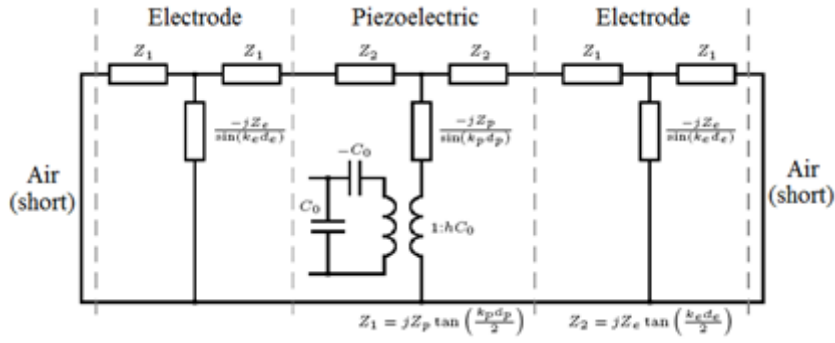


Figure 3.10: Equivalent circuit diagram of a multilayer acoustic resonator.

For multiple layers, it can be used Eq. (3.35) considering Z_{in} as the Z_S for the following layer.

3.4 FEM model

A general purpose, computer-aided numerical method for predicting the behavior of a physical system in response to external loads is the FEM (Finite Element Method). The method is well established and has been widely used in numerous engineering disciplines. FEM has been extensively applied in the simulation of piezoelectric devices, such as ultrasonic transducers, surface acoustic wave devices, Lamb wave delay lines and BAW resonators.

The governing equations in the FEM formulation for a piezoelectric material are: the constitutive relations for linear piezoelectricity (equations (1.15) and (1.16))

$$\mathbf{D} = \boldsymbol{\varepsilon}^S \mathbf{E} + \mathbf{e}^T \mathbf{S}$$

$$\mathbf{T} = -\mathbf{e} \mathbf{E} + \mathbf{c}^E \mathbf{S}$$

the mechanical balance (Newton's Law, Eq. (1.36))

$$\nabla \cdot \mathbf{T} = \rho \frac{\partial^2 \mathbf{u}}{\partial t^2}$$

and the electrostatic balance

$$\nabla \cdot \mathbf{D} = 0 \tag{3.38}$$

with

$$\mathbf{S} = \frac{1}{2} (\nabla \mathbf{u} + \nabla^T \mathbf{u}) \tag{3.39}$$

and

$$\mathbf{E} = -\nabla \phi$$

where \mathbf{S} is the symmetric part of the displacement gradient matrix with $\nabla^T \mathbf{u}$ the transpose of $\nabla \mathbf{u}$. In these equations \mathbf{T} (6x1) is the mechanical stress vector, \mathbf{S} (6x1) the mechanical strain vector, \mathbf{E} (3x1) the electrical field vector, \mathbf{D} (3x1) the electrical displacement vector, \mathbf{c} (6x6) the linear elastic matrix, $\boldsymbol{\varepsilon}$ (3x3) the dielectric coefficients matrix at constant strain, \mathbf{e} (6x3) the piezoelectric coupling matrix, \mathbf{u} (3x1) the mechanical displacement vector, $\ddot{\mathbf{u}} = \partial^2 \mathbf{u} / \partial t^2$ the acceleration and ϕ the electrical potential.

For a unique solution, the mechanical (for displacement or stress) and electrical (for electric potential or electric displacement) boundary conditions need to be imposed on the entire boundary of the problem domain. The boundary conditions, together with the equation shown above, then completely determine the motion of the piezoelectric material.

3.4.1 Discretization

The finite element method is an approximation of the governing equations that is particularly well suited to computation. Whereas the differential form of the governing equations requires the solution to be exact at every point in space, the FEM is based on an equivalent variational or *weak* statement that enforces the *exactness* of the solution in a weighted average sense over small sub-regions of the space (the finite elements). For the class of formulations considered here, convergence and uniqueness of the solution can be established mathematically. In other words, error bounds on the approximation can always be determined and the approximation can always be improved such that the weighted error tends to zero at the limit, or equivalently, the finite element solution tends to the exact solution.

Consider a volume Ω constituting the problem domain as illustrated in Figure 3.11 for a piezoelectric resonator:

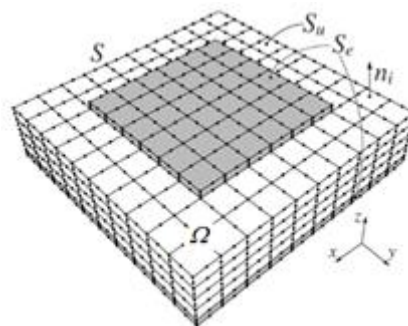


Figure 3.11: Simple piezoelectric resonator defining the problem domain Ω . For clarity, only the part of the volume-element mesh located on the boundary S of volume Ω is shown. The boundary S with unit outward normal n_i is divided into two parts: the part covered with electrodes S_e and the remaining non-metalized part S_u . The piezoelectric material (white) is between two electrodes (gray).¹⁰

In FEM, the physical problem domain Ω is discretized, i.e., subdivided into small elementary volumes (Ω^e) called elements. The continuous field quantities (the three components of the mechanical displacement u_i , $i = 1, 2, 3$ and the electric potential ϕ) are approximated in each element through linear sums of interpolation functions (shape functions):

$$\begin{cases} u_i(\mathbf{x}) = \sum_{j=1}^n a_{ij} N_j(\mathbf{x}), & i=1,2,3 \\ \phi(\mathbf{x}) = \sum_{j=1}^n b_j N_j(\mathbf{x}), & \mathbf{x} \in V_e \end{cases} \quad (3.40)$$

Here $\mathbf{x} = (x_1, x_2, x_3)$ is the position vector, n is the number of specific so-called *node points* of the element, and a_{ij} and b_j are the displacement and electrical degrees of freedom (DOF), respectively. The DOFs are the unknowns, whose values finally result from the solution of the FEM equations.

In (3.40), $N_j(\mathbf{x}) = N_j(x_1, x_2, x_3)$ are the shape functions (chosen to be polynomials) associated with the element, and they satisfy the interpolation property:

$$N_j(\mathbf{x}_i) = N_j(x_{i1}, x_{i2}, x_{i3}) = \delta_{ij} \quad i, j=1, \dots, n \quad (3.41)$$

where \mathbf{x}_i is the location of node point i and δ_{ij} is the Kronecker delta. This implies that the DOFs equal the values of the field variables at the nodes.

FEM interpolation functions are local or element-based, implying that the solution within an element is entirely determined by the solution at that element's nodes. It is this localization that permits element-by-element operations, and therefore allows the FEM to solve large-scale complex problems as an assembly of tractable elemental contributions.

3.4.2 Finite Element Equations

The incorporation of the spatial discretization (showed in the previous section) into the above mentioned variational statement results in a semidiscrete finite element system of linear algebraic equations, expressed in matrix form as follows:¹¹

$$\mathbf{M}_{uu} \ddot{\mathbf{u}} + \mathbf{C}_{uu} \dot{\mathbf{u}} + \mathbf{K}_{uu} \mathbf{u} + \mathbf{K}_{u\phi} \phi = \mathbf{F} \quad (3.42)$$

$$\mathbf{K}_{u\phi}^T \mathbf{u} + \mathbf{K}_{\phi\phi} \phi = \mathbf{Q} \quad (3.43)$$

where

- Mechanical mass matrix -

$$\mathbf{M}_{uu} = \mathbf{A}_{e=1}^{n_e} \int_{\Omega^e} \rho \mathbf{N}_u^{eT} \mathbf{N}_u^e d\Omega^e \quad (3.44)$$

- Mechanical stiffness matrix -

$$\mathbf{K}_{uu} = \mathbf{A}_{e=1}^{n_e} \int_{\Omega^e} (\nabla \mathbf{N}_u^e)^T \mathbf{C} (\nabla \mathbf{N}_u^e) d\Omega^e \quad (3.45)$$

- Piezoelectric coupling matrix -

$$\mathbf{K}_{u\phi} = \mathbf{A}_{e=1}^{n_e} \int_{\Omega^e} (\nabla \mathbf{N}_u^e)^T \mathbf{e}^T (\nabla \mathbf{N}_\phi^e) d\Omega^e \quad (3.46)$$

- Dielectric stiffness matrix -

$$\mathbf{K}_{\phi\phi} = \mathbf{A}_{e=1}^{n_e} \int_{\Omega^e} (\nabla \mathbf{N}_\phi^e)^T \boldsymbol{\epsilon}^T (\nabla \mathbf{N}_\phi^e) d\Omega^e \quad (3.47)$$

are the elementary matrices with \mathbf{N}^e the shape functions vector, Ω^e the volume of the piezoelectric medium, \mathbf{C}_{uu} the damping matrix, \mathbf{F} the nodal mechanical force vector, \mathbf{Q} the vector of nodal electrical charge, \mathbf{u} the nodal displacement vector, $\dot{\mathbf{u}}$ the nodal velocity vector, ϕ the nodal potential vector and $\mathbf{A}_{e=1}^{n_e}$ the assembly operator representing the assembled elemental contributions to form the global system matrices.

Equation (3.42) governs the mechanical or elastic portion of the problem, while equation (3.43) describes the electrical field, and both are coupled through the piezoelectric coupling matrix. For passive materials, the coupling is null and equation (3.42) fully describes the behavior of elastic materials. These equations are referred to as the semidiscrete FE equations in which space has been discretized whereas time is still represented as a continuous function.

3.4.3 Boundary Conditions

On the entire boundary of the domain (S in Figure 3.11), it is need to define either a natural or an essential boundary condition (BC). For the mechanical quantities, these are expressed, respectively as:

$$(\mathbf{t}_n)_i = \sum_{j=1}^3 T_{ij} n_j - \sum_k (\mathbf{f}_{pk})_i \delta(\mathbf{r} - \mathbf{r}_{pk}) = (\bar{\mathbf{t}}_n)_i \quad (3.48)$$

or

$$\mathbf{u}_i = \bar{\mathbf{u}}_i \text{ on } S \quad (3.49)$$

Here, \mathbf{f}_{pk} is the mechanical point force at position \mathbf{r}_{pk} on the surface S and δ is the Dirac delta function; $\mathbf{t}_n = \left(\sum_{j=1}^3 T_{1j} n_j, \sum_{j=1}^3 T_{2j} n_j, \sum_{j=1}^3 T_{3j} n_j \right)$ is the mechanical surface force (the traction) (T_{ij} is the stress tensor element and n_j is the j th component of the unit outward normal to the domain boundary). The sum k is over the point forces. Furthermore, $\bar{\mathbf{u}}_i$ and $(\bar{\mathbf{t}}_n)_i$ (with $i=1,2,3$) are the prescribed components of displacement and surface traction, respectively. The electrical BCs are expressed through

$$q = -\sum_{j=1}^3 D_j n_j - \sum_k \rho_{pk} \delta(\mathbf{r} - \mathbf{r}_{pk}) = \bar{D}_n \quad (3.50)$$

or

$$\phi = \bar{\phi} \quad \text{on } S \quad (3.51)$$

where $\bar{\phi}$ is the prescribed potential and ρ_{pk} denotes the point charge at position \mathbf{r}_{pk} on the surface S ; $q = -D_j n_j$ is the inward-normal component of the electric displacement on the domain boundary. The sum k is over the point charges. On the dielectric part of the boundary, \bar{D}_n is the prescribed inward normal component of the electric displacement. On the part of the piezoelectric material boundary covered with electrodes, \bar{D}_n is replaced with the prescribed surface charge density $\bar{\sigma}$.

3.4.4 Harmonic Analysis

In the frequency-domain analysis, when the dynamic phenomenon is steady-state, with periodic forcing function and response at angular frequency $\omega = 2\pi f$, time dependence can be eliminated from the problem and the system unknowns convert to harmonic complex variables:

$$\mathbf{u} = \hat{\mathbf{u}} e^{j\omega t} \quad (3.52)$$

$$\phi = \hat{\phi} e^{j\omega t} \quad (3.53)$$

$$\partial(\cdot)/\partial t = j\omega(\cdot) \quad (3.54)$$

$$\partial(\cdot)^2/\partial t^2 = -\omega^2(\cdot) \quad (3.55)$$

In the frequency domain, according to Eq. (3.42) and Eq. (3.43), the following matrix form equations are obtained:

$$-\omega^2 \mathbf{M}_{uu} \mathbf{u} + j\omega \mathbf{C}_{uu} \mathbf{u} + \mathbf{K}_{uu} \mathbf{u} + \mathbf{K}_{u\phi} \phi = \mathbf{F} \quad (3.56)$$

$$\mathbf{K}_{u\phi}^T \mathbf{u} + \mathbf{K}_{\phi\phi} \phi = \mathbf{Q} \quad (3.57)$$

In the computed implementation, the harmonic excitation loads are specified and assumes harmonic response with the same angular frequency as the excitation load; the frequency response analysis is carried out with a parametric solver, performing a frequency sweep over several excitation frequencies.

3.4.5 Admittance

The admittance Y is obtained through dividing total charge Q on an electrode by the amplitude of the driving voltage V :

$$Y(\omega) = \frac{i\omega Q}{V} \quad (3.58)$$

The total charge on the electrode is computed as a sum of nodal charges:

$$Q = -\mathbf{I}_{el}^T \mathbf{Q}_Q \quad (3.59)$$

where \mathbf{Q}_Q is the nodal charge at nodes with fixed potential and \mathbf{I}_{el} is a vector with unity at positions corresponding to those electrical DOFs that belong to the given electrode, and zeros elsewhere. The minus sign results from the definition of the current as positive into the piezoelectric body.

Computing the frequency response (e.g., admittance vs. frequency) requires the solution of the FEM equations at each of the desired frequencies.

3.5 Implementation of FEM model

3.5.1 About the software

For modeling and simulation of resonator devices, it was implemented the piezoelectricity into the commercial finite element package COMSOL Multiphysics[®]. It is a powerful interactive environment for modeling and solving all kinds of scientific and engineering problems based on partial differential equations (PDEs). The Facultad de Ingeniería-Bioingeniería at the Universidad Nacional de Entre Ríos has the license for using the COMSOL 3.2.

With this software it is easily extend conventional models for one type of physics into multiphysics models that solve coupled physics phenomena. Thanks to the built-in physics modes it is possible to build models by defining the relevant physical quantities -such as

material properties, loads, constraints, sources and fluxes- rather than by defining the underlying equations. It can be applied these variables, expressions, or numbers directly to solid domains, boundaries, edges and points independently of the computational mesh. COMSOL Multiphysics[®] then internally compiles a set of PDEs representing the entire model. It can be accessed to the software as a standalone product through a flexible graphical user interface, or by script programming in the COMSOL Script language or in the MATLAB language.

The CAD Import Module provides the possibility to import CAD data using the following formats: IGES, SAT (Acis), Parasolid and Step. Additional add-ons provide support for CATIA V4, CATIA V5, Pro/ENGINEER, Autodesk Inventor and VDA-FS. It also supports bidirectional interfaces with SolidWorks and Autodesk Inventor.

It can be built models of all types in the COMSOL Multiphysics user interface[®]. For additional flexibility, it also provides its own scripting language, COMSOL Script, where it can be accessed to the model as a Model M-file or a data structure. The software also provides a seamless interface to MATLAB. This gives the freedom to combine PDE-based modeling, simulation and analysis with other modeling techniques. For instance, it is possible to create a model in COMSOL and then export it to *Simulink* as part of a control-system design.

The Structural Mechanics Module is an optional package that extends the COMSOL Multiphysics[®] modeling environment with customized user interfaces and functionality optimized for structural analysis. Piezoelectric materials, coupling the electric field and strain in both directions are fully supported inside the module through special application modes solving for both the electric potential and displacement.

3.5.2 Piezoelectrical Constitutive Relations

It is possible to express the relation between the stress, strain, electric field and electric displacement field in either a stress-charge or strain-charge form (equations (1.15), (1.16), (1.17) and (1.18)):

STRESS-CHARGE

$$\mathbf{D} = \boldsymbol{\varepsilon}^S \mathbf{E} + \mathbf{e}^T \mathbf{S}$$

$$\mathbf{T} = -\mathbf{e} \mathbf{E} + \mathbf{c}^E \mathbf{S}$$

STRAIN-CHARGE

$$\mathbf{D} = \boldsymbol{\varepsilon}^T \mathbf{E} + \mathbf{d} \mathbf{T}$$

$$\mathbf{S} = \mathbf{d}^T \mathbf{E} + \mathbf{s}^E \mathbf{T}$$

3.5.3 Electrical Formulations

The default formulation of the equations in the piezoelectrical application modes is such that the resulting equation system with piezoelectric material is symmetric. This allows reduced memory requirements with solvers that utilize symmetry information. The default formulation is that the variational electrical energy is written using a positive sign:

$$\delta W_e = \int (\mathbf{D} \cdot \hat{\mathbf{E}}) d\Omega \quad (3.60)$$

Here $\hat{\mathbf{E}}$ is the test function for the electric field and Ω is the integration domain.

3.5.4 Piezoelectric Dissipation

In order to define dissipation in the piezoelectric material for a time-harmonic analysis, all material properties in the constitutive relations can be complex-valued matrices where the imaginary part defines the dissipative function of the material.

Generally, and independently of the microscopic origin of the loss, it can be modeled the dissipative behavior of the material using complex-valued material properties. For the case of piezoelectric materials, this means that the constitutive equations can be written as follows:

For the stress-charge formulation

$$\mathbf{D} = \tilde{\boldsymbol{\varepsilon}}^S \mathbf{E} + \tilde{\mathbf{e}}^T \mathbf{S}$$

$$\mathbf{T} = -\tilde{\mathbf{e}} \mathbf{E} + \tilde{\mathbf{c}}^E \mathbf{S}$$

and for the strain-charge formulation

$$\mathbf{D} = \tilde{\boldsymbol{\varepsilon}}^T \mathbf{E} + \tilde{\mathbf{d}} \mathbf{T}$$

$$\mathbf{S} = \tilde{\mathbf{d}}^T \mathbf{E} + \tilde{\mathbf{s}}^E \mathbf{T}$$

where $\tilde{\boldsymbol{\varepsilon}}$, $\tilde{\mathbf{e}}$, $\tilde{\mathbf{c}}$, $\tilde{\mathbf{d}}$ and $\tilde{\mathbf{s}}$ are complex-valued matrices, where the imaginary part defines the dissipative function of the material.

It can be typed the complex-valued data directly or it can be used the concept of loss factors. Similarly to the loss factor damping, the complex data \mathbf{X} is represented as pairs of a real-valued parameter $\mathbf{X} = \text{real}(\mathbf{X})$ and a loss factor $\eta_x = \text{imag}(\mathbf{X}) / \text{real}(\mathbf{X})$, the ratio of the imaginary and real part, and the complex data is then:

$$\mathbf{X} = \mathbf{X}(1 \pm j\eta_x)$$

where the sign depends on the material property used.

Usually the quality factor Q is defined for a material. The quality factor and the loss factor η_i are inversely related: $\eta_i = 1/Q$, where η_i is the loss factor for \mathbf{c}^E , \mathbf{s}^E , or the structural loss factor depending on the material. The piezoelectric application modes allow defining the loss factors as full matrices or as scalar isotropic loss factors independently of the material and the other coefficients.

3.6 Bibliography

-
- ¹ G. Sauerbrey, “Verwendung von schwingquarzen zur wägung dünner schichten und zur mikrowägung”, *Z. Phys.*, vol. 155, pp.206-222, 1959.
- ² K. Kanazawa and Nam-Joon Cho, “Quartz Crystal Microbalance as a Sensor to Characterize Macromolecular Assembly Dynamic”, Hindawi Publishing Corporation, *Journal of Sensors*, 2009.
- ³ M. Mecea, “From Quartz Crystal Microbalance to Fundamental Principles of Mass Measurements”, *Analytical Letters*, vol. 38, pp. 753-767, 2005.
- ⁴ D. Wu, Y. Tsai, Y. Yen, “Robust Design of Quartz Crystal Microbalance Using Finite Element and Taguchi Method”, *Sensors and Actuators B*, vol. 92, pp. 337-344, 2003.
- ⁵ R. Cernosek, S. Martin, R. Hillman and H. Bandey, “Comparison of Lumped-Element and Transmission-Line Models for Thickness-Shear-Mode Quartz Resonator Sensors”, *IEEE Transactions on Ultrasonics, Ferroelectrics, and Frequency Control*, vol. 45, n. 5, 1998.
- ⁶ IEEE Standard on Piezoelectricity, ANSI/IEEE Std 176-1987.
- ⁷ L. Brown, “Design Considerations for Piezoelectric Polymer Ultrasound Transducers” *IEEE Trans Ultrason Ferroelect Freq Contr*, vol. 47, no.6, pp. 1377-1396, Nov. 2000.
- ⁸ R. Lucklum, and P. Hauptmann, “The quartz crystal microbalance: mass sensitivity, viscoelasticity and acoustic amplification”, *Sensors and Actuators B*, vol. 70, pp. 30-36, 2000.
- ⁹ J. Rosenbaum, *Bulk Acoustic Wave Theory and Devices*, Artech House, Inc., 2000.
- ¹⁰ T. Makkonen, A. Holappa, Juha Ellä, and M. Salomaa, “Finite Element Simulations of Thin-Film Composite BAW Resonators”, *IEEE transactions on ultrasonics, ferroelectrics, and frequency control*, vol. 48, no. 5, 2001.
- ¹¹ N. Abboud, G. Wojcik, D. Vaughan, J. Mould, D. Powell, and L. Nikodym, “Finite element modeling for ultrasonic transducers,” in *Proc. SPIE Int. Symp. Medical Imaging*, vol. 3341, pp. 19-42, 1998.

CHAPTER 4: Devices simulations

In this chapter, the implementation of different models for the analysis of piezoelectric sensors performances is described. *Section 4.1* presents the modeling of a quartz crystal microbalance as published by Zalazar et al. 2009.¹ *Sections 4.2* and *4.3* describe the modeling of a PVDF mass microsensor and AlN mass microsensor respectively, both based on the work done by Zalazar et al. 2010.² *Section 4.4* depicts the analysis of a PVDF pressure microsensor. In regard of the simulations, *Appendix A* presents the microtransponder chip circuit design and simulation for the energization of an active microvalve for the treatment of glaucoma as published by Zalazar et al. 2012.³

4.1 Quartz Crystal Microbalance

As shown in *Section 1.4.2*, quartz crystal microbalance devices are highly sensible to small mass variations due to changes in quartz crystal resonance frequency (some microbalances reach a resolution up to 0,05 ng).⁴ QCMs have mayor sensibility than conventional analytical microbalances actually used in laboratories. Since the quartz crystal microbalance was first introduced by Sauerbrey in 1959, it has become a largely used instrument for small mass measurements in vacuum, gas, and liquid phase.

Quartz is probably the most widely used piezoelectric crystal. The quartz is an oxide (SiO₂) of triclinic crystal symmetry. It belongs to crystal class 32 (trigonal). Its high melting point, with a phase transition point at 573 °C, limits the useful temperature span for both applications and processes. Moreover, quartz is an anisotropic material, i.e. its material coefficient changes with cutting plane from different angles or directions. Therefore, with cutting from different angles or directions, quartz will have different resonant frequency and vibration modes. In general, AT-cut quartz crystal is suitable for the substrate of QCM due to its low temperature coefficient at room temperature with only minimal frequency changes and higher resonant frequency than other kinds of quartz crystals. AT-cut quartz crystal is the quartz crystal cut from a specific orientation 35°15'

with respect to the optical axis (Figure 1.7). In this shear mode, the coefficient d_{66} dominates the other piezoelectric constants in the constitutive equations and as a result, shear vibrations appear. The following picture (Figure 4.1) describes a typical quartz disk where it shows the aspect of the QCM (left) and the shear displacement of the generated vibrations (right):

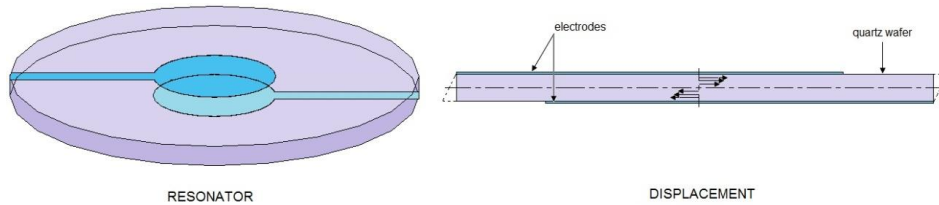


Figure 4.1: Typical quartz disk showing the QCM aspect (left) and the shear displacement of the generated vibrations (right).

In order to evaluate the QCM performance, it was used a FEM model in order to perform simulations of the QCM for different thicknesses of deposition layer. It was used Parylene[®] coating. Parylene[®] is a thin film polymer coating that delivers unsurpassed barrier protection in a wide range of products and applications. In medical device industry it offers an unequalled level of protection to critical components. No other coating can boast similar properties. It is biocompatible, pinhole-free, extremely thin, and protects against the effects of fluids and solvents, so the knowledge of the deposition thickness is very important for biomedical applications.

In this section it is conducted the analysis of the behavior of a QCM for different amounts of deposited material on its surface. It was carried out the design and simulation using two models: circuital (*Section 3.2*) and FEM (*Section 3.4*) model. These two models were compared with the analytical (Sauerbrey) solution (*Section 3.1*). The numerical model considers constructive aspects of the QCM, unable to be addressed with the circuital one.

4.1.1 Design

Dimensions and geometries of the crystal and electrodes are determinant on the functional characteristics of the QCM. For instance, it has been demonstrated through FEM simulations that circular-shaped electrodes has yielded better results than the annular one and that increment in thickness reduce the QCM sensitivity⁵. It has also been applied this numerical technique to observe the vibrational displacement profile of the crystal⁶. Another feature that shows the relevance in the microbalance geometry is improvement in the separation of spurious vibration modes from the fundamental one as a consequence of reducing the electrode diameter⁷. It was observed also, that crystal vibrations are focused on the center of the disk, losing amplitude beyond electrodes dimension; in addition, the displacement distribution is not circular but elliptical.^{6,8}

For this model, the dimensions of the device were chosen based on the most common dimensions used in different publications.^{5,8} The thickness of the crystal was chosen to produce a resonant frequency of around 5 MHz, thereby ensuring not a so thin thickness, thus reducing their fragility and avoiding spurious modes close to fundamental vibration mode.⁷ Used dimensions were:

	Value	Unit
Quartz diameter	12	mm
Quartz thickness	330	μm
Electrode diameter	8	mm
Electrode thickness	10	μm

Table 4.1: Dimensions for the proposed QCM.

4.1.2 Circuital model

The circuital model was implemented using *Simulink*, a tool of *Matlab* and *LTspice*, a freeware high performance SPICE simulator software. The following simulations were performed: *i) Unloaded QCM*: f_r was obtained and contrasted with the analytic one (using Eq. (3.6)); the values for the electrical components were obtained based on the quartz dimensions and its material parameters for an AT-cut quartz crystal, and *ii) QCM with Parylene[®] deposition*: Parylene[®] was used as the deposition layer. The deposition thickness ranges from 1 μm up to about 20 μm . Frequency shifts were contrasted with the analytical ones (see Sauerbrey equation (3.1)). The used model parameters for quartz and Parylene[®] are shown in the following table:

Parameter	Value	Unit	Description
c_p	2.901e10	N/m ²	Quartz stiffness coefficient
k_t^2	7.74e-3		Quartz electromechanical coupling constant
η_p	35e-3	kg/m/s	Quartz viscosity
ε_p	3.982e-11	A ² s ⁴ kg ⁻¹ m ⁻³	Quartz permittivity
ρ_p	2649	kg/m ³	Quartz density
ρ_f	1289	kg/m ³	Parylene [®] density
A_e	$\pi(4\text{e-}3)^2$	m ²	electrode area

Table 4.2: Parameters used for the QCM with Parylene[®] deposition.

where ρ_f is the density of the Parylene[®].

i) Unloaded QCM

The BVD equivalent circuit was used as follows:

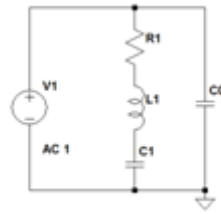


Figure 4.2: Butterworth-Van Dike equivalent circuit for a QCM.

The values of the electrical components of the circuit were calculated using the equations (3.2), (3.3), (3.4) and (3.5) as shown previously:

$$R_1 = 0.005 \, \Omega$$

$$L_1 = 4.2083 \, \mu\text{H}$$

$$C_1 = 239.43 \, \text{pF}$$

$$C_0 = 38.163 \, \text{nF}$$

Using these values, the graph obtained in Figure 4.3 shows the equivalent impedance and phase spectra of the circuit (Z [dB] and Phase [deg] vs frequency [MHz]). It is noted that the resonance frequency gives a value close to 5.0139MHz.

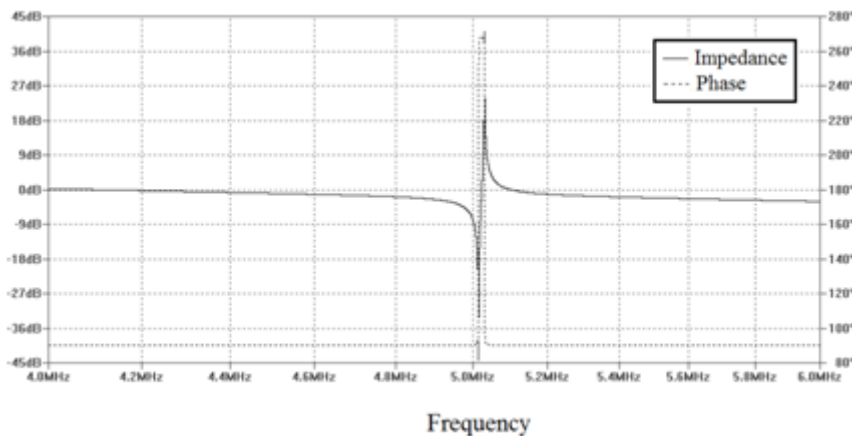


Figure 4.3: Equivalent impedance and phase spectra for a QCM using the Butterworth-Van Dike equivalent circuit.

It can be obtained more information from the picture shown above; the admittance and impedance maxima, respectively, coincide with the resonance frequency, f_r and the antiresonance frequency f_a :

$$f_r = 5.0139 \, \text{MHz}$$

$$f_a = 5.02968 \, \text{MHz}$$

In the case of quartz, the resonator loss is not so high, thus it is a good approximation to consider the series resonance frequency f_s equivalent to the resonance frequency and the parallel resonance frequency f_p equivalent to the antiresonance frequency.

Using equation (1.54), it can be determined the electromechanical coupling constant from f_s and f_p :

$$k_t^2 = 0.0077$$

which clearly coincides with the value obtained from literature.

ii) QCM with Parylene[®] deposition

For a material deposition on the surface of the resonator, the Modified Butterworth-Van Dike equivalent circuit (Figure 3.6) has to be used by applying equation (3.11). It was simulated the Parylene[®] deposition with a thickness ranging from 1 μm up to 20 μm . The results were compared with the analytical solution and the extracted the frequency shifts are shown in Table 4.3:

h_f [m]	Δf_a [Hz]	Δf_c [Hz]	E [%]
1e-6	7,37e3	7314	7,63e-1
4e-6	2,95e4	29130	1,19
7e-6	5,16e4	50640	1,84
1e-5	7,37e4	71880	2,47
1.4e5	1,03e5	99780	3,30
1.7e5	1,25e5	120400	3,90
2e5	1,47e5	140750	4,51

Table 4.3: Comparison of analytical and circuital values for Parylene[®] deposition , where h_f is the film thickness, Δf_a the analytical frequency shift, Δf_c the frequency shift of the circuital model and E the error of Δf_c with respect to Δf_a .

The frequency shift of the circuit model compared to analytical model for thicknesses of Parylene[®] deposition between 1 μm -20 μm , presented an average error of 2.57% with a standard deviation of 1.4%. It can be noted the increment in the error estimate with the augmented thickness; it may be due to the limitations that impose the Sauerbrey equation ($\Delta f_a > 2\%$)⁹ as stated in *Section 3.1*.

The frequency shifts in the circuital model can be observed in the following picture:

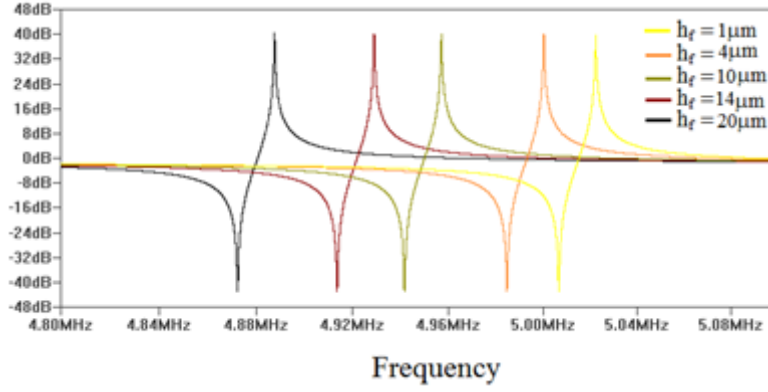


Figure 4.4: Frequency shifts obtained by applying the Modified Butterworth-Van Dike equivalent circuit for the QCM.

4.1.3 FEM model

It was used a 3D piezoelectric elastic linear solid for the quartz (trigonal 32). The electric potential was applied on both principal surfaces of the disc avoiding electrodes modeling but respecting its area (where the potential was applied), thus neglecting mechanical effects of the metal films. This simplifies the model and reduces simulation times without losing accuracy.

For such a crystal with a trigonal axis and a diagonal axis, the matrices are:

$$\mathbf{c} = \begin{bmatrix} c_{11} & c_{12} & c_{13} & c_{14} & 0 & 0 \\ c_{12} & c_{22} & c_{23} & c_{24} & 0 & 0 \\ c_{13} & c_{23} & c_{33} & c_{34} & 0 & 0 \\ c_{14} & c_{24} & c_{34} & c_{44} & 0 & 0 \\ 0 & 0 & 0 & 0 & c_{55} & c_{56} \\ 0 & 0 & 0 & 0 & c_{56} & c_{66} \end{bmatrix} \text{ Pa}$$

$$\mathbf{e} = \begin{bmatrix} e_{11} & e_{12} & e_{13} & e_{14} & 0 & 0 \\ 0 & 0 & 0 & 0 & e_{25} & e_{26} \\ 0 & 0 & 0 & 0 & e_{35} & e_{14} \end{bmatrix} \frac{\text{C}}{\text{m}^2}$$

$$\boldsymbol{\varepsilon} = \begin{bmatrix} \varepsilon_{11} & 0 & 0 \\ 0 & \varepsilon_{11} & \varepsilon_{23} \\ 0 & \varepsilon_{23} & \varepsilon_{13} \end{bmatrix}$$

For the AT-cut quartz disk, the rotation of $35^{\circ}15'$ on the optical axis of the crystal has to be taken into account. In COMSOL Multiphysics, for the material orientation it can be selected the 3D material properties orientation relative the 2D/axial symmetric analysis plane. There are six options: xy , yz , zx , yx , zy , and the default xz -plane (Figure 4.5).

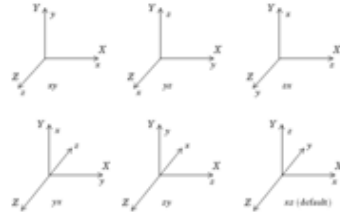


Figure 4.5: Orientation of 3D material xyz relative to the 2D analysis coordinate system XYZ .

Plates of different cuts have different material matrices with respect to coordinate systems in and normal to the plane of the plates. One class of cuts of quartz plates, called rotated Y-cuts, has an orientation of $\varphi=0$ and is particularly useful in device applications.

Instead of rotating $35^\circ 15'$ the Z coordinate axis and X on Y, this turning was achieved by using the material matrices with rotated coordinates; AT-cut quartz is a special case of rotated Y-cut quartz whose material constants are:¹⁰

c	[GPa]	e	[C/m ²]	ϵ_r	
c_{11}	86.74	e_{11}	0.171	ϵ_{11}/ϵ_0	39.21
c_{12}	-8.25	e_{12}	-0.152	ϵ_{22}/ϵ_0	39.82
c_{13}	27.15	e_{13}	-0.0187	ϵ_{23}/ϵ_0	0.86
c_{14}	-3.66	e_{14}	0.067	ϵ_{33}/ϵ_0	40.42
c_{22}	129.77	e_{25}	0.108		
c_{23}	-7.42	e_{26}	-0.095		
c_{24}	5.7	e_{35}	-0.0761		
c_{33}	102.83				
c_{34}	9.92				
c_{44}	68.81				
c_{55}	0.59				
c_{56}	2.53				
c_{66}	0.70				

Table 4.4: QCM Matrix constants.

The parameter values used for Parylene[®] were:

	Value	Unit
Parylene [®] Young modulus	2.7579	MPa
Parylene [®] Poisson relation	0.4	
Parylene [®] thermal expansion coefficient	1.27e3	1/K

Table 4.5: Parameter values for Parylene[®].

Environment damping effects were neglected for the resonator and edges were fixed. Quadratic interpolation and 4th order integration were used. For this 3D geometry it was chosen a free mesh containing tetrahedral elements.

COMSOL has a free mesher available in all space dimensions, and it can be used for all types of geometries regardless of the topology and shape of the geometry; the free mesher automatically creates an unstructured mesh. The number of mesh elements is determined from the shape of the geometry and various mesh parameters. In can be specified local mesh-element sizes and can be controled the element distribution. All mesh parameters aim at prescribing the maximum allowed mesh element size.

The normal stress (σ_n) at the boundaries was set null and an electric potential was applied on the disk top and bottom faces (Γ_g and Γ_e respectively) thus arriving at the following boundary conditions:

$$\begin{aligned}\sigma_n &= 0 && \text{on } \partial\Omega \\ \phi &= 0 && \text{on } \Gamma_g \\ \phi &= 1V && \text{on } \Gamma_e \\ \mathbf{D} \cdot \mathbf{n} &= 0 && \text{on } \partial\Omega \setminus (\Gamma_g \cup \Gamma_e)\end{aligned}$$

In this software, harmonic excitation loads were specified and assumes harmonic response with the same angular frequency as the excitation load. The frequency response analysis was done with a parametric solver. It performs a frequency sweep over several excitation frequencies. The following equation for the impedance characteristics $Z(\omega)$ was used:

$$Z(\omega) = \frac{V}{I(\omega)}$$

where $I(\omega)$ is the Fourier transformation of the current $i(t)$, this last obtained as the integration of the current density on the loaded electrode.

For the QCM, the unknown variables were solved, i.e., the displacement (u_x, u_y, u_z) and the electric potential (V). For the Parylene[®], a layer with the same diameter of the quartz disk was situated on the top of the piezoelectric and the displacements variables in the three directions were solved.

The following simulations were performed: *i) Unloaded QCM*: f_0 was obtained and contrasted with the analytic one, and *ii) QCM with Parylene[®] deposition*: Parylene[®] was used as the deposition layer. The deposition thickness ranges from 1 μ m up to about 20 μ m. Frequency shifts were contrasted with the analytical ones.

i) Unloaded QCM

The resonance frequency was found to be close to 5.0302MHz. The following picture shows the admittance value for frequencies ranging from 4.5 MHz to 5.5 MHz:

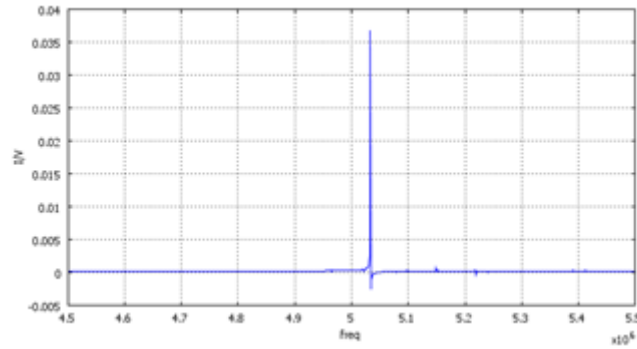


Figure 4.6: Resonance frequency for the QCM with no deposition (air-loaded).

This f_r was found for a mesh of about 6600 elements. It presents an error of 0.325% with respect to the circuital one.

A resonator's vibration was excited close to resonance frequency in order to visualize the lateral view of the vibrations of a quartz crystal. In the shear vibrational mode, the crystal has an AT-cut which has a specific orientation of $35^{\circ}15'$ with respect to the optical axis as shown in previous sections. As depicted in Figure 4.7, it can be shown the shear vibrations corresponding to this kind of Thickness-Shear-Mode resonator and its deformation.

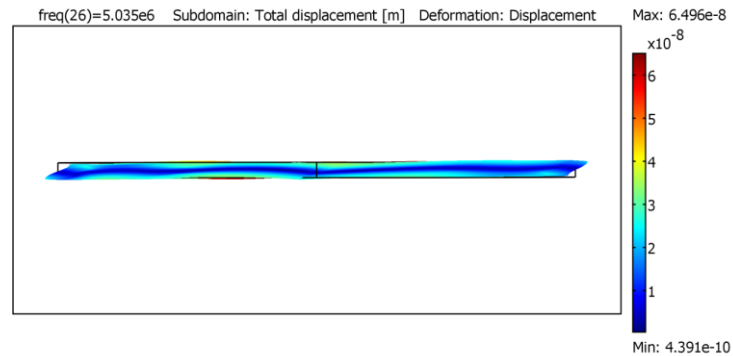


Figure 4.7: Shear vibrations of the QCM at resonance.

As shown in *Section 3.1*, the displacement of the device is not uniform over the surface and has a maximum at the center as stated by Mecea, 2005⁸. This phenomenon can be appreciated in Figure 4.8, where the displacements have a maximum at the center of the disk and decrease towards the electrode edges (note the area of the electrode on the main face smaller than the area of the quartz disk).

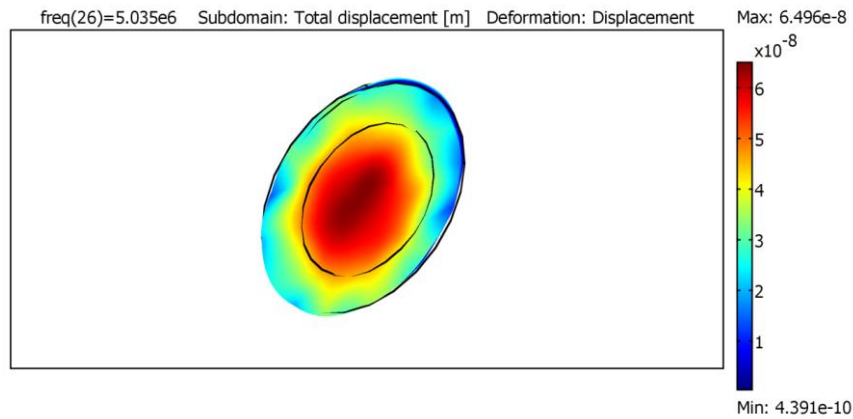


Figure 4.8: Distribution of the displacement in the bulk of the resonator QCM.

The distribution of the displacement amplitude can be seen in Figure 4.9, where a cross-section of the quartz resonator showing the displacements was done.

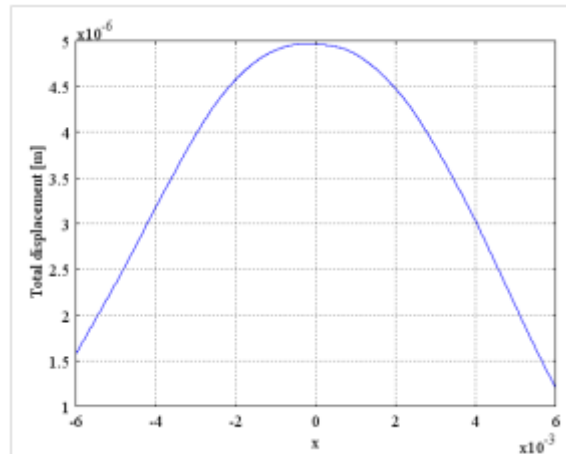


Figure 4.9: Cross-section of the quartz resonator showing the displacement amplitude.

It also can be depicted in the distribution of the displacement, the effect of the shear stress, showing a non-symmetric distribution with respect to the center of the disk ($x=0$).

ii) QCM with Parylene® deposition

In order to model this situation, it was located on the top face of the quartz, another disk with the same radius and variable thickness. This new disk represents the deposited material film (Parylene®).

In this case, meshing between 5000 and 8000 elements was used considering the increasing thicknesses of Parylene® depositions. The model for this new system is shown in Figure 4.10, exhibiting the physical aspect of the disk with material deposition, their meshing and its vibrational response.

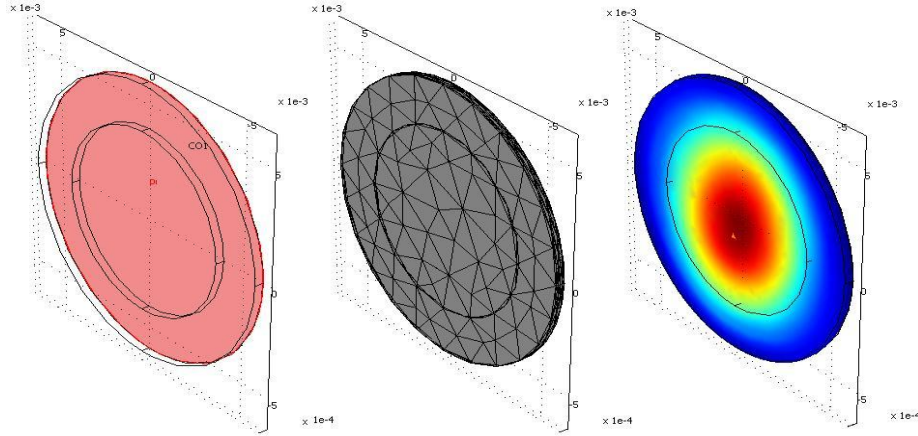


Figure 4.10: Physical aspect of the quartz disk for a 20 μm Parylene[®] deposition (red) (left), meshing (center) and vibrational response (right).

For a 1 μm -Parylene[®] deposition, the response of the electric admittance versus frequency is depicted in Figure 4.11. The resonance frequency was found to be 4.992MHz, showing a frequency shift of 38.2 kHz.

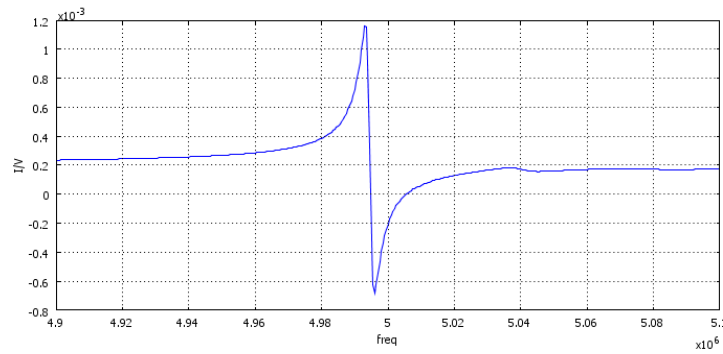


Figure 4.11: Input admittance for a 1 μm -Parylene[®] loaded QCM.

From the picture above it can be visualized the increased separation between f_r and f_a as a consequence of the decrease in the quality factor (Q) of the resonator due to mass loading; in addition, it can be observed the attenuation of the admittance.

For thicknesses of 1 μm , 5 μm , 10 μm , 15 μm and 20 μm , the frequency shifts were obtained. Comparison with analytical values is shown in Table 4.6 and Figure 4.12.

h_f [m]	Δf_a [Hz]	Δ_{ffem} [Hz]	E [%]
1e-6	7370.2	8200	11,26
5e-6	36851	38200	3,6
1e-5	73702	73200	0,68
1.5e-5	110550	109200	1,22
2e-5	147400	145200	1,49

Table 4.6: Comparison of analytical and FEM values for Parylene[®] deposition, where h_f is the film thickness, Δf_a the analytical frequency shift, Δ_{ffem} the frequency shift of the FEM model and E the Δ_{ffem} error with respect to Δf_a .

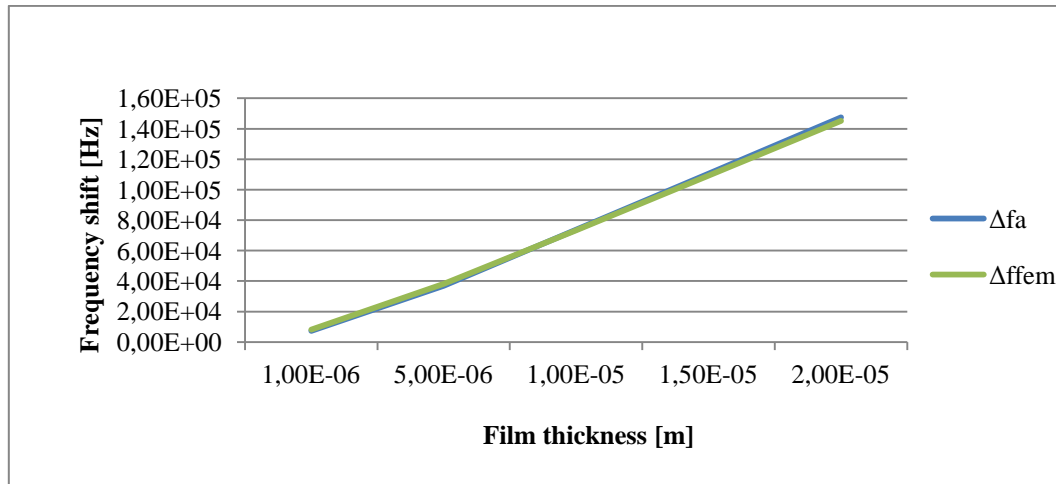


Figure 4.12: Frequency shifts (analytical and FEM) for different Parylene[®] deposition films.

These results show an average error of 3.66% with a standard deviation of 4.39%.

4.1.4 Discussion and conclusions

The resonance frequency obtained with the FEM model for the QCM showed that, in terms of geometric parameters, it depends on crystal thickness and remains invariant with diameter in concordance with literature.

It has been seen that results obtained with the circuit model approach are fairly close to the analytical solutions (average error of 2.57% with a standard deviation of 1.4%) found for the QCM presented in this section and considering the deposition of a material. These results suggest the use of a reliable tool for modeling, within its working range, the deposition of Parylene[®] on the disc.

The small difference (0.325%) found in the resonance frequency obtained using these two models is mainly due to the nature of a more complete 3D modeling used in the FEM model, represented by the stiffness, piezoelectric and dielectric matrices. The latter proposes a more realistic solution; it deals with constructive aspects, absent in the circuit model, allowing the modeling of complex geometries.

The FEM model used for Parylene[®] deposition shows linearity between thicknesses and frequency shifts as indicated by the Sauerbrey equation. This motivates the use of the model to estimate the deposition behavior.

4.2 PVDF mass microsensors

Acoustic wave devices and sensors have been in commercial use for several years. Piezoelectric materials had been mainly used as sensors and actuators in a huge field of applications. An important drawback in the use of QCM is related with its fragility with the decreasing thickness when looking for highest frequencies. Thin film bulk acoustic resonators are BAW sensors based in thickness mode waves. This technology allows a reduction in piezoelectric thickness layers, increasing its resonance frequency. Thickness modes are the so-called high frequency modes whose frequencies are determined by the plate thickness, the smallest dimension.

Piezoelectric polymers are a good option to develop piezoelectric-based acoustic wave devices as sensors as well as actuators. The polyvinylidene fluoride and its copolymers are the polymers with the highest piezoelectric effect. It has high dynamic range and wideband and belongs to a new class of piezoelectric plastics characterized by relative low dielectric constant, moderate piezoelectric coupling, low acoustic velocities and low density.¹¹ One of the major advantages of these piezoelectric films is the low acoustic impedance close to the water, human tissue and other organic materials, allowing a more efficient transduction of acoustic signals due to close impedance match thus been suitable for BioMEMS applications.

Even though there are several works involving PVDF applications, the design and development of PVDF devices is usually done by experiments.^{12,13} In this sense, computer simulation tools have been largely used in order to improve not only the design but also the functionality of the piezoelectric device. In addition it will help reducing time therefore improving solutions.

Analytical equation like the Sauerbrey equation considers a small phase shift of the acoustic wave while it travels throughout the deposition material and its application is limited to rigid thin films.¹⁴ A more complete model for acoustic systems can be built using the three-port one-dimensional multilayer Mason model;¹¹ this model has been used for a variety of applications.^{15,16,17,18,19,20,21} In order to get a more realistic model as reference, FEM model fits very well. FEM is a flexible method capable of modeling complicated device geometries, nonuniform materials properties and quite general boundary conditions.

In this section, the analysis of the behaviour of a FBAR piezoelectric sensor was carried out for different amounts of deposited material on it. It was used PVDF as the piezoelectric material for the FBAR sensor. A macromodel (Mason model) was implemented (section 3.3) for the resonator with polymer deposition and results were compared with the FEM model (section 3.4).

4.2.1 Design

Various designs used in piezoelectric actuation and sensing devices were carried out using FEM models, e.g., microactuator models regarding piezoelectric and electrodes geometric characteristics,²² different piezoelectric structures^{23,24} and a circular multi-material plate model for micro-fluidic applications.²⁵ Moreover, FEM analysis of a BAW resonator using 3D linear models was presented in a book.²⁶

The PVDF has orthorhombic symmetry (mm2 class) and is usually operated in thickness mode when the frequency of operation is more than 500 kHz.²⁷ It has three main actuation/sensing modes depending on the fabrication process: inplane mode (d_{31} , d_{32}), the thickness mode (d_{33}) and shear mode (d_{15} , d_{24}).

A circular shape was adopted with the same diameter for the electrodes and the PVDF film. Dimensions were based on the most-used values found in literature^{27,28,29} for a resonant frequency of around of 45.8MHz: 2mm of diameter and 10 μm of thickness (Table 4.7). The effect of electrodes, usually aluminum, was neglected due to its small thickness and low acoustic impedance.

	Value	Unit
PVDF diameter	2	mm
PVDF thickness	10	μm

Table 4.7: Dimensions for the proposed PVDF resonator.

4.2.2 Mason model

The Mason model describes the ideal one-dimensional behavior of the resonator, using electro-acoustic coupling equations and modeling each resonator layer by lumped elements or transmission lines, imposing boundary conditions at the ends.

Therefore, the input impedance as a function of frequency for a piezoelectric resonator is given by the following equations as shown previously by equations (3.35), (3.36) and (3.37):

$$Z_{in} = \frac{1}{j\omega C_0} + P(\omega) \frac{R_0}{\omega_2 C_0^2}$$

where

$$R_0 = \frac{k_t^2 v_0 C_0}{d}$$

and

$$P(\omega) = \frac{(Z_s/Z_T)\sin(kd) + 2j(1 - \cos(kd))}{\sin(kd) - j(Z_s/Z_T)\cos(kd)}$$

Here the resonator impedance $Z_T = \sqrt{\rho_p c_p}$ and Z_s is the impedance of the substrate (surface mechanical impedance), that become zero for the unloaded resonator. For the case of a resonator with film deposition, impedance $Z_s = i\omega\rho_f d$. The layer must be sufficiently thin and rigid so that a shear acoustic wave traversing the layer has a negligible phase shift; it moves synchronously with the piezoelectric surface.

Equations of the Mason model were implemented in *Matlab*. The following simulations were performed: *i) Unloaded PVDF microbalance*: The input impedance as a function of frequency for the piezoelectric resonator was obtained as well as f_r , and *ii) PVDF microbalance with Parylene[®] deposition*: Frequency shifts were obtained from the difference between the resonance frequency of the unloaded microbalance and that of the microbalance with Parylene[®] depositions. Depositions in a range between 100 nm and 500 nm were used.

The PVDF and Parylene[®] parameters used^{27,28} are shown in Table 4.8:

Parameter	Value	Unit	Description
c_p	1.51e9	N/m ²	PVDF stiffness coefficient
k_t^2	19.6e-3		PVDF electromechanical coupling constant
ε_p	11.3e-11	A ² s ⁴ kg ⁻¹ m ⁻³	PVDF permittivity
ρ_f	1289	kg/m ³	Parylene [®] density
ρ_p	1800	kg/m ³	PVDF density

Table 4.8: Parameters used for the piezoelectric PVDF with Parylene[®] deposition.

i) Unloaded PVDF microbalance

In this case the piezoelectric resonator is stress free on either side (no metallic or substrate layers); the metallic layers are assumed to be acoustically thin enough to neglect and the substrate is infinitely long (only the resonator supports standing waves).

The resonance frequency was found to be in 46.315MHz for a frequency sweep between 46MHz-46.6MHz, as shown in Figure 4.13.

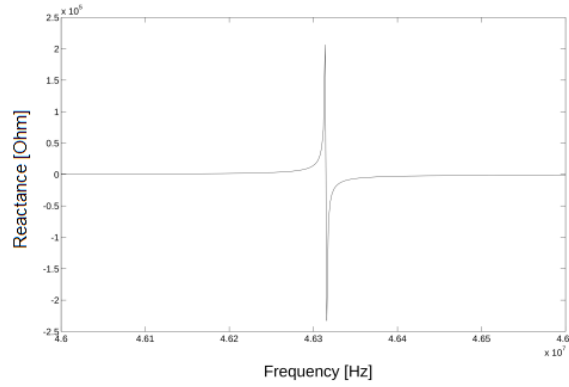


Figure 4.13: Imaginary part of the acoustic contribution to the input impedance for the unloaded PVDF resonator with a thickness of 10 μm .

ii) *PVDF microbalance with Parylene[®] deposition:*

There were simulated a PDVF resonator with deposition thicknesses of 100 nm, 200 nm, 300 nm, 400 nm and 500 nm. This model was used to validate the FEM model showed in next section.

4.2.3 FEM model

It was used a 3D piezoelectric elastic linear solid for the PVDF resonator. As in the QCM case, the electric potential was applied on both principal surfaces of the disc avoiding electrodes modeling; this simplifies the model and reduces simulation times without losing accuracy. The resonator is in thickness excitation mode where the electric field is in direction of acoustic wave propagation.

The elastic matrix \mathbf{c} , the piezoelectric coupling matrix \mathbf{e} and the dielectric coefficients matrix at constant strain $\boldsymbol{\varepsilon}$ are expressed as follows:

$$\mathbf{c} = \begin{bmatrix} c_{11} & c_{12} & c_{13} & 0 & 0 & 0 \\ c_{12} & c_{22} & c_{23} & 0 & 0 & 0 \\ c_{13} & c_{23} & c_{33} & 0 & 0 & 0 \\ 0 & 0 & 0 & c_{44} & 0 & 0 \\ 0 & 0 & 0 & 0 & c_{55} & 0 \\ 0 & 0 & 0 & 0 & 0 & c_{66} \end{bmatrix} \text{Pa}$$

$$\mathbf{e} = \begin{bmatrix} 0 & 0 & 0 & 0 & e_{15} & 0 \\ 0 & 0 & 0 & e_{24} & 0 & 0 \\ e_{31} & e_{32} & e_{33} & 0 & 0 & 0 \end{bmatrix} \frac{\text{C}}{\text{m}^2}$$

$$\boldsymbol{\varepsilon} = \begin{bmatrix} \varepsilon_{11} & 0 & 0 \\ 0 & \varepsilon_{22} & 0 \\ 0 & 0 & \varepsilon_{33} \end{bmatrix}$$

The three major axes are unique in the orthorhombic symmetry where the presence of three separate longitudinal diagonal terms and three separate shear diagonal terms are shown in the elastic matrix \mathbf{c} .

For the PVDF, values are showed in Table 4.9.²⁸ Even though the symmetric circular shape of the film, the used constants were for uniaxial films²⁸ considering the use of thickness mode.

\mathbf{c}	[GPa]	\mathbf{e}	[C/m ²]	$\boldsymbol{\varepsilon}_r$	
c_{11}	3.70	e_{15}	-0.0159	$\varepsilon_{11}/\varepsilon_0$	12
c_{12}	1.47	e_{24}	-0.0127	$\varepsilon_{22}/\varepsilon_0$	12
c_{13}	1.23	e_{31}	0.0449	$\varepsilon_{33}/\varepsilon_0$	12
c_{22}	3.20	e_{32}	0.0129		
c_{23}	1.00	e_{33}	-0.0061		
c_{33}	1.51				
c_{44}	0.55				
c_{55}	0.59				
c_{66}	0.70				

Table 4.9: PVDF Matrix constants.

4.2.3.1 Meshing

Models with large geometric scale variations are sometimes problematic to mesh, in particular if they contain thin layers. This problem can be avoided by using a mapped mesher in 2D and the swept mesher in 3D, thus being less sensitive to thin regions.

It was used a swept mesh structured in the sweep direction. The 3D mesh was created by extruding a 2D mesh into a 3D mesh; triangular elements in the 2D mesh were extruded into prism (wedge) elements in the resulting 3D mesh.

For a 5 element layers along the extrusion and a number of 8720 prism elements (157036 degrees of freedom), the meshing aspect look like:

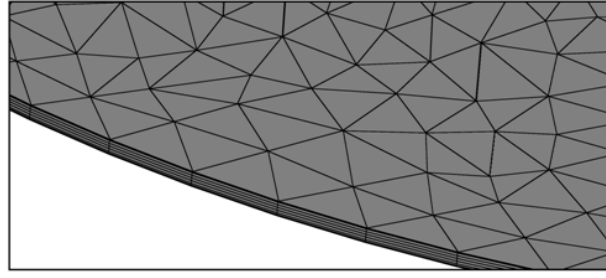


Figure 4.14: Meshing aspect of the unloaded PVDF resonator using a structured mesh of 8720 prism elements.

In Figure 4.14 it can be observed the good aspect ratio that present the prism elements used in the FEM model for the unloaded PVDF resonator.

4.2.3.2 Simulation tool

COMSOL Multiphysics was used for the modeling and simulation of the PVDF disk. Environment damping effects were neglected for the resonator and edges were fixed. Quadratic interpolation and 4th order integration were used. The normal stress (σ_n) at the boundaries was set null and an electric potential was applied on the disk top and bottom faces (Γ_g and Γ_e respectively) thus arriving at the following boundary conditions:

$$\begin{aligned} \sigma_n &= 0 && \text{on } \partial\Omega \\ \phi &= 0 && \text{on } \Gamma_g \\ \phi &= 1V && \text{on } \Gamma_e \\ \mathbf{D} \cdot \mathbf{n} &= 0 && \text{on } \partial\Omega \setminus (\Gamma_g \cup \Gamma_e) \end{aligned}$$

In the software used, harmonic excitation loads were specified and assumes harmonic response with the same angular frequency as the excitation load. The frequency response analysis was done with a parametric solver. It performs a frequency sweep over several excitation frequencies. The following equation for the impedance characteristics $Z(\omega)$ was used:

$$Z(\omega) = \frac{V}{I(\omega)}$$

where $I(\omega)$ is the Fourier transformation of the current $i(t)$, this last obtained as the integration of the current density on the loaded electrode.

For the PVDF resonator, the unknown variables were solved, i.e., the displacement (u_x , u_y , u_z) and the electric potential (V). For the Parylene[®] deposition, a layer with the same

diameter of the quartz disk was situated on the top of the piezoelectric and the displacements variables in the three directions were solved.

The following simulations were performed: *i) Unloaded PVDF microbalance*: The input impedance as a function of frequency for the piezoelectric resonator was obtained as well as f_r , and *ii) PVDF microbalance with Parylene[®] deposition*: Frequency shifts were obtained from the difference between the resonance frequency of the unloaded microbalance and that of the microbalance with Parylene[®] depositions. Depositions in a range between 100 nm and 500 nm were used.

The parameter values used for Parylene[®] were:

	Value	Unit
Parylene [®] Young modulus	2.7579	MPa
Parylene [®] Poisson relation	0.4	
Parylene [®] Thermal expansion coefficient	1.27e3	1/K

Table 4.10: Parameter values used for Parylene[®].

i) Unloaded PVDF microbalance

The resonance and antiresonance frequencies were:

$$f_r = 45.802 \text{ MHz}$$

$$f_a = 45.803 \text{ MHz}$$

The frequency response of the system is shown in Figure 4.15:

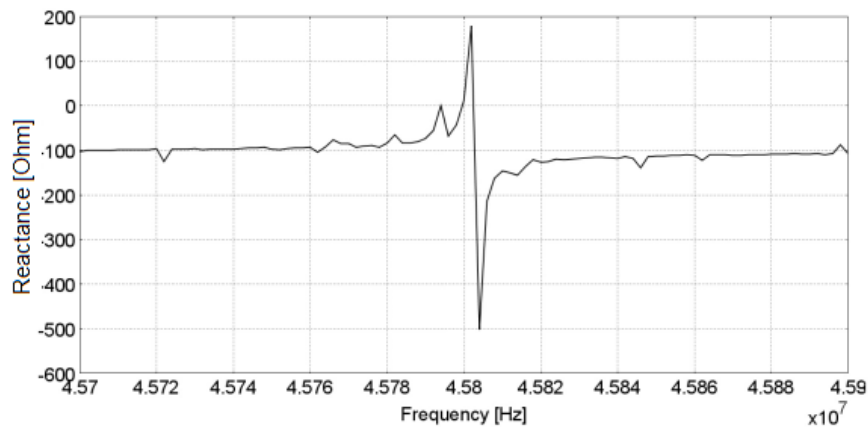


Figure 4.15: Imaginary part of the acoustic contribution to the input impedance for the unloaded PVDF resonator extracted from the FEM model for a thickness of 10 μm .

These frequencies were obtained with a mesh of 157036 degrees of freedom (DOF). Performing a mesh convergence study, the obtained results are shown in Table 4.11. These

values show an accurate solution starting from 73612 DOF and using a small computational time.

DOF	40124	73612	123772	157036
f_r [MHz]	45.833	45.803	45.803	45.802

Table 4.11: Mesh convergence study for the unloaded PVDF microbalance.

The resonance frequency obtained with the macromodel presented a relative deviation of 1.10% with respect to this case. The modeling of this system is shown in Figure 4.16, where it is depicted the meshing and the vibrational response.

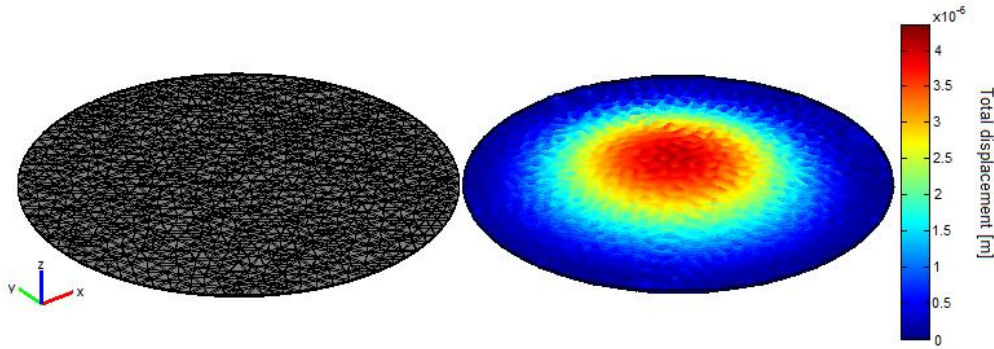


Figure 4.16: Meshing aspect of the 10 μm thickness PVDF (left) and its vibrational response (right).

ii) PVDF microbalance with Parylene[®] deposition

Meshing between 123606 and 184680 DOF were used for the material deposited range. The frequency shifts obtained and the comparison with the macromodel results are shown in Table 4.12 and Figure 4.17:

h_f [m]	Δ_{fM} [Hz]	Δ_{ffem} [Hz]	E [%]
100	0.325	0.327	0.428
200	0.646	0.646	0.093
300	0.962	0.956	0.700
400	1.270	1.274	0.016
500	1.580	1.582	0.145

Table 4.12: Comparison between Mason model and FEM model results for Parylene[®] deposition, where h_f is the film thickness, Δ_{fM} the Mason frequency shift, Δ_{ffem} the frequency shift of the FEM model and E the Δ_{ffem} error with respect to Δ_{fa} .

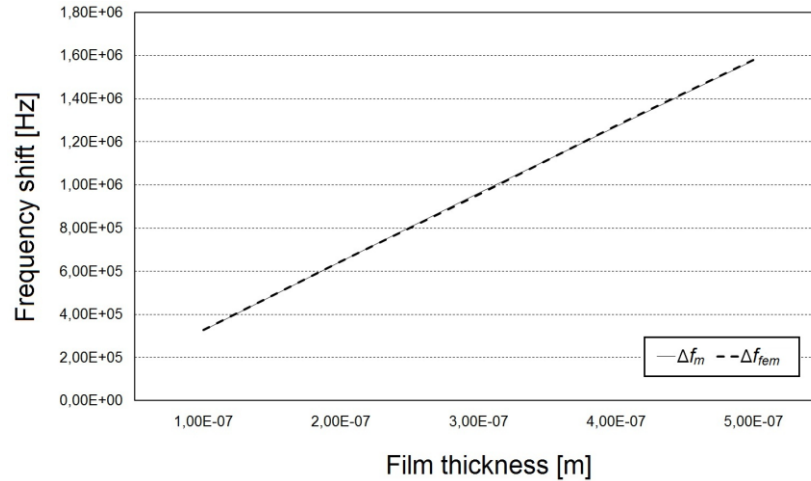


Figure 4.17: Shift frequency (Mason and FEM) for Parylene[®] deposition.

The results obtained with the macromodel shows an average relative deviation of 0.28% with respect to the FEM model.

4.2.4 Discussion and conclusions

A comparison between a macromodel and a FEM model for a PVDF thin film acoustic resonator with Parylene[®] polymer deposition was carried out. It was seen that the resonance frequency obtained with the macromodel for the PVDF resonator approaches fairly close to the reference results found for the FEM model presented in this work for the unloaded microbalance. This slight difference (1.10%) may be due to the 1D nature of the Mason model compared with the 3D geometry used for the FEM model; while using only the c_{33} component of the elastic matrix for the Mason model, in the FEM model it is important the contribution of the whole elastic matrix.

For Parylene[®] deposition, the small average relative deviation (0.28%) found in the macromodel compared with the FEM model, states the reliability of the macromodel. It motivates the application of the macromodel for modeling the Parylene[®] deposition on the PVDF resonator in the range of deposition used. Moreover it is a very good alternative to the analytical model in cases where the amount of deposited material is such that the Sauerbrey equation become inaccurate.

4.3 AlN mass microsensors

Nowadays it is in constant growing the development of thin film bulk acoustic resonator. This technology was born as a direct extension of the quartz crystal resonators. These are BAW-based thickness mode wave resonators, permitting a reduction in the piezoelectric thickness of the resonator thus conducting to an increased resonance frequency. Therefore it is reached a high sensibility in gravimetric applications in addition to their compatibility with the integrated circuit technology.

Aluminium Nitride is a piezoelectric material, primarily used before in the electronics industry as circuit substrates due to its relatively high thermal conductivity in combination with being an electrical insulator. It is a very attractive piezoelectric material for use in BioMEMS because it is biocompatible, exhibits high resistivity, high breakdown voltage, high acoustic velocity and it can be grown by reactive sputtering technique at relatively low temperature thus being compatible with CMOS technology.^{30,31} Material compatibility with IC fabrication opens the way for monolithic integration of the traditionally incompatible IC and electro-acoustic technologies.

The most common materials for thin film electro-acoustic devices today include AlN, ZnO and lead zirconium titanate (PZT). Extensive research and development of AlN thin film synthesis for high frequency SAW and BAW applications has resulted in that AlN so far appears to be the best compromise between performance and manufacturability and is the prime candidate for mass production of FBARs and filters. Material compatibility with IC fabrication opens the way for monolithic integration of the traditionally incompatible IC and electro-acoustic technologies.

Biosensors are used for detecting target molecules, such as the analytical studies of bimolecular interaction with other molecules or with solid surfaces. Biomolecules used as recognition elements in biosensors could be based on either proteins, such as antibodies, enzymes and receptors or nucleic acids such as aptamers. For a FBAR biosensor principle, the reaction must result in a binding to or release of molecules from the surface, where the most common approach is the use of antibodies, or various engineered derivatives such as antibody fragments or single chain variable fragments.

In this section, the analysis of the behaviour of an FBAR piezoelectric biosensor was achieved for protein deposition. It was used AlN as the piezoelectric material for the FBAR biosensor. A macromodel (Mason model) was implemented (*Section 3.3*) for the biosensor with protein deposition and also considering an aqueous media. Results for the unloaded resonator obtained by the Mason model were compared with the FEM model (*Section 3.4*).

4.3.1 Biosensor

The term biosensor is applied for sensors using biomolecules as selective recognition elements. These biological recognition elements selectively react with the analyte and the biochemical reaction is then recorded by a transducer, which is sending a signal to the read-out unit. In the following picture the principle of a general biosensor is illustrated:

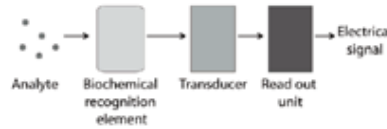


Figure 4.18: Schematic definition of a general biosensor.²⁰

The antibodies and their derivatives are proteins containing amino acids linked together by peptide bonds, which are strong covalent bonds restricting the rotation possibilities at these points. The protein will have a 3-dimensional structure depending on the interactions between the amino acids themselves and with the surrounding media. The interactions include Coulomb, dipole-dipole, van der Waals, or hydrophobic interactions, and often all of these must be present in order to preserve the three dimensional structure of the protein and consequently the functionality of the protein. Therefore, all analysis involving proteins or other biomolecules as selective recognition element must take place in an aqueous and saline environment with well-controlled pH and salt concentration, i.e. an environment in which proteins are normally found. It is consequently essential for the applicability of the FBAR biosensor utilizing protein-based biochemistry to operate with high performance in a liquid environment.

4.3.2 Design

AlN is most often in the Wurtzite hexagonal crystallographic system around the c-axis, which is also the direction with the highest piezoelectric constant in addition to a high acoustic wave velocity.³² The AlN film exhibits a columnar microstructure which is perpendicular to the substrate surface with orientation (002).

An square shape was adopted for the AlN resonator with the same diameter for the electrodes and piezoelectric film. Dimensions were based on the published by Wingqvist et al. 2006²⁰ and Bjurström et al. 2006³³ for a resonant frequency of around of 1.5 GHz: 300 μm side and 2 μm of thickness (Table 4.13). The effect of electrodes was neglected due to its small thickness and low acoustic impedance.

	Value	Unit
AlN square	300	μm
AlN thickness	2	μm

Table 4.13: Dimensions for the proposed AlN resonator.

4.3.3 Mason model

The Mason model describes the ideal one-dimensional behavior of the resonator, using electro-acoustic coupling equations and modeling each resonator layer by lumped elements or transmission lines, imposing boundary conditions at the ends. The input impedance as a function of frequency for a piezoelectric resonator is given by the equations shown previously by equations (3.35), (3.36) and (3.37).

The shear acoustic wave excited in the polycrystalline AlN film is not a pure mode but a quasi-shear mode. The displacement motion is not parallel to the surface, so it has a small deviation angle (polarization angle) causing a slight compressional motion in combination with the shear one.

Equations of the Mason model were implemented in *Matlab*. The following simulations were performed: *i) Unloaded AlN microbalance*: The input impedance as a function of frequency for the piezoelectric resonator was obtained as well as f_r , *ii) AlN microbalance with proteins deposition*: Frequency shifts were obtained from the difference between the resonance frequency of the unloaded microbalance and that of the microbalance with streptavidin as the deposited protein, and *iii) AlN microbalance with proteins deposition in an aqueous media*: Frequency shifts and resonance frequency were obtained. Protein depositions in a range between 1 nm and 50 nm were used.

The AlN, streptavidin and water parameters used^{27,28} are shown in the following table:

Parameter	Value	Unit	Description
c_p	120e9	N/m ²	AlN stiffness coefficient
c_f	0.28e6	N/m ²	Streptavidin stiffness coefficient
η_f	0.082	kg/m/s	Streptavidin viscosity
η_a	1e-3	kg/m/s	Water viscosity
k_t^2	20e-3		AlN electromechanical coupling constant
ϵ_p	9.027e-11	A ² s ⁴ kg ⁻¹ m ⁻³	AlN permittivity
ρ_f	1060	kg/m ³	Streptavidin density
ρ_p	3260	kg/m ³	AlN density
ρ_a	1000	kg/m ³	Water density

Table 4.14: Parameters used for the piezoelectric AlN, streptavidin and water.

i) Unloaded AlN microbalance

It was observed the resonance frequency close to 1.5043 GHz as shown in the input impedance response in Figure 4.19:

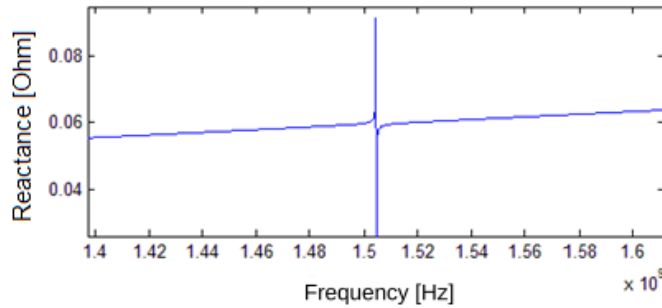


Figure 4.19: Imaginary part of the acoustic contribution to the input impedance for the unloaded PVDF resonator with a thickness of 10 μm .

ii) AlN microbalance with proteins deposition

It is common to model the biomolecular layers in the same way as polymers, i.e. as homogeneous layers obeying the Kelvin-Voigt description of viscoelastic materials, in which the complex dynamic modulus (G) can be described as:²⁰

$$G = G' + iG'' = c_f + i\omega\eta_f \quad (4.1)$$

where G' and G'' are the storage and the loss moduli respectively. c_f is the stiffness coefficient, η_f is the viscosity and ω is the angular frequency. Further, c_f and η_f are assumed to be real and constant, causing the storage modulus (G') to be constant and the loss modulus (G'') to be frequency dependent. That is the loss modulus and hence the viscosity dependence is expected to be amplified in the case of high frequency FBAR compared to QCM.

In general, the film is viscoelastic and acoustically thick, so the shear wave will suffer loss and some phase shift as it propagates. The chemical sensor load layer is treated as a transmission line with nonpiezoelectric properties as shown in the following figure:

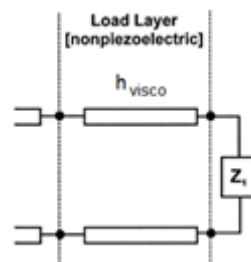


Figure 4.20: The transmission line representation of a nonpiezoelectric sensing film on a piezoelectric resonator surface. The additional mechanical load Z_l can be produced by any of several materials at the film surface.³⁴

In this situation, the resonator sees a surface mechanical impedance (impedance of substrate) Z_L , now consisting of the viscoelastic film impedance plus a load impedance Z_1 (e.g. the impedance of the water), at the layer surface. This mechanical impedance is described by the expression:³⁴

$$Z_L = Z_0 \frac{Z_1 \cosh(\beta h_{visco}) + Z_0 \sinh(\beta h_{visco})}{Z_0 \cosh(\beta h_{visco}) + Z_1 \sinh(\beta h_{visco})} \quad (4.2)$$

where $Z_0 = \sqrt{\rho_f G}$ is the viscoelastic film characteristic impedance, $\beta = j\omega \sqrt{\rho_f / G}$ is the complex wave propagation constant, h_{visco} is the film thickness and ρ_f is the film density. In this case, Z_s is replaced by Z_L in equation (3.37).

An AlN resonator was simulated with surface attached streptavidin with thickness ranging from 1-50 nm. Frequency shift results are shown in

Table 4.15:

h_{visco} [nm]	Δ_{fM} [MHz]
1	0.2
5	1.1
10	2.4
25	5.9
50	11.4

Table 4.15: Frequency shifts for the Mason model using streptavidin depositions, where h_{visco} is the viscoelastic streptavidin film thickness and Δ_{fM} the Mason shift frequency.

In order to figure out the behaviour of a viscoelastic layer, the frequency response of the system was simulated for "forced" streptavidin film thicknesses of 50 nm, 100 nm, and 150 nm as shown in Figure 4.21.

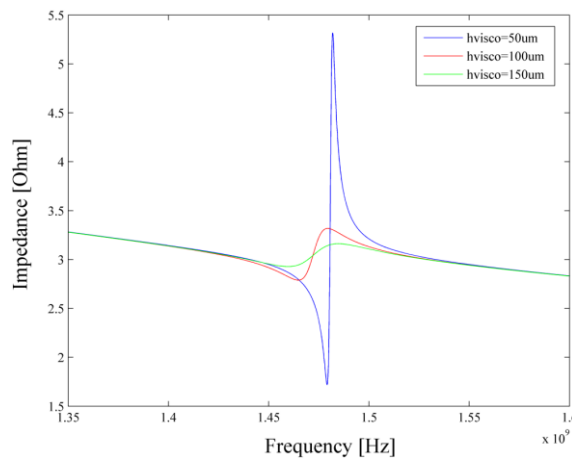


Figure 4.21: Frequency response of the AlN mass microsensor for a streptavidin film depositions of 50nm, 100nm and 150nm.

It can be observed the decrease in the resonance frequency of the AlN mass microsensor with the increasing thickness as predicted by the Sauerbrey equation. In addition, it can be seen the attenuation of the impedance amplitude with the streptavidin thickness, thus getting worse the quality factor Q ; it make sense due to the dissipation added by the viscous load.

iii) AlN microbalance with proteins deposition in an aqueous media

A liquid at the surface of a quartz resonator is viscously-entrained. The resulting surface mechanical impedance for a Newtonian fluid is:³⁴

$$Z_1 = (1 + j) \sqrt{\frac{\omega \rho_a \eta_a}{2}} \quad (4.3)$$

where ρ_a and η_a are the liquid density and viscosity respectively.

The comparison between the AlN mass microsensor with liquid load and unloaded was carried out. The liquid load was chose to be water, representing the natural environment of proteins. Results are shown in Figure 4.22, where a streptavidin thickness of 50 nm was used.

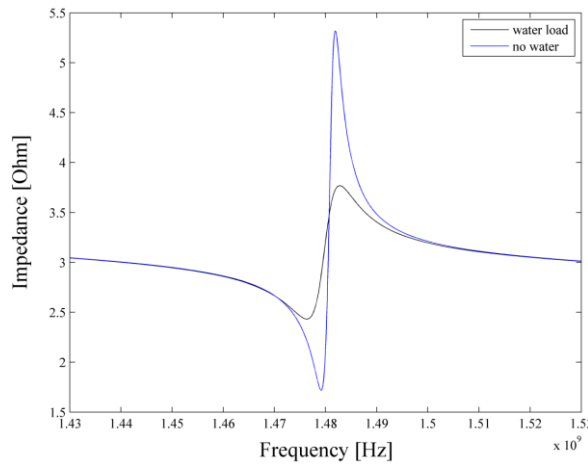


Figure 4.22: AlN mass microsensor water loaded and unloaded.

It is clear the attenuation of the quality factor Q in the AlN resonator due to water load. The shear acoustic wave excited in the polycrystalline AlN film is not a pure mode but a quasi-shear mode, thus the quasi-longitudinal resonance is notably damped when in contact with water. These results revealed the influence of the liquid media in this kind of sensor applications.

It can be observed also, that the resonance frequency does not change with the addition of a liquid media. The water layer only provides losses to the system but it has no influence in the frequency shifts.

4.3.4 FEM model

The displacement motion is not parallel to the surface (quasi-shear mode) as shown in the previous section, so it has an small deviation angle (polarization angle) causing a slight compressional motion in combination with the shear one. In order to develop a biosensor, good efficient excitation of the shear mode would be essential. It was shown that the c-axis needs to be grown tilted at least 20 degrees or more for high efficiency operation in viscous media.²⁰

Thus, for the AlN disk, a rotation of 35° on the optical axis of the piezoelectric has to be taken into account. It was used a 3D piezoelectric elastic linear solid for the AlN resonator. As in the QCM case, the electric potential was applied on both principal surfaces of the disc avoiding electrodes modeling.

The elastic matrix \mathbf{c} , the piezoelectric coupling matrix \mathbf{e} and the dielectric coefficients matrix at constant strain $\boldsymbol{\varepsilon}$ for the AlN are expressed as follows:

$$\mathbf{c} = \begin{bmatrix} c_{11} & c_{12} & c_{13} & 0 & 0 & 0 \\ c_{12} & 0 & 0 & 0 & 0 & 0 \\ c_{13} & 0 & c_{33} & 0 & 0 & 0 \\ 0 & 0 & 0 & c_{44} & 0 & 0 \\ 0 & 0 & 0 & 0 & c_{55} & 0 \\ 0 & 0 & 0 & 0 & 0 & c_{66} \end{bmatrix} \text{Pa}$$

$$\mathbf{e} = \begin{bmatrix} 0 & 0 & 0 & 0 & e_{15} & 0 \\ 0 & 0 & 0 & 0 & 0 & 0 \\ e_{31} & 0 & e_{33} & 0 & 0 & 0 \end{bmatrix} \frac{\text{C}}{\text{m}^2}$$

$$\boldsymbol{\varepsilon} = \begin{bmatrix} \varepsilon_{11} & 0 & 0 \\ 0 & 0 & 0 \\ 0 & 0 & \varepsilon_{33} \end{bmatrix}$$

For the AlN, values are showed in Table 4.16:

c	[GPa]	e	[C/m ²]	ϵ_r	
c_{11}	3.45e11	e_{15}	-0.48	ϵ_{11}/ϵ_0	10.2
c_{12}	1.25e11	e_{31}	-0.58	ϵ_{33}/ϵ_0	10.2
c_{13}	1.2e11	e_{33}	1.55		
c_{22}	1.25e11				
c_{33}	3.95e11				
c_{44}	1.2e11				
c_{66}	1.1e11				

Table 4.16: AlN Matrix constants.

Environment damping effects were neglected for the resonator and edges were fixed. Quadratic interpolation and 4th order integration were used.

The number of mesh elements was determined from the shape of the geometry and various mesh parameters; it was used a mesh with 4500 element in the domain. It was used a swept mesh structured in the sweep direction. The 3D mesh was created by extruding a 2D mesh into a 3D mesh; triangular elements in the 2D mesh were extruded into prism elements in the resulting 3D mesh.

The normal stress at the boundaries was set null and an electric potential was applied on the disk top and bottom faces (Γ_g and Γ_e respectively) thus arriving at the following boundary conditions:

$$\begin{aligned}
 \sigma_n &= 0 && \text{on } \partial\Omega \\
 \phi &= 0 && \text{on } \Gamma_g \\
 \phi &= 1V && \text{on } \Gamma_e \\
 \mathbf{D} \cdot \mathbf{n} &= 0 && \text{on } \partial\Omega \setminus (\Gamma_g \cup \Gamma_e)
 \end{aligned}$$

In the software used, harmonic excitation loads were specified and assumes harmonic response with the same angular frequency as the excitation load. The frequency response analysis was done with a parametric solver. It performs a frequency sweep over several excitation frequencies. For the PVDF, the unknown variables were solved, i.e., the displacement (u_x, u_y, u_z) and the electric potential (V).

i) Unloaded AlN microbalance

The modeling of this system is shown in Figure 4.23, where it is depicted the meshing used and the vibrational response. The resonance frequency was found to be close to 2.46GHz.

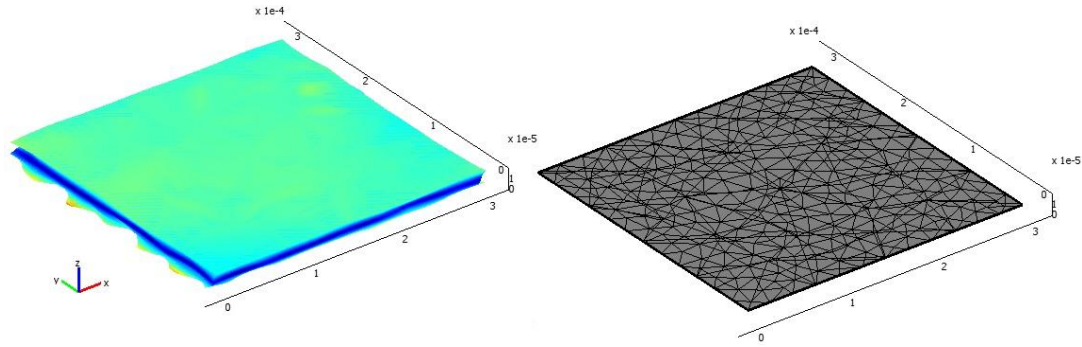


Figure 4.23: Vibrational response of the 2 μm -thickness AlN (left) and its meshing aspect (right).

The picture shown above describes the vibrations developed by the AlN resonator. As stated previously, it presents a quasi-shear vibration mode meaning that there is not only shear but longitudinal vibrations depending on the orientation of the c -axis. In this particular case, the piezoelectric AlN was tilted 35 degrees from the optical axis, therefore showing longitudinal and shear vibrations as expected.

4.3.5 Discussion and conclusions

The behaviour of a piezoelectric AlN microbalance was analyzed using the Mason model. Proteins deposition, as well as liquid media (water) were used as the natural media.

Results fit well with the expected outcome. The protein depositions (streptavidin) showed the dissipation added by the viscous load to the system as well as the attenuation of the quality factor Q . When in contact with water, the observed damping obey to the quasi-shear vibration mode being independent of the frequency shifts; the frequency shift is mainly dependent on elasticity and viscosity of the added layer, not on the water.

It was seen that the resonance frequency obtained with the macromodel for the AlN resonator presents a marked difference with the result found for the FEM model presented in this work for the unloaded microbalance. This difference (63.5%) may be due to the 1D nature of the Mason model compared with the 3D geometry used for the FEM model; while using only the c_{33} component of the elastic matrix for the Mason model, in the FEM model it is important the contribution of the whole elastic matrix.

4.4 PVDF pressure microsensor

Piezoelectric sensors have been widely used for force measurement due to its sensibility and low cost. These sensors generate electrical signals in response to the applied force working as dynamic force sensors. When used as static force sensors, the resulting charge flux and voltage decays to zero. Thus, the relaxation time depends of the material and size of the device, the electrical resistance of the external circuitry and the parasitic resistance of the sensor.

In order to overcome this problem, it was proposed several electronic circuits-based solutions to compensate charge loss.³⁵ To obtain a simpler device, it was used a physical parameter independent of the time: the resonance frequency of the piezoelectric sensor. Under this principle it has been developed excellent force sensors.^{36,37,38,39}

Piezoelectric polymers are a good option to develop piezoelectric-based acoustic wave devices, like the polyvinylidene fluoride (PVDF). Although there exist several works related with PVDF applications, the design and development of PVDF-based microdevices is mainly experimental.^{39,40,41} For flexible structures it is important to consider geometric nonlinearity, as is the case of the PVDF.⁴² The effect of a mechanical load on an structure such as the PVDF requires to consider not only geometric nonlinearity but electric nonlinearity (e.g. electrostriction^{43,44}). Therefore, simulation studies have become in a very important tool in order to decrease costs and improve the designs and functionalities.

In the work presented in this section, it was carried out the analysis of the behaviour of a PVDF piezoelectric sensor subjected to different amounts of pressure on its surface. A FEM model (section 3.4) was used to design and simulate the device performance for an FBAR, using PVDF polymers. Results were compared with those found in literature.

4.4.1 Design

A circular shape was adopted with the same diameter for the electrodes and the PVDF film. Dimensions of the device were chosen based on the most common dimensions used in different publications.^{27,28,29} The thickness of the crystal was chosen to produce a resonant frequency of around 45.8 MHz (Table 4.17). The effect of electrodes was neglected due to its small thickness and low acoustic impedance.

	Value	Unit
PVDF diameter	7	mm
PVDF thickness	10	μm

Table 4.17: Dimensions for the proposed PVDF pressure sensor.

4.4.2 FEM model

The equations from continuum mechanics to be used in this work are the balance of linear momentum and the kinematic relation between the infinitesimal generalized strain (strains proper plus rotations) and the displacement, namely:

$$\nabla \cdot \mathbf{T} + f^{\text{mech}} = \rho \frac{\partial^2 \mathbf{u}}{\partial t^2}$$

$$\mathbf{S} = \nabla^s \mathbf{u}$$

where f^{mech} is the elastic body force per unit volume, e.g. gravity, considered null for this case.

If uniaxial pre-stress is applied along the active strain direction of the piezoelectric device when working as a pressure sensor, the equilibrium equation presents the following form:

$$\rho \ddot{\mathbf{u}} = \nabla \cdot (\mathbf{T}_C + \mathbf{T}_0) \quad (4.4)$$

where the term \mathbf{T}_C correspond to the complete Cauchy stress tensor and \mathbf{T}_0 is the pre-stress tensor. This last term is introduced in this way to model devices working under pre-stress, thus helping to visualize the effect in the resonance frequency of the system.

The pre-stress \mathbf{T}_0 is introduced here for the following two reasons:

- (a) to model devices that work under mechanical bias, and
- (b) to appreciate the effect of pre-stresses in the natural frequencies.

It is convenient to use the so-called theory of ‘small displacements superposed upon large’ developed by Hughes, 1987⁴⁵, and also used by Aparicio y Pérez, 2004.⁴⁶ in which the pre-stress is regarded as a ‘geometric’ or ‘initial’ contribution to the stiffness. In this proposed approach, only the perturbation of the elastic constants are considered.

Applying this modification to the constitutive equation (1.39) (Hooke's Law) the modified elastic matrix can be expressed as follows:

$$\mathbf{T} = \mathbf{T}_C + \mathbf{T}_0 = \mathbf{c} \cdot \mathbf{S} + \mathbf{T}_0 = \mathbf{c}_{\text{modif}} \cdot \mathbf{S} \quad (4.5)$$

$$\mathbf{c}_{\text{modif}} = \mathbf{c} + \mathbf{1} \otimes \mathbf{T}_0 = \mathbf{c} + \mathbf{1} \otimes \mathbf{1P} \quad (4.6)$$

where \mathbf{P} is the pressure body force.

The elastic matrix \mathbf{c} is transversely isotropic for the PVDF resonator and the pre-stress tensor is isotropic due to the applied pressure body force. The latter has nonzero stress component only in direction normal to the main faces. Therefore, the modified elastic matrix has the following form:

$$\mathbf{c}_{\text{modif}} = \begin{bmatrix} c_{11} & c_{12} & c_{13} & 0 & 0 & 0 \\ c_{12} & c_{22} & c_{23} & 0 & 0 & 0 \\ c_{13} & c_{23} & c_{33} & 0 & 0 & 0 \\ 0 & 0 & 0 & c_{44} & 0 & 0 \\ 0 & 0 & 0 & 0 & c_{55} & 0 \\ 0 & 0 & 0 & 0 & 0 & c_{66} \end{bmatrix} + \begin{bmatrix} 0 & 0 & 0 & 0 & 0 & 0 \\ 0 & 0 & 0 & 0 & 0 & 0 \\ 0 & 0 & T_{33} & 0 & 0 & 0 \\ 0 & 0 & 0 & 0 & 0 & 0 \\ 0 & 0 & 0 & 0 & 0 & 0 \\ 0 & 0 & 0 & 0 & 0 & 0 \end{bmatrix} \text{Pa}$$

It was used a 3D piezoelectric elastic linear solid for the PVDF resonator. The electric potential was applied on both principal surfaces of the disc avoiding electrodes modeling; this simplifies the model and reduces simulation times without losing accuracy.

The elastic matrix \mathbf{c} , the piezoelectric coupling matrix \mathbf{e} and the dielectric coefficients matrix at constant strain $\boldsymbol{\varepsilon}$ are expressed as follows:

$$\mathbf{c} = \begin{bmatrix} c_{11} & c_{12} & c_{13} & 0 & 0 & 0 \\ c_{12} & c_{22} & c_{23} & 0 & 0 & 0 \\ c_{13} & c_{23} & c_{33} & 0 & 0 & 0 \\ 0 & 0 & 0 & c_{44} & 0 & 0 \\ 0 & 0 & 0 & 0 & c_{55} & 0 \\ 0 & 0 & 0 & 0 & 0 & c_{66} \end{bmatrix} \text{Pa}$$

$$\mathbf{e} = \begin{bmatrix} 0 & 0 & 0 & 0 & e_{15} & 0 \\ 0 & 0 & 0 & e_{24} & 0 & 0 \\ e_{31} & e_{32} & e_{33} & 0 & 0 & 0 \end{bmatrix} \frac{\text{C}}{\text{m}^2}$$

$$\boldsymbol{\varepsilon} = \begin{bmatrix} \varepsilon_{11} & 0 & 0 \\ 0 & \varepsilon_{22} & 0 \\ 0 & 0 & \varepsilon_{33} \end{bmatrix}$$

The three major axes are unique in the orthorhombic symmetry where the presence of three separate longitudinal diagonal terms and three separate shear diagonal terms are shown in the elastic matrix \mathbf{c} .

For the PVDF, values are showed in Table 4.18.²⁸ Even though the symmetric circular-shape of the film, the used constants were for uniaxial films considering the use of thickness mode.

c	[GPa]	e	[C/m ²]	ϵ_r	
c_{11}	3.70	e_{15}	-0.0159	ϵ_{11}/ϵ_0	12
c_{12}	1.47	e_{24}	-0.0127	ϵ_{22}/ϵ_0	12
c_{13}	1.23	e_{31}	0.0449	ϵ_{33}/ϵ_0	12
c_{22}	3.20	e_{32}	0.0129		
c_{23}	1.00	e_{33}	-0.0061		
c_{33}	1.51				
c_{44}	0.55				
c_{55}	0.59				
c_{66}	0.70				

Table 4.18: PVDF Matrix constants.

The normal stress at the boundaries was set null and an electric potential was applied on the disk top and bottom faces (Γ_g and Γ_e respectively) thus arriving at the following boundary conditions:

$$\begin{aligned} \sigma_n &= 0 && \text{on } \partial\Omega \\ \phi &= 0 && \text{on } \Gamma_g \\ \phi &= 1V && \text{on } \Gamma_e \\ \mathbf{D} \cdot \mathbf{n} &= 0 && \text{on } \partial\Omega \setminus (\Gamma_g \cup \Gamma_e) \end{aligned}$$

For the PVDF, the unknown variables were solved, i.e., the displacement (u_x, u_y, u_z) and the electric potential. Environment damping effects were neglected for the resonator and edges were fixed. Quadratic interpolation and 4th order integration were used.

The number of mesh elements was determined from the shape of the geometry and various mesh parameters; it was used a mesh with 45456 DOF. It was used a swept mesh structured in the sweep direction. The 3D mesh was created by extruding a 2D mesh into a 3D mesh; triangular elements in the 2D mesh were extruded into prism elements in the resulting 3D mesh.

The following simulations were performed: *i) Unloaded PVDF pressure microsensor*: The input impedance as a function of frequency for the piezoelectric resonator was obtained as well as the resonance frequency, *ii) PVDF pressure microsensor with pressure load*: The elastic matrix was modified using equation (4.5) for a pressure range between 0 MPa and 2.08 MPa. Frequency shifts were obtained, and *iii) Static analysis contrast*: It was carried out a pre-stress static analysis and changes in disk thickness was found; after that, it was carried out a harmonic analysis using the new thickness and was compared with the harmonic analysis using the modified elastic matrix.

i) Unloaded PVDF pressure microsensor

The resonance frequency was found to be in 6.801MHz. The modeling of this system is shown in Figure 4.24 where it is depicted the meshing used and the vibrational response

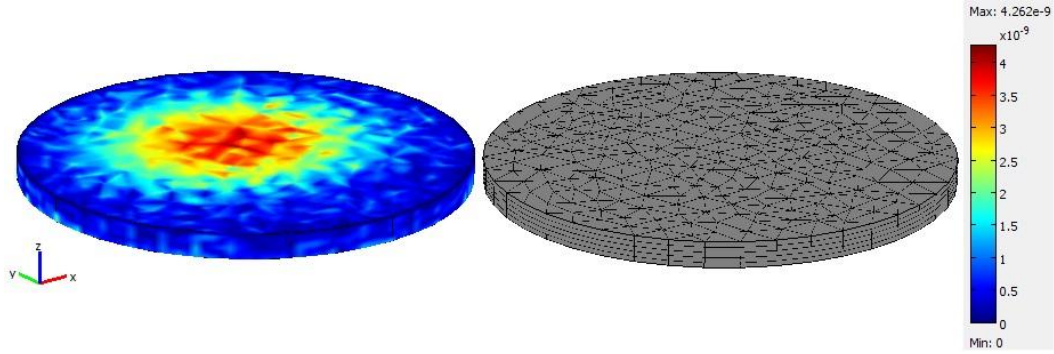


Figure 4.24: Vibrational response of the 10 μm -thickness PVDF pressure microsensor (left) and its meshing aspect (right).

ii) PVDF pressure microsensor with pressure load

The applied pressure range and the frequency shifts for the numerical model and experimental results are shown in the following table:

Pressure [MPa]	0	0.65	1.3	2.08
Simulated frequency shift [Hz]	0	1000	1500	2000
Experimental frequency shift [Hz]	0	80000	170000	270000

Table 4.19: Frequency shifts for numerical model and experimental results.

In Figure 4.25 it can be observed the admittance of the PVDF disk with an applied pressure of 0.65MPa ($f_r = 6.802$ MHz):

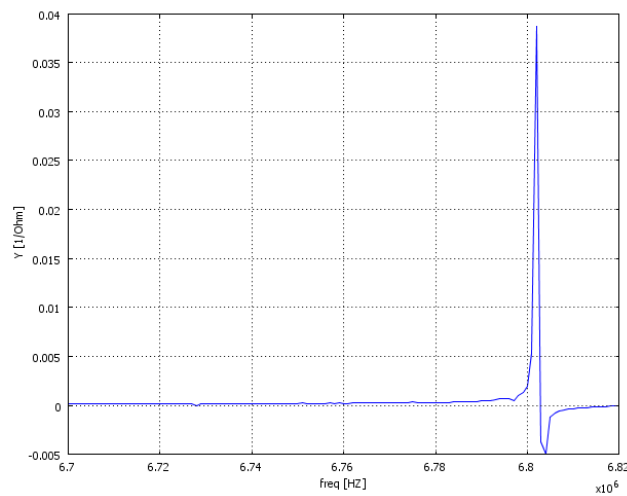


Figure 4.25: Resonance frequency of the PVDF disk for a pressure of 0.65MPa

iii) Static analysis contrast

It was carried out a static analysis of the disk for a pre-stress of 300 MPa as shown in Table 4.20:

Analysis type	Disk thickness [μm]	Elastic matrix	f_r [MHz]
Static+harmonic	94	\mathbf{c}	7.88
harmonic	110	\mathbf{c}_{modif}	7.05

Table 4.20: Results after the comparison between the two analyses: static+harmonic and harmonic.

4.4.3 Discussion and conclusions

Values obtained for the frequency shifts were validated with the results achieved with the comparison between the static+harmonic and harmonic analyses.

The resonance frequency for the 94 μm -thickness disk due to pre-stress was 7.88 MHz; this value is near to that of 110 μm -thickness using the modified matrix (7.05 MHz). As a result of this comparison, it was shown that the use of the modified matrix \mathbf{c}_{modif} is equivalent to static analysis and subsequent harmonic analysis but using the reduced thickness due to the 300 MPa-pre-stress.

The difference found may be due to the reduction only in one dimension, the thickness. It would be interesting using the real geometry deformed by pressure.

Using the FEM model it was obtained the expected frequency shift, showing a linear response of the shift vs. the applied pressure.

4.5 Bibliography

-
- ¹ M. Zalazar and F. Guarnieri, “Quartz Cristal Microbalance: Design and Simulation”, *Mecánica Computacional* Vol XXVIII, 2123-2136, 2009.
- ² M. Zalazar and F. Guarnieri, “Analysis and Evaluation of Piezoelectric Sensors Behaviour”, *Mecánica Computacional*, Vol XXIX, 6665-6684, 2010.
- ³ M. Pérez, M. Zalazar, N. Vottero, A. De La Plaza and F. Guarnieri, “A 13.56 MHz RFID Microtransponder for Active Micro-valve for the treatment of Glaucoma”, III Congreso de Microelectrónica aplicada, Facultad de Ciencias Exactas, Ingeniería y Agrimensura. Universidad Nacional de Rosario, Santa Fe, Argentina, 2012..
- ⁴ C. O’Sullivan, G. Guilbault, Commercial quartz crystal microbalances – theory and applications, *Biosensors & Bioelectronics*, 14:663–670, 1999.
- ⁵ D. Wu, Y. Tsai, Y. Yen, Robust design of quartz crystal microbalance using finite element and Taguchi method, *Sensors and Actuators B*, 92:337–344, 2003.
- ⁶ C. Kurosawa, et al., Computational Simulation of Vibration Displacement on Piezoelectric Quartz Crystal Using Finite Element Method, IEEE International Ultrasonics, Ferroelectrics, and Frequency Control Joint 50th Anniversary Conference, 2004.
- ⁷ V. Hung, et al., High-frequency one-chip multichannel quartz crystal microbalance fabricated by deep RIE, *Sensors and Actuators A*, 108:91–96, 2003.
- ⁸ V. Mecea, “From Quartz Crystal Microbalance to Fundamental Principles of Mass Measurements”, *Analytical Letters*, 38:753-767, 2005.
- ⁹ K. Kanazawa and Nam-Joon Cho, “Quartz Crystal Microbalance as a Sensor to Characterize Macromolecular Assembly Dynamic”, Hindawi Publishing Corporation, Journal of Sensors, 2009.
- ¹⁰ J. Yang, *Analysis of Piezoelectric Devices*, World Scientific Publishing Co. Pte. Ltd., 2006.
- ¹¹ J. Rosenbaum, *Bulk Acoustic Wave Theory and Devices*. Artech House, Inc., 2000.
- ¹² A. Shirinov and W. Schomburg, “Pressure sensor from a PVDF film,” *Sensors and Actuators A Physical*, vol. 142, no. 1, pp. 48–55, Mar. 2008.
- ¹³ J. Ketterling, O. Aristizábal, and D. Turnbull, “High-frequency piezopolymer transducers with a copper-clad polyimide backing layer”, *IEEE Trans Ultrason Ferroelect Freq Contr*, vol. 53, no. 7, pp. 1376–1380, Jul. 2006.
- ¹⁴ A. Arnau, *Piezoelectric transducers and applications*. Springer Verlag, 2008.
- ¹⁵ V. Granstaff and S. Martin, “Characterization of a thickness-shear mode quartz resonator with multiple nonpiezoelectric layers,” *Journal of Applied Physics*, vol. 75, no. 3, pp. 1319–1329, 1994.
- ¹⁶ H. Bandey, A. Hillman, M. Brown, and S. Martin, “Viscoelastic characterization of electroactive polymer films at the electrode/solution interface,” *Faraday Discussions*, vol. 107, pp. 105–121, 1997.
- ¹⁷ H. Bandey, S. Martin, R. Cernosek, and A. Hillman, “Modeling the responses of thickness-shear mode resonators under various loading conditions,” *Anal. Chem*, vol. 71, no. 11, pp. 2205–2214, 1999.
- ¹⁸ S. Martin, H. Bandey, R. Cernosek, A. Hillman, and M. Brown, “Equivalent-circuit model for the thickness-shear mode resonator with a viscoelastic film near film resonance,” *Anal. Chem*, vol. 72, no. 1, pp. 141–149, 2000.

-
- ¹⁹ M. Benetti, D. Cannata, F. Di Pietrantonio, V. Foglietti, and E. Verona, "Microbalance chemical sensor based on thin-film bulk acoustic wave resonators," *Applied Physics Letters*, vol. 87, no. 17, p. 173504, 2005.
- ²⁰ G. Wingqvist, Thin film electroacoustic devices for biosensor applications, p. 99, 2009.
- ²¹ G. Sharma, L. Liljeholm, J. Enlund, J. Bjurström, I. Katardjiev, and K. Hjort, "Fabrication and characterization of a shear mode AlN solidly mounted resonator-silicone microfluidic system for in-liquid sensor applications," *Sensors and Actuators A: Physical*, vol. 159, no. 1, pp. 111–116, 2010.
- ²² O. Myers, M. Anjanappa, and C. Freidhoff, "Designing piezoelectric interdigitated microactuators using comsol," in *COMSOL Conference*, Boston, MA, USA, 2008.
- ²³ V. Piefort, "Finite element modelling of piezoelectric active structures," Ph.D. dissertation, Université Libre de Bruxelles, 2001.
- ²⁴ A. Dobrucki and P. Pruchnicki, "Theory of piezoelectric axisymmetric bimorph," *Sensors & Actuators: A. Physical*, vol. 58, no. 3, pp. 203–212, 1997.
- ²⁵ O. Myers, "Modeling of a piezoelectric actuated planar capacitor actuator," in *COMSOL Conference*, Boston, MA, USA, October 22-26 2006.
- ²⁶ G. Petrone and G. Cammarata, *Modeling and Simulation*, ser. Systems Engineering. I-Tech Education and Publishing, 2008.
- ²⁷ Measurement Specialties, Inc., *Piezo Film Sensors-Technical Manual*, 1999.
- ²⁸ S. Sokhanvar, et al., "Investigating The Effect Of The Orthotropic Property Of Piezoelectric PVDF", *Transactions of the CSME/SCGM*, Vol. 31, No. 1, 2007.
- ²⁹ Y. Roh, V. Varadan, and V. Varadan, "Characterization of all the elastic, dielectric, and piezoelectric constants of uniaxially oriented poled PVDF films," *Ultrasonics, Ferroelectrics and Frequency Control, IEEE Transactions on*, vol. 49, no. 6, pp. 836–847, 2002.
- ³⁰ C. H. Chou, Y. C. Lin, J. H. Huang, N. H. Tai, and I. Lin, *Diamond Relat. Mater.* 15, 404 (2006).
- ³¹ M. Dubois and P. Muralt, *Appl. Phys. Lett.* 74, 3032 (1999).
- ³² J. Meinschen, G. Behme, F. Falk, H. Stafast, *Appl. Phys. A: Mater. Sci. Process.*, 69, 673 (1999).
- ³³ J. Bjurström, "Advanced Thin Film Electroacoustic Devices", p. 87, 2007.
- ³⁴ R. Cernosek, S. Martin, R. Hillman and H. Bandey, "Comparison of Lumped-Element and Transmission-Line Models for Thickness-Shear-Mode Quartz Resonator Sensors", *IEEE Transactions on Ultrasonics, Ferroelectrics, and Frequency Control*, vol. 45, n. 5, 1998.
- ³⁵ K. Park, R. Klafter, P. Bloomfield, "A charge readout algorithm for piezoelectric force transducers", *Applications of Ferroelectrics. 1986 Sixth IEEE International Symposium on* pp. 715—717, 1986.
- ³⁶ S. Bah, G. Quezel, P. Benech, L. Ngalamou, J. Legrand, "Effect of compressive stress on a composite resonator based on PVF2", *Ultrasonics Symposium, Proceedings, IEEE* 1992.
- ³⁷ L. Ngalamou, et al., "Analysis of the sensitivity and the temperature influence of a static force sensor based on a PVDF resonator", *Sensors and Actuators A*, vol. 57, pp. 173-177, 1996.
- ³⁸ P. Sekalski, A. Napieralski, M. Fouaidy, A. Bosotti, R. Paparella, "Measurement of static force at liquid helium temperature", *Measurement Science and Technology*, vol. 18, 2007.
- ³⁹ K. Shin, S. Lee, K. Min, D. Ko, J. Mun, "Methodology for Force Measurement Using Piezoelectric Ceramic", *World Congress on Medical Physics and Biomedical Engineering 2006*, pp. 853-856, 2007.
- ⁴⁰ A. Shirinov, W. Schomburg, "Pressure sensor from a PVDF film", *Sensors and Actuators A: Physical*, vol. 142, no. 1, pp. 48–55, 2008.

-
- ⁴¹ J. Ketterling, O. Aristizabal, D. Turnbull, “High-frequency piezopolymer transducers with a copper-clad polyimide backing layer”, *Ultrasonics, Ferroelectrics and Frequency Control, IEEE*
- ⁴² A. Mukherjee, and A. Saha Chaudhuri, “Piezolaminated beams with large deformations”, *International Journal of Solids and Structures*, vol. 39, pp. 4567-4582, 2002.
- ⁴³ J. Debus, B. Dubus, J. Coutte, “Finite Element Modeling of Lead Magnesium Niobate Electrostrictive Materials: Static Analysis”, *The Journal of the Acoustical Society of America*, vol.103, pp 3336, 1998.
- ⁴⁴ N. Goulbourne, E. Mockensturm, M. Freckerb, “Electro-elastomers: Large deformation analysis of silicone membranes”, *International Journal of Solids and Structures*, vol. 44, , pp. 2609-2626, 2007.
- ⁴⁵ T. Hughes, “The Finite Element Method. Linear Static and Dynamic Analysis”, Englewood Cliffs, NJ:Prentice-Hall, 1987
- ⁴⁶ J. Pérez-Aparicio and H. Sosa, “A continuum three-dimensional, fully coupled, dynamic, non-linear finite element formulation for magnetostrictive materials”, *Smart materials and structures*, vol. 13, pp. 493, 2004.

CHAPTER 5: Fabrication and Characterization

Experimental works is a very important stage in the research and development process. Experimental results permit the comparison with simulations results and therefore start the iteration method in order to find the best outcome.

This chapter deals with the fabrication and characterization of the piezoelectric proposed devices, previously designed and simulated as showed in the last chapter. In *Section 5.1* the PVDF resonator is presented and in *Section 5.2* the FEM-based parameter extraction from a PVDF resonator is presented as published by Zalazar et al. 2012.¹ *Section 5.3* describes the AlN resonator and *Section 5.4* the integration of AlN and UNCD films, based in the work done by Zalazar et al. 2012.² *Section 5.5* depicts the AlN FBAR on UNCD and *Appendix B* deals with the UNCD-based Drug Delivery Devices as presented by Zalazar et al. 2012^{3,4,5} in several congresses.

5.1 PVDF Resonator

Piezoelectricity can be obtained by orientating the molecular dipoles of polar polymers such as Polyvinylidene Fluoride in the same direction. The PVDF can be made piezoelectric because fluorine is much more electronegative than carbon. The fluorine atoms will attract electrons from the carbon atoms to which they are attached. The $-CF_2-$ groups in the chain will be very polar so when they are placed in an electrical field, they will align. Conversely, when the piezopolymer deforms, a macroscopic dipole appears.

This can be obtained by submitting the film of polymer to a sufficiently high electric field after a mechanical stretching. The obtained polarization is mainly due to the spatial rearrangement of polar segments of the macromolecular chains.

By machining the material in one or two perpendicular directions prior to the polarization process, different piezoelectric behaviours can be obtained (Figure 5.1). A uni-axial stretching will induce nearly unidirectional piezoelectric properties. A bi-axial stretching will induce piezoelectric properties that are isotropic in the plane.

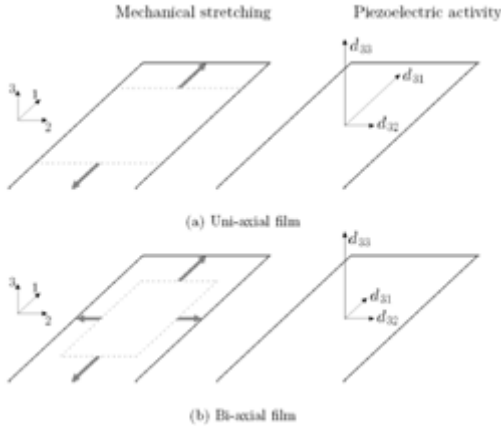


Figure 5.1: Unidirectional and bidirectional PVDF.

The aim of the experiments shown in this section is to obtain the frequency response of a PVDF-based piezoelectric resonator with copper and silver electrodes. To achieve this, it is necessary to carry out a frequency response analysis of the piezopolymer, thus measuring impedance and phase values, and finally obtaining the resonance frequency of the system.

5.1.1 Resonator fabrication

A disk-shaped piezoelectric was obtained from the commercial metallized PVDF piezoelectric film sheet (Measurement Specialties, <http://www.meas-spec.com/>) as shown in Figure 5.2. The piezopolymer is commercialized in metallized sheets of copper or silver. The PVDF resonator was chose to have a thickness of 110 μm .



Figure 5.2: Disk-shaped piezoelectric PVDF with silver ink electrodes.

Rolls of piezo film are produced in a clean room environment. The process begins with the melt extrusion of PVDF resin pellets into sheet form, followed by a stretching step that reduces the sheet. Stretching at temperatures well below the melting point of the polymer causes chain packing of the molecules into parallel crystal planes, called “beta phase”. To

obtain high levels of piezoelectric activity, the beta phase polymer is then exposed to very high electric fields to align the crystallites relative to the poling field.⁶

The circular disk has a diameter of 20mm and a thickness of 110 μm . Silver ink printed electrodes and copper electrodes were patterned with standard lithography on both sides of the disk. Printed inks have low sheet resistivity, high current density capability and are robust mechanically.⁷ The overlap between top and bottom electrode defines an active circular area of 490 mm^2 where the electrical signal for impedance measurements was applied through metal patterned PVDF arms. Table 5.1 shows these characteristics:

	Value	Unit
PVDF diameter	25	mm
PVDF thickness	110	μm
Electrode area	490	mm^2
Silver electrode thickness	6	μm
Copper electrode thickness	70	nm

Table 5.1: Dimensions for the PVDF disk-shaped resonator with silver ink electrodes.

Screen printed electrodes of conductive silver ink have a thickness of 6 μm meanwhile copper metallization is made by sputtering technique, having a thickness of 70 nm.

5.1.2 Characterization

The piezoelectric sensor behaves like a series RLC resonator circuit. At resonance frequency the impedance changes its magnitude, therefore measuring the electric potential will give the wanted response. A faster and easier way to achieve it is by using an Impedance Gain-Phase Analyzer device.

One port electrical characterization was performed with a Precision Impedance Analyzer (Solartron Impedance / Gain-Phase Analyzer) by measuring the absolute impedance value as a function of frequency. Custom polyamide fixation was used to make a proper contact to the surface of the electrode arms and to provide the clamped mechanical boundary conditions as is depicted in Figure 5.3 (left). The admittance measurement was obtained in the frequency range of 2-10 MHz in order to excite the thickness mode resonance frequency. Thickness modes are the so-called high frequency modes whose frequencies are determined by the plate thickness, the smallest dimension.⁸ In this case the electric field is in the direction of the acoustic wave propagation. The connection of the system can be seen in Figure 5.3 (right).



Figure 5.3: Custom polyamide setup (left) and system connection (right).

In order to characterize these resonator disks, i.e., Ag/PVDF/Ag and Cu/PVDF/Cu, several experiments were performed using different dimensions and electrode material. A qualitative analysis of the obtained results was done.

A. Cu electrode vs. Ag electrode

The frequency responses (admittance vs. frequency) for two resonator disks were obtained using copper and silver electrodes. It was applied a voltage signal of 1 V and a frequency sweep between 7-12 MHz was used at room temperature. Results are shown in Figure 5.4:

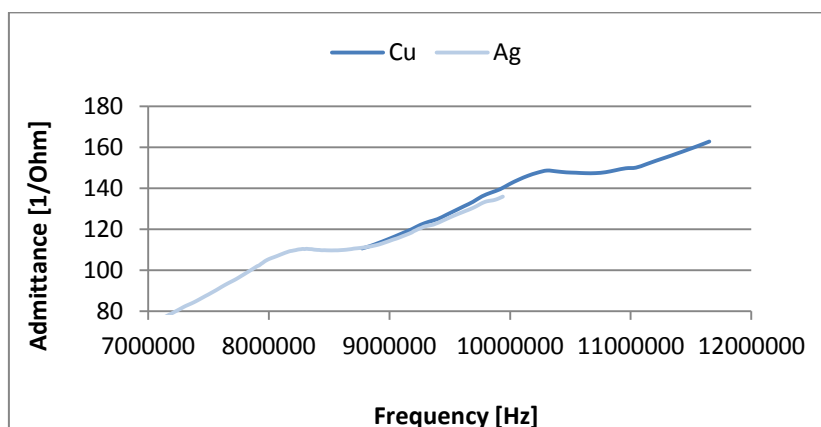


Figure 5.4: Cu-electrode PVDF vs. Ag-electrode PVDF.

It is clear to see that the PVDF resonant disk with silver electrodes has a lower resonance frequency than the one with copper electrodes. As predicted by Sauerbrey equation, this lower frequency is due to the thicker thickness of the silver electrode, thus producing a shift in the frequency response of the resonator compared with the disk with copper electrodes.

B. Thin film deposition

In this experiment, it was deposited on one face of the disk, a rigid thin film of photoresist. Photoresist AZ 1500 was deposited by spinning and subsequent soft bake on a hot plate. It

was used a copper-electrode disk and the frequency response obtained with photoresist deposition was contrasted with the unload disk. It was applied a voltage signal of 1 V and a frequency sweep between 8-13 MHz was used at room temperature. Results are shown in Figure 5.5:

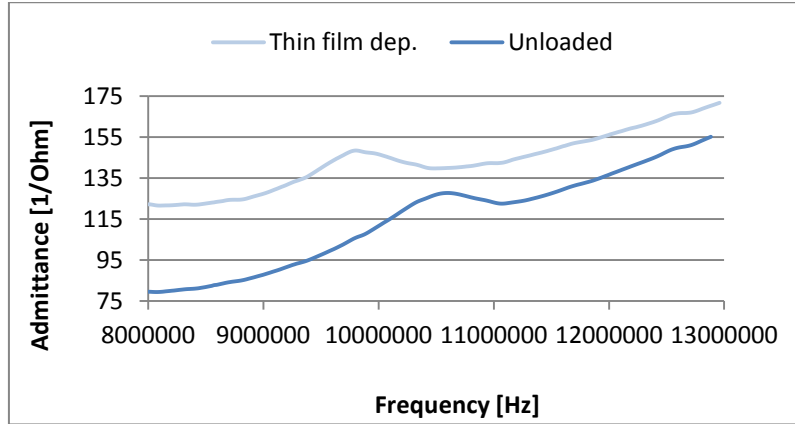


Figure 5.5: Comparison between unloaded copper-electrode disk and with photoresist thin film deposition.

As shown in the previous example, the unloaded PVDF disk has a lower resonance frequency than the disk with film deposition. Therefore, the frequency shift is predicted by the Sauerbrey equation.

C. Disk diameter effect

It was compared the effect caused by the use of two different disk diameters (20 mm and 25 mm). The smaller one presents an active circular area of 314 mm². It was used silver-electrode disk. It was applied a voltage signal of 1 V and a frequency sweep between 5-11 MHz was used at room temperature. Results are shown in Figure 5.6:

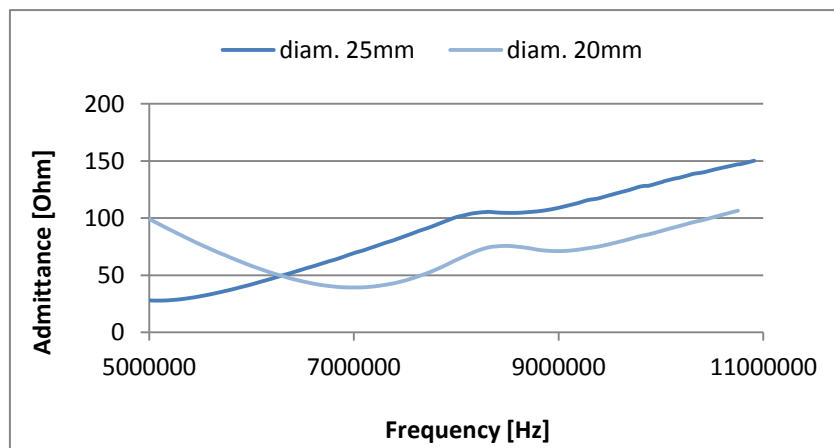


Figure 5.6: Effect caused by the use of two different disk diameters (20 mm and 25 mm).

The smaller resonator disk presents a more marked change in the frequency response. It may be due to the lower energy needed to excite the resonator because of the lower mass.

5.1.3 Conclusions

It is shown that simulations done in the previous chapter are in a good agreement with the experimental results showed in this section. The frequency shift predicted by the Sauerbrey equation is evidenced in the comparison between the unloaded PVDF disk and the disk with film deposition. In the same manner, it is clear to see that the PVDF resonant disk with silver electrodes has a lower resonance frequency than the one with copper electrodes.

5.2 FEM-Based Parameter Extraction of a PVDF Resonator

A PVDF film under an electric field with controlled temperature after a mechanical stretch shows very strong piezoelectric and pyroelectric properties.^{9,10} Thin piezoelectric films can also be obtained using Soft Lithographic techniques by casting and poling¹¹ allowing compatibility with MEMS technology.

Even though there are several works involving PVDF applications, the design and development of PVDF devices is usually done by experiments.^{12,13} In this sense, computer simulation tools have been largely used in order to improve not only the design but also the functionality of the piezoelectric device. In addition it will help reducing time therefore improving solutions.

FEM is a flexible method capable of modeling complicated device geometries, nonuniform materials properties and quite general boundary conditions. Various designs used in piezoelectric actuation and sensing devices were carried out using FEM models, e.g., microactuator models regarding piezoelectric and electrodes geometric characteristics,¹⁴ different piezoelectric structures^{15,16} and a circular multi-material plate model for micro-fluidic applications.¹⁷ Moreover, FEM analysis of a bulk acoustic wave resonator using 3D linear models was presented in a book.¹⁸

The needed parameters to fulfill the FEM model for the PVDF material have to be extracted from experiments. However this parameters extraction is not an easy task and there exist different methods. Lahmer et al. 2008¹⁹ introduced an optimized algorithm to obtain parameters from FEM-based models for piezoceramics. The values accuracy obtained thus depend on the method and material used. In addition, due to the PVDF visco-elastic nature, these parameters are extracted in a certain frequency and temperature range thus limiting its usefulness.

In this section, the parameters of a PVDF disk resonator were obtained from experimental and 3D FEM model. The experimental frequency response (impedance vs. frequency) of a PVDF disk was obtained. The elastic, dielectric and piezoelectric properties of PVDF piezoelectric polymer obtained from literature experimental data were used to fulfill the FEM model; the values were adjusted to fit the simulated frequency response with the experimental one. The obtained values thus were used to characterize the PVDF disk obtaining a set of valuable parameters as is the case of the electromechanical coupling constant k_t and the quality factor Q . In addition, the frequency responses for the resonator using two different types of metal electrodes were compared.

5.2.1 Materials and Methods

A. Fabrication

A disk-shaped piezoelectric was obtained from a commercial metallized PVDF piezoelectric film sheet (Measurement Specialties, Inc.) as shown in Figure 5.7. The circular disk has a diameter of 20 mm, a thickness of 110 μm and a density of 1800 kg/m^3 . Silver ink printed electrodes were patterned with standard lithography on both sides of the disk. Printed inks have low sheet resistivity, high current density capability and are robust mechanically.²⁰ The silver ink printed electrode has a thickness of 6 μm and a density of 4000 kg/m^3 . The overlap between top and bottom electrode defines an active circular area of 314 mm^2 where the electrical signal for impedance measurements was applied through silver patterned PVDF arms.

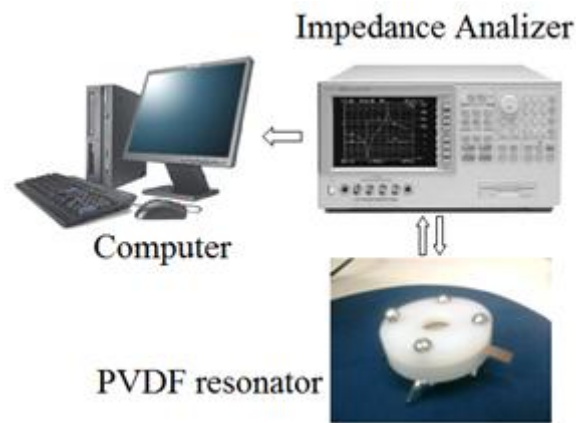


Figure 5.7: PVDF resonator experiment setup.

B. Electrical characterization

One port electrical characterization was performed with a Precision Impedance Analyzer (Agilent 4294A) by measuring the absolute impedance value as a function of frequency (Figure 5.7). Custom polyamide fixation was used to make a proper contact to the surface of the electrode arms and to provide the clamped mechanical boundary conditions. The impedance measurement was obtained in a frequency range of 2-10 MHz with a frequency sweep (resolution) of 30 kHz in order to excite the thickness mode resonance frequency. Thickness modes are the so-called high frequency modes whose frequencies are determined by the plate thickness, the smallest dimension.²¹ In this case the electric field is in the direction of the acoustic wave propagation.

C. FEM model

The PVDF has orthorhombic symmetry (mm2 class) and is usually operated in thickness mode. A 3D piezoelectric elastic linear solid was implemented for the PVDF and a 3D elastic linear isotropic solid was used to model the silver ink electrodes.

The elastic matrix \mathbf{c} , the piezoelectric coupling matrix \mathbf{e} and the dielectric coefficients matrix at constant strain $\boldsymbol{\varepsilon}$ are expressed as follows:

$$\mathbf{c} = \begin{bmatrix} c_{11} & c_{12} & c_{13} & 0 & 0 & 0 \\ c_{12} & c_{22} & c_{23} & 0 & 0 & 0 \\ c_{13} & c_{23} & c_{33} & 0 & 0 & 0 \\ 0 & 0 & 0 & c_{44} & 0 & 0 \\ 0 & 0 & 0 & 0 & c_{55} & 0 \\ 0 & 0 & 0 & 0 & 0 & c_{66} \end{bmatrix} \text{Pa}$$

$$\mathbf{e} = \begin{bmatrix} 0 & 0 & 0 & 0 & e_{15} & 0 \\ 0 & 0 & 0 & e_{24} & 0 & 0 \\ e_{31} & e_{32} & e_{33} & 0 & 0 & 0 \end{bmatrix} \frac{\text{C}}{\text{m}^2}$$

$$\boldsymbol{\varepsilon} = \begin{bmatrix} \varepsilon_{11} & 0 & 0 \\ 0 & \varepsilon_{22} & 0 \\ 0 & 0 & \varepsilon_{33} \end{bmatrix}$$

The three major axes are unique in the orthorhombic symmetry where the presence of three separate longitudinal diagonal terms and three separate shear diagonal terms are shown in the elastic matrix \mathbf{c} .

COMSOL Multiphysics finite element analysis software environment was used for the modeling and simulation of the PVDF disk. Environment damping effects were neglected for the resonator and edges were fixed. Quadratic interpolation and prism elements in the discretization and 4th order integration were used. The normal stress (σ_n) at the boundaries was set null and the electric potential (ϕ^e) was applied on the PVDF disk top and bottom faces (Γ_g and Γ_e respectively) thus arriving at the following boundary conditions:

$$\sigma_n = 0 \quad \text{on } \partial\Omega$$

$$\phi = 0 \quad \text{on } \Gamma_g$$

$$\phi = \phi^e \quad \text{on } \Gamma_e$$

$$\mathbf{D} \cdot \mathbf{n} = 0 \quad \text{on } \partial\Omega \setminus (\Gamma_g \cup \Gamma_e)$$

In this software, harmonic excitation loads were specified and assumes harmonic response with the same angular frequency as the excitation load. The frequency response analysis was done with a parametric solver. It performs a frequency sweep over several excitation frequencies.

In this case of harmonic excitation, the damping nature of the PVDF resonator was taken into account. Thus, the complex values of the material parameters were entered in the elastic, dielectric and piezoelectric matrices in the FEM model.

For the PVDF material, the unknown variables were solved. Silver ink electrodes were modeled similarly solving the displacements variables in the three directions. The resonator works in thickness excitation mode where the electric field is in direction of acoustic wave propagation. The equivalent impedance of the resonator versus frequency was obtained in a frequency range of 6-10 MHz with a resolution of 5 kHz. For the electrodes, two disks with the same diameter of the PVDF were situated one each on top and bottom of the piezoelectric disk.

D. Parameter Identification

Some researchers have been working on characterizing and modeling PVDF fitting the parameters of Mason's model instead of FEM models.^{22,23} In this work, the constitutive piezoelectric, dielectric and elastic parameters were obtained by fitting FEM-based simulation with experimental data obtained from PVDF samples.

Initially, the first parameters used in the FEM model were obtained from the literature⁹ (Table 5.2). The constitutive parameters given in the manufacturer's datasheet of the PVDF sheets (Measurement Specialties, Inc., Norristown, USA) were incomplete (or based on 1D models). A FEM based inverse method was formulated in order to obtain the 3D parameters. These experimental parameters are complex, i.e. all nine complex elastic stiffness constants, the three complex dielectric constants and all five complex piezoelectric constants.

Values obtained from the literature⁹ were extracted as a function of frequency in the range of 200-600 kHz. Because of the high resonance frequency of the PVDF thickness mode resonator, values obtained for the highest frequency (600 kHz) were used as shown in Table 5.2:

c	[GPa]	e	[C/m ²]	ϵ_r	
c_{11}	$3.69 + 0.12i$	e_{15}	$-0.0105 - 0.0045i$	ϵ_{11}/ϵ_0	$6.3 + 1.9i$
c_{12}	$1.64 + 0.053i$	e_{24}	$-0.0100 - 0.0036i$	ϵ_{22}/ϵ_0	$7.9 + 1.75i$
c_{13}	$1.445 + 0.055i$	e_{31}	$0.0092 + 0.0051i$	ϵ_{33}/ϵ_0	$7 + 1.4i$
c_{22}	$3.155 + 0.112i$	e_{32}	$-0.0109 - 0.0021i$		
c_{23}	$1.335 + 0.04i$	e_{33}	$-0.0236 - 0.0095i$		
c_{33}	$1.617 + 0.127i$				
c_{44}	$0.549 + 0.0295i$				
c_{55}	$0.591 + 0.03i$				
c_{66}	$0.697 + 0.0175i$				

Table 5.2: PVDF matrix constants.

The piezoelectric PVDF disk was poled in the thickness direction meaning that it is strongly piezoelectric in that direction while the effect is smaller in the other directions of propagation. Thus, the electromechanical coupling constant of the piezoelectric device is:²⁴

$$k_{33}^t = \sqrt{\frac{e_{33}^2}{\epsilon_{33}c_{33}}} \quad (5.1)$$

where the coupling constant k_{33}^t is a measure of how strongly the electrical potential and mechanical displacements associated with a wave interact.

E. Cu electrodes

The frequency response of a PVDF piezoelectric resonator using Cu electrodes instead of silver ink was obtained in order to compare both electrodes performances. The same geometry and setup were used in the experiments in a frequency range of 7-13 MHz and the properties of the Cu (thickness of 70 nm and density of 8700 kg/m³) were used to fulfill the FEM model.

5.2.2 Results and Discussion

The first simulated frequency response (impedance vs. frequency) of the PVDF resonator using the constants above mentioned were obtained as depicted in Figure 5.8.

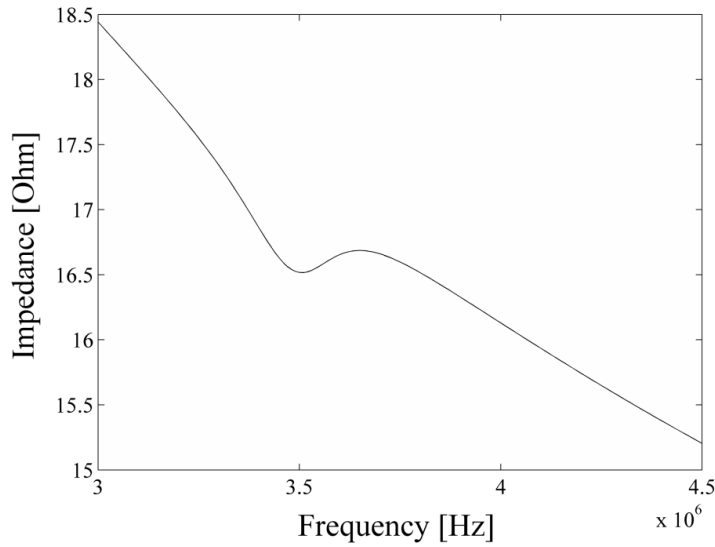


Figure 5.8: Frequency response of the PVDF resonator using the initial set of parameters.

After the first simulated result, a reduced set of material constants values were varied in order to fit with the experimental frequency response. The fitted impedance values of the frequency response were obtained for a frequency range close to resonance and antiresonance frequencies. These reduced set of material constants are the ones used in the 1D models for a piezoelectric resonator (analytical model, lumped elements model and Mason model). Each parameter was modified manually in order to reduce the difference (error) between the experimental and simulated frequency response until the error was lower than 3% of the impedance (Table 5.3).

Tuning parameter	Iteration number	Error (exp vs simulated)
$c_{33}, e_{33}, \epsilon_{33}/\epsilon_0$	1	>100%
$c_{33}, e_{33}, \epsilon_{33}/\epsilon_0$	2	>50%
$c_{33}, e_{33}, \epsilon_{33}/\epsilon_0$	10	<3%

Table 5.3: FEM-based parameter extraction (inverse method) showing the tuned parameters, the iterations done and the error found.

The obtained values are shown in Table 5.4:

c	[GPa]	e	[C/m ²]	ϵ_r	
c_{33}	$8.63 + 0.85i$	e_{33}	$-0.079 - 0.0i$	ϵ_{33}/ϵ_0	$7 + 3.95i$

Table 5.4: Material constants extracted from curve fitting.

As a final step, the rest of the constants were varied and the experimental frequency response was fitted. In Figure 5.9, the fitting result including both curves is depicted.

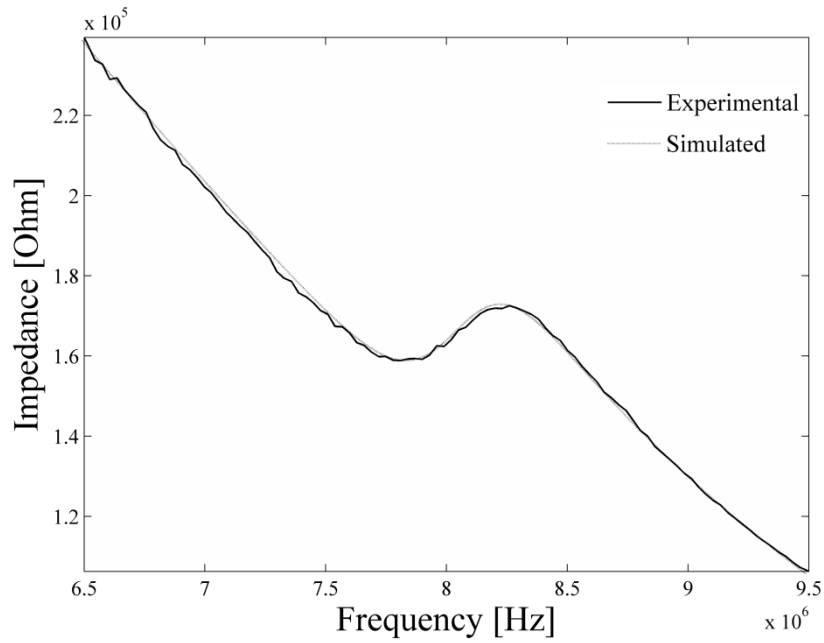


Figure 5.9: Experimental and simulated frequency response of the PVDF resonator with silver ink printed electrodes.

The simulation of the system is shown in Figure 5.10 where is depicted the vibrational response of the resonator; in the picture it can be observed the thickness vibration (d_{33}) in direction normal to the main faces due to the polarization process in the fabrication step.

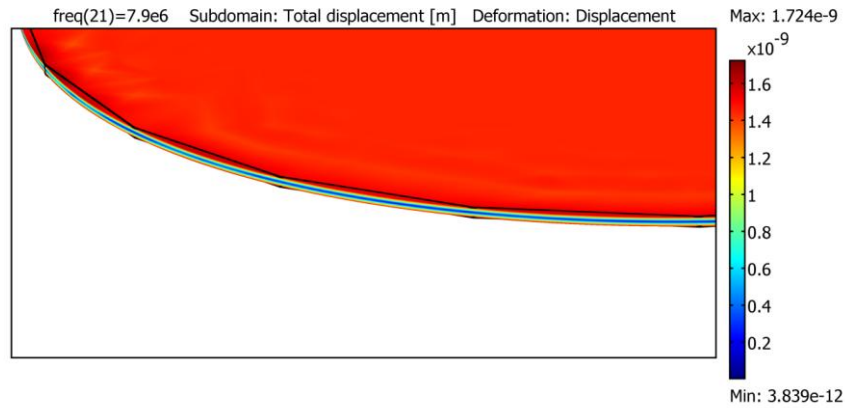


Figure 5.10: Vibrational response of the 110 μm thickness PVDF.

The resonator theory described in the *IEEE Standard on Piezoelectricity*²⁵ applies to ideal lossless materials, in which case the resonator impedance is purely reactive and the characteristic frequencies f_1 and f_2 are well defined as the impedance minima and maxima, respectively. The dissipation present in this kind of materials makes hard the definition of these frequencies. Hence the critical frequencies f_1 and f_2 each have three associated frequencies, f_1 (f_m, f_s, f_r) and f_2 (f_n, f_p, f_a) corresponding to maximum absolute admittance (impedance), maximum conductance (resistance), and zero susceptance (reactance), respectively, where f_s is the series resonance frequency, f_p the

parallel resonance frequency, f_r the resonance frequency and f_a the antiresonance frequency. When the figure of merit is not $M \gg 1$ (not small effective coupling factor k_{eff}) due to the lossy nature of the material properties, the relations among the frequencies f_m, f_s, f_r, f_p, f_a and f_n ²⁶ are not exact, thus f_p and f_s cannot be measured accurately.

Taking into account the extracted parameters, the electromechanical coupling factor of the resonator (Eq. (5.1)) is $k'_{33}=10.8\%$ while the quality factor is $Q=Real(c_{33})/Im(c_{33})=10.15$. The figure of merit of the resonator is $M=Q/r$, where r is the capacitance ratio as a function of the obtained k'_{33} ; the figure of merit thus obtained is $M=0.096$. f_m and f_n values corresponding to maximum absolute admittance and impedance respectively, are $f_m=8.23\text{MHz}$ and $f_n=7.84\text{MHz}$.

On the other hand, the experimental frequency response of the PVDF resonator with Cu electrodes was obtained. In this case, $f_m=10.13\text{MHz}$ and $f_n=9.69\text{MHz}$. This frequency response fitted good with the simulated values using the properties of the Cu in the FEM model. Figure 5.11 shows a comparative image of the simulated frequency response of the resonator for both, Cu and Ag electrodes.

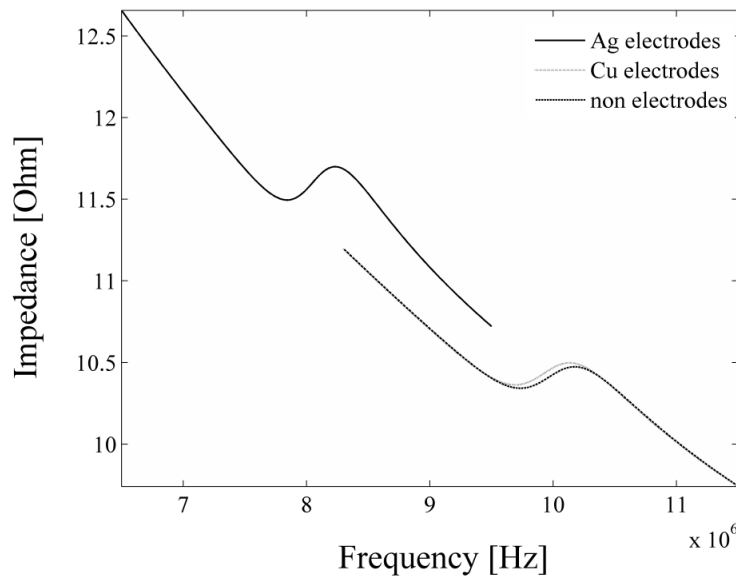


Figure 5.11: Experimental and simulated frequency response of the PVDF resonator for Cu and silver ink electrodes in addition to the electrodeless case.

Using Cu electrodes, it can be shown that the resonance frequency grows up. This change appears because of the decrement in the surface load due to the thinner electrode as predicted by the Sauerbrey equation (Eq. (3.1)); as shown, this equation relates the change in the resonance frequency with the deposited mass on the surface of piezoelectric resonator:

$$\Delta f_r = -\frac{2f_r^2 \rho_s}{\sqrt{\rho_p c_p}}$$

where Δf_r is the frequency shift, ρ_s is the mass per area of the deposited layer, ρ_p is the density of the piezoelectric material and c_p the elastic constant (c_{33} for the piezoelectric PVDF). This equation was used to calculate the analytical frequency shift between the resonance frequencies of the resonator with Cu electrodes and the one with Ag. It can be shown that there exists a shift of 2.237 MHz between these two cases, considering the simulated resonance frequency for the electrodeless case as reference. The calculated frequency shift from the simulated results yields a value of 1.9 MHz. The difference found between these two values is mainly due to the nature of the Sauerbrey equation being for quartz crystal piezoelectric materials (thickness shear vibrating quartz crystal resonator, having AT or BT cut). Also, this difference could be because of the mass loading causing a non linear frequency shift due to the elastic loss within the deposited film.

Therefore, changing the acoustic properties at the interface between the PVDF and the electrode will produce a change in the frequency response of the system as seen in the difference found between the frequency responses for both resonators. In addition, it can be seen that the impedance magnitude decrease. This is due to the decrease in the surface load mechanical impedance due to the small thickness of the Cu electrode film although mass density of Cu is larger than that of Ag.

Energy trapping concept is related with the generated standing acoustic waves confined in the existing region between electrodes. When the thickness of the electrode is too thin, as in the case of these Cu electrodes, the resonant frequencies of regions with and without electrodes are very similar, thus the acoustic wave is not confined to the electrode-covered region, and as a consequence the quality factor Q of the resonator decreases.²⁷ This reduction in the quality factor appears as an increment in the width of the frequency response. The small thickness of the Cu also produces an increment in the electrode resistivity thus adding electrical loading.

5.2.3 Conclusions

This work presented the extracted parameters of a PVDF disk resonator from experimental and 3D FEM model. The values were adjusted to fit the simulated frequency response with the experimental one and the obtained values were used to characterize the PVDF disk. A set of useful constants were extracted from the curve fitting of the frequency response of the PVDF resonator by tuning the complex material parameters in the FEM model.

The values of k_{33}^t and Q have demonstrated to be in agreement with the datasheet of the material. The FEM model has demonstrated to be a reliable tool for modeling and simulate

non trivial geometries including materials with high internal viscoelastic losses such as the case of PVDF. It also was found to be an important tool for extracting valuable information from experimental data.

The agreement of the extracted values with the datasheet of the material reveals a good accuracy for the developed procedure. It motivates the application of the FEM model for modeling the performance of the PVDF as a thickness mode resonator.

5.3 AlN Resonator

Piezoelectric materials are being used for a variety of applications including defense, robotics and biomedical devices. For the latter and if the piezoelectric material is going to be implanted in the human body as it occurs with ultrasound transducers or cochlear implants, an important requirement is that the material needs to be biocompatible. It would be desirable to have a biocompatible piezoelectric material, thus avoiding the need for packaging that represents a significant portion of the cost to the device. In this regard, AlN has emerged as an attractive alternative to other piezoelectric materials (such as PZT that contains lead) as have been shown by several authors.^{28,29}

Aluminum Nitride is a very attractive piezoelectric material for use in BioMEMS due to the excellent properties commented previously. AlN is most often in the Wurtzite hexagonal crystallographic system around the c-axis which is also the direction with the highest piezoelectric constant in addition to a high acoustic wave velocity.

Regarding the crystal structure of the AlN, there are two main crystallographic orientations that provide piezoelectric behaviour. The crystallographic orientation (002) has the highest piezoelectric constant and has a diffraction peak in 36° while the crystallographic orientation (100) has the diffraction peak in 33° .

In this section it was carried out the deposition of AlN on silicon substrate. Platinum was used as bottom electrode with titanium as an adhesion layer. Deposition processes were carried out in a clean room facility (CNM, Argonne National Laboratory, USA)

5.3.1 Deposition process

The Pt layer was grown by magnetron sputter deposition on top of a Ti film deposited on the SiO₂ surface as an adhesion layer. The Pt bottom electrode was grown by sputter deposition (AJA ATC Orion thin film deposition system). The Ti film provides an adhesion layer for growing highly c-axis (002) oriented AlN films. Films were deposited with a target RF power of 150W, pressure of 3 mTorr, Ar flow rate of 26sccm and base pressure of 1e-7 Torr. The thicknesses of the Platinum and Titanium were 150nm (720s deposition) and 10nm (310s deposition) respectively. In addition, this coating provides seeding capability and serves as a buffer layer, lowering the discrepancy in lattice parameter between substrate and film.

The Pt layer will serve as bottom and top electrode to apply voltage to excite the piezoelectric effect on the AlN layer for actuation of MEMS devices. An scheme of the proposed piezoelectric heterostructure is shown in Figure 5.12.



Figure 5.12: Scheme of the heterostructure of AlN/Pt/Ti/SiO₂/Si.

AlN (002) oriented films were grown on the Pt layers at different temperatures, using reactive sputter deposition (AJA ATC Orion thin film deposition system), via sputtering material from an Al metallic target, using an Ar-plasma to produce Ar ions to sputter the Al material in a N₂ atmosphere to provide the nitrogen needed to produce the AlN films. Aluminum target with a diameter of 2" and a purity of 99.999% was used. The sputtering deposition system is shown in Figure 5.13.



Figure 5.13: AJA ATC Orion thin film deposition system.

There were performed several experiments until reach to the crystallographic orientation (002) of the AlN with the diffraction peak in 36°. AlN layers with thickness in the 260-420 nm range were synthesized on silicon oxide (SiO₂) and silicon nitride (Si₃N₄) were used as intermediate layer grown on Si.

5.3.2 Characterization

An easier way to know the crystalline structure of a material and its preferential orientation is by using X-ray diffraction (XRD). It is a nondestructive technique that reveals detailed information of the chemical composition and the crystalline structure of a material. Atoms in a material are organized in a tridimensional arrangement forming a series of parallel planes separated by a distance that depends of the nature of the material. When a monochromatic X-ray beam is projected on the material, it is obtained a diffraction pattern according to the Bragg's Law:

$$n \lambda = 2 d \sin(\theta) \quad (5.2)$$

where λ is the wavelength X-ray beam, d is the distance between atomic crystal layers, θ is the incidence angle and n is an entire.

A. SiO_2/Si substrate

The used silicon wafers were a N-type mirror polished Si (100). In Table 5.5 it is described the used parameters and the XRD spectra are shown in Figure 5.14.

Substrate	Growth parameters							
	Power DC [W]	Ar [sccm]	N_2 [sccm]	T° [C]	Time [s]	P [mTorr]	Sputt. Machine	Notes
Pt/Ti/SiO ₂	150	3	20	500	10800 (3h)	3	CNM lab	Pt: 150nm- Ti: 10nm

Table 5.5: Deposition parameters for the AlN/Pt/Ti/SiO₂/Si heterostructure.

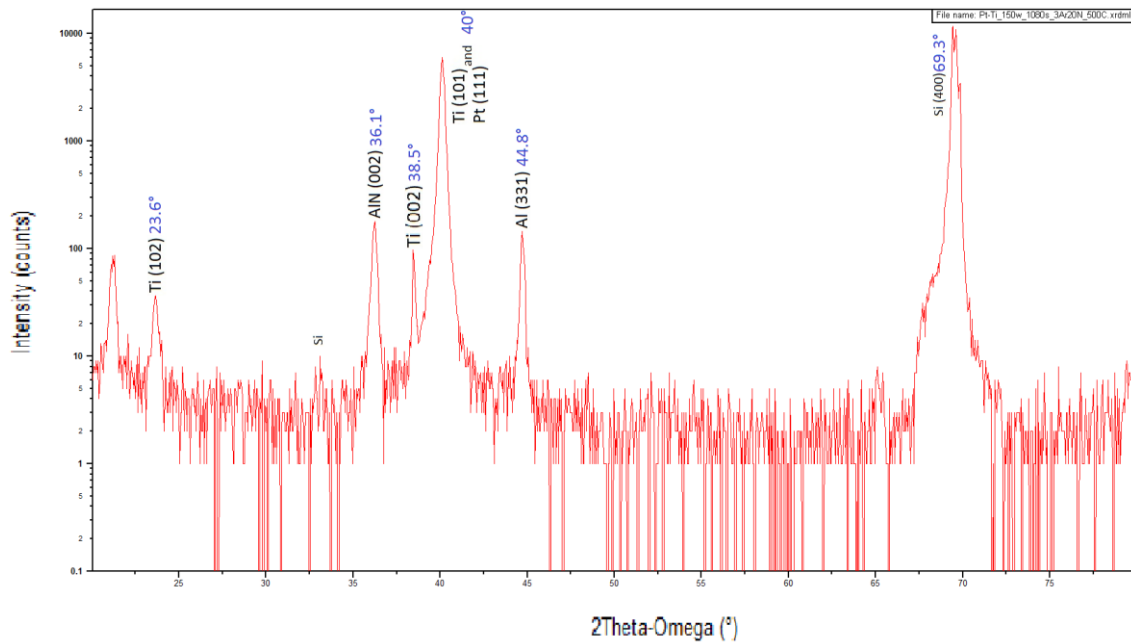


Figure 5.14: XRD spectrum of an AlN/Pt/Ti/SiO₂/Si heterostructure showing the characteristic peaks of the Pt and Ti layers and the Si substrate, in addition to the critical AlN (002) peak that reveals the high orientation of AlN necessary to yield the high piezoelectric coefficient measured for these films.

The XRD $2\theta/\omega$ diffraction pattern taken from the XRD analysis of the AlN/Pt/Ti/SiO₂/Si multilayer was scanned between 20° and 80°. Figure 5.14 shows an XRD $2\theta/\omega$ scan of the AlN/Pt/Ti/SiO₂/Si layered film exhibiting high c-axis orientation for the AlN film. It is noted the presence of hexagonal AlN (002) diffraction peak at 36.1° (note the logarithmic scale) in addition to the spurious Si diffraction peak at 33.1° (not to confuse with the AlN(100) diffraction peak at 33.1°). These results reveal the presence of mainly a (002) textured AlN film. It is also shown the diffraction peaks of Pt (111) at 40° and Ti (002) at

38.5° of the electrode and a peak for the Al (331) at 44.8°. The latter indicates the presence of an amount of Al that has not been nitrided.

As pointed out previously, there were performed several experiments until reach to the crystallographic orientation (002) of the AlN. Table 5.6 sums up these experiments:

Bid	SUBSTRATE	TARGET POWER [W]	PRESSURE [Torr]	Ar sccm	N2 sccm	TIME [h]	Temp. [C]	POS.	ANGLE	RESULTS [peaks]	Date	Note
MSD	Pt/TiAl/SiO2/Si	Al	50	5,00E-03	6	4	1	450	44	0.15 33 - 41.5 - 45 - 48 - 69		33 could belong to Si?
MSD	Pt/TiAl/SiO2/Si	Al	50	5,00E-03	6	2	2	450	40	0.15 33 - 41.5 - 48 - 69		
MSD	Pt/TiAl/SiO2/Si	Al	50	5,00E-03	6	6	1	450	40	0.15 33 - 41.5 - 48 - 69		
MSD	Pt/TiAl/SiO2/Si	Al	50	5,00E-03	6	6	1	350	40	0.15 33 - 41.5 - 48 - 69		dep #4
MSD	Pt/TiAl/SiO2/Si	Al	100	5,00E-03	6	6	1	450	40	0.15 41.5 - 48 - 69		41.5 and 48 very wide
MSD	Pt/TiAl/SiO2/Si	Al	50	5,00E-03	6	6	1	350	40	0.15 38.5 - 41.5 - 45 - 48 - 65 - 69		Repeated dep #4
MSD	Si	Al	50	5,00E-03	6	6	1	350	40	0.15 38.5 - 45 - 65 - 69		Repeated dep #4
MSD	Pt/TiAl/SiO2/Si	Al	100	5,00E-03	6	6	1	450	40	0.15 38.5 - 45 - 69		substrate characterization
MSD	Si	Al	100	5,00E-03	6	6	1	450	40	0.15 38.5 - 45 - 69		substrate characterization
CNM	Si	Al	100	5,00E-03	15	10	1	350		33 - 69	11 10 11	#1
CNM	Pt/TiAl/SiO2/Si	Al	100	5,00E-03	15	10	1	350		38.5 - 41.5 - 45 - 48 - 69	11 10 11	#2
CNM	Si	Al	100	5,00E-03	15	10	1	350		38.5 - 45 - 69	11 11 11	#1 repeated
CNM	Pt/TiAl/SiO2/Si	Al	100	5,00E-03	15	10	1	350		33 - 38.5 - 41.5 - 45 - 48 - 69	11 11 11	#2 repeated
CNM	Si	Al	100	5,00E-03	15	10	1	350		33 - 38.5 - 45 - 69	11 22 11	#1 bonding Ag paint
CNM	Pt/TiAl/SiO2/Si	Al	100	5,00E-03	15	10	1	350		33 - 38.5 - 41.5 - 45 - 48 - 69	11 22 11	#2 bonding Ag paint
CNM	Si	Al	100	5,00E-03	15	10	1	200		33 - 38.5 - 45 - 69	11 22 11	bonding Ag paint
CNM	Si	Al	100	5,00E-03	15	10	1	300		33 - 38.5 - 45 - 69	11 22 11	bonding Ag paint
CNM	Si	Al	100	5,00E-03	15	10	1	400		33 - 38.5 - 45 - 69	11 22 11	bonding Ag paint
MSD	Pt/Ti/SiO2/Si	AIN	50	5,00E-03	6	2	1	300	40	0.15 33 - 38.5 - 40 - 45 - 69		40 peak broad and intense (Pt)
MSD	Si	AIN	50	5,00E-03	6	2	1	300	40	0.15 33 - 38.5 - 45 - 69		
MSD	Pt/Ti/SiO2/Si	AIN	50	5,00E-03	6	2	1	400	40	0.15 33 - 38.5 - 40 - 45 - 69		40 peak broad and intense (Pt)
MSD	Si	AIN	50	5,00E-03	6	2	1	400	40	0.15 33 - 38.5 - 45 - 69		
MSD	Pt/Ti/SiO2/Si	AIN	50	5,00E-03	6	2	1	300	40	0.15 33 - 38.5 - 40 - 45 - 69		Josh parameters #1
MSD	Si	AIN	50	5,00E-03	6	2	1	300	40	0.15 33 - 38.5 - 45 - 69		Josh parameters #2

Table 5.6: Performed experiments.

B. Si₃N₄/Si substrate

As a substrate, polish low stress, low pressure chemical vapor deposition silicon nitride wafer (LSLPCVD, commercial grade, University wafer Inc.) was used. In Table 5.7 it is described the used parameters and the XRD spectra are shown in Figure 5.15.

Substrate	Growth parameters							
	Power DC [W]	Ar [sccm]	N ₂ [sccm]	T° [C]	Time [s]	P [mTorr]	Sputt. Machine	Notes
Pt/Ti/Si ₃ N ₄	150	3	20	500	18000 (5hs)	3	CNM	SiN ₃ commercial-Pt:150nm-Ti:10nm

Table 5.7: Deposition parameters for the AlN/Pt/Ti/ Si₃N₄/Si heterostructure.

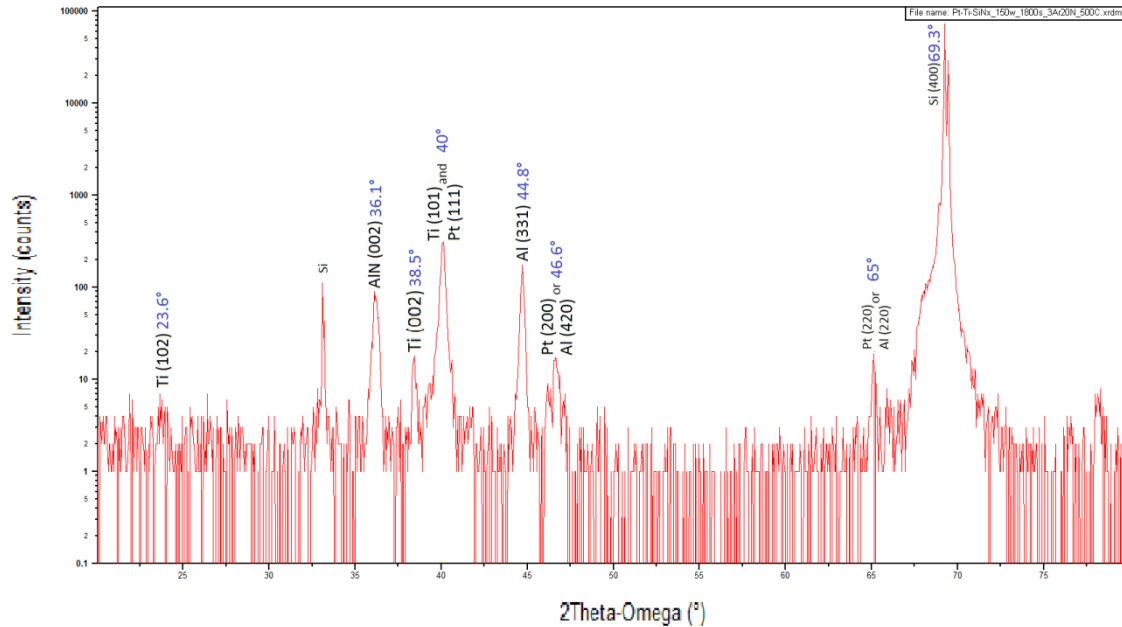


Figure 5.15: XRD spectrum of an AlN/Pt/Ti/Si₃N₄/Si heterostructure showing the characteristic peaks of the Pt and Ti layers and the Si substrate, in addition to the critical AlN (002) peak that reveals the high orientation of AlN necessary to yield the high piezoelectric coefficient measured for these films.

The XRD 2θ/ω diffraction pattern taken from the XRD analysis of the AlN/Pt/Ti/Si₃N₄/Si multilayer was scanned between 20° and 80°.

5.3.3 Conclusions

A direct method of deposition of AlN on Si substrate avoiding polishing steps and thus reducing fabrication times has been demonstrated. It has been shown that thin AlN films with high (002) orientation can be produced on surfaces with rms roughness ≤ 1 nm, as is the case of atomically flat SiO₂ surfaces. This statement is supported by the XRD spectra

shown in Figure 5.14, which indicates that AlN films exhibit higher intensity for the (002) peak when grown on an atomically flat SiO₂ surface than Si₃N₄ (Figure 5.15).

The columnar structure of the obtained AlN shows a highly textured film thus allowing the fabrication of SAW resonators and piezoelectric actuators. The Pt film has proven to be a good buffer layer serving also as bottom and top electrodes. In it is the opinion of the author that a huge field for biomedical devices based on AlN is awaiting to be explored.

5.4 Integration of AlN and UNCD Films

Piezoelectric materials are being used for a variety of applications including defense, robotics and implantable biomedical devices. For the latter, an important requirement is that the material needs to be biocompatible; in this regard, AlN is an attractive alternative.

It is also becoming important to be able to integrate piezoelectric films with materials used in medical devices. Ultrananocrystalline diamond (developed and patented at Argonne National Laboratory), in thin film form, is a multifunctional material, which is extremely bioinert and biocompatible.^{30,31,32,33} For example, UNCD has been developed as an hermetic bioinert/biocompatible encapsulating coating for a Si-microchip³⁴ to enable implantation inside the eye on the retina, as a critical component of an artificial retina,³⁵ and as a biocompatible coating for glaucoma valves³⁶ and dental implants.³⁷ Since both UNCD and AlN films can be processed via photolithography and reactive ion etching processes used in fabrication of micro/nanoelectromechanical systems, it is expected that the integration of UNCD and AlN films will provide the bases for developing a new generation of biocompatible Bio-MEMS/NEMS. These devices will have a profound impact in drug delivery inside the human body for treatment of different pathological conditions, since the drug delivery can be actively controlled to tune the pharmacokinetics of the delivered drug. In addition, the implanted MEMS/NEMS devices will enable local drug delivery inhibiting toxic side effects.

The use of piezoelectric materials as the active part of DDS is appealing. Piezoelectric actuation could be used to break a membrane covering drug reservoirs, as a switch valve for opening the reservoirs, or by pushing the liquid outside of the reservoir. AlN is a very attractive piezoelectric material for use in BioMEMS because it is biocompatible, exhibits high resistivity, high breakdown voltage, high acoustic velocity and it can be grown by reactive sputtering technique at relatively low temperature thus being compatible with CMOS device technology.^{38,39} AlN films for MEMS devices are most often synthesized in the Wurtzite hexagonal crystallographic structure with c-axis (002) orientation perpendicular to the surface, which is the orientation that yields the highest piezoelectric constant in addition to a high acoustic wave velocity.⁴⁰

Olivares et al.⁴¹ have shown the piezoelectric actuation of a microbridge based on an AlN thin film, Sinha et al.⁴² reported AlN films with nanoscale thickness for nanoelectromechanical switches and Iborra et al.⁴³ demonstrated surface micromachined bimorph based on AlN films grown on polysilicon. New types of piezoelectrically based DDS under development are microfluidic-based devices. Surface acoustic wave devices have been used mainly for radio frequency communication. However, other powerful applications of SAW devices are for chemical and biochemical sensors and optical modulators,⁴⁴ and as acoustical devices for application to microfluidic systems.^{44,45,46,47,48} This technology present advantages on the classical actuation mechanisms in microfluidics

due to its fast operation, simple setup and strong actuation.^{44,46,48} Because diamond-based substrates exhibit the highest sound velocity among all materials⁴⁹ and AlN exhibits the highest phase velocity among all piezoelectric materials,⁵⁰ the AlN/diamond heterostructure provides a very promising platform for fabrication of a wide range of devices from SAW to microfluidics. In this sense, SAW devices could be exploited to breakdown liquids into droplets to develop aerosol DDS for respiratory diseases.

Crystallization and adhesion of the piezoelectric film to the underlying supporting matrix material are the main factors regarding the quality of the piezoelectric activity and is still a great challenge in the deposition of AlN films on diamond. Benedic et al. have demonstrated SAW devices based on AlN/nanocrystalline diamond (NCD) layered structure but with weak filtering performances (acoustic losses and diffusion).⁵¹ Chou et al. deposited AlN thin films on UNCD using a TiN/Ti buffer layer and polished UNCD to improve the adhesion between layers.³⁸ Rodriguez-Madrid et al. deposited AlN on microcrystalline diamond (MCD) polished substrates at room temperature.⁵² Elmazria et al. demonstrated AlN/diamond SAW devices fabrication without mechanical polishing of the diamond surface.⁵³

In this section, the integration of AlN with as-deposited UNCD and nitrogen-incorporated (in grain boundaries) UNCD (N-UNCD) as well as with Boron doped UNCD (B-UNCD) supporting layers was demonstrated. The study was focused on determining which process produced the best AlN film with the highest piezoelectric coefficient integrated on UNCD layers for optimum actuation of piezoelectric based MEMS drug delivery devices for biomedical applications. The investigated methods include: a) direct deposition of AlN film on as grown Pt/Ti/UNCD films with rms surface roughness of ~2-5 nm without any additional chemical mechanical polishing (CMP) or especial buffering layer, which would minimize fabrication steps and cost, and b) a method involving a CMP step to produce extremely smooth surface, which produce (002) oriented AlN layers with the highest piezoelectric coefficient due to control of AlN film orientation. The proposed research is focused on developing biomedical devices that will harness both, the piezoelectric and biocompatibility properties of AlN and the biocompatibility and multifunctionality of UNCD, N-UNCD and B-UNCD to create a new generation of drug delivery devices.

5.4.1 Experimental procedure for synthesis of thin Films and characterization

A. UNCD and NUNCD Thin Film Synthesis

Pt/AlN/Pt heterostructure layers were grown on as-deposited UNCD and N-UNCD layers with a Ti adhesion film on the surface. The Pt/AlN/Pt/Ti/UNCD and N-UNCD multilayer structures were grown in a clean room facility. N-type Si (100) wafers with surface

polished to mirror finish were used as substrates. A nanodiamond seeding (layer) was produced first, via exposure of the Si-substrate surface to a solution of nanodiamond particles in methanol in an ultrasonic bath, whereby the diamond nanoparticles are embedded on the substrate surface to provide the seeds upon which the UNCD or N-UNCD films were grown.^{30,31,32,33,34} N-type Si (100) wafers with surface polished to mirror finish were used as substrates. The N-UNCD films were grown in a microwave plasma enhanced chemical vapor deposition (MPCVD) system using an Ar rich/ CH₄ mixture with added N₂. The power was set at 2300 W and the absorbed power ranged between 1900-2000W with a pressure set at 50 mbar (Ar flow: 79 sccm (sccm denotes standard cubic centimeter per minute at standard temperature and pressure, STP), N₂ flow: 20 sccm and CH₄ flow: 1 sccm). The UNCD films were grown in the same MPCVD systems used to grow the N-UNCD films, but using 90 mbar pressure with forward power of 1216 W and a mixture of CH₄, Ar and H₂ (Ar flow: 48.7 sccm, H₂ flow: 0.5 sccm and CH₄ flow: 0.8 sccm).

B. Pt and AlN piezoelectric film synthesis

The Pt layer was grown by magnetron sputter-deposition on top of a Ti film deposited on the UNCD surface as an adhesion layer. The Pt/Ti heterostructure layer contributes to induce a highly c-axis (002) oriented AlN films, which provides the highest piezoelectric coefficient. The Pt layer serves as bottom and top electrode to apply voltage to excite the piezoelectric effect on the AlN layer for actuation of the MEMS device. Films were grown using the conditions shown in Table 5.8.

AlN (002) oriented films were grown on the Pt layers at about 500 °C, using reactive sputter-deposition, using an Ar-plasma to sputter Al atoms from a solid target in a N₂ atmosphere to provide the nitrogen needed to produce the AlN films. After 5 hours of deposition, the thickness of this piezoelectric AlN layer was 417 nm with a deposition rate of 83.4 nm/h. This rate is affected by the low Ar flow used that reduces the amount of heavy ions impacting on the target. A list of deposition parameters can be seen in Table 5.8:

Parameter	Material		
	AlN	Pt	Ti
Base pressure (Torr)	$<1 \times 10^{-7}$	$<1 \times 10^{-7}$	$<1 \times 10^{-7}$
Process pressure (mTorr)	3	5	5
Power (W)	150 ^a	150 ^b	150 ^b
Substrate temperature (°C)	500	25	25
Ar flow (sccm)	3	26	26
N ₂ flow (sccm)	20	0	0
Target	Al (99.999%)	Pt (99.99%)	Ti (99.995%)
Target-substrate distance (cm)	10	11	11

^a DC power
^b RF power

Table 5.8: Sputtering parameters for AlN, Pt and Ti depositions.

C. Characterization of UNCD, N-UNCD and AlN films structures and properties

UNCD and N-UNCD were characterized using Raman Spectroscopy, involving a 632 nm wavelength laser to determine the chemical bonding of Carbon atoms in the films. A typical Raman spectrum from the analysis of the UNCD films is shown in Figure 5.16. Measurements were taken on three different points on the surface of the wafer. The main resonance peaks in the spectrum are the 1332 cm^{-1} , characteristic of the diamond sp^3 carbon bonding, and the 1532 cm^{-1} , which reveals the existence of disordered sp^2 -bonded carbon at the grain boundaries of the film.³⁰

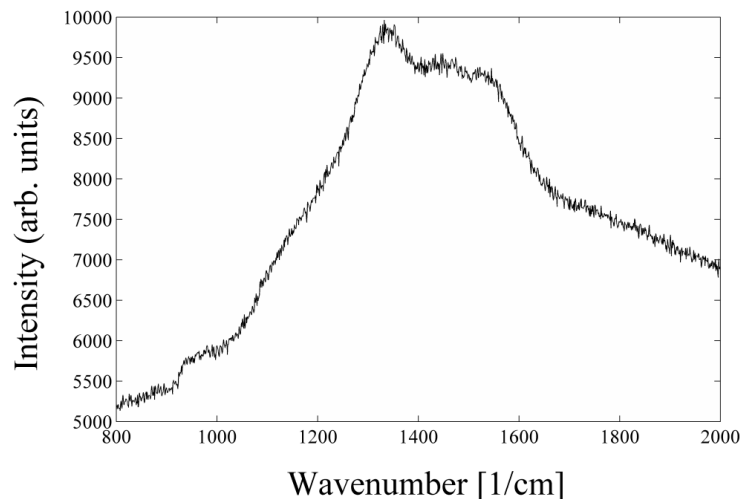


Figure 5.16: Typical Raman spectrum from the Raman analysis of a typical UNCD film showing the 1332 cm^{-1} peak characteristic of diamond sp^3 c-atoms bonding and the 1532 cm^{-1} revealing the presence of sp^2 -bonded carbon at the grain boundaries of the film.

The thicknesses of the UNCD films were measured firstly with a reflectometer tool and then using cross-sectional SEM samples. In addition, SEM imaging was used to analyze the microstructure and morphology of the UNCD and AlN films. The crystal structure and the preferred orientation (texture) of the piezoelectric layer were identified by theta/theta X-Ray diffractometry. The piezoelectric coefficient of the AlN films was measured using the Piezoresponse Force Microscopy (PFM) technique,⁵⁴ which involves using an AFM Pt coated silicon cantilever to apply AC voltages that excite the piezoelectric activity in the AlN film and monitor the mechanical deformation through the piezo-mechanical deformation of the film, producing a piezoresponse imaging of the polarization.⁵⁴

5.4.2 Influence of surface roughness on AlN synthesis and properties

AlN layers with thickness in the 260-420 nm range were synthesized on SiO₂ (100nm) on Si substrate, on as grown UNCD and chemical mechanical polished B-UNCD substrates, respectively, to investigate the effect of the substrate surface nature and rms roughness on the orientation of the AlN film, which makes a substantial impact on the corresponding piezoelectric properties. Their thicknesses were obtained firstly with a reflectometer tool (Filmetric F20 Thin Film Analyzer) and then by making cross-sectional SEM.

A SEM micrograph of the top surface of the AlN layer and the cross-section of the AlN/Pt/Ti/UNCD heterostructure is shown in Figure 5.17. The thicknesses of the Platinum and Titanium layers, used as the bottom electrode heterostructure, were 150 nm and 10 nm, respectively, and provided the underlying substrate for growing the piezoelectric AlN layer on the UNCD platform substrate. The AlN film exhibits a columnar microstructure which is perpendicular to the substrate surface with orientation (002) as revealed by the XRD analysis shown in Figure 5.18a.

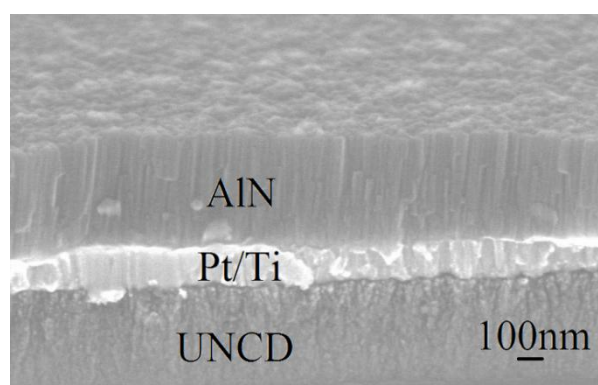


Figure 5.17: SEM micrograph of the surface morphology of the AlN layer and cross-section of the AlN/Pt/Ti/UNCD/SiO₂/Si heterostructure

Figure 5.18 (top) shows a cross section SEM analysis of AlN films grown on different substrates with different roughness. The X-ray diffraction spectra for each of the samples is

also provided in Figure 5.18 (bottom). These figures indicate the influence of the roughness of the substrate to produce highly (002) oriented AlN films.

The XRD $2\theta/\omega$ diffraction pattern from the XRD analysis of AlN/Pt/Ti/UNCD/SiO₂/Si, AlN/Pt/Ti/B-UNCD/SiO₂/Si and AlN/Pt/Ti/SiO₂/Si multilayers were obtained by scanning between 20° and 80°. Pt and Ti layers, used as the bottom electrode heterostructure, provided the underlying substrate for growing the piezoelectric AlN layer on the UNCD platform substrate. Figure 5.18 (bottom) shows an XRD $2\theta/\omega$ scan of these multilayers films exhibiting high c-axis orientation for the AlN film. It is noted the presence of hexagonal AlN (002) diffraction peak at 36.05°, indicating that the AlN layers are highly (002) oriented, which correlates with the high piezoelectric coefficient exhibited by this film. It is also shown the diffraction peaks of Pt (111) at 40.05° and Ti (002) at 38.45° corresponding to the electrode and a peak at 44.7° which can be attributed to diamond (111) or Ti.

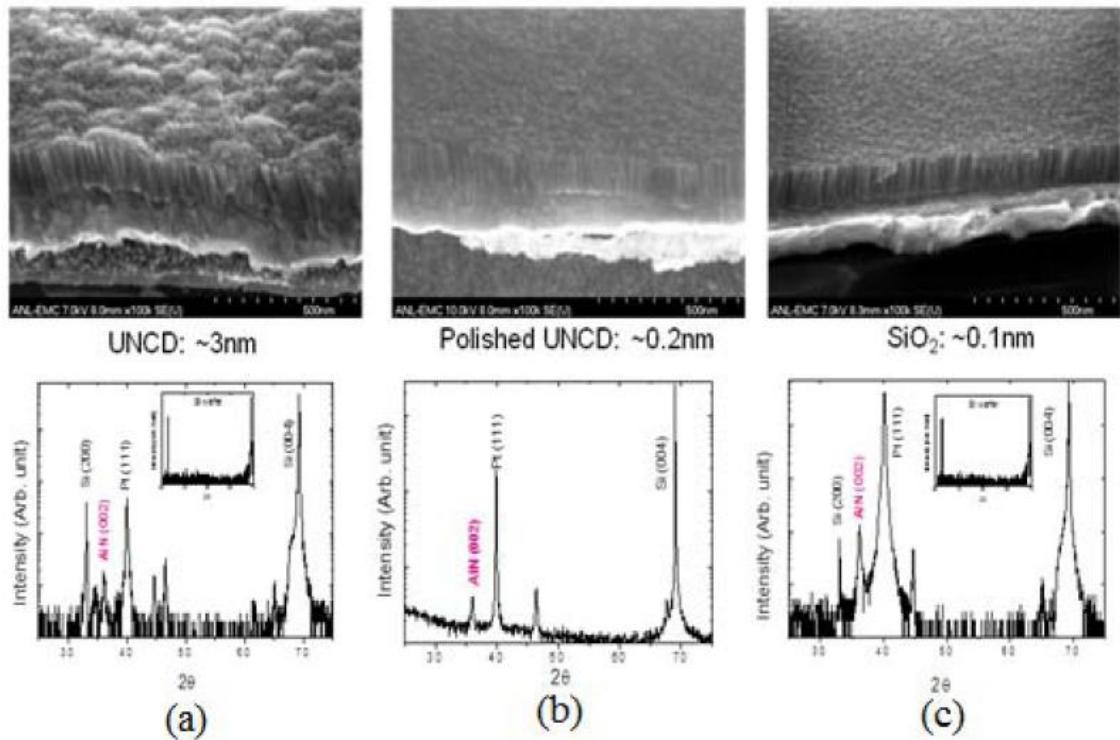


Figure 5.18: Cross-section SEM analysis of AlN growth on different substrates and the corresponding XRD spectra for each substrate.

In the figure also appears a peak at 33.20°; this narrow peak comes from the silicon wafer substrate and is the result of Si crystalline imperfections. In addition, the very narrow width is an indication that it comes from a single crystal. In Figure 5.19 it can be observed the XRD scan of a Si wafer showing the mentioned ghost peak.

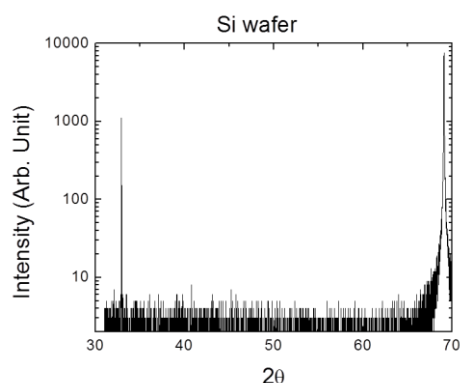


Figure 5.19: XRD scan of a Si wafer showing the peak coming from the silicon wafer.

The X-ray wavelength was $\lambda=1.540598\text{\AA}$ ($K\alpha_1$, Long Fine focus, Cu Anode radiation). By using Bragg's law, c-lattice constant for the AlN layer was calculated (4.9681\AA), which is in a good agreement with the value of the AlN found in the literature.⁵⁵

While the thick AlN films at $>400\text{nm}$ thickness on different substrates show similar XRD patterns, the crystallization of thinner AlN films are largely affected by substrate conditions mostly by their roughness. Thinner AlN films with high (002) orientation can be produced on surfaces with rms roughness $\leq 1\text{ nm}$, as is the case of atomically flat SiO_2 surfaces (Figure 5.18c), unlike the UNCD and N-UNCD layers that exhibit roughness of 5-7 nm and 7-10 nm respectively, as previously measured extensively by Auciello et al.⁵⁴ AlN films grown on CMP boron-doped UNCD (B-UNCD) films with Pt bottom electrode exhibit surface roughness of about 0.2 nm and high (002) orientation (see XRD spectrum in Figure 5.18b) as for films grown on atomically flat semiconductor surfaces. The results presented here indicate that the smoothness of substrate surface is critical to achieve highly (002) oriented very thin AlN films.

5.4.3 Piezoelectric response of AlN films

The piezoelectric coefficient of AlN films grown on UNCD, N-UNCD and B-UNCD layers were measured using the PFM technique described above. When applied an AC voltage to AlN films between AFM tip and bottom electrode, the piezoresponse of AlN films appears as function of applied AC signal. Using the average piezoresponse amplitude of AlN films and inverse optical lever sensitivity between the AFM tip and AlN films, the piezoelectric coefficients of AlN films were calculated. These measurements revealed a uniform piezoresponse (Figure 5.20). However, the AlN films grown on as deposited UNCD and N-UNCD surfaces exhibited piezoelectric coefficient of 1.91 pm/V and 1.97 pm/V respectively, while the AlN films grown on the CMP B-UNCD surfaces exhibit $\sim 5.3\text{ pm/V}$, which is the highest among currently reported values for AlN films.

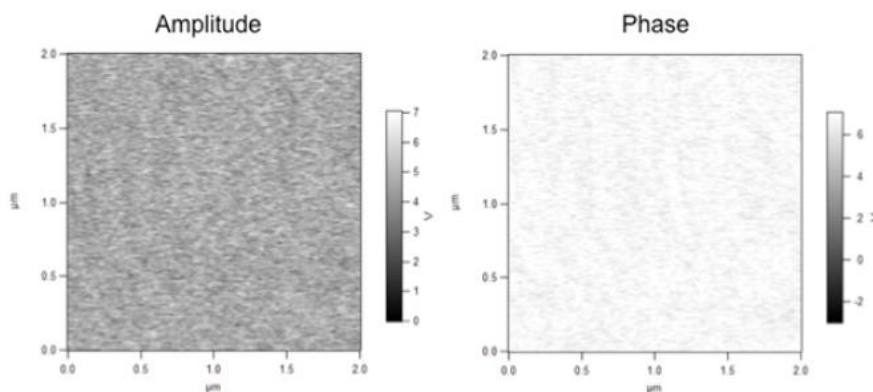


Figure 5.20: PFM imaging of piezoelectric activity in (002) oriented AlN film (~200 nm thick) grown on CMP BUNCD with rms surface roughness of about 0.2 nm. The PFM measurement was used to determine the piezoelectric coefficient of the AlN film, which was 5.3 pm/V, one of the highest demonstrated today for AlN.

The data shown above indicates that the surface roughness of the substrates is critical to produce highly (002) oriented AlN films. Growth of highly oriented (002) AlN films on UNCD layers is critical to achieve the highest possible piezoelectric coefficient, which results of paramount importance to achieve optimum actuation in piezoelectrically actuated MEMS devices. In addition, the Pt (111) oriented electrode layers used to grow the AlN films contribute to produce oriented AlN layers by inducing local epitaxial correlation between the Pt and AlN lattices.⁵⁶

It has been observed in the past that AlN films grown on smooth Si surface exhibit highly c-oriented crystallites, while similar films grown on rough surfaces exhibit a weak (002) orientation.⁵⁷ The hypothesis is that a rough surface favors a heterogeneous orientation of the AlN crystallites. This phenomenon is established when the local surface inclination varies on a scale between the diameters of the AlN grain and the nuclei, thus hampering the c-axis (002) orientation; therefore, the high density of oblique crystallographic orientations prevents the growth of highly textured material as stated by Artieda et al.⁵⁷

The same concept of Si surface roughness effect on AlN films, should apply to UNCD surfaces, and indeed, the data presented here shows that the atomically smooth B-UNCD surface induced the growth of (002) oriented AlN film exhibiting one of the highest piezoelectric coefficient seen for AlN films today.

In addition to the effect of the substrate surface roughness, it is important to take into account the effect of the microstructure of Pt electrode layers grown on the substrate, used to apply voltages to induce the piezoelectric effect on the AlN layer to achieve actuation. In this sense, Artieda et al.⁵⁷ showed that AlN films grown on Pt (111) electrode layers are highly (002) oriented largely independently of the roughness of the Pt film. This can be explained due to a good alignment of Pt (111) planes on top of the Pt grains where the AlN (002) nucleates epitaxially. The Pt roughness can be due to facets at grain boundaries, on which epitaxy of AlN is still compatible with c-planes parallel to the substrate surface. In the case of rough amorphous substrates, the large number of germination sites having various orientations prevents the formation of a dense, well-aligned, c-oriented fiber

structure of AlN, inducing a disordered microstructure with pores and, consequently, resulting in low residual tensile stresses.⁵⁷ The stress increases gradually from compressive (negative values) to slightly tensile (positive values) with the surface roughness of the substrate. Large compressive stress was observed by Artieda et al. for AlN films grown on smoother SiO₂ surfaces.⁵⁷ The large amount of germination sites for AlN growth on rougher substrates leads to smaller grains and a high density of voided grain boundaries.⁵⁷ On the other hand, AlN growth on smooth surfaces is facilitated by high mobility of the atoms landing on the surface leading to dense grain boundaries and compressive stresses. The impact of roughness to the stress seems to follow quite general rules in as much as a Pt electrode surface leads to a stress that fits the trend observed with Si surfaces.

5.4.4 Conclusions

The research described in this paper provides information for understanding the fundamental physical and chemical processes involved in the integration of piezoelectric AlN films with underlying UNCD, N-UNCD and B-UNCD layers. AlN films deposited on as grown UNCD or N-UNCD films exhibit relatively good (002) orientation, due to the fact that these diamond films exhibit rms surface roughness of about 5-10 nm, which is the size of the grains. The columnar structure of the (002) oriented AlN films grown on the UNCD layers enable relatively high piezoelectric coefficient (~ 1.91 pm/V), but still require AlN film thickness $\geq \sim 400$ nm to achieve the high (002) ALN orientation. A relatively high voltage (> 10 V), applied between the bottom and top electrodes sandwiching the AlN layer, is needed to produce the actuating piezoelectric effect in films as thick as 400 nm. It would be desirable to achieve high (002) AlN orientation with films ≤ 100 nm to produce actuation at much lower voltages (≤ 2.5 V). In this sense, the CMP B-UNCD film, with rms surface roughness of about 0.2 nm, used as substrate, yielded a highly oriented (002) AlN films even as thin as 80 nm. The 200 nm thick AlN on UNCD layers exhibited a piezoelectric coefficient of about 5.3 pm/V, one of the highest for AlN film demonstrated today.

Although the first research on integration of AlN films with CMP UNCD layers was done here using CMP B-UNCD films, further work is now proceeding to extend the integration of AlN films on CMP UNCD films in general, to determine what is the thinnest (002) oriented AlN film that can be grown on CMP UNCD layers to produce low voltage piezoelectrically actuated UNCD-based MEMS drug delivery devices. The low temperature of the UNCD, N-UNCD and B-UNCD growth and also the AlN deposition makes this innovative system compatible with CMOS chips and CMOS-driven MEMS and NEMS systems. Successful integration of piezoelectric AlN and BUNCD films may enable the development of a new generation of biocompatible piezoelectric-based drug delivery MEMS devices implantable in the human body.

5.5 AlN FBAR on UNCD

This section is focused on the fabrication of the previously modeled and simulated AlN/UNCD-based thin film bulk acoustic resonator for biosensor applications. Even though it was carried out the analysis of the behaviour of a FBAR piezoelectric mass sensor, it can be extended to this new type of sensor transducer device.

Biomedical MicroElectroMechanical Systems technology is inherited from the Integrated Circuit Industry and results from the integration of structural and functional microparts such as micro channels, microreservoirs, microsensors and microactuators; it have recently been developed to overcome several limitations imposed by the current state of the art in medical technology.

In spite of these remarkable advantages that BioMEMS technology brings, there still exist the need for a biocompatible–bionert material capable of persisting in the harsh environment of the human body without suffering from biofouling and that could sustain microfabrication processes keeping its properties intact. In this sense, aluminum nitride and UNCD have demonstrated to accomplish these aspects.

As shown in last sections, UNCD fulfills such requirements as is capable of being microfabricated and even integrated with CMOS technologies. In addition, UNCD also exhibits biocompatibility and bioinertness.^{30,31,32,33} Furthermore, AlN has shown to be a compatible material for BioMEMS applications. Because of diamond based substrates have the highest sound velocity among all materials,⁵⁰ AlN/diamond structure is a very promising device for FBAR applications. In this sense, AlN-UNCD integration becomes an important option for implantable resonators sensors as well as actuators.

5.5.1 Geometry design

The simplest configuration of the membrane FBAR involves the acoustic resonance cavity formed by the creation of an air cavity underneath the bottom electrode by etching completely the Si substrate.

A typical thickness of the piezoelectric film is a few microns while that of the metal electrodes is an order of magnitude less. To acoustically isolate the resonance cavity, parts of the substrate are removed to create a freestanding membrane.

Devices composed of multilayer structures where the layers exhibit different thermal expansion coefficients often suffer from intrinsic residual stresses, which can be reduced using low temperature processes. In addition, being a low temperature process makes it promising for integrating to the IC technology.

An scheme of the FBAR device can be observed in Figure 5.21. In Figure 5.21a it can be seen the freestanding heterostructure membrane. It is composed of a Pt/Ti/AlN/Pt/Ti/UNCD multilayer on a silicon substrate as shown in Figure 5.21b. Top electrode (Pt/Ti) is similar to the bottom electrode used in last section.

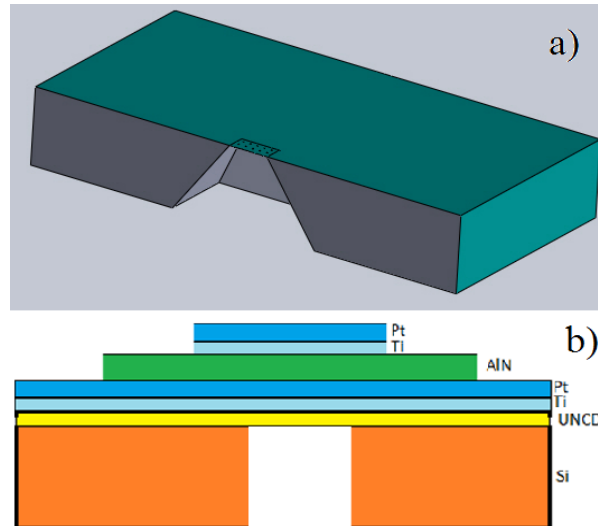


Figure 5.21: AlN FBAR on UNCD. a) 3D longitudinal cut image of the freestanding FBAR heterostructure and b) lateral view scheme of the device describing the deposited layers.

5.5.2 Mask design and fabrication

For the design of the masks, it was used the *Layout Editor* of the *Tanner EDA* software. Layout is essentially a drawing process where the 2D drawings of the geometries will end up on the desired mask. Layout tools are essentially CAD (computer aided design) drawing tools, but include additional useful features.

It was designed and fabricated three different masks for the entire device:

- Mask 1: cavity on Si
- Mask 2: piezoelectric AlN
- Mask 3: top electrode

The electric stimulation take advantage of the difference found in the piezoelectric AlN layer size and the top and bottom electrodes: it allows the access for the electrical contacts between top and bottom electrodes in order to actuate de piezolayer.

Figure 5.22 shows the mask for the cavity on the Si substrate. It can be observed the four different sizes used in this experimental step in order to compare performances. There were designed square membranes as FBARs.

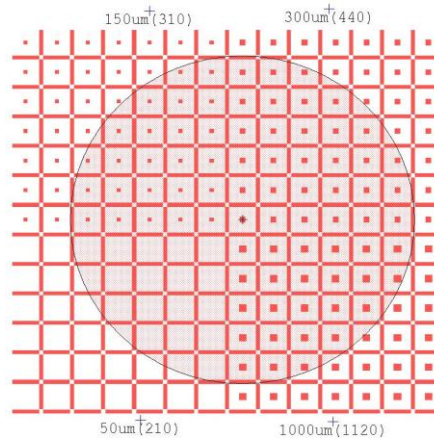


Figure 5.22: Mask layout for the Si cavity. It can be observed the four different sizes used in this experimental step, where the value in microns is the calculated length of the square and in brackets is the real length due to undercuts.

Also, for cavity design it has to be considered the substrate material as well as the used etching method. For the case of silicon, a common etching method is by using wet anisotropic etching; potassium hydroxide is a strong base capable of attack the Si substrate in an anisotropic way. It was used N-type Si (100) wafers with surface polished to mirror finish as substrate, so the KOH will etch the Si preferably in the [100] plane. It produces the characteristic V anisotropic etch of the walls, forming an angle of 54.7° with respect to the main surface (Figure 5.23).



Figure 5.23: Si (100) showing characteristic V anisotropic etch of the walls forming an angle of 54.7° with respect to the main surface.

The used masks have a multilayer structure with the following layers: PR/ Cr_2O_3 /Cr/glass. The photoresist (PR) is the last layer and the Cr_2O_3 serves as antireflective film. The glass is very flat and made of borosilicate glass.

The fabrication of the masks was done by a Laser Pattern Generator (LW405). It was generated the pattern over the photoresist on the chrome mask on glass (square of 125 mm) during 24 hs. After that the photoresist was developed (developer 351) and a wet etching of the chrome film was done. The generated chrome pattern is shown in Figure 5.24.

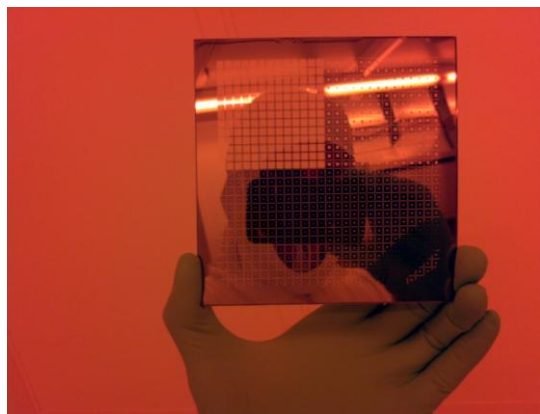


Figure 5.24: Generated chrome pattern on glass substrate.

5.5.3 Membrane fabrication

The membrane fabrication on the Si substrate involves several steps:

- *UNCD growth:* it was deposited 400nm of UNCD on the front of the silicon wafer (N-type mirror polished Si (100)). The UNCD films were grown using a MPCVD system (Lambda Technologies), powered by a 915 MHz magnetron generator with 2300 W power to produce a plasma from a mixture of Ar (99%)/CH₄ (1%) gases that produce C₂ dimers as the growth species and a pressure of 80mTorr. This layer was used as a substrate for the AlN and also serves as a stop layer for the anisotropic wet etching of the Si by using KOH.
- *Si₃N₄ deposition:* Silicon Nitride (Si₃N₄) was used as a mask for the wet etching of the Si using KOH. It was used a commercial, polished, low stress Si₃N₄ residual (LSLPCVD, commercial grade, University wafer Inc). Si₃N₄ pattern for the cavities was performed by photoresist spin coating with S1813, UV exposure for 5 seconds (mask aligner Karl Suss MA6), resist development (351 developer diluted in a 3: 1 ratio in DI water) and dry etching of the Si₃N₄ in a Tetrafluoromethane (CF₄) plasma (Oxford CS-1701 RIE).
- *Pt/Ti deposition:* A platinum electrode was grown by sputter deposition (AJA sputtering tool, ATC 2200 IBAD) using a titanium adhesion layer. Films were deposited with a target RF power of 150W, pressure of 3 mTorr, Argon flow rate of 26 sccm and base pressure of 1e-7 Torr. The thicknesses of the Pt and Ti were 150nm (720s deposition) and 10nm (310s deposition) respectively. In addition, this coating provides seeding capability for the AlN and serves as a buffer layer. It also helps to improve the adhesion of the AlN to the UNCD.
- *AlN deposition:* On the Pt/Ti electrode, AlN reactive sputter deposition was performed (AJA sputtering tool, ATC 2200 IBAD). AlN (002) was grown in a gas mixture of

Argon and Nitrogen at a temperature of 500°C at a pressure of 3mTorr. Aluminum target with a diameter of 4" and a purity of 99.999% was used.

- *AlN pattern:* The pattern was transferred to the AlN film by performing photoresist spin coating (ma-N 415 negative photoresist), UV exposure for 30 seconds (mask aligner Karl Suss MA6), resist development (533) and dry etching using anisotropic Cl₂-based reactive ion etching (Oxford CS-1701 RIE).
- *Electrode pattern:* Patterning of Pt/Ti top electrode was done by applying lift off techniques. Firstly a spin coating with S1813 on the frontside of the wafer, UV exposure and resist development were done. Finally a Pt/Ti sputter deposition and posterior removal of the photoresist was performed.
- *Cavity:* The cavity etching was done on the backside by using KOH (30%). Also, it was used hermetic protection to avoid frontside etching. Time etching was estimated in 9hs at a temperature of 85°C with stirring at 250 rpm.
- In the following picture it can be seen the first cavity prototype, using only UNCD as a membrane on the Si wafer substrate:

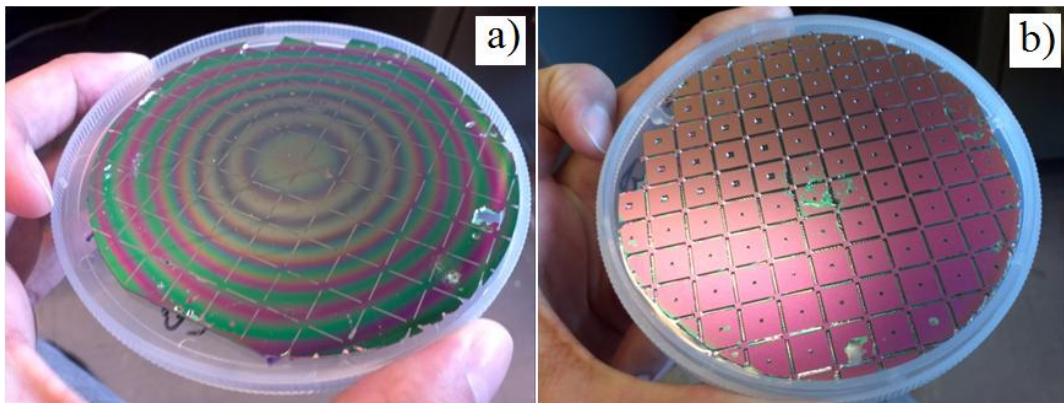


Figure 5.25: First cavity prototype. a) Frontside of the UNCD film and b) backside showing the different sizes of the cavities within dices.

5.5.4 Characterization

A. Optical Microscope

The first analysis tool is the optical microscope. The obtained images help evaluate the quality of the KOH etching. The morphology of the membranes and cavities are shown in Figure 5.26. Because of the difference in the square membranes between frontside and backside of the Si, it is can be seen the classical pyramid shaped that obeys the preferential 54.7° isotropic etching of the (100) crystal plane of the Si wafer.

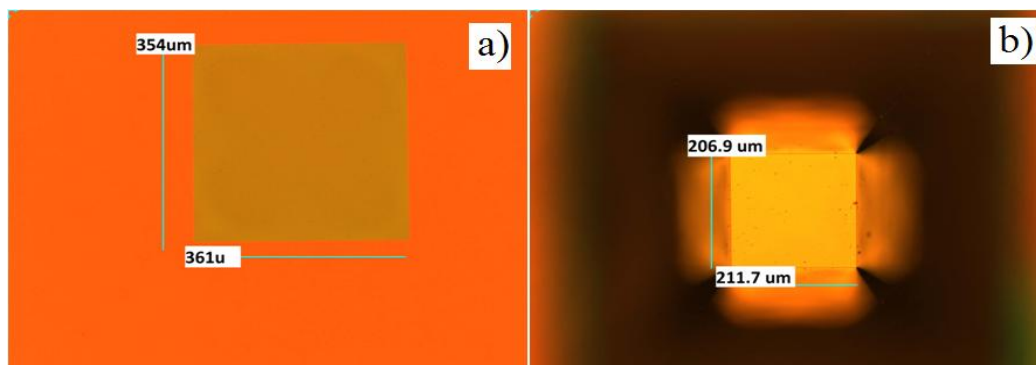


Figure 5.26: Square UNCD membranes. a) Membrane (mask 300 μm) seen from the frontside, and b) membrane (mask 150 μm) seen from the backside (cavity).

It is shown that the size of each membrane is moderately higher than the expected due to the generated undercuts below the membranes. Undercuts increase the squares size in a range between 50-170 μm . The calculated etching rate for the Si using KOH was 1.16 $\mu\text{m}/\text{min}$

B. Reflectometer

It was used to have the first approximation of the depositions. UNCD thickness was obtained using a reflectometer tool (Filmetric F20 Thin Film Analyzer).

C. Scanning Electron Microscope

The scanning electron microscope (SEM) is today a routinely used instrument for the examination of fine detail of a variety of samples. The instrument is, in simple terms, analogous to an optical microscope: the electron source (gun) is equivalent to the light source and the glass lens is replaced by electromagnetic lens. Information from the sample is collected and displayed on a viewing screen for visual interpretation.

In Figure 5.27a it is depicted a cross section of the AlN/Pt/Ti/UNCD membrane (cantilevered). It exhibits a columnar microstructure. These columnar crystals are perpendicular to the substrate surface in agreement with the XRD results where the AlN film is highly textured. The piezoelectric film reached a thickness of 417nm after 5hs of growth (Figure 5.27b).

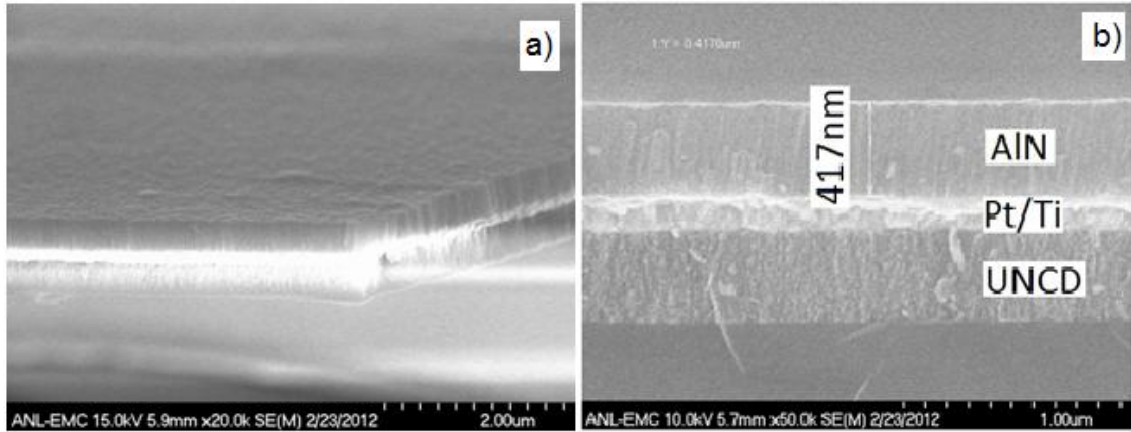


Figure 5.27: SEM cross section of the film for the AlN/Pt/Ti/UNCD membrane. a) Cantilevered membrane and b) measurements on the SEM image.

A clarified view of the generated Si cavity can be appreciated in the SEM image of the freestanding AlN/Pt/Ti/UNCD membrane on the Si substrate (Figure 5.28). It can be seen an in-focus image of the tilted Si walls (54.7°) where the big square have the dimensions of the mask and the smaller is the AlN/Pt/Ti/UNCD membrane. The white frame surrounding the big square is produced by the generated undercuts under the UNCD.

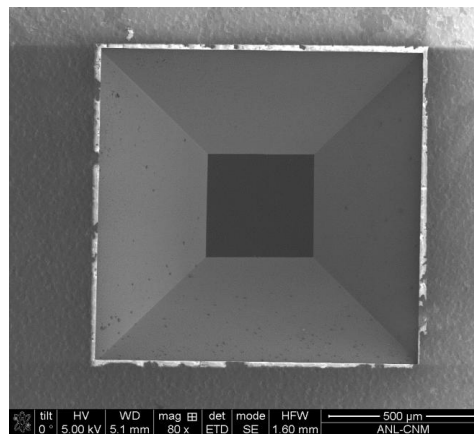


Figure 5.28: SEM image of the freestanding AlN/Pt/Ti/UNCD membrane on the Si substrate.

5.5.5 Conclusions

The feasibility in the fabrication of an FBAR AlN/diamond structure has been demonstrated. AlN/diamond structure is a very promising device for FBAR applications so it opens a huge field of biomedical applications.

5.6 Bibliography

-
- ¹ M. Zalazar and F. Guarnieri, “FEM-based parameter extraction of a PVDF resonator”, *Sensors & Actuators: A. Physical*, July 2012-in revision.
- ² M. Zalazar, P. Gurman, J. Park, D. Kim, S. Hong, L. Stan, R. Divan, D. Czaplewski and O. Auciello, “Integration of Piezoelectric Aluminum Nitride and Ultrananocrystalline Diamond Films for Biomedical MEMS Devices”, *Appl. Phys. Lett.* 102, 104101 (2013).
- ³ P. Gurman, M. Zalazar, J. Park, and O. Auciello, “Design, Fabrication and Characterization of Ultrananocrystalline Diamond (UNCD) Membranes for Drug Delivery Devices”, Abstract for Contributed Talk at MRS Fall Meeting: Diamond Electronics and Biotechnology–Fundamentals to Applications VI Symposium, Boston, MS, 2012.
- ⁴ P. Gurman, M. Zalazar and O. Auciello, “A New Generation of UNCD Based Drug Delivery Devices”, XXI International Materials Research Congress, Mexico, 2012.
- ⁵ M. Zalazar, P. Gurman, O. Auciello and F. Guarnieri, “Design, Fabrication and Characterization of Ultrananocrystalline Diamond (UNCD) Membranes for Drug Delivery Devices”, New Diamond and Nano Carbons Conference, San Juan, Puerto Rico, 2012.
- ⁶ Measurement Specialties, Inc., *Piezo Film Sensors-Technical Manual*, 1999.
- ⁷ M. Thompson, M.Toda and M. Ciccarone, “High Frequency Length Mode PVDF Behavior over Temperature”, *Mater. Res. Soc. Symp. Proc.* vol. 1134, 2009.
- ⁸ J. Yang, *Analysis of piezoelectric devices*. World Scientific Pub Co Inc, 2006.
- ⁹ Y. Roh, V. Varadan, and V. Varadan, “Characterization of all the elastic, dielectric, and piezoelectric constants of uniaxially oriented poled PVDF films”, *IEEE Trans Ultrason Ferroelect Freq Contr*, vol. 49, no. 6, pp. 836–847, Jun. 2002.
- ¹⁰ S. Sokhanvar, A. Zabihollah, and R. Sedaghati, “Investigating the Effect of the Orthotropic Property of Piezoelectric PVDF”, *Transactions of the Canadian Society for Mechanical Engineering*, vol. 31, no. 1, pp. 111–125, 2007.
- ¹¹ M. Koucky, “Piezoelectric polymer microstructures for biomedical applications,” Ph.D. dissertation, The Ohio State University, 2009.
- ¹² A. Shirinov and W. Schomburg, “Pressure sensor from a PVDF film”, *Sensors and Actuators A Physical*, vol. 142, no. 1, pp. 48–55, Mar. 2008.
- ¹³ J. Ketterling, O. Aristizabal, and D. Turnbull, “High-frequency piezopolymer transducers with a copper-clad polyimide backing layer”, *IEEE Trans Ultrason Ferroelect Freq Contr*, vol. 53, no. 7, pp. 1376–1380, Jul. 2006.
- ¹⁴ O. Myers, M. Anjanappa, and C. Freidhoff, “Designing piezoelectric interdigitated microactuators using comsol”, in *COMSOL Conference*, Boston, MA, USA, 2008.
- ¹⁵ V. Piefort, “Finite element modelling of piezoelectric active structures”, Ph.D. dissertation, Universite Libre de Bruxelles, 2001.
- ¹⁶ A. Dobrucki and P. Pruchnicki, “Theory of piezoelectric axisymmetric bimorph”, *Sensors & Actuators: A. Physical*, vol. 58, no. 3, pp. 203–212, 1997.
- ¹⁷ O. Myers, “Modeling of a piezoelectric actuated planar capacitor actuator,” in *COMSOL Conference*, Boston, MA, USA, October 22-26 2006.
- ¹⁸ G. Petrone and G. Cammarata, *Modeling and Simulation*, ser. Systems Engineering. I-Tech Education and Publishing, 2008.

-
- ¹⁹ T. Lahrner, M. Kaltenbacher, B. Kaltenbacher, R. Lerch, and E. Leder, "FEM-Based Determination of Real and Complex Elastic, Dielectric, and Piezoelectric Moduli in Piezoceramic Materials", *IEEE Trans Ultrason Ferroelect Freq Contr*, vol. 55, no. 2, pp. 465–475, Feb. 2008.
- ²⁰ M. Thompson, M. Toda and M. Ciccione, "High Frequency Length Mode PVDF Behavior over Temperature", *Mater. Res. Soc. Symp. Proc.* vol. 1134, 2009.
- ²¹ J. Yang, *Analysis of piezoelectric devices*. World Scientific Pub Co Inc, 2006.
- ²² H. Ohigashi, "Electromechanical properties of polarized polyvinylidene fluoride films as studied by the piezoelectric resonance method", *J. Appl. Phys.*, vol. 47, no. 3, pp.949, 1976.
- ²³ L. Brown, "Design Considerations for Piezoelectric Polymer Ultrasound Transducers" *IEEE Trans Ultrason Ferroelect Freq Contr*, vol. 47, no.6, pp. 1377–1396, Nov. 2000.
- ²⁴ J. Yang, *An Introduction To The Theory Of Piezoelectricity*. Springer Science, 2005
- ²⁵ IEEE Standard on Piezoelectricity, ANSI/IEEE Std 176-1987.
- ²⁶ Standard Definitions and Methods of Measurement for Piezoelectric Vibrators, *IEEE Std 177-1966*.
- ²⁷ A. Janshoff, H.J. Galla and C. Steinem, "Piezo mass-sensing devices as biosensors-An alternative to optical sensors?", *Angew. Chem. Int. Ed.*, vol. 39, pp. 4004-4032, 2000.
- ²⁸ K. H. Chung, G.T. Liub, J.G. Duhb, and J.H. Wang, *Surface & Coatings Technology* 188-189, 745 (2004).
- ²⁹ C. C. Chen, C. T Lin, S. Y. Lee, L. H. Lin, C. F. Huang, and K. L. Ou, *Applied Surface Science* 253, 5173 (2007).
- ³⁰ O. Auciello and A. V. Sumant, *Diamond Relat. Mater.* 19, 699 (2010).
- ³¹ O. Auciello and B. Shi, *Biological and Medical Physics, Biomedical Engineering*, 63 (2010).
- ³² P. Bajaj, D. Akin, A. Gupta, D. Sherman, B. Shi, O. Auciello, and R. Bashir, *Biomed. Microdevices* 9, 787 (2007).
- ³³ O. Auciello, J. Birrell, J. A. Carlisle, J. E. Gerbi, X. Xiao, B. Peng, and H. D. Espinosa, *J. Phys.: Condens. Matter* 16, 539 (2004).
- ³⁴ X. Xiao, J. Wang, C. Liu, J. A. Carlisle, B. Mech, R. Greenberg, D. Guven, R. Freda, M. S. Humayun, J. Weiland, and O. Auciello, *J. Biomed. Mater. Res. B Appl. Biomater.* 77B, 273 (2006).
- ³⁵ D. D. Zhou and E. Greenbaum (Eds.), "Implantable Neural Prostheses" vols. 1 and 2, *Techniques and Engineering Approaches*, Springer (2010).
- ³⁶ O. Auciello, P. Gurman, A. Berra, M.J. Saravia, and R. Zysler, "Biocompatible Ultrananocrystalline Diamond Film and Magnetic Nanoparticle Technologies for Ophthalmological Implants for Eye Pathologies Treatment", Ch. 6, in *Diamond- Based Materials for Biomedical Applications*, R. Narayan (Ed.), Woodhead Publishing Ltd, Cambridge, UK (in press, 2012).
- ³⁷ B. Langer and M. E. Fritz, *Journal of Periodontology*, 63, 859 (1992).
- ³⁸ C. H. Chou, Y. C. Lin, J. H. Huang, N. H. Tai, and I. Lin, *Diamond Relat. Mater.* 15, 404 (2006).
- ³⁹ M. Dubois and P. Muralt, *Appl. Phys. Lett.* 74, 3032 (1999).
- ⁴⁰ J. Meinschen, G. Behme, F. Falk, H. Stafast, *Appl. Phys. A: Mater. Sci. Process.*, 69, 673 (1999).
- ⁴¹ J. Olivares, E. Iborra, M. Clement, L. Vergara, J. Sangrador, and A. Sanz-Hervas, *Sensors and Actuators A*, 123–124, 590 (2005).
- ⁴² N. Sinha, G. E. Wabiszewski, R. Mahameed, V. V. Felmetger, S. M. Tanner, R. W. Carpick, and G. Piazza, *Appl. Phys. Lett.* 95, 053106 (2009).

-
- ⁴³ E. Iborra, J. Olivares, M. Clement, L. Vergara, A. Sanz-Hervás, and J. Sangrador, *Sensors and Actuators A*, 115, 501 (2004).
- ⁴⁴ T. D. Luong and N. T. Nguyen, *Micro and Nanosystems* 2, 1 (2010).
- ⁴⁵ W. B. Zimmerman, *Chemical Engineering Science* 66, 1412 (2011).
- ⁴⁶ L. Schmid, A. Wixforth, D. A. Weitz, and T. Franke, *Microfluid and Nanofluid*, 12, 229 (2011).
- ⁴⁷ G. Su, P. Worth Longest, and R. M. Pidapartia, *Biomicrofluidics*, 4, 044108 (2010).
- ⁴⁸ L. Y. Yeo and J. R. Friend, *Biomicrofluidics*, 3, 012002 (2009).
- ⁴⁹ M. B. Assouar, O. Elmazria, P. Kirsch, and P. Alnot, *J. Appl. Phys.* 101, 114507 (2007).
- ⁵⁰ M. Ishihara, T. Nakamura, F. Kokai, and Y. Koga, *Diamond Relat. Mater.* 11, 408 (2002).
- ⁵¹ F. Bénédic, M. B. Assouar, P. Kirsch, D. Monéger, O. Brinza, O. Elmazria, P. Alnot, and A. Gicquel, *Diamond Relat. Mater.* 17, 804 (2008).
- ⁵² J. G. Rodríguez-Madrid, G.F. Iriarte, D. Araujo, M.P. Villar, O.A. Williams, W. Müller-Sebert, and F. Calle, *Materials Letters*, 66, 339 (2012).
- ⁵³ O. Elmazria, V. Mortet, M. El Hakiki, M. Nesladek, and P. Alnot, *IEEE Transactions on Ultrasonics, Ferroelectrics and Frequency Control*, 50, 710 (2003).
- ⁵⁴ O. Auciello, A. Gruverman, H. Tokumoto, S.A. Prakash, S. Aggarwal and R. Ramesh, *MRS Bulletin*, 23, 37 (1998).
- ⁵⁵ K. Hirama, Y. Taniyasu and M. Kasu, *Japanese Journal of Applied Physics*, 49 (2010).
- ⁵⁶ M. Dubois and P. Muralt, *J. Appl. Phys.* 89, 6389 (2001).
- ⁵⁷ A. Artieda, M. Barbieri, C. S. Sandu and P. Muralt, *J. Appl. Phys.* 105, 024504 (2009).

Conclusions and Future Works

This thesis was focused on the design, simulation, fabrication and characterization of MEMS-based mass microsensors with protein sensing as the final goal. The thesis started with a modeling&simulation chapter where it was developed different types of MEMS-based mass microsensors using piezoelectric resonators in addition to a microtransponder chip circuit for the energization of the microvalve. It followed a fabrication chapter where it was described the production and characterization of the used materials, and the mass microsensors as had been designed and simulated previously.

Simulation

Related with the implementation of different numerical models for the analysis of the piezoelectric sensors performances, it have been shown that numerical simulation is of vital importance in a system design stage since it allows checking assumptions and a deep understanding of the represented phenomena. Furthermore, the design insights provided by these models are of vast importance in order to improve the performance of the device.

In the case of the QCM simulations (*Section 4.1*), it have been seen that results obtained with the circuital model approach fairly close to the analytical solutions (average error of 2.57% with an standard deviation of 1.4%) considering the deposition of Parylene[®]. The FEM model used for Parylene[®] deposition shows linearity between thicknesses and frequency shifts as indicated by Sauerbrey equation. This motivates the use of the model to estimate the deposition behavior.

For the PVDF material (*Section 4.2*) it was evidenced the importance of using the Mason model for particular cases; for instance, it is a very good alternative to the analytical model in cases where the amount of deposited material is such that the Sauerbrey equation becomes inaccurate. It was seen that the resonance frequency obtained with the macromodel for the PVDF resonator approaches fairly close to the reference results found for the FEM model presented for the unloaded microbalance. This slight difference (1.10%) may be due to the 1D nature of the Mason model compared with the 3D geometry used for the FEM model.

In the piezoelectric AlN microbalance case (*Section 4.3*), results fit well with the expected outcome. The protein depositions (streptavidin) showed the dissipation added by the viscous load to the system as well as the attenuation of the quality factor Q . When in contact with water, the observed damping obey to the quasi-shear vibration mode being independent of the frequency shifts.

The PVDF piezoelectric sensor subjected to different amounts of pressure on its surface (*Section 4.4*) showed the expected frequency shift, with a linear response of the shift vs. the applied pressure using a FEM model.

In summary, these results suggest the use of a reliable tool for modeling, as is the case of FEM models. This motivates the use of the employed models to estimate the performance of the proposed mass microsensors.

Fabrication

In the case of the PVDF resonator (*Section 5.1*), it was shown that simulations done previously are in a good agreement with the experimental results showed in that section. The frequency shift predicted by the Sauerbrey equation was evidenced in the comparison between the unloaded PVDF disk and the disk with film deposition. In the same manner, it was clear to see that the PVDF resonant disk with silver electrodes has a lower resonance frequency than the one with copper electrodes.

In the work presenting the extracted parameters of a PVDF disk resonator from experimental and 3D FEM model (*Section 5.2*), the values of k'_{33} and Q have demonstrated to be in agreement with the datasheet of the material. The FEM model has demonstrated to be a reliable tool for modeling and simulate non trivial geometries including materials with high internal viscoelastic losses such as the case of PVDF. It also was found to be an important tool for extracting valuable information from experimental data, revealing a good accuracy for the developed procedure.

A direct method of deposition of AlN on Si substrate avoiding polishing steps and thus reducing fabrication times has been demonstrated (*Section 5.3*). It have been shown that thin AlN films with high (002) orientation can be produced on surfaces with rms roughness ≤ 1 nm, as is the case of atomically flat SiO₂ surfaces. The columnar structure of the obtained AlN showed a highly textured film thus allowing the fabrication of SAW resonators and piezoelectric actuators. The Pt film has proven to be a good buffer layer serving also as bottom and top electrodes.

The research described in *Section 5.4* provides information for understanding the fundamental physical and chemical processes involved in the integration of piezoelectric AlN films with underlying UNCD, N-UNCD and B-UNCD layers. AlN films deposited on as grown UNCD or N-UNCD films exhibit relatively good (002) orientation, due to the fact that these diamond films exhibit rms surface roughness of about 5-10 nm, which is the size of the grains. The columnar structure of the (002) oriented AlN films grown on the UNCD layers enable relatively high piezoelectric coefficient (~ 1.91 pm/V), but still require AlN film thickness $\geq \sim 400$ nm to achieve the high (002) ALN orientation. A relatively high voltage (> 10 V), applied between the bottom and top electrodes sandwiching the AlN layer, is needed to produce the actuating piezoelectric effect in films as thick as 400 nm. It

would be desirable to achieve high (002) AlN orientation with films ≤ 100 nm to produce actuation at much lower voltages (≤ 2.5 V). In this sense, the CMP B-UNCD film, with rms surface roughness of about 0.2 nm, used as substrate, yielded a highly oriented (002) AlN films even as thin as 80 nm. The 200 nm thick AlN on UNCD layers exhibited a piezoelectric coefficient of about 5.3 pm/V, one of the highest for AlN film demonstrated today.

The feasibility in the fabrication of an FBAR AlN/diamond structure has been demonstrated in *Section 5.5*. AlN/diamond structure is a very promising device for FBAR applications so it opens a huge field of biomedical applications.

Future Works

Although the first research on integration of AlN films with CMP UNCD layers was done here using CMP B-UNCD films, further work is now proceeding to extend the integration of AlN films on CMP UNCD films in general, to determine what is the thinnest (002) oriented AlN film that can be grown on CMP UNCD layers to produce low voltage piezoelectrically actuated UNCD-based MEMS drug delivery devices. The low temperature of the UNCD, N-UNCD and B-UNCD growth and also the AlN deposition makes this innovative system compatible with CMOS chips and CMOS-driven MEMS and NEMS systems. Successful integration of piezoelectric AlN and BUNCD films may enable the development of a new generation of biocompatible piezoelectric-based drug delivery MEMS devices implantable in the human body.

Biomolecules used as recognition elements in biosensors could be based on either proteins, such as antibodies, enzymes and receptors or nucleic acids such as aptamers. For a FBAR biosensor principle, the reaction must result in a binding to or release of molecules from the surface, where the most common approach is the use of antibodies. In this sense, a mass microsensor capable of sensing protein deposition related with glaucoma pathology is desirable to be integrated in the implantable active microvalve. Works in this direction will be carried out by the author; in addition, the use of a biocompatible material like UNCD will be an excellent candidate to be functionalized with specific biomolecules.

Appendix A

CMOS Microtransponder for implantable microvalve

A.1 Introduction

Glaucoma is the “condition” associated with the optic nerve damage produced by increased intraocular pressure (IOP) resulting from the clogging of the tubes in the trabecular meshwork, which drain the eye’s humor to keep the IOP constant. This pathology leads to a progressive and irreversible loss of vision. The IOP is determined by the production, circulation and drainage of ocular aqueous humor (AH).¹

The treatment of glaucoma consists of topical or systemic IOP lowering agents or laser treatment. When these treatments are not effective, surgery is required and more complex cases require an implant of an aqueous shunt or glaucoma drainage device. These devices do not offer enough hydraulic resistance, and they can originate complications related with the hypotony in the post-operative period. Another cause of failure of implants is associated with an increase in the IOP caused by the tissue–implant reaction.² There have been attempts to replace the passive valves by active micro-valves using electrochemical^{3,4} or electromagnetic actuators,⁵ but several questions arise about biocompatibility and size issues.

In the patent of Guarnieri⁶ is described an active implantable micro-valve. The mechanism of the micro-valve includes a diaphragm made of a conjugated polymer (CP) that shows high deformation and the volume of which depends on the electric potential applied to a pair of electrodes.

In Figure A.1Figure, a schematic diagram and the components that comprise the active valve are shown. The regulator was designed to control the IOP by varying its resistance to the AH flow, by means of the deflection of the diaphragm. The regulator is conceptually a normally closed valve, with a small leakage flow. The hydraulic resistance of the regulator has a passive component due to the effects of fluid pressure on the diaphragm and an active component due to the change in the geometry. When a voltage difference in the range of 1–2 V is applied between the actuators' face, a deformation in the plane of the CPs in the range of 1–3% of its initial dimensions is produced.⁷

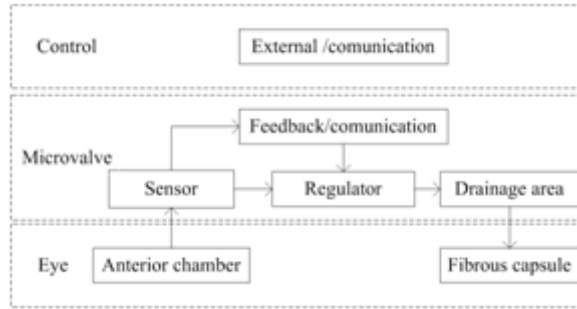


Figure A.1: Conceptual schematic of active valve for treatment of glaucoma.

The energization of the actuator is performed remotely based on the principles of radio frequency identification. In recent years, RFID technology has seen rapid growth in areas of supply chain management, access control, public transportation, airline baggage tracking and biomedical applications such as implantable sensors and actuators.⁸

This section presents an RF microtransponder circuit design and simulation for the energization of an active microvalve for the treatment of glaucoma. Simulation results show that the transponder operates to detect an Amplitude Shift Keying (ASK) signal with modulation index from 20% to 80% for a data rate of 500 kbits/s at a carrier frequency 13.56 MHz, with the possibility of varying the tension action of the membrane polymer.

The first part of this document shows the circuit block diagram and the specifications required, followed by the design considerations of the circuit design. Finally, the simulated results and conclusions are presented.

A. 2 Circuit Block Diagram

The implantable device operates based on the inductive coupling RFID principle.^{9,10} Figure A.2 shows the circuit block diagram of the device. An RFID reader transfers data and energy by sending a modulated RF wave using a Printed Circuit Board (PCB) antenna which couples with an off-chip microinductor that resonates at 13.56 MHz. The microtransponder circuits are on-chip as indicated by the rectangle. An RF voltage is induced by the magnetic field strength and boosted by the resonant circuit to a level that can power up the chip after rectification. In strong field case, the RF voltages are too high, causing potential damage to the circuit. To avoid this situation, RF clamping circuits must be added to limit the chip operating voltage to a safe level. A voltage rectifier circuit is used to convert the RF voltage to a DC voltage onto a capacitor. A voltage regulator is designed to maintain a constant voltage level used as the power supply for the chip.

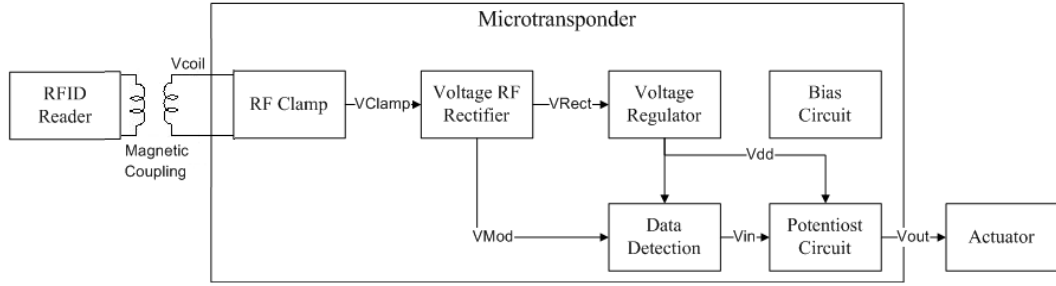


Figure A2: Circuit block diagram of active valve for treatment of glaucoma.

The bias circuit generates a bias current for analog blocks. The data is low pass filtered and detected by a data comparator. The DC converter takes the signal demodulated and passes a low-pass filter to generate a continuous voltage in the range of 0 to 1 V. Finally, the potentiostat circuit maintains a constant voltage on an electro-active polymer membrane, immersed in a wet electrolyte.

A.3 Circuit Design

A. RF Resonant and Clamp Circuit

Figure A.3 shows RF resonant and clamp circuit. L_r and C_r form an RF tank circuit with resonant frequency f_0 , and quality factor Q as:

$$f_0 = \frac{1}{2\pi\sqrt{L_r C_r}} \quad (A.1)$$

$$Q = \frac{R_L}{2\pi f_0 L_r}$$

where R_L is the equivalent load resistance of the transponder chip. The step-up RF voltage at the chip input is proportional to the circuit Q , which relates to the power consumption of the chip. The PMOS devices provide a voltage clamping function when the electromagnetic field strength is strong. $P1-P3$ will clamp V_{coil} in the positive direction while $P4-P7$ in the negative one. When these devices are on, they essentially conduct high currents and decrease the circuit Q , thus limiting the RF step-up voltage at V_{coil} node to less than 5.0 V for this 0.5 μm AMI process

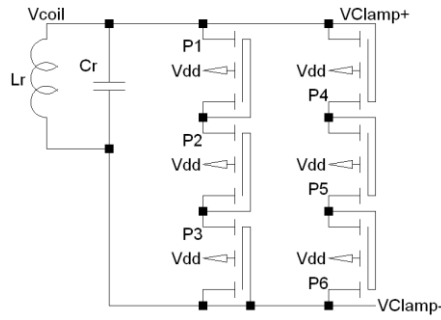


Figure A.3: RF resonant and clamp circuit.

B. RF Rectification

The voltage RF rectifier includes $P1-P2$, $N1-N2$ and $Crect$. The converted DC voltage is on $Crect$ (Figure A.4).

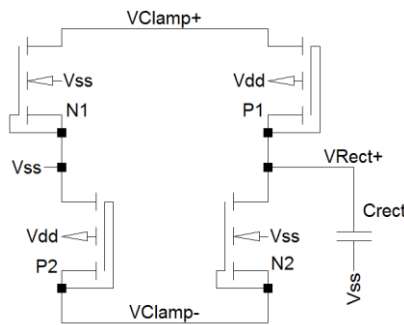


Figure A.4: Voltage rectifier circuit.

C. Voltage Regulator Circuit

A voltage regulator includes $P1-P3$, $N1-N7$, $R1$, $R2$, and $Creg$. This subcircuit is designed to maintain a constant voltage level of 2 V used as the power supply for the chip (Figure A.5).

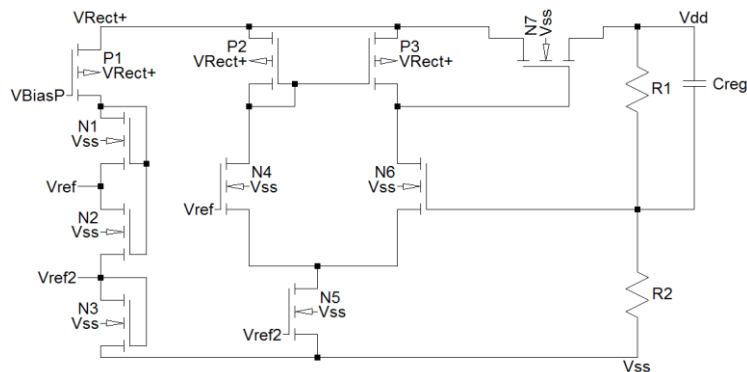


Figure A.5: Voltage regulator circuit.

D. Bias Circuit

As shown in Figure A.6, the bias current is generated using a current mirror circuit. The generated bias current has a typical value around $1\mu\text{A}$, which serves as the bias current for the data comparator and the potentiostat circuit.

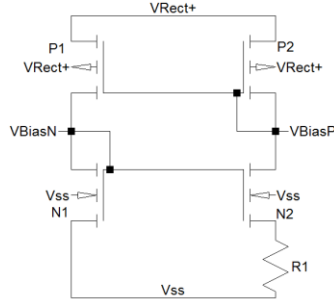


Figure A.6: Bias Circuit.

E. Data Detection

The microtransponder operates to detect an Amplitude Shift Keying (ASK) signal with modulation index from 20% to 80% for a data rate of 500 kbits/s at a carrier frequency 13.56 MHz. The data detection circuit demodulates the incoming ASK modulated signal and detected by a data comparator. The DC converter takes the signal demodulated and passes a low-pass filter to generate a continuous voltage in the range of 0 to 1 V (Figure A.7).

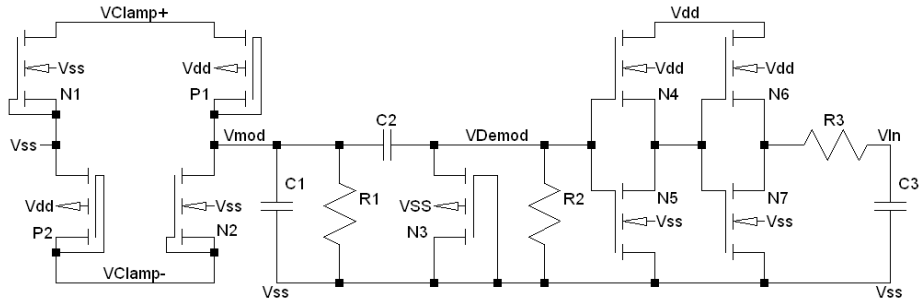


Figure A.7: Data detection circuit.

F. Potentiostat Circuit

The potentiostat circuit maintains a constant voltage on an electro-active polymer membrane. A fully differential (FD) potentiostat architecture is used (Figure A.8). In contrast to the single-ended (SE) architecture, the FD potentiostat can dynamically control the voltages on the auxiliary electrode (AE) and the working electrode (WE). The FD potentiostat can, thus, double the dynamic voltage range of the SE.^{11,12,13}

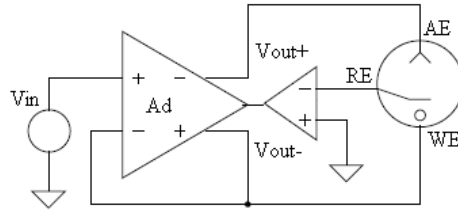


Figure A.8: Fully differential potentiostat architecture.

A.4 Simulations and Results

The circuit model of RFID reader consists of a voltage generator, the impedance matching network and the electric model of the external PCB antenna. The coupling coefficient between both antennas used is 0.02, which is a typical value for a weak coupling due to attenuation of the tissues.³ The circuit model of the implantable device includes RF circuit model of the resonant circuit, the Microtransponder circuit and an electric model of the actuator.

A. Inductive Coupling Modeling

Figure A.9 shows the simulated inductive coupling with 50% modulation index.

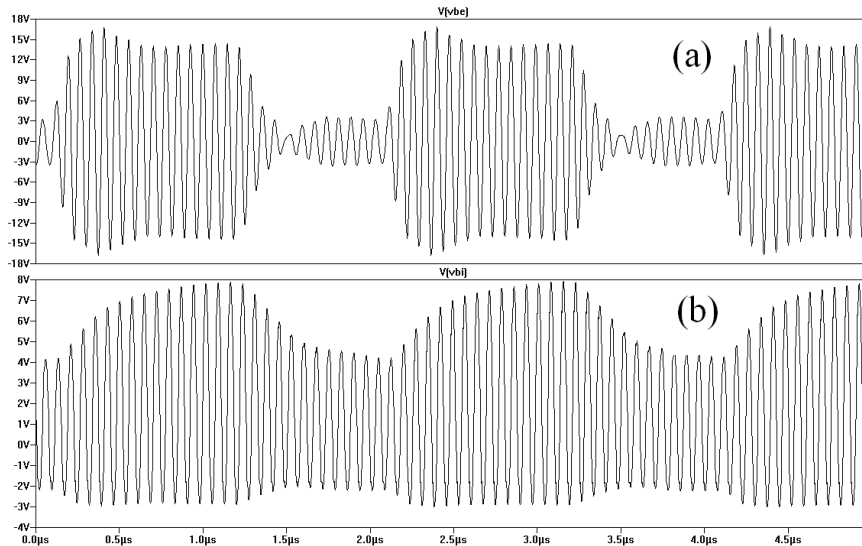


Figure A.9: Simulation plots of inductive coupling with 50% modulation index. (a) Voltage on the reader antenna. (b) Induced voltage in implantable antenna.

B. Supply Circuit Modeling

Figure A.10 shows the Simulation plots of Clamp, Rectifier and Regulator Circuits with 50% modulation index.

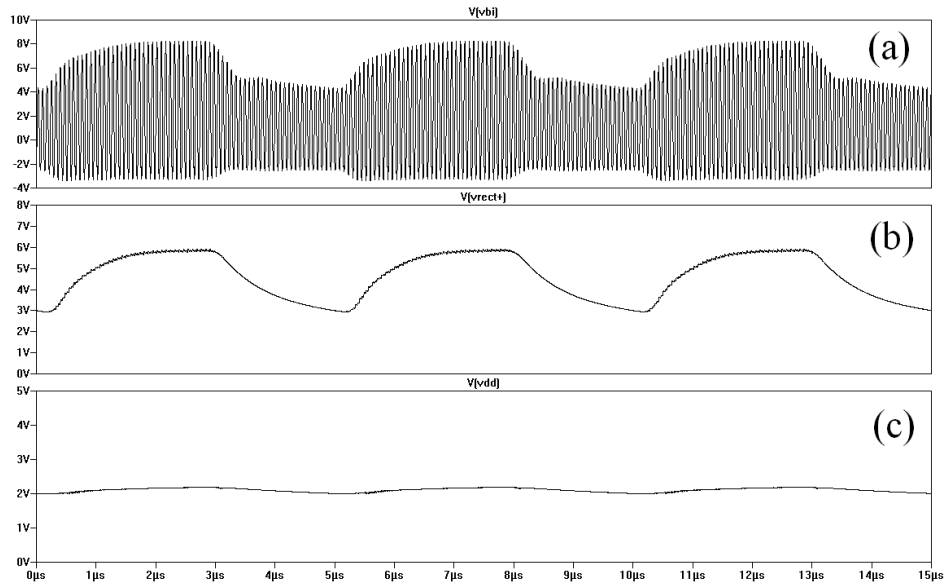


Figure A.10: Simulation plots of Clamp, Rectifier and Regulator Circuits with 50% modulation index. (a) Voltage RF Clamp. (b) Voltage RF Rectifier, (c) Voltage Regulator.

C. Data Detection Circuit Modeling

Figure A.11 shows the simulated data detection diagram with 50% modulation index.

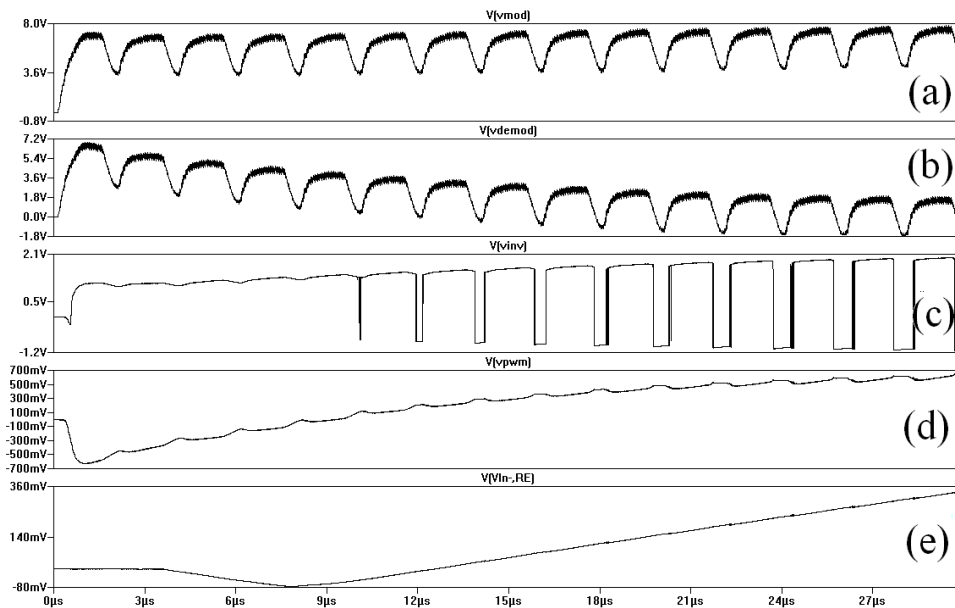


Figure A.11: Data modulation simulations with 50% modulation index. (a) Input modulated ASK signal. (b) Demodulated signal. (c) Voltage Comparator (d) Low pass Voltage. (e) Actuator Voltage.

The data modulation was simulated with modulation index from 20% to 80%. Table A.1 presents the results of actuator voltage.

Modulation Index [%]	Actuator Voltage [mV]
20	30
30	210
40	430
50	650
60	800
70	930
80	1050

Table A.1: Actuator Voltage vs Modulation Index.

Finally, Figure A.12 shows the complete layout of the circuit, that occupies a surface of 2.25 mm^2 .

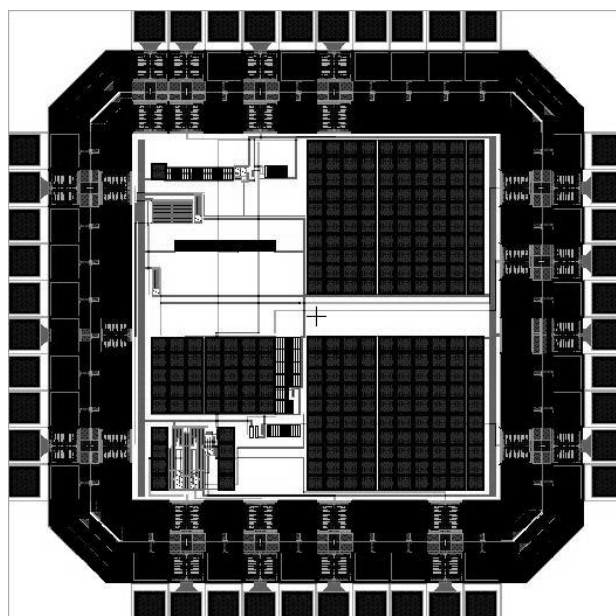


Figure A.12: Complete Circuit Layout.

A.5 Conclusions

An integrated RFDI Microtransponder for implantable medical devices applications was designed, simulated and it is currently under fabrication in AMI C5 ($0.5 \mu\text{m}$) technology.

It converts RF power to DC for the actuation of a CP. The transponder operates to detect an ASK signal with modulation index from 20% to 80% for a data rate of 500 kbits/s at a carrier frequency 13.56 MHz. Simulation results show that the DC converter takes the signal demodulated to generate a continuous voltage in the range of 0 to 1 V for the actuation of the polymer.

A.6 Bibliography

-
- ¹ F. Sassetti, F. A. Guarnieri, L. Garelli and M. A. Storti “Characterisation and simulation of an active microvalve for glaucoma,” *Computer Methods in Biomechanics and Biomedical Engineering*, DOI:10.1080/ 10255842.2011. 585978, 2011.
- ² CH. Hong, A. Arosemena, D. Zurakowski, R.S. Ayyala, “Glaucoma drainage devices: a systematic literature review and current controversies,” *Surv Ophthalmol.* 50(1):28–60, 2005.
- ³ C.R. Neagu, “A medical microactuator based on an electrochemical principle,” Universiteit Twente – Elektrotechniek. Available from: <http://doc.utwente.nl/13878/>, 2008.
- ⁴ T. Pan, A. Baldi and B. Ziaie, “Remotely adjustable check-valves with an electrochemical release mechanism for implantable biomedical Microsystems,” *Birck Nanotechnology Center Nanotechnology, Publications Purdue Libraries*, 2007.
- ⁵ B. Byunghoon, “In vitro experiment of the pressure regulating valve for a glaucoma implant,” *J Micromech Microeng.* 13:613–619, 2003.
- ⁶ F.A. Guarnieri, “Implantable ocular microapparatus to ameliorate glaucoma or an ocular overpressure causing disease,” Available from: <http://www.wipo.int/pctdb/en/wo.jsp?WO/2008084350>, 2007.
- ⁷ E. Smela, “Microfabrication of PPy microactuators and other conjugated polymer devices,” *J Micromech Microeng.* 9:1–18, 1999.
- ⁸ Q. Huang and M. Oberle, “A 0.5-mW Passive Telemetry IC for Biomedical Applications,” *IEEE Journal of Solid-state Circuits*, vol. 33, pp. 937-946, 1998.
- ⁹ K. Finkenzeller, *RFID Handbook*. John Wiley & Sons, pp. 53-104, 1999.
- ¹⁰ Y.L. Li and J. Liu, “A 13.56 MHz RFTD Transponder front-end with Merged Load Modulation and Voltage Doubler-clamping Rectifier Circuits,” III Congreso de Microelectrónica aplicada, Facultad de Ciencias Exactas, Ingeniería y Agrimensura. Universidad Nacional de Rosario, Santa Fe, Argentina, 2012.
- ¹¹ F.A. Guarnieri, M. Garcia Inza, J. Lipovezky, A. De La Plaza, “Potenciostato Implantable Integrado en Tecnología CMOS,” *II Congreso de Microelectrónica aplicada*, 2011
- ¹² S. M. Martin, F. H. Gebara, T. D. Strong and R. B. Brown, "A fully differential potentiostat," *IEEE Sensors J.*, vol. 9, p.135, 2009.
- ¹³ M.H. Nazari and R. Genov, "A fully differential CMOS potentiostat," *Circuits and Systems, ISCAS 2009. IEEE International Symposium*, vol., no., pp.2177-2180, 2009.

Appendix B

UNCD-based Drug Delivery Devices

An increasing demand to fulfill unmet clinical needs in healthcare has brought about a variety of new technologies to detect and treat a disease at an early stage and achieve a prompt therapeutic intervention. Early therapeutic interventions would result in higher survival rates, better quality of life for the patient and decreasing on healthcare costs for the healthcare system. From a therapeutic standpoint, searching for a better performance in therapeutic systems represents better compliance with the therapeutic regimen, decrease potential of adverse reactions and decreasing on health care costs. As a consequence a “medical technology paradigm shift” towards more reliable, faster, actively controlled and low cost technologies is urgently needed. Fortunately these kinds of technologies already exist in the market known as BioMEMS. This technology results from the integration of structural and functional microparts such as micro channels, microreservoirs, microsensors and microactuators and have recently been developed to overcome several limitations imposed by the current state of the art in pharmaceutical technology. In the case of drug delivery systems these limitations include poor control over geometry, poor control over payload of the drug, stability constraints on the systems influenced by thermodynamic or kinetic parameters, poor reproducibility between lots, lack of active control over the drug release among others. On the other hand BioMEMS for therapeutic applications are highly reproducible, could be integrated with electronics and actively controlled, their geometry could be tuned as desired, they are cost effective when batch production is needed, and drugs could be contained in a precise amount in a sealed environment keeping their properties intact. Drug delivery systems are important medical devices providing significant medical (improve pharmacokinetics decreasing drug dose and toxicity) and commercial (increasing product portfolio by adding new products and decreasing drug discovery costs by recycling old drugs) advantages.

In this section the design, fabrication and characterization of two different kinds of UNCD-based membranes for drug delivery devices were carried out. The first being a passive device where the drug diffuses through holes with controlled size, shape and spacing

between them. The second approach is an active system, where a piezoelectrically actuated valve allows a controlled drug release from a microreservoir by the application of an electric field.

B.1 Experimental

UNCD membranes were fabricated in a clean room facility using thin film deposition and microfabrication techniques, including: 1) UNCD thin film growth by microwave plasma chemical vapor deposition on a Si substrate after a nanodiamond seeding process on the silicon surface, 2) photolithography using a specially designed mask to define a window on the backside of the wafer, 3) reactive ion etching to pattern the Si_3N_4 mask for the cavity sustaining the UNCD membrane on the backside of the wafer, and 4) wet chemical etching to create the cavity sustaining the UNCD membrane. Square membranes of 200-1000 μm in size with a thickness ranging between 100-500 nm were fabricated and characterized by Raman spectroscopy, optical microscopy, scanning electron microscopy (SEM) and reflectometry.

1. Passive system

The passive system consists of a thin UNCD membrane where an array of microholes were performed. Size, shape and spacing between holes control the amount of drug diffusing from the interior of the DDS reservoir to the outside. Thus, an accurate design permits a predictable release of the drugs to the media.

Fabrication of passive drug delivery devices was done using the focused ion beam (FIB) technique to produce holes with micron size dimensions in the UNCD membranes to enable controlled drug diffusion through the latter (Figure B.1).

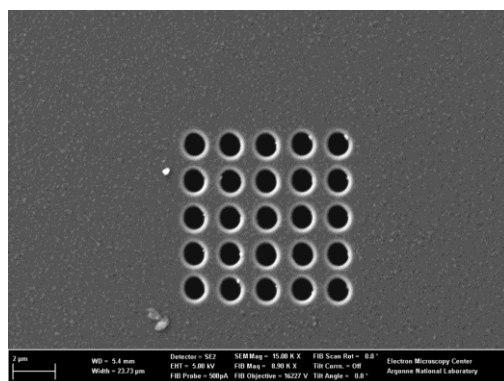


Figure B.1: SEM micrograph of the passive UNCD drug delivery device.

For this passive system, it can be seen in Figure B.1 an array of 5×5 circular holes with 1.217 μm diameter and 2.086 μm periodicity with a magnification of 8k x and no tilting of

the sample. Exposing the 5x5 array of 1 μm holes at a depth of $\sim 500\text{nm}$ took around 15 minutes.

The proposed drug delivery system is depicted in the following picture (Figure B.2), where the silicon substrate sustaining the holey membrane is attached to a polymer reservoir containing the drug solution to be released:

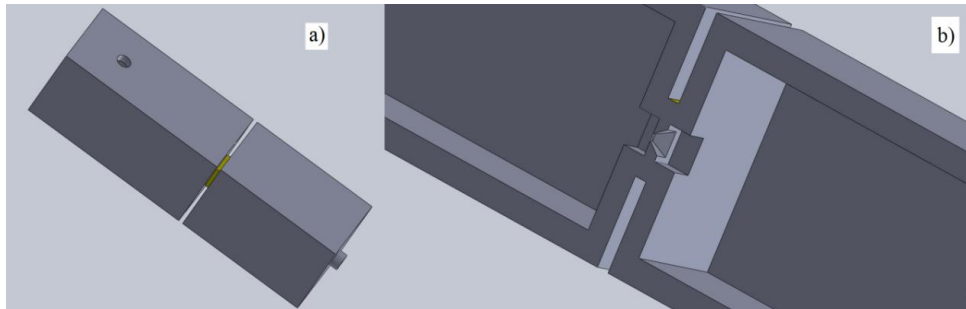


Figure B.2: Drug delivery device with selective UNCD membrane and polymer reservoirs. a) Complete system and b) holey membrane attached to polymer reservoirs.

PDMS was used to seal the bottom face of the Si substrate, where the integrated UNCD membrane/cavity structure was fabricated to create the reservoirs.

2. Active system

For the active drug delivery device based on a piezoelectrically actuated valve, a Pt/piezoelectric AlN/Pt layer heterostructure was grown on the UNCD membrane with a Ti adhesion layer, followed by FIB etching to define the valve aperture. The UNCD cantilever valve as the main part of the active system is depicted in Figure B.3:

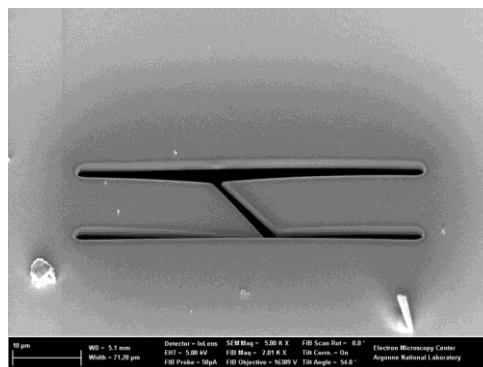


Figure B.3: Cantilever as part of the active system.

The active system involves the actuation of a piezoelectric valve made of Aluminum Nitride, capable of controlling drug delivery dose with an applied electric field. The active material, the piezoelectric AlN, works as a cantilever valve allowing the displacement of an aqueous media from a reservoir to the outside. The electric field along the thickness of the piezoelectric film is generated by the application of an electric potential between platinum top and bottom electrodes sandwiching the piezoelectric material.

The morphology and operation of the cantilever actuator is shown in the following numerical simulation (Figure B.4), where the piezoelectric layer is grown onto the top of the UNCD membrane, occupying a small part of the latter thus increasing the strain of the membrane of the valve.

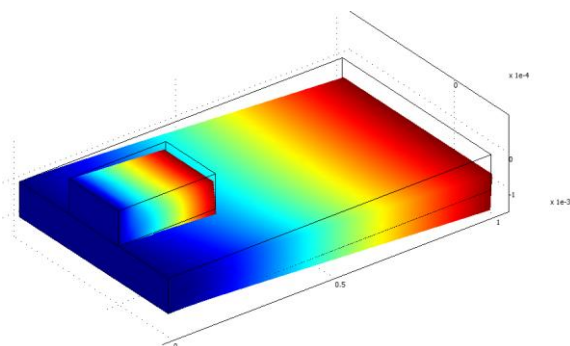


Figure B.4: Morphology and operation of the cantilever actuator.

B.2 Conclusions

Results of the experimental have showed a very promising way of producing drug delivery systems. The designs seems to be acceptable, supported by the fabrications done and the material used. Simulations helped to achieve a good design and to understand the principle of actuation. Works in this direction are need.

Appendix C

Resumen extendido



UNIVERSIDAD NACIONAL DEL LITORAL
Facultad de Ingeniería y Ciencias Hídricas
Instituto de Desarrollo Tecnológico para la Industria Química

**DISEÑO, SIMULACIÓN, FABRICACIÓN Y
CARACTERIZACIÓN DE MICROSENSORES DE MASA
INTEGRABLES A MICROVÁLVULA PARA EL
TRATAMIENTO DE GLAUCOMA**

Martín Zalazar

Tesis remitida al Comité Académico del Doctorado
como parte de los requisitos para la obtención
del grado de
DOCTOR EN INGENIERIA
Mención Mecánica Computacional
de la
UNIVERSIDAD NACIONAL DEL LITORAL

2013

Comisión de Posgrado, Facultad de Ingeniería y Ciencias Hídricas, Ciudad Universitaria, Paraje “El Pozo”,
S3000, Santa Fe, Argentina

Introducción

La línea de investigación más importante que está llevando cabo el Grupo de BioMEMS (FI-UNER y CIMEC-UNL/CONICET), al cual pertenece el autor de esta Tesis de Doctorado, está relacionada con el desarrollo de una microválvula implantable para aliviar la presión intraocular (IOP) en pacientes con glaucoma. Los antecedentes más importantes de este trabajo se enfocan en el diseño de una microválvula activa propuesta y patentada por el Dr. Guarnieri, director del grupo de investigación.^{1,2,3}

El glaucoma es una de las causas más frecuentes de ceguera. El glaucoma es un patología que afecta 1.2 % de la población. Las presiones elevadas (mayores a 20 mmHg.) pueden provocar una pérdida de visión si se mantienen durante un período prolongado. En pacientes con glaucoma, para evitar la ceguera es necesario bajar la presión ocular a través de medicación o mediante técnicas quirúrgicas. Cuando los tratamientos anteriores no logran su objetivo, se implantan válvulas para permitir el drenaje de humor acuoso y bajar la presión intraocular.

El desarrollo de la tecnología MEMS (Micro ElectroMechanical Systems) y la generación de nuevos materiales permiten abordar el desarrollo de microdispositivos implantables, tales como la microválvula, con mejoras en la biocompatibilidad como también en la reducción del tamaño y el consecuente daño ocasionado en el procedimiento quirúrgico.

La válvula ideal sería aquella que cambie su resistencia hidráulica manteniendo la presión intraocular en el rango fisiológico, considerando las características particulares del paciente y evitando las complicaciones que devienen de la hipertensión y de la hipotensión ocular. Para ello, la estrategia es sumar a la estructura de la microválvula sensores que permitan detectar los parámetros más relevantes, como IOP y proteínas relacionadas con el aumento de la misma.

La IOP ha sido considerada el factor de riesgo más importante de la aparición y progreso del glaucoma. En los últimos años se ha encontrado que el daño del nervio óptico en personas con glaucoma continúa progresando aún cuando la IOP está controlada. Es por esto que las investigaciones actuales se están enfocando en elucidar los mecanismos intervinientes en la supervivencia, adaptación y muerte de las células ganglionares de la retina para hallar los factores que causan el daño celular.

¹ F. A. Guarnieri, PICT 2004. Número 25791 Proyecto Diseño, Simulación y fabricación de BioMEMS.

² F. A. Guarnieri, Concurso Nacional de Innovaciones - Innovar 2007 www.innovar.gov.ar/galeria/ver-proyecto?proyecto=1879

³ F. A. Guarnieri, Patente de Invención AR058947 (A1) "Microaparato implantable en el ojo para aliviar glaucoma o enfermedad causante de sobrepresión ocular"; WO2008084350 (A2) "implantable ocular microapparatus to ameliorate glaucoma or n ocular overpressure causing disease"

Los nuevos descubrimientos podrían contribuir al desarrollo de medios terapéuticos eficaces para proteger las células nerviosas de la retina y contrarrestar los procesos fisiopatológicos implicados en el glaucoma. En este sentido, Alexandrescu et al. 2010 ha encontrado la influencia de la glicoproteína CD44 y algunas moléculas (TGF-beta2, TNF alfa) relacionadas con el glaucoma. Grus et al. 2008 encontró que la Transtiretina podría desempeñar un papel en la aparición de glaucoma, ya que se ha demostrado la formación de depósitos amiloides que causan obstrucciones de flujo de salida lo que aumenta la IOP. También, Rao et al. 2008 demostró que la inhibición de la isoprenilación de proteínas CaaX en la vía de salida del humor acuoso, aumenta su salida.

La microválvula activa ideal tiene que ser capaz de sensor la IOP y actuar en función de los valores sensados. De esta manera, el conocimiento de ciertas moléculas involucradas en el progreso del glaucoma hará más eficiente el funcionamiento del implante. En este sentido, un microsensor de masa (o sensor gravimétrico) capaz de detectar la deposición de masa (por ejemplo proteínas) es deseable; el microsensor también tiene que poseer la capacidad de ser implantado e integrado con la microválvula activa. Además de estos aspectos, la microválvula activa ideal debe cumplir con los requisitos de un implante activo: la comunicación inalámbrica, lo que permite la medición telemétrica y el suministro de energía a distancia.

Esta tesis se centra en el diseño, simulación, fabricación y caracterización de microsensors de masa desarrollados con tecnología en MEMS para la detección de proteínas. La tesis parte de un capítulo de modelado y simulación donde se desarrollan diferentes tipos de microsensors de masa utilizando resonadores piezoeléctricos además de un chip microtransponder para la energización de la microválvula. De ello se deduce un capítulo de fabricación donde se describe la producción y caracterización de los materiales utilizados y los microsensors de masa diseñados y simulados.

Descripción de las secciones

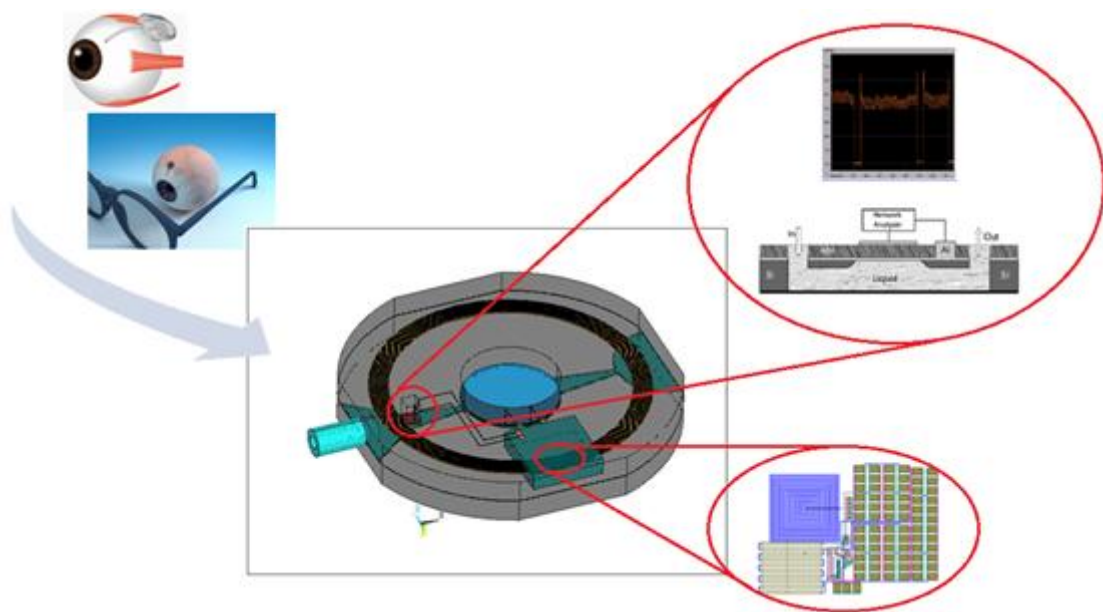
El diseño, desarrollo y eventual implementación de un dispositivo con características innovadoras requiere de tiempo y recursos para poder ser llevado a cabo. En el caso de la aplicación de tecnologías novedosas es necesaria la maduración de nuevos conceptos además de la aplicación de conocimientos. Existen herramientas que facilitan de alguna forma estas tareas permitiendo, entre otras cosas, ahorro de tiempo. La simulación numérica es una herramienta fundamental a la hora el diseño de un sistema, ya que permite comprobar supuestos y comprender con mayor claridad el fenómeno representado y de esta manera ahorrar tiempos y optimizar recursos.

Los trabajos llevados a cabo en esta Tesis de Doctorado están vinculados principalmente al diseño, simulación, fabricación y caracterización de microsensors resonantes como sensores de masa para la detección de deposición de proteínas. Debido a su gran sensibilidad a la deposición de pequeñas cantidades de masa, estos sensores se presentan como una excelente opción para el sensado de proteínas y células del humor acuoso directamente relacionadas con la variación de la presión intraocular.

Considerando la biocompatibilidad del implante, se hizo uso de diamante ultrananocristalino (UNCD) como material estructural de los microsensors resonantes, que es un material novedoso y altamente bioinerte. También se trabajó con materiales como el Parylene®, que es utilizado en la actualidad como revestimiento biocompatible. Como material piezoeléctrico, se halló interesante el uso de polivinilideno fluoruro (PVDF), que reviste de gran importancia en aplicaciones biomédicas debido a sus propiedades acústicas.

Para bajar costos y mejorar la compatibilidad de la electrónica asociada, se requiere que los sensores estén integrados con la misma. Uno de los materiales mayormente utilizado como resonador para aplicaciones electroacústicas es el Nitruro de Aluminio (AlN) debido a su excelente calidad para la fabricación de resonadores acústicos y su compatibilidad con los procesos de fabricación de los circuitos integrados. De esta manera, se consideró de mucha importancia profundizar en el uso de este material.

La gráfica a continuación describe la integración de los sensores gravimétricos para la detección de proteínas y el chip microtransponder con la microválvula:



Diseño de la microválvula describiendo la integración del sistema con el microsensor piezoeléctrico y el chip microtransponder.

Objetivos

Objetivo general

- Diseñar, simular, fabricar y caracterizar prototipos de microsensores de masa integrables a microválvula implantable para el tratamiento de glaucoma.

Objetivos particulares

- Modelar y simular microsensores gravimétricos mediante el método de elementos finitos.
- Fabricar microsensores gravimétricos utilizando tecnología MEMS y caracterizarlos.
- Optimizar los diseños de los microsensores gravimétricos interactuando entre resultados de la simulación y los resultados experimentales.
- Evaluar funcionalidad y eficiencia de los microsensores de masa utilizando diferentes materiales potencialmente biocompatibles.
- Determinar el mejor film de AlN con el mayor coeficiente piezoeléctrico sobre películas de UNCD.
- Diseñar, fabricar y caracterizar diferentes tipos de membranas basadas en películas de UNCD para suministro de drogas.
- Modelar y simular chip microtransponder para comunicación inalámbrica con microsensores.
- Analizar factibilidad de desarrollo de microsensores de presión.

C.1 Dispositivos acústicos

C.1.1 Piezoelectricidad

C.1.1.1 Origen de la polarización

Piezoelectricidad se denomina a las cargas acumuladas en determinados materiales sólidos en respuesta a la tensión mecánica aplicada al mismo. Cuando el material piezoeléctrico no se encuentra sujeto a tensiones mecánicas externas, los centros de simetría de las cargas positivas y negativas de cada molécula coinciden en su ubicación. De esta manera los efectos externos de las cargas positivas y negativas se cancelan mutuamente. Como resultado se obtiene una molécula eléctricamente neutra. Cuando se ejerce presión sobre el material, su estructura interna reticular se deforma, causando la separación de los centros de gravedad positivos y negativos de las moléculas, generando pequeños dipolos. La distribución de cargas en las superficies del material hace que el mismo esté polarizado. Esta polarización genera un campo eléctrico el cual puede ser usado para transformar energía mecánica en energía eléctrica.

C.1.1.2 Formulación matemática del efecto piezoeléctrico

La piezoelectricidad implica el acoplamiento entre las propiedades mecánicas y eléctricas del material. La relación existente entre estas dos propiedades está dada por el vector de polarización piezoeléctrica \mathbf{P} (1x3).

Un campo eléctrico causa una separación física entre cargas positivas y negativas creando un momento dipolar por unidad de volumen \mathbf{p} (1x3) en Cm . La polarización \mathbf{P} en C/m^2 se define como:

$$\mathbf{P} = N\mathbf{p}$$

donde N es el número de dipolos por unidad de volumen. La polarización \mathbf{P} es un vector y, en general, es proporcional al campo eléctrico:

$$\mathbf{P} = \varepsilon_0 \boldsymbol{\kappa} \mathbf{E}$$

donde \mathbf{E} (3x1) es el campo eléctrico externo, $\varepsilon_0 = 8.85 \times 10^{-12}$ F/m es la permitividad del espacio libre y la susceptibilidad eléctrica $\boldsymbol{\kappa}$ provee la conexión entre \mathbf{E} y \mathbf{P} . La susceptibilidad es una propiedad exclusiva del material que establece cuán fácil el material se polariza cuando se encuentra sujeto a un campo eléctrico. Ya que \mathbf{E} y \mathbf{P} son vectores, $\boldsymbol{\kappa}$ debe ser una matriz de 3x3. El vector desplazamiento se define como:

$$\mathbf{D} = \varepsilon_0 \mathbf{E} + \mathbf{P} = \varepsilon_0 \mathbf{E} + \varepsilon_0 \boldsymbol{\kappa} \mathbf{E} = \varepsilon_0 (1 + \boldsymbol{\kappa}) \mathbf{E} = \boldsymbol{\varepsilon} \mathbf{E}$$

Para un medio isotrópico, la matriz $\boldsymbol{\varepsilon}$ se reduce a un escalar quedando

$$\boldsymbol{\varepsilon} = \varepsilon_r \varepsilon_0$$

En un medio piezoeléctrico, un vector de polarización es creado no solo por un campo eléctrico externo sino también por la tensión mecánica aplicada que deforma la estructura cristalina del piezoeléctrico causando la separación de cargas. La polarización resultante se adiciona a la causada por el campo eléctrico externo. Se tiene:

$$\mathbf{P} = \mathbf{d} : \mathbf{T}$$

donde \mathbf{d} es la matriz de deformación piezoeléctrica en C/N . Ahora \mathbf{D} posee dos componentes, uno proporcional a \mathbf{E} y el otro a \mathbf{T} . Pero este acoplamiento entre la polarización y la tensión mecánica depende de la clase de simetría del material. Considerando la simetría de la matriz $\mathbf{T} \rightarrow (T_{ij} = T_{ji})$, la matriz \mathbf{d} tiene 18 componentes independientes. En notación indicial, el índice i toma valores del 1 al 3 y el índice j toma valores del 1 al 6. El efecto piezoeléctrico inverso queda definido con la siguiente relación:

$$S_j = d_{ji} E_i$$

donde d_{ji} es la traspuesta de d_{ij} y poseen las mismas unidades. Resumiendo, se puede escribir:

$$P_i = \kappa_{ij} \varepsilon_0 E_j + d_{ij} T_j$$

$$S_j = d_{jk} E_k + s_{jk} T_k$$

Llevando las variables eléctricas a \mathbf{E} y \mathbf{D} :

$$D_i = \varepsilon_{ij}^T E_j + d_{ij} T_j$$

$$S_j = d_{jk} E_k + s_{jk}^E T_k$$

Los supraíndices T y E denotan que la permitividad y la complianza deben ser medidas bajo condiciones de tensión y campo eléctrico constantes. Modificando las ecuaciones anteriores para tener como variable independiente la deformación, quedan las siguientes dos ecuaciones:

$$D_i = \varepsilon_{ik}^S E_k + e_{ij} S_j$$

$$T_l = -e_{lk} E_k + c_{lj}^E S_j$$

donde $e_{lk} = c_{kj}^E d_{jk}$ con c_{kj}^E la matriz elástica. En forma matricial se obtiene:

$$\mathbf{D} = \boldsymbol{\varepsilon}^S \mathbf{E} + \mathbf{e}^T \mathbf{S}$$

$$\mathbf{T} = -\mathbf{e} \mathbf{E} + \mathbf{c}^E \mathbf{S}$$

con \mathbf{T} (6x1) el vector de esfuerzo mecánico, \mathbf{S} (6x1) el vector de deformación mecánica, \mathbf{E} (3x1) el vector de campo eléctrico, \mathbf{D} (3x1) el vector de desplazamiento eléctrico, \mathbf{c} (6x6) la matriz elástica con \mathbf{E} constante, $\boldsymbol{\varepsilon}$ (3x3) la matriz de coeficientes dieléctricos a deformación constante y \mathbf{e} (6x3) la matriz de acoplamiento piezoeléctrico.

C.1.2 Tecnología electroacústica

La electroacústica implica la transformación de energía acústica en energía eléctrica y viceversa. Comúnmente esta transformación se lleva a cabo a través de materiales piezoeléctricos. Los más utilizados han sido los dispositivos de onda acústica de volumen (BAW) y los dispositivos de onda acústica de superficie (SAW). Solamente la industria de las telecomunicaciones consume billones de filtros anualmente.

Como sensores, los más comúnmente utilizados basan su principio de funcionamiento en el cambio en las características del camino acústico de la onda viajera. Existen varias formas de detectar los cambios antes mencionados. En la forma activa, el sensor forma parte de un circuito electrónico oscilante en donde el cambio en las características del camino acústico de la onda, produce un cambio en la frecuencia del oscilador. Otra alternativa es la de obtener la información de estos sensores acústicos en forma pasiva. Esto se logra proporcionando una señal eléctrica de test y determinando la respuesta del sensor a dicha señal.

C.1.3 Resonador electroacústico

C.1.3.1 Modo de operación

El principio de funcionamiento básico de un sensor de onda acústica genérico es una onda viajera confinada dentro de una estructura, produciendo así ondas estacionarias; su frecuencia es determinada por la velocidad de la onda y las dimensiones de la estructura.

Es común hallar sensores resonantes tipo BAW excitados en el espesor; estos representan un plato acústico resonador, generalmente constituido por material piezoeléctrico en donde las ondas acústicas son generadas aplicando un campo eléctrico perpendicular a la superficie principal del plato que además se reflejan en los bordes del plato. A continuación, en la Figura C.1 muestra un esquema de las ondas incidentes y reflejadas dentro de una cavidad resonante:

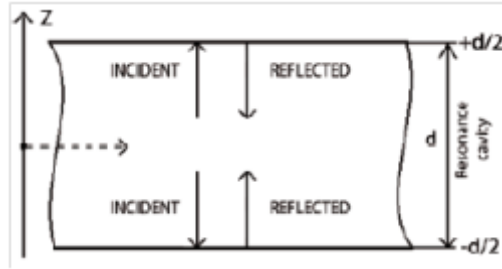


Figura C.1: Esquema de las ondas generadas y reflejadas dentro de una cavidad resonante.

El campo eléctrico es aplicado generalmente a través de una señal senoidal, y a la frecuencia de resonancia, las ondas incidentes y reflejadas interfieren en forma constructiva dentro de la cavidad, generando la *resonancia mecánica*.

La frecuencia de resonancia depende de la cavidad resonante (configuración, material, espesor) y del medio en que se encuentra. Por otra parte, las propiedades de todos los materiales involucrados y, consecuentemente, la frecuencia de resonancia, son directamente afectadas por la temperatura y la tensión mecánica.

C.2 Modelado

C.2.1 Modelo Analítico (Ecuación de Sauerbrey)

Como lo establece la ecuación de Sauerbrey, el cambio en la frecuencia de resonancia (f_r) de un material piezoeléctrico debido a la deposición de un film, para el modo vibracional de corte es:

$$\Delta_f = \frac{f_0 \rho_f h_f}{\rho_p h_p}$$

donde ρ_p es la densidad del piezoeléctrico, ρ_f la densidad del film, h_f el espesor del film y h_p el espesor del piezoeléctrico. Este modelo se empleó para validar el modelo FEM y el modelo circuital para los resonadores piezoeléctricos.

Esta ecuación considera un corrimiento de fase pequeño de la onda acústica mientras atraviesa el material de deposición y esta condición impone la limitación de ser aplicable a la deposición de películas rígidas y delgadas.

C.2.2 Modelo de Mason

Un modelo más real para dispositivos acústicos puede ser construido utilizando el modelo de Mason. Este modelo presenta un circuito equivalente exacto que separa el material piezoeléctrico en un puerto eléctrico y dos puertos acústicos utilizando un transformador electromecánico ideal como el de la Figura C.2.

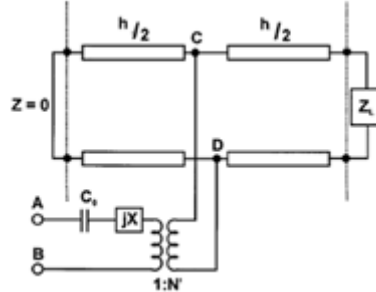


Figura C.2: Representación en líneas de transmisión de un resonador piezoeléctrico con una superficie libre de tensión y la otra con carga, basado en el modelo de Mason de tres puertos.

El puerto eléctrico está caracterizado por una reactancia eléctrica jX y un transformador con una relación de transformación de N' que acopla electromecánicamente el voltaje aplicado en A-B al desplazamiento en C-D. De esta manera se representa el dispositivo resonante como una línea de transmisión acústica formada por una capa piezoeléctrica y una o más cargas mecánicas de superficie (Z_L) compuestas por impedancias discretas, imponiendo condiciones de contorno en sus extremos. Este tratamiento produce una descripción matemática generalizada de la superficie del resonador que no usa otra aproximación más que la suposición de unidimensionalidad.

La impedancia compleja eléctrica de entrada para un resonador es:

$$Z = Z_{AB} = \frac{1}{j\omega C_0} + jX + \frac{1}{(N')^2} Z_{CD}$$

donde Z_{CD} es la impedancia acústica en C-D y C_0 la capacitancia estática. Esta impedancia puede ser representada como la capacidad C_0 en paralelo con una impedancia de movimiento Z_m proveniente de la resonancia mecánica.

Se utilizó este modelo como una aproximación más exacta que la solución analítica, siendo capaz además de modelar materiales compuestos y una gran variedad de materiales de deposición incluyendo medios líquidos.

C.2.3 Modelo Circuital

El circuito equivalente Butterworth-Van Dike (BVD) tiene la siguiente forma:

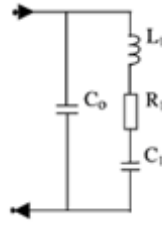


Figura C.3: Circuito equivalente BVD para un material piezoeléctrico.

Esta situación corresponde al caso en el cual el piezoeléctrico se encuentra sin perturbación, esto es, sin un cambio en la masa debido a la deposición de algún material. En el caso en que la superficie del resonador se encuentre con alguna carga, esta nueva situación se puede modelar utilizando el circuito equivalente Butterworth-Van Dike Modificado (MBVD). Esta nueva configuración agrega una impedancia en serie, la impedancia de movimiento creada por la carga en la superficie. Pero estos cambios en la masa no aparecen directamente como cambios lineales en los parámetros eléctricos, sino que resultan de cambios en las propiedades acústicas en la interfase entre el resonador y el material depositado. Para el caso de espesores suficientemente pequeños y rígidos de deposición de material (módulo de corte $G > 1 \text{MPa}$), en donde estos se mueven en forma sincrónica con la superficie del material oscilante, la ecuación de esta impedancia es:

$$Z_m^L = \left(\frac{\pi}{4K_e^2 \omega_0 C_0} \right) \left(\frac{Z_L}{Z_p} \right)$$

Esta nueva impedancia Z_m^L se implementa como una inductancia L_f en serie con L_1 , C_1 y R_1 y cuyo valor está dado por Z_m^L / ω_0 . Los modelos del circuito eléctrico se implementaron en *LTSpice* que es un simulador de circuitos electrónicos.

C.2.4 Modelo de Elementos Finitos

Se modelaron geometrías diferentes para cada material piezoeléctrico. Se utilizaron sólidos 3D elástico lineal piezoeléctrico para los materiales piezoeléctricos. Para modelar el material depositado y los electrodos se utilizaron sólidos 3D elástico lineal y para la deposición de proteínas, sólidos 3D viscoelásticos.

Las ecuaciones que gobiernan el problema de piezoelectricidad son la relación constitutiva de la piezoelectricidad lineal

$$\mathbf{D} = \boldsymbol{\varepsilon}^S \mathbf{E} + \mathbf{e}^T \mathbf{S}$$

$$\mathbf{T} = -\mathbf{e} \mathbf{E} + \mathbf{c}^E \mathbf{S}$$

y las ecuaciones de balance mecánico

$$\nabla \cdot \mathbf{T} = \rho \frac{\partial^2 \mathbf{u}}{\partial t^2}$$

y eléctrico

$$\nabla \cdot \mathbf{D} = 0$$

donde

$$\mathbf{S} = \frac{1}{2} (\nabla \mathbf{u} + \nabla^T \mathbf{u})$$

$$\mathbf{E} = -\nabla \phi$$

con \mathbf{T} (6x1) el vector de esfuerzo mecánico, \mathbf{S} (6x1) el vector de deformación mecánica, \mathbf{E} (3x1) el vector de campo eléctrico, \mathbf{D} (3x1) el vector de desplazamiento eléctrico, \mathbf{c} (6x6) la matriz elástica con E constante, $\boldsymbol{\varepsilon}$ (3x3) la matriz de coeficientes dieléctricos a deformación constante, \mathbf{e} (6x3) la matriz de acoplamiento piezoeléctrico, \mathbf{u} el vector de desplazamiento mecánico, $\ddot{\mathbf{u}} = \partial^2 \mathbf{u} / \partial t^2$ la aceleración y ϕ el potencial eléctrico.

La forma matricial del problema luego de la discretización espacial en el problema variacional es:

$$\mathbf{M}_{uu} \ddot{\mathbf{u}} + \mathbf{C}_{uu} \dot{\mathbf{u}} + \mathbf{K}_{uu} \mathbf{u} + \mathbf{K}_{u\phi} \phi = \mathbf{F}$$

$$\mathbf{K}_{u\phi}^T \mathbf{u} + \mathbf{K}_{\phi\phi} \phi = \mathbf{Q}$$

Donde

$$\mathbf{M}_{uu} = \mathbf{A}_{e=1}^{n_e} \int_{\Omega^e} \rho \mathbf{N}_u^{eT} \mathbf{N}_u^e d\Omega^e$$

$$\mathbf{K}_{uu} = \mathbf{A}_{e=1}^{n_e} \int_{\Omega^e} (\nabla \mathbf{N}_u^e)^T \mathbf{C} (\nabla \mathbf{N}_u^e) d\Omega^e$$

$$\mathbf{K}_{u\phi} = \mathbf{A}_{e=1}^{n_e} \int_{\Omega^e} (\nabla \mathbf{N}_u^e)^T \mathbf{e}^T (\nabla \mathbf{N}_\phi^e) d\Omega^e$$

$$\mathbf{K}_{\phi\phi} = \mathbf{A}_{e=1}^{n_e} \int_{\Omega^e} (\nabla \mathbf{N}_\phi^e)^T \boldsymbol{\varepsilon}^T (\nabla \mathbf{N}_\phi^e) d\Omega^e$$

son las matrices elementales, con \mathbf{C}_{uu} la matriz de amortiguamiento, \mathbf{F} el vector de fuerzas mecánicas nodales, \mathbf{Q} el vector de carga eléctrica nodal, \mathbf{u} el vector de desplazamiento nodal, ϕ el vector de potencial nodal y $\mathbf{A}_{e=1}^{n_e}$ el operador de ensamblado representando las contribuciones elementales de ensamblaje para el sistema global de matrices.

En el análisis en el dominio frecuencial, cuando el fenómeno dinámico se encuentra en estado estacionario con función de fuerza periódica y respuesta con frecuencia angular

$\omega = 2\pi f$, la dependencia del tiempo puede ser eliminada del problema y las incógnitas del sistema se convierten en variables armónicas complejas:

$$\mathbf{u} = \hat{\mathbf{u}}\mathbf{e}^{j\omega t}$$

$$\phi = \hat{\phi}\mathbf{e}^{j\omega t}$$

$$\partial(\cdot)/\partial t = j\omega(\cdot)$$

$$\partial(\cdot)^2/\partial t^2 = -\omega^2(\cdot)$$

En el dominio frecuencial se obtienen las siguientes formas matriciales:

$$-\omega^2\mathbf{M}_{uu}\mathbf{u} + j\omega\mathbf{C}_{uu}\mathbf{u} + \mathbf{K}_{uu}\mathbf{u} + \mathbf{K}_{u\phi}\phi = \mathbf{F}$$

$$\mathbf{K}_{u\phi}^T\mathbf{u} + \mathbf{K}_{\phi\phi}\phi = \mathbf{Q}$$

El software de elementos finitos COMSOL Multiphysics fue usado para modelar y simular los dispositivos propuestos en esta tesis. El potencial eléctrico se aplica sobre las caras principales del disco resonador. Inicialmente los efectos de amortiguamiento del entorno son despreciados y los bordes son fijados. Se utilizó en todos los casos interpolación cuadrática y elementos prismáticos en la discretización e integración de 4to. orden.

En este software la excitación armónica es especificada y se asume una respuesta armónica de igual frecuencia angular que la excitación. El análisis de respuesta en frecuencia es llevado a cabo con un resolvidor paramétrico. Éste realiza un barrido en frecuencia con varias frecuencias de excitación. Para la obtención de la admitancia característica $Y(\omega)$, se utilizó la siguiente ecuación:

$$Y(\omega) = \frac{I(\omega)}{V}$$

donde $I(\omega)$ es la transformada de Fourier de la corriente, esta última obtenida como la integración de la densidad de corriente $i(t)$ en una de las caras principales del dispositivo.

C.3 Simulación

C.3.1 Microbalanza de cristal de cuarzo (QCM)

Las QCMs están constituidas por un delgado disco de cristal de cuarzo al cual se le fijan los electrodos para la estimulación y sensado. Los modos de oscilación de los cristales se corresponden con su deformación, la cuál es dependiente del corte del cristal. Para un

modo vibracional de corte, el cristal tiene un corte AT, el cuál posee una orientación específica de 35°15' respecto del eje óptico y en donde las ondas acústicas se propagan en dirección perpendicular a la superficie del cristal.

En esta sección se realizó un análisis del comportamiento de una QCM para diferentes cantidades de material depositado en su superficie. Se llevó a cabo su diseño y también su simulación mediante dos modelos: circuital y de elementos finitos.

C.3.1.1 Metodología

a) QCM sin material depositado usando Modelo Circuital y FEM

Se obtuvo la f_r y se la contrastó con la analítica y la del modelo FEM. Los valores de los componentes se obtuvieron en base a las dimensiones del cuarzo y sus parámetros materiales para un corte AT.

b) QCM con deposición de Parylene[®] usando Modelo Circuital y FEM

Para la masa depositada se utilizó el polímero Parylene[®] que es un material en donde la medición de su deposición es una potencial aplicación para una QCM. Su espesor de deposición se encuentra en un rango que va desde el micrón hasta los 20 μm aproximadamente.

C.3.1.2 Resultados

a) QCM sin material depositado

Se obtuvieron gráficas mostrando la admitancia equivalente y la fase del circuito en función de la frecuencia. Se observó que la f_r se encuentra en los 5.0139MHz para el modelo circuital. Para el modelo FEM la frecuencia de resonancia se encuentra cerca de 5.0302MHz.

El desplazamiento del dispositivo no es uniforme en toda la superficie y tiene un máximo en el centro. Este fenómeno puede apreciarse en la Figura C.4 a partir del modelo FEM, donde los desplazamientos tienen un máximo en el centro del disco y disminuyen hacia los bordes del electrodo:

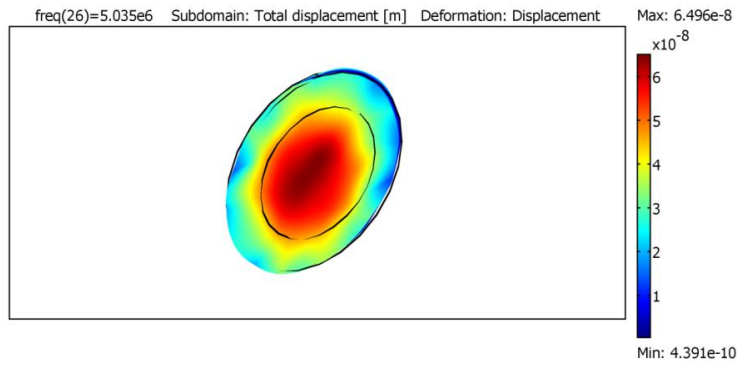


Figura C.4: Respuesta vibracional de la QCM.

b) QCM con deposición de Parylene®

El modelado FEM de este sistema se muestra en la Figura C.5, en la cual se exhibe el aspecto físico del disco con material depositado, su respectivo mallado y la respuesta vibracional. Se utilizaron mallados que variaron entre 5000 y 8000 elementos, considerando los diferentes espesores de material depositado.

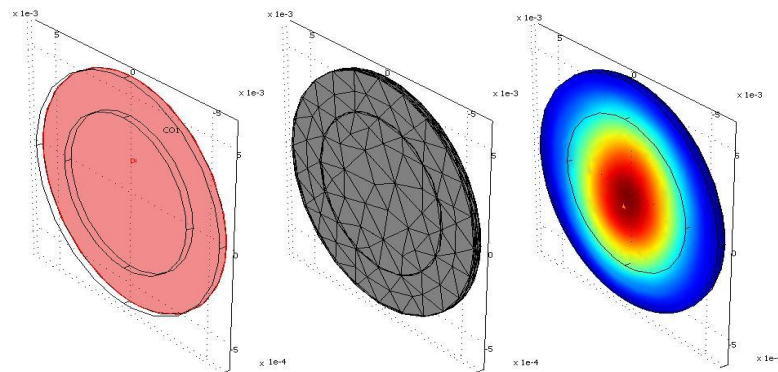


Figura C.5: Aspecto físico del disco de cuarzo con deposición de 20 μ m de parylene (rojo)(izq.), mallado (centro) y respuesta vibracional (der.).

Se utilizaron mallados que variaron entre 5000 y 8000 elementos, considerando los diferentes espesores de material depositado. La f_r se encontró en aproximadamente 4.992MHz, estableciendo un corrimiento de frecuencia de 38.2kHz.

Este resultado se lo contrastó con el corrimiento analítico que arrojó un valor de 36.851kHz; esto significa un error del 3.6%. Los corrimientos muestran un error promedio de 3.66% con una desviación estándar de 4.39%.

C.3.1.3 Conclusiones

Para el caso de la QCM, la pequeña diferencia (0.64%) existente entre la frecuencia de resonancia obtenida con el modelo circuital, como así también la analítica, y la obtenida con el modelo de elementos finitos se debe a las distintas formas encontradas en la caracterización del cristal de cuarzo: en este último modelo las características del cuarzo se ven representadas de forma más completa por la matriz elástica, la dieléctrica y la matriz de acoplamiento piezoeléctrico para un sólido. Los resultados obtenidos con el modelo circuital y el de elementos finitos, para la deposición de Parylene® entre 1µm-20µm, se aproximan con mucha exactitud a las soluciones analíticas encontradas (error promedio de 3.66%).

C.3.2 Microsensor de masa de PVDF

Hoy en día se encuentra en constante crecimiento el desarrollo de resonadores acústicos de volumen de película delgada (FBAR). La tecnología FBAR nace como una extensión directa de los resonadores de cristal de cuarzo. Esta tecnología permite reducir el espesor de las capas piezoeléctricas de los resonadores y así aumentar su frecuencia de resonancia. Dentro de esta tecnología se encuentran los sensores de polímeros piezoeléctricos. El polivinilidenofluoruro (PVDF) y sus copolímeros son los polímeros con mayor efecto piezoeléctrico.

En esta sección se realizó un análisis del comportamiento de un sensor piezoeléctrico polimérico FBAR de PVDF para diferentes cantidades de material depositado en su superficie. Se implementó el modelo de Mason y se contrastaron los resultados del modelo FEM.

C.3.2.1 Metodología

Se implementaron las ecuaciones del modelo de Mason en Matlab y los resultados se contrastaron con los obtenidos con el modelo FEM. De esta forma se obtuvieron gráficas mostrando la admitancia equivalente y la fase del resonador en función de la frecuencia. Se realizaron las siguientes simulaciones:

a) PVDF sin material depositado

Se obtuvo la f_r . Para el disco PVDF también se consideraron despreciables los efectos del amortiguamiento mecánico. Se resolvieron las variables desplazamiento (u_x , u_y , u_z) y el potencial eléctrico (V) y se realizó un análisis de respuesta en frecuencia.

b) PVDF con deposición de Parylene®

Se ubicó sobre una de las caras principales del disco de PVDF otro disco de igual radio y espesor variable representando el Parylene[®] depositado (rango 80-400nm). Se obtuvieron los corrimientos de frecuencia

C.3.2.2 Resultados

a) PVDF sin material depositado

Se encontró para el modelo FEM que la frecuencia de resonancia se aproxima a los 45.8MHz. Esta fr se halló para un mallado de 5000 elementos. Presentó un error de 0.82% respecto a la obtenida con el Modelo de Mason.

d) PVDF con deposición de Parylene[®]

Para el modelo FEM se utilizaron mallados que variaron entre 4000 y 6000 elementos, considerando los diferentes espesores de material depositado. La comparación con los valores del Modelo de Mason muestran un error promedio de 4.18% con una desviación estándar de 4.55%. Las frecuencias de resonancia y antirresonancia fueron:

$$f_r = 45.802 \text{ MHz}$$

$$f_a = 45.803 \text{ MHz}$$

La frecuencia de resonancia del sistema se muestra en la Figura C.6:

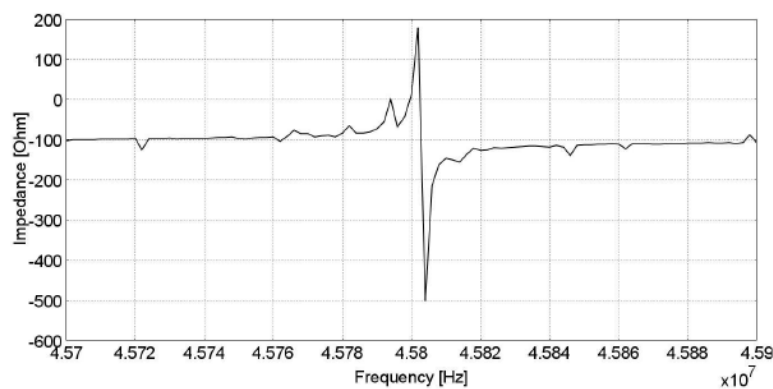


Figura C.6: Respuesta en frecuencia del resonador de PVDF sin carga

La f_r obtenida con el Modelo de Mason presenta una desviación relativa de 1.10% con respecto a este caso.

C.3.2.3 Conclusiones

En este caso del FBAR con PVDF, se ha visto que los resultados obtenidos con el modelo de elementos finitos se aproximan con mucha exactitud a las soluciones obtenidas con el Modelo de Mason. Teniendo en cuenta la simplicidad de implementación del Modelo de Mason, queda expuesta la ventaja de su aplicación.

C.3.3 Microsensor gravimétrico de nitruro de aluminio (AlN)

Para bajar costos y mejorar la compatibilidad de la electrónica asociada, se requiere que los sensores estén integrados con la electrónica. Uno de los materiales mayormente utilizado para aplicaciones electroacústicas es el nitruro de aluminio (AlN) debido a su excelente calidad para la fabricación de resonadores acústicos.

En esta sección se realizó un análisis del comportamiento de un sensor piezoeléctrico FBAR de AlN para diferentes cantidades de proteínas (estreptavidina) depositadas en su superficie en un medio acuoso. Se llevó a cabo el diseño y simulación utilizando el modelo de Mason.

C.3.3.1 Metodología

Las ecuaciones del modelo de Mason fueron implementados en *Matlab*. Se realizaron las siguientes simulaciones: *a) Microbalanza de AlN sin carga*: se obtuvo la impedancia de entrada en función de la frecuencia para el resonador piezoeléctrico, *b) Microbalanza de AlN con deposición de proteínas*: se obtuvieron los corrimientos en frecuencia para la microbalanza con estreptavidina como proteína, y *c) Microbalanza de AlN con deposición de proteínas en un medio acuoso*: se obtuvieron los corrimientos en frecuencia.

C.3.3.2 Resultados

a) Microbalanza de AlN sin carga

Se observó que la frecuencia de resonancia se encuentra en los 1.5043GHz.

b) Microbalanza de AlN con deposición de proteínas:

Con el fin de analizar el comportamiento de una capa viscoelástica, se llevó a cabo la respuesta de frecuencia del sistema para un film de estreptavidina con espesores de 50 nm, 100 nm y 150 nm como se muestra en la Figura C.7:

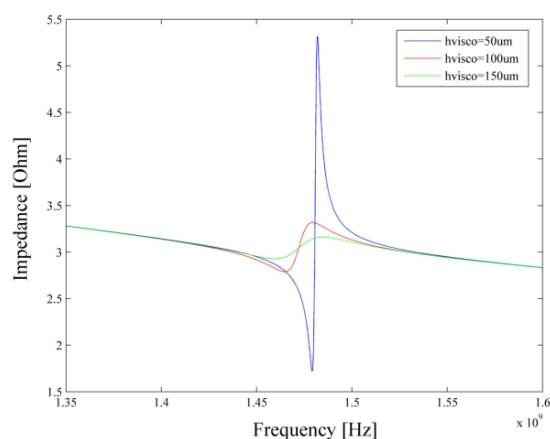


Figura C.7: Respuesta en frecuencia del sensor de AIN para films de estreptavidina de 50nm, 100nm y 150nm.

c) AIN con deposición de proteínas en un medio líquido

Se manifiesta la atenuación del factor de calidad del resonador debido a la carga de agua. Se puede observar también que la frecuencia de resonancia no cambia con la adición de un medio líquido; la capa de agua sólo proporciona pérdidas en el sistema pero no tiene influencia sobre los cambios de frecuencia.

C.3.3.3 Conclusiones

Al incluir el medio líquido sobre la superficie del resonador se evidencia la disminución del factor de calidad de la respuesta en frecuencia debido a que la resonancia es de cuasi-corte, ya que posee componentes de resonancia longitudinal como se ha visto en la literatura.

Se concluyó que el Modelo de Mason es una muy buena alternativa al modelo analítico y al circuital cuando los materiales utilizados no son lo suficientemente rígidos ni delgados.

C.3.4 Microsensor de presión de PVDF

Los sensores piezoeléctricos han sido ampliamente utilizados para medir fuerza debido a su sensibilidad y bajo costo. Estos generan señales eléctricas en respuesta a cambios en la fuerza aplicada trabajando como sensores de fuerza dinámicos. Cuando se los utiliza como sensores de fuerza estáticos, el flujo de cargas y la tensión eléctrica resultante decaen a cero. El tiempo de relajación depende así del material y tamaño del dispositivo, la resistencia eléctrica de la circuitería externa y la resistencia parasítica del sensor.

Para superar este inconveniente se han propuesto varias soluciones basadas en circuitos electrónicos para compensar la pérdida de carga. Para obtener un dispositivo más sencillo,

se ha hecho uso de un parámetro físico independiente del tiempo: la frecuencia de resonancia del sensor piezoeléctrico. Bajo este principio de funcionamiento se han desarrollado excelentes sensores de fuerza.

En esta sección se realizó un análisis del comportamiento de un sensor piezoeléctrico de PVDF sometido a diferentes valores de presión en su superficie. Se llevaron a cabo el diseño y simulación de modelos FEM para el FBAR con polímero PVDF. Se contrastaron los resultados con resultados experimentales de la bibliografía.

C.3.4.1 Metodología

Al considerar tensiones mecánicas aplicadas al piezoeléctrico, la ecuación de equilibrio presenta la siguiente forma:

$$\rho \ddot{u} = \nabla \cdot (T_C + T_0)$$

en donde T_C es el término correspondiente al tensor de tensiones completo y T_0 es el tensor de pre-stress, generalmente en función del espacio y no del tiempo. Este término se introduce de esta forma para modelar dispositivos que trabajan bajo pre-stress y para apreciar el efecto en la frecuencia de resonancia del mismo.

Este método fue desarrollado por Hughes, 1987 y consiste en la modificación de la matriz elástica \mathbf{c} debido al pre-stress. Aplicando esta modificación a la ley constitutiva, la matriz elástica modificada se puede expresar como se muestra a continuación:

$$T = T_C + T_0 = C \cdot S + T_0 = C_{\text{modif}} S$$

En este nuevo caso se debe utilizar un nuevo tensor de tensiones de 9x1 componentes que incluye los simétricos y los antisimétricos. Estos componentes rotacionales extras se agregaron para modelar el pre-stress.

C.3.4.2 Resultados

a) Microsensor de presión de PVDF sin carga:

Se encontró que la frecuencia de resonancia se aproxima a los 6.801MHz. Esta f_0 se halló para un mallado de 45456 grados de libertad.

b) Microsensor de presión de PVDF sometido a carga de presión

El rango de presiones utilizadas y los corrimientos de frecuencia respecto de la f_r para el modelo numérico y los resultados experimentales, se muestran en Tabla C.1:

Presión [MPa]	0	0.65	1.3	2.08
Corrimiento de frecuencia simulado [Hz]	0	1000	1500	2000
Corrimiento de frecuencia experimental [Hz]	0	80000	170000	270000

Tabla C.1: Corrimientos de frecuencia simulados y experimentales.

c) Comparación con análisis estático

Se realizó un análisis estático con una precarga de 300 MPa (Tabla C.2):

Tipo de análisis	Espesor del disco [μm]	Matriz elástica	f_r [MHz]
estático + armónico	94	c	7.88
armónico	110	c_{modif}	7.05

Tabla C.2: Resultados de la comparación entre los dos análisis realizados (estático+armónico y armónico).

C.3.4.3 Conclusiones

La frecuencia de resonancia para el disco de 94 μm de espesor debido a la precarga es de 7.88 MHz, valor muy cercano al del disco de 110 μm utilizando la matriz deformada (7.05 MHz). Con el modelo numérico se obtuvo un corrimiento en frecuencia esperado, evidenciándose una respuesta lineal de dicho corrimiento con la presión aplicada.

C.3.5 Microtransponder CMOS para microválvula implantable

En la Figura C.8 se muestra el diagrama esquemático de la microválvula. El regulador se ha diseñado para controlar la IOP variando la resistencia al flujo del humor acuoso por medio de la deflexión del diafragma. El regulador es conceptualmente una válvula normalmente cerrada. La resistencia hidráulica del regulador tiene un componente pasivo debido a los efectos de la presión del fluido en el diafragma y un componente activo, debido al cambio en la geometría. Cuando se aplica al actuador una diferencia de voltaje en el intervalo de 1-2V se produce una deformación en el rango de 1-3% de sus dimensiones iniciales.

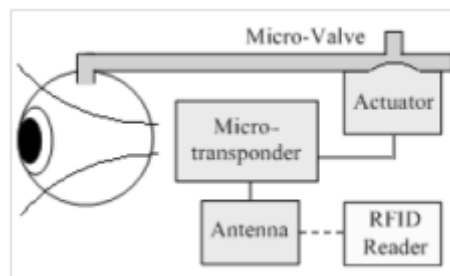


Figura C.8: Esquema de la microválvula para el tratamiento del glaucoma.

La activación del actuador se realiza de forma remotamente basada en los principios de la identificación por radiofrecuencia (RFID). En los últimos años, la tecnología RFID ha experimentado un rápido crecimiento en las áreas de la gestión de la cadena de suministro, control de acceso, transporte público, seguimiento de equipaje de las aerolíneas y aplicaciones biomédicas tales como sensores y actuadores implantables.

C.3.5.1 Resultados

Se presentó el diseño y simulación de un microtransponder integrado CMOS para la energización de una microválvula activa para el tratamiento del glaucoma. Los resultados de la simulación muestran que el transponder opera para detectar señales Amplitude Shift Keying (ASK) con un índice de modulación del 20% al 80% para una velocidad de datos de 500 kHz con una frecuencia de 13.56MHz de la señal portadora, con la posibilidad de variar la tensión de acción de la membrana del polímero.

La Figura C.9 muestra el layout completo del circuito del Microtransponder, el cual ocupa 2.25 mm².

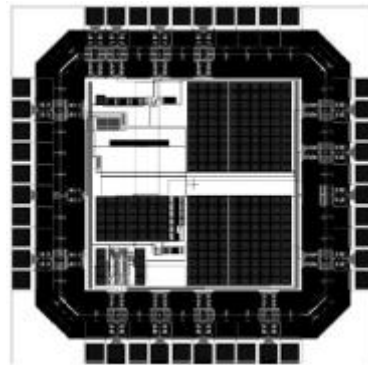


Figura C.9: Layout del circuito del microtransponder.

C.3.5.2 Conclusiones

En este trabajo se presentó el diseño y simulación de un microtransponder integrado CMOS para aplicaciones de dispositivos médicos implantables. El mismo se diseñó utilizando la tecnología AMI C5 (0.5µm) y actualmente se encuentra en proceso de fabricación. El circuito convierte señales de RF a DC para el accionamiento de un polímero conjugado, el cual presenta grandes deformaciones para pequeños voltajes. El transponder opera para detectar una señal ASK con índice de modulación del 20% al 80% para una velocidad de datos de 500 KHz y una señal portadora de 13.56MHz. Los resultados de la simulación muestran que el convertidor DC toma la señal demodulada para generar una tensión continua en el intervalo de -0.5V a 1V para el accionamiento del polímero.

C.4 Fabricación y Caracterización

C.4.1 Resonador de PVDF

Como ya se comentó, la piezoelectricidad puede ser obtenida orientando las moléculas dipolares de polímeros polares como el PVDF en la misma dirección. El PVDF puede hacerse piezoeléctrico ya que el flúor es mucho más electronegativo que el carbono. Los átomos de flúor atraen electrones de los átomos de carbono a los cuales están unidos. Los grupos $-CF_2-$ en la cadena son muy polares, por lo que cuando se encuentran sometidos a un campo eléctrico, se alinean.

El objetivo general de esta experimentación es la obtención de la respuesta en frecuencia de un sensor piezoeléctrico. Para llevar a cabo este objetivo es necesario medir la impedancia y la fase del sensor (resonador piezoeléctrico) en función de la frecuencia y así hallar su frecuencia de resonancia Figura C.10.

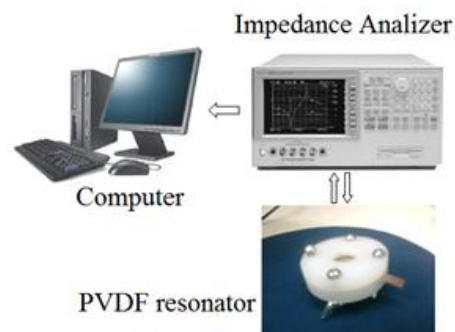


Figura C.10: Setup para el resonador de PVDF.

C.4.1.1 Fabricación

El disco es un polímero piezoeléctrico de PVDF de 110 μm de espesor. El mismo se comercializa en hojas con ambas caras principales metalizadas con cobre o plata. El metalizado de plata se lleva a cabo por impresión de tinta y tiene un espesor de 6 μm , mientras que el metalizado de cobre se obtiene por deposición de sputtering, llegando a un espesor de 70 nm.

C.4.1.2 Caracterización

Con el fin de caracterizar estos discos resonantes, se llevaron a cabo diferentes experimentos teniendo en cuenta diferentes tamaños de disco y selección del material de electrodo. Posteriormente se realizó un análisis de los diferentes casos.

a) Electrodo de Cu vs. electrodo de Ag

En este caso se comparó la respuesta en frecuencia (impedancia vs. frecuencia) de dos discos piezoeléctricos de igual diámetro pero con diferentes tipo de electrodos (cobre y plata). Se estimuló con una señal de 1V en un rango de frecuencia entre 7-12 MHz a temperatura ambiente. Los resultados se muestran en la Figura C.11.

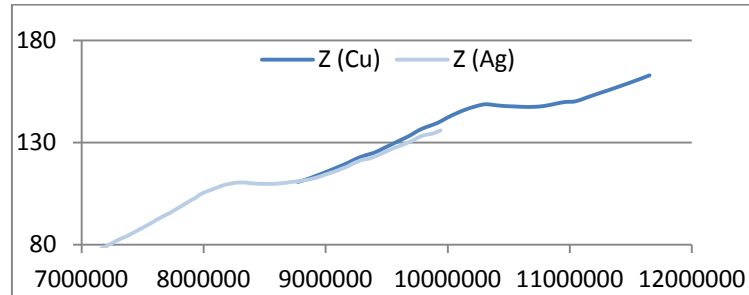


Figura C.11: PVDF con Electrodo de Cu vs. PVDF con electrodo de Ag.

Claramente se puede observar que el disco con electrodos de plata resuena a frecuencia menor que el que posee electrodos de cobre. Como se intuye, y teniendo presente la ecuación de Sauerbrey, esta disminución se debe al mayor espesor que presenta la película de plata, produciendo un corrimiento de la frecuencia de resonancia con respecto al disco con electrodos de cobre.

b) Diámetro mayor vs. diámetro menor

En este caso se comparó la respuesta en frecuencia de dos discos piezoeléctricos de diferente diámetro pero con igual tipo de electrodo (plata). Se estimuló con una señal de 1V en un rango de frecuencia entre 5-11 MHz a temperatura ambiente.

El disco de menor diámetro presentó una curva de respuesta en frecuencia más marcada que el disco mayor. Esto se cree se debe a la menor energía necesaria para excitar al resonador debido a la menor masa.

c) Deposición de película delgada

En este experimento se depositó sobre una de las caras principales de un disco con electrodos de cobre, un film delgado y rígido. Se utilizó fotorresina (AZ 1500) depositada mediante spinning y posterior horneado. Se comparó la respuesta en frecuencia del disco con y sin deposición de fotorresina. Se estimuló con una señal de 1V en un rango de frecuencia entre 8-13 MHz a temperatura ambiente.

Se pudo observar que el disco con deposición de fotorresina resuena a frecuencia menor que el que no la posee. Como sentencia la ecuación de Sauerbrey, esta disminución se debe a la masa depositada, produciendo un corrimiento de la frecuencia de resonancia.

C.4.1.3 Extracción de parámetros

Aquí, los parámetros del disco de PVDF se obtuvieron experimentalmente y con el modelo FEM. Se obtuvo la respuesta de frecuencia experimental del disco. Las propiedades elásticas, dieléctricas y piezoeléctricas del polímero piezoeléctrico obtenidas a partir de datos experimentales de la literatura se utilizaron en el modelo FEM; los valores se tunearon para ajustar la respuesta de frecuencia simulada con la experimental. Los valores así obtenidos se utilizaron para caracterizar el disco PVDF y obtener un conjunto de parámetros de importancia, como es el caso de la constante de acoplamiento electromecánico kt y el factor de calidad Q .

C.4.1.4 Resultados

Las principales constantes materiales se variaron para hacer coincidir la respuesta en frecuencia experimental. Como paso final, el resto de las constantes se variaron y fue obtenida la respuesta en frecuencia experimental.

C.4.1.5 Conclusiones

Se extrajo un conjunto de constantes importantes mediante el ajuste de los parámetros materiales complejos en el modelo FEM para el resonador de PVDF. Los valores de kt y Q han demostrado estar de acuerdo con la hoja de datos del material.

El modelo FEM ha demostrado ser una herramienta fiable para modelar y simular geometrías no triviales que incluyen materiales con altas pérdidas viscoelásticas internas, como el caso del PVDF.

La coincidencia de los valores extraídos con la hoja de datos del material revela una buena precisión para el procedimiento desarrollado. Esto motiva la aplicación del modelo FEM para el resonador de PVDF.

C.4.2 Resonador piezoeléctrico de AlN

C.4.2.1 Proceso de deposición

Una capa de Pt se hizo crecer por sputtering en la parte superior de una película de Ti depositada sobre una superficie de SiO₂. La película de Ti proporciona una capa de adhesión para el crecimiento del AlN altamente orientado den el eje c (002), el cual ofrece el mayor coeficiente piezoeléctrico. La capa de Pt sirve como electrodo inferior y superior para aplicar voltaje y excitar al piezoeléctrico.

El AlN (002) se depositó sobre el Pt a diferentes temperaturas, mediante sputtering utilizando target de Al y plasma de Ar para producir iones Al en una atmósfera rica en N₂ y generar las películas de AlN. Se llevaron a cabo muchos experimentos hasta dar con el juego de parámetros con la mejor performance del AlN. Se probó además con diferentes películas buffer sobre el sustrato de silicio, como el SiO₂ y Si₃N₄.

C.4.2.2 Caracterización

Una manera rápida y contundente de conocer la estructura cristalina de un material y su orientación preferencial es haciendo uso de Difracción de rayos X (XRD). Es una técnica no destructiva que revela información detallada de la composición química y estructura cristalina de un material. Los átomos de un material están en un arreglo tridimensional que forman una serie de planos paralelos separados una distancia que depende de la naturaleza de cada material. Cuando un haz de rayos X monocromático es proyectado en el material, se obtiene un patrón de difracción de acuerdo con la ley de Bragg:

$$n \lambda = 2 d \sin(\theta)$$

donde λ es la longitud de onda del haz de rayos X, d es la distancia entre capas atómicas del cristal, θ es el ángulo de incidencia y n es un entero.

C.4.3 Integración de AlN sobre películas de UNCD

Es importante integrar las películas piezoeléctricas con los materiales utilizados en dispositivos médicos. El Diamante Ultrananocristalino (UNCD) es un material multifuncional desarrollado y patentado en Argonne National Laboratory que ha demostrado ser extremadamente bioinerte y biocompatible. Se espera que la integración UNCD-AlN sea una herramienta valiosa para el desarrollo de una nueva generación de BioMEMS en el campo de la terapia médica.

En esta sección se llevó a cabo la integración de AlN con UNCD, UNCD con nitrógeno incorporado (N-UNCD), así como con UNCD dopado con boro (B-UNCD). El estudio se centró en la determinación del proceso que produjera la película de AlN integrado en capas de UNCD con el mayor coeficiente piezoeléctrico. Los métodos investigados incluyeron: a) deposición directa de AlN sobre Pt/Ti/UNCD sin pulido químico ni mecánico adicional (CMP) y b) un método con etapa CMP que produjera AlN (002) con el mayor coeficiente piezoeléctrico debido al control de orientación de la película. La investigación propuesta se centra en el desarrollo de dispositivos biomédicos que aprovechen tanto, las propiedades piezoeléctricas y biocompatibilidad de AlN y la biocompatibilidad y la multifuncionalidad del UNCD, N-UNCD y B-UNCD para crear una nueva generación de dispositivos de administración de fármacos.

C.4.3.1 Proceso de deposición

a. Deposición de Pt y AlN

Los films de AlN (002) se depositaron sobre Pt a aproximadamente 500° C, utilizando sputtering con target de Al en atmósfera de N₂. Después de 5 horas de deposición, el espesor de AlN fue de 417 nm, con una tasa de deposición de 83,4 nm/h. Esta velocidad se ve afectada por el bajo flujo de Ar usado que reduce la cantidad de iones pesados que impactan sobre el objetivo. El listado de los parámetros de deposición se puede apreciar en la Tabla C.3:

Parámetro	Material		
	AlN	Pt	Ti
Base pressure (Torr)	$<1 \times 10^{-7}$	$<1 \times 10^{-7}$	$<1 \times 10^{-7}$
Process pressure (mTorr)	3	5	5
Power (W)	150	150	150
Substrate temperature (°C)	500	25	25
Ar flow (sccm)	3	26	26
N ₂ flow (sccm)	20	0	0
Target	Al (99.999%)	Pt (99.99%)	Ti (99.995%)
Target-substrate distance (cm)	10	11	11

Tabla C.3: Parámetros de deposición de AlN.

La Figura C.12 (parte superior) muestra la sección transversal SEM de las películas de AlN crecidas en diferentes sustratos con diferente rugosidad. Los espectros de difracción de rayos X para cada una de las muestras también se proporcionan en la Figura C.12 (parte inferior). Estos valores indican la influencia de la rugosidad del sustrato para producir películas de AlN (002).

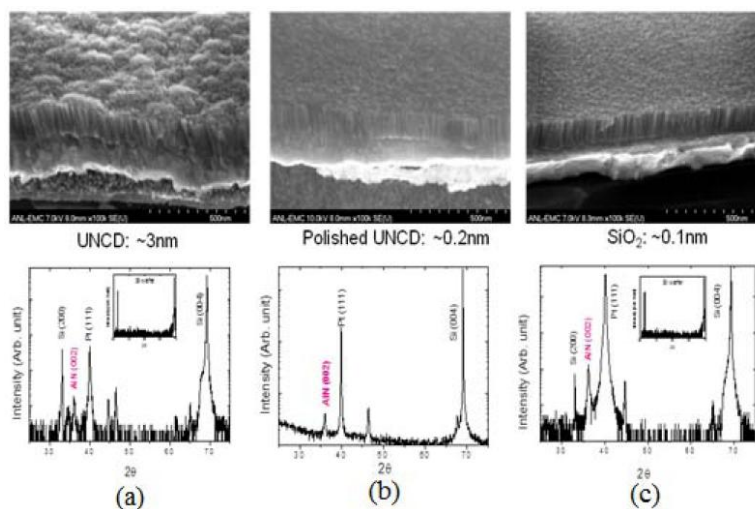


Figura C.12: Sección transversal SEM del crecimiento de AlN en diferentes sustratos y los correspondientes espectros XRD para cada sustrato.

C.4.3.2 Respuesta piezoeléctrica de los films de AlN

El coeficiente piezoeléctrico de los films de AlN depositados en UNCD, N-UNCD y B-UNCD se midió usando la técnica de PFM. Estas mediciones revelaron una piezorespuesta uniforme; los films de AlN crecidos sobre UNCD y N-UNCD mostraron un coeficiente piezoeléctrico de 1.91 pm/V y 1.97 pm/V respectivamente, mientras que los films de AlN crecidos en las superficies CMP de B-UNCD mostraron un coeficiente piezoeléctrico de 5.3 pm/V, el más alto entre los reportados en la actualidad para las películas de AlN.

C.4.3.3 Conclusiones

La investigación descrita en esta sección proporciona información para la comprensión de los procesos físicos y químicos fundamentales que intervienen en la integración de las películas de AlN piezoeléctrico con UNCD, N-UNCD y B-UNCD. Los films de AlN depositados sobre UNCD y N-UNCD exhiben relativamente buena orientación (002) debido a la rugosidad superficial de 5-10 nm, que es el tamaño de los granos; aún requieren un espesor de película de AlN ≥ 400 nm para alcanzar la orientación (002) del ALN. En este aspecto, el CMP B-UNCD, con rugosidad superficial rms de aproximadamente 0.2 nm que se utiliza como sustrato, produjo orientación (002) del ALN a espesores tan delgados como 80 nm. Además exhibe un coeficiente piezoeléctrico de 5.3 pm/V, el mayor alcanzado hasta el día de hoy.

C.4.4 FBAR de AlN sobre UNCD

Como se ha mencionado a lo largo del desarrollo de esta Tesis Doctoral, uno de los objetivos principales de este trabajo radica en el desarrollo de un resonador FBAR como sensor de masa. Basándose en las grandes ventajas que presentan el AlN y el UNCD para el desarrollo propuesto, se utilizó la integración de estos materiales para generar membranas resonantes con características novedosas.

El esquema del dispositivo se puede apreciar en la Figura C.13, en donde se puede ver el electrodo superior de similares características que el inferior descrito en las secciones anteriores. Se utilizó sustrato de silicio como soporte para las capas depositadas.

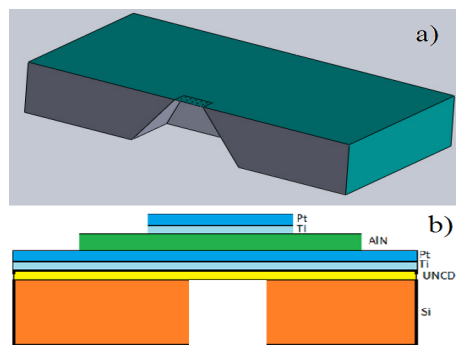


Figura C.13: FBAR de AlN sobre UNCD. a) esquema 3D de un corte longitudinal de la membrana de UNCD sobre el sustrato de silicio y b) vista lateral del esquema del dispositivo terminado.

C.4.4.1 Máscaras

Para la fabricación de las máscaras se utilizó el editor de layouts del software *Tanner EDA*. Se fabricaron tres juegos de máscaras para la totalidad del dispositivo:

- Máscara 1: conformado de material piezoeléctrico de AlN
- Máscara 2: conformado de electrodo superior de Pt/Ti
- Máscara 3: conformado de cavidad posterior en sustrato de Si

Para el diseño de estas máscaras se tuvo que tener en cuenta el material a atacar y el método utilizado. Ya que el sustrato usado es silicio, una forma muy utilizada para atacarlo es usando ataque húmedo con hidróxido de potasio (KOH). Para esto hay que tener en cuenta que esta base ataca al Si preferencialmente en el plano [100], produciendo el característico ataque anisotrópico en forma de V con las paredes que forman un ángulo de 54.7° respecto a la superficie

Una vez finalizado el diseño del layout de la máscara, se procedió a la fabricación de la misma mediante un generador de patrones láser. Se generó el patrón sobre fotorresina en una máscara de cromo en cuarzo de 125 mm de lado durante 24 hs. Posteriormente se procedió a revelar la fotorresina no polimerizada y acto seguido se atacó la película de cromo.

C.4.4.2 Cavidad

Para lograr la cavidad se tuvieron que llevar a cabo varios pasos de fabricación:

- *Crecimiento de UNCD*: Se depositó 400 nm de UNCD en la cara frontal de la oblea de silicio (N-type mirror polished Si (100)). El UNCD además de servir como sustrato para el AlN, cumple la función de stop layer en el ataque húmedo del silicio para la cavidad.
- *Deposición Si_3N_4* : como máscara para el ataque húmedo del silicio en la conformación de la cavidad se usó Si_3N_4 comercial, pulido, de baja tensión residual. Para generar el

patrón se usó photoresist spin coating con S1813, exposición UV, remoción de la fotorresina y ataque seco de Si_3N_4 en CF_4 -plasma.

- *Deposición de Pt/Ti*: Para el electrodo de base se usó Pt con Ti como capa de adhesión.
- *Deposición de AlN*: Se depositó AlN como se describió en secciones anteriores.
- *AlN pattern*: para llegar al patrón de AlN se realizó un ataque seco (RIE Oxford tool).
- *Electrode pattern*: se efectuó lift off con fotorresina y máscara diseñada para conformar el electrodo superior.
- *Cavidad*: Se realizó ataque húmedo mediante una base fuerte como el KOH para atacar el silicio y generar la cavidad resonante. Se utilizó protección hermética para no afectar la cara superior ya trabajada. Se dejó actuar por 9 hs a temperatura de 80°C y agitador a 250 rpm.

En la siguiente gráfica (Figura C.14) se puede apreciar el primer prototipo de cavidades, donde se usó UNCD solamente como membrana sobre el sustrato de silicio:

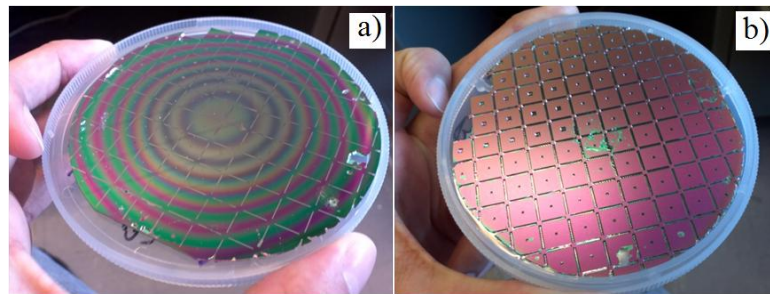


Figura C.14: Cavidades con membranas de UNCD. a) Cara frontal mostrando el film de UNCD y b) cara posterior mostrando las cavidades de diferentes tamaños dentro de los dices.

C.4.4.3 Caracterización

a. Microscopía óptica

Se pudo corroborar la calidad del ataque al silicio por parte del KOH y las dimensiones de las membranas. Las dimensiones finales de las membranas no son las estimadas en los cálculos. Esto es debido principalmente a los undercuts que se producen debajo del stop layer de UNCD que están en el rango de $50\text{-}170\ \mu\text{m}$.

b. Microscopía electrónica de barrido (SEM)

Con esta herramienta se permite visualizar con absoluta exactitud la geometría de dispositivos en la micro y nanoescala. En la gráfica a continuación, se puede observar un corte de la membrana (quedando en voladizo) de AlN sobre UNCD usando Pt/Ti como capa de adhesión (Figura C.15). Se puede apreciar además, la rugosidad que presenta la superficie de AlN.

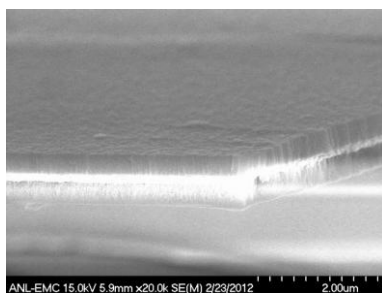


Figura C.15: Corte de la membrana de AlN sobre UNCD usando Pt/Ti como capa de adhesión.

C.4.5 Membrana de UNCD para delivery de drogas

Los sistemas de suministro de fármacos son dispositivos médicos que proporcionan ventajas médicas y comerciales. Esta sección se centra en el diseño, fabricación y caracterización de membranas UNCD para dispositivos pasivos y activos de suministro de drogas

Las membranas de UNCD fueron fabricadas en una sala limpia usando deposición de película delgadas y técnicas de microfabricación, incluyendo: 1) crecimiento de la película de UNCD por MPCVD sobre sustrato de Si, 2) fotolitografía usando una máscara especialmente diseñada para definir una ventana en la parte posterior de la oblea, 3) ataque por iones reactivos (RIE) para el patrón de la máscara de Si₃N₄ para mantener la cavidad de la membrana de UNCD en la parte posterior de la oblea, y 4) el ataque químico húmedo para crear la cavidad que sostiene la membrana de UNCD. Se fabricaron membranas cuadradas de 200-1000 μm de tamaño con un espesor que oscila entre 100-500 nm y se caracterizó por espectroscopia de Raman, microscopía óptica, SEM y reflectometría.

C.5.5.1 Fabricación y caracterización

La fabricación de dispositivos pasivos para delivery de drogas se realizó utilizando FIB para producir orificios de tamaño micrométrico en las membranas de UNCD para permitir la difusión controlada de fármacos a través de esta última (Figura C.16).

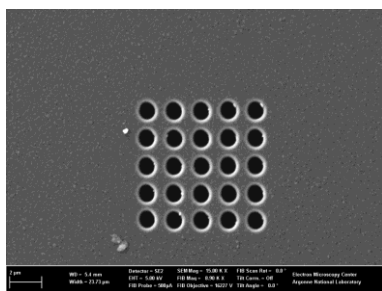


Figura C.16: Micrografía SEM de la fabricación de dispositivos pasivos

C.5 Conclusiones

En la simulación de la QCM, la pequeña diferencia (0.64%) existente entre la frecuencia de resonancia obtenida con el modelo circuital, como así también la analítica, y la obtenida con el modelo de elementos finitos se debe a las distintas formas encontradas en la caracterización del cristal de cuarzo. Los resultados obtenidos con el modelo circuital y el de elementos finitos, para la deposición de Parylene[®] se aproximan con mucha exactitud a las soluciones analíticas encontradas.

Respecto al FBAR con PVDF, se ha visto que los resultados obtenidos con el modelo de elementos finitos se aproximan con mucha exactitud a las soluciones obtenidas con el Modelo de Mason. Teniendo en cuenta la simplicidad de implementación del Modelo de Mason, queda expuesta la ventaja de su aplicación. La fabricación del resonador de PVDF mostró la extracción de un conjunto de constantes importantes mediante el ajuste de los parámetros materiales complejos en el modelo FEM para el resonador de PVDF. Los valores de k_t y Q han demostrado estar de acuerdo con la hoja de datos del material.

En cuanto a las simulaciones realizadas para el microsensar gravimétrico de nitruro de aluminio, al incluir el medio líquido sobre la superficie del resonador se evidencia la disminución del factor de calidad de la respuesta en frecuencia debido a que la resonancia es de cuasi-corte, ya que posee componentes de resonancia longitudinal como se ha visto en la literatura.

En el caso del Microtransponder CMOS para microválvula implantable, se presentó el diseño y simulación de un microtransponder integrado CMOS para aplicaciones de dispositivos médicos implantables. El mismo se diseñó utilizando la tecnología AMI C5 (0.5 μm) y actualmente se encuentra en proceso de fabricación. El circuito convierte señales de RF a DC para el accionamiento de un polímero conjugado, el cual presenta grandes deformaciones para pequeños voltajes. El transponder opera para detectar una señal ASK con índice de modulación del 20% al 80% para una velocidad de datos de 500 kHz y una señal portadora de 13.56 MHz. Los resultados de la simulación muestran que el convertidor DC toma la señal demodulada para generar una tensión continua en el intervalo de -0.5 V a 1 V para el accionamiento del polímero.

La investigación descrita en el Resonador piezoeléctrico de AlN, proporciona información para la comprensión de los procesos físicos y químicos fundamentales que intervienen en la integración de las películas de AlN piezoeléctrico con UNCD, N-UNCD y B-UNCD. Los films de AlN depositados sobre UNCD y N-UNCD exhiben relativamente buena orientación (002) debido a la rugosidad superficial de 5-10 nm, que es el tamaño de los granos; aún requieren un espesor de película de AlN ≥ 400 nm para alcanzar la orientación (002) del ALN. En este aspecto, el CMP B-UNCD, con rugosidad superficial rms de aproximadamente 0.2 nm que se utiliza como sustrato, produjo orientación (002) del ALN

a espesores tan delgados como 80 nm. Además exhibe un coeficiente piezoeléctrico de 5.3 pm/V, el mayor alcanzado hasta el día de hoy.

Se mostró experimentalmente la potencialidad de los diseños de los sistemas de suministro de fármacos, caracterizando membranas basadas en UNCD y heteroestructuras tales como AlN/Pt/Ti/SiO₂/Si y membranas perforadas para la fabricación de dispositivos pasivos.

Doctorado en Ingeniería
mención mecánica computacional

Título de la obra:

**Diseño, Simulación, Fabricación y Caracterización de
Microsensores de Masa Integrables a Microválvula para el
Tratamiento de Glaucoma**

Autor: Martín Zalazar

Lugar: Santa Fe, Argentina

Palabras Claves:

Piezoelectric Resonator, BioSensor, Microfabrication,
MicroElectroMechanical Systems, Quartz Crystal Microbalance,
Aluminum Nitride, Ultrananocrystalline Diamond,
Polyvinylidene fluoride, Parameter Extraction,
Numerical Simulation, Finite Element Method.